UNIVERSITÀ
DEGLI STUDI
DI PADOVA

UNIVERSITÀ
DEGLI STUDI
DI NAPOLI
FEDERICO II

RESEARCH DOCTORATE IN FUSION SCIENCE AND ENGINEERING

CYCLE XXXVIII

Numerical exploration of fast ion distributions in fusion devices and their characterization through various mixes of NBI and ICRH systems in view of ITER operations

Supervisors

Dr. Tommaso Bolzonella

Dr. Mireille Schneider

Dr. Pietro Vincenzi

Academic supervisor

Prof. Flavio Seno

Ph.D. Candidate

Chiara De Piccoli

Academic Year 2025/2026

A Maddalena, Benedetta e Pietro,
con la speranza che la ricerca di oggi
contribuisca a costruire loro un domani
migliore, sostenibile e in pace.

“Nothing in life is to be feared;
it is only to be understood.”
— Marie Curie

This thesis was carried out with the financial support of the
ITER Organization and Consorzio RFX, which jointly funded the
doctoral scholarship.

ABSTRACT

Energetic particles (EPs) play a crucial role in magnetically confined fusion plasmas, as they contribute to sustain fusion-relevant temperatures, as well as provide current and torque. EPs can be generated by an auxiliary heating systems, such as the Neutral Beam Injection (NBI) and the Ion Cyclotron Resonance Heating (ICRH) systems, and are also produced intrinsically by fusion reactions, for instance in the form of alpha particles. Their interaction with plasma backgrounds and waves can induce instabilities, leading to enhanced transport, energy losses, and reduced confinement. A detailed characterisation of EP dynamics and their distribution functions is therefore essential to maximise their beneficial effects while mitigating adverse impacts on plasma performance.

The aim of this thesis is to characterise the behaviour and distribution functions of EPs in tokamak plasmas, with particular emphasis on populations generated by NBI and ICRH systems and their combined operation. State-of-the-art numerical tools are used to study three major devices: JET, DTT, and ITER, each requiring distinct modelling strategies. Part of this work is performed within the Integrated Modelling and Analysis Suite (IMAS). In JET, simulations are used to validate the modelling of ICRH-accelerated EPs through an updated implementation of the orbit-following Monte Carlo code ASCOT coupled with the RFOF wave–particle interaction operator. For DTT, the analysis focusses on NBI EPs and their impact on plasma performance. In ITER, both NBI and ICRH generated EPs are addressed, with particular attention to synergistic effects relevant to performance optimisation under reactor conditions. These studies support the optimisation of heating systems, assess the applicability of existing modelling tools in reactor-relevant regimes, and contribute to the development of new IMAS-compatible tools.

SOMMARIO

Le particelle energetiche (Energetic Particles, EPs) svolgono un ruolo cruciale nei plasmi da fusione a confinamento magnetico, poiché contribuiscono al mantenimento di temperature rilevanti per la fusione, oltre a fornire corrente e momento. Le EPs possono essere generate da sistemi di riscaldamento ausiliari, quali l'iniezione di fasci neutri (Neutral Beam Injection, NBI) e il riscaldamento a risonanza ciclotronica ionica (Ion Cyclotron Resonance Heating, ICRH), e sono inoltre prodotte intrinsecamente dalle reazioni di fusione, ad esempio sotto forma di particelle alfa. La loro interazione con il plasma di fondo e con le onde può indurre instabilità, portando a un aumento del trasporto, a perdite di energia e a una riduzione del confinamento. Una caratterizzazione dettagliata della dinamica delle EPs e delle loro funzioni di distribuzione è pertanto essenziale per massimizzarne gli effetti benefici e mitigare gli impatti negativi sulle prestazioni del plasma.

L'obiettivo di questa tesi è caratterizzare il comportamento e le funzioni di distribuzione delle EPs nei plasmi di tokamak, con particolare attenzione alle popolazioni generate dai sistemi NBI e ICRH e al loro funzionamento combinato. Per questo scopo vengono utilizzati strumenti numerici allo stato dell'arte per lo studio di tre dispositivi di primaria importanza: JET, DTT e ITER, ciascuno dei quali richiede strategie di modellazione distinte. Parte di questo lavoro è svolta nell'ambito dell'Integrated Modelling and Analysis Suite (IMAS). In JET, le simulazioni sono impiegate per validare la modellazione delle EPs accelerate da ICRH mediante un'implementazione aggiornata del codice Monte Carlo orbit-following ASCOT, accoppiato all'operatore di interazione onda–particella RFOF. Per DTT, l'analisi si concentra sulle EPs generate da NBI e sul loro impatto sulle prestazioni del plasma. In ITER, vengono considerate sia le EPs prodotte da NBI sia quelle da ICRH, con particolare attenzione agli effetti sinergici rilevanti per l'ottimizzazione delle prestazioni in condizioni di reattore. Questi studi supportano l'ottimizzazione dei sistemi di riscaldamento, valutano l'applicabilità degli strumenti di modellazione esistenti in regimi rilevanti per il reattore e contribuiscono allo sviluppo di nuovi strumenti compatibili con IMAS.

LIST OF ACRONYMS AND ABBREVIATIONS

ASCOT	Accelerated Simulation of Charged Particle Orbits in a Tokamak
BBNBI	Beamlet-Based Neutral Beam Injection
CoM	Constant of Motion
CPO	Consistent Physical Object
CYRANO	for CYclotron Resonance Analysis with No Obfuscation
DN	Double Null
DNB	Diagnostic Neutral Beam
DTT	Divertor Tokamak Test
ELM	Edge Localized Mode
EPs	Energetic Particles
FLR	Finite Larmor Radius
FP	Fokker-Planck
FW	First Wall
GC	Guiding Center
GO	Gyro-Orbit
HFS	High Field Side
HNB	Heating Neutral Beam
I/O	Input/Output
ICRF	Ion Cyclotron Range of Frequency
ICRH	Ion Cyclotron Resonance Heating
IDS	Interface Data Structure
IMAS	Integrated Modelling and Analysis Suite

JET	Joint European Torus
LCFS	Last Closed Flux Surface
LFS	Low Field Side
MPI	Message Passing Interface
N-NBI	Negative - Neutral Beam Injection
NBCD	Neutral Beam Current Drive
NBI	Neutral Beam Injection
PFC	Plasma Facing Component
P-NBI	Positive - Neutral Beam Injection
RF	Radio Frequency
RFOF	Radio Frequency interactions in Orbit Following code
RFP	Reverse Field Pinch
RMSE	Root Mean Square Error
SN	Single Null
SOL	Scrape-Off Layer
ST	Shine-Through
TTMP	Transit Time Magnetic Pumping

CONTENTS

CHAPTER

1

INTRODUCTION

Replicating on Earth the same nuclear processes that power the stars represents one of the most complex scientific and engineering challenges faced by humanity. Achieving this goal demands a high level of dedication from those working in the field, close collaboration between physicists and engineers to address both technological and physical aspects, and substantial support from parties committed to advancing this technology. This introduction will briefly present the fundamental principles of fusion science and technology and the international roadmap guiding its development, with a particular focus on the configuration of tokamak devices and the major experimental projects currently under construction. While much of this content may be familiar to those already working in the field, it is intended to offer a concise and informative overview for readers interested in a general understanding of fusion technology and the progress made toward its realization.

1.1 Nuclear fusion in the energetic panorama

Nuclear energy is presented as a promising investment to mitigate climate change [1]. In addition to being one of the safest and cleanest energy sources available, as accurately described in figure 1.1, it has the potential to generate a large amount of energy from a relatively small amount of fuel. Indeed, one gram of fusion fuel can produce energy equivalent to the combustion of several tons of fossil fuel and a few grams of fission fuel [2]. Since the 1960s, nuclear energy has contributed to the production of energy within the sustainable sources. However, its application greatly depends on the national energy strategy and available infrastructures. These differences are shown in figure 1.2, where the distributions of energy consumption by source across different continents are reported. The nuclear energy currently in use derives entirely from fission reactions. Indeed, fusion energy is still not exploitable as an energy source.

Contrary to fission, which involves the splitting of a nucleus into two parts, fusion, as suggested by the name itself, involves the merging of two nuclei. The release of energy that happens in these two processes can be used for the electricity production. The most favourable fusion reactions on Earth involve hydrogen (H) isotopes, such as deuterium and tritium (see equations 1.1-1.4).

$$D + T \rightarrow He^4 + n + 17.6\ MeV \tag{1.1}$$

$$D + He^3 \rightarrow He^4 + p + 18.34\ MeV \tag{1.2}$$

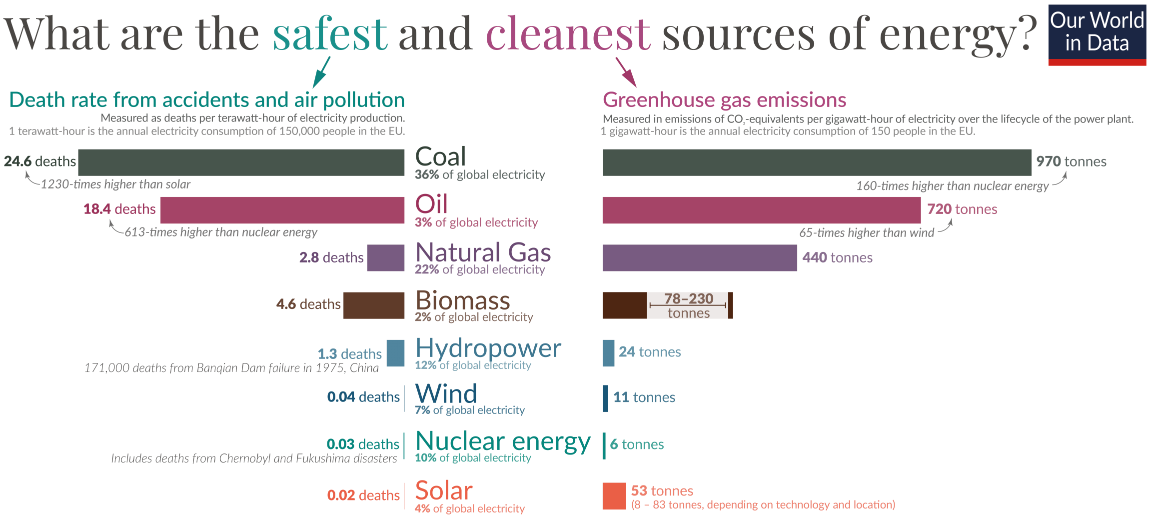

Figure 1.1: Death rates and greenhouse gas emissions data per source in Europe. Nuclear energy and wind represent the sources of energy with one of the lowest death rates and greenhouse gas emissions [3].

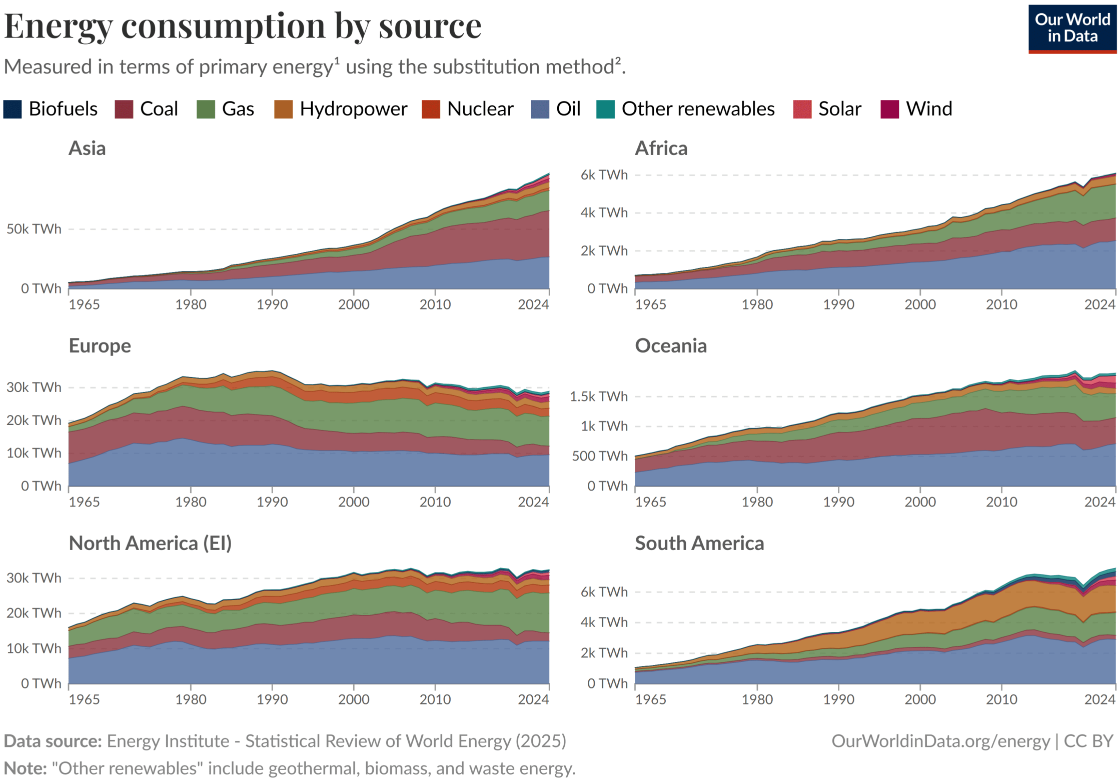

Figure 1.2: Energy consumption by source, divided per continent [4].

$$D + D \rightarrow He^3 + n + 3.27\ MeV \tag{1.3}$$

$$D + D \rightarrow T + p + 4.03\ MeV \tag{1.4}$$

Deuterium (D) is a stable isotope of hydrogen, with one proton and one neutron. It is found naturally in water, from which it can be easily extracted. Tritium (T) is instead an unstable isotope of H with a half-life of 12.3 years. It is composed of one proton and two neutrons and must be produced in a fusion reactor through lithium blankets ($Li^6 +\ n \rightarrow\ T +\ He^4 +$ 4.8 MeV). The products of reactions 1.1-1.4 are helium nuclei He^3 and He^4 (also referred to as alpha particles), neutrons or protons and kinetic energy derived from the mass-energy principle [2]. To obtain these products, the reactants of 1.1-1.4 must reach high temperature (on the order of 10-100 keV) to overcome the repulsive force that prevents two nuclei from merging. D-T reactions (1.1) are the primary focus of the current fusion research. Indeed, the large fusion cross-section σ, i.e. the probability that two particles will interact when they collide, of D-T reactions make them the most energetically favourable and probable reaction among the available options, as well illustrated in figure 1.3.

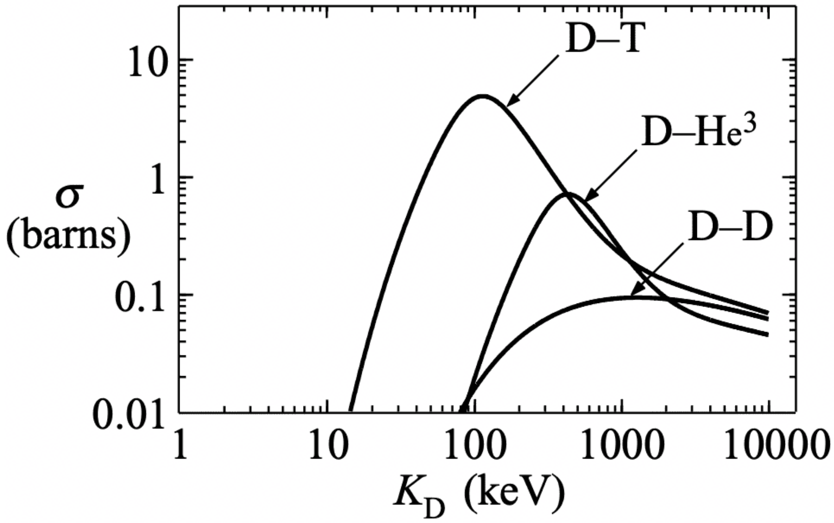

Figure 1.3: Experimental measured fusion cross sections σ for different fusion reactions (D-T, D-He^3, D-D) as a function of the kinetic energy of a deuterium ion K_D [2].

The technology of fission nuclear power plant is already well-developed and established, as strongly proven by the amount of fission power plants available all over the world. This is not the same for fusion, where several challenges are still open, both from a technological and scientific point of view, and a fusion power plant is not available yet. Several different experiments are running to develop the knowledge and expertise required to achieve the energy production from a fusion power plant, expected not before 2050. In addition to public research, growing interest and investment from the private sector have been observed lately, promising an acceleration of fusion power plant realization. In the next sections, a better description of how to produce fusion energy on Earth and a roadmap towards the first fusion power plant are provided.

1.2 Plasma confinement and heating

At 10-100 keV, the optimal temperature for fusion on Earth, matter exists in a regime known as plasma. The plasma is an ionized gas, where atoms are stripped of their electrons. Although composed of charged particles, it is globally neutral, and it responds collectively to electric and magnetic fields. Plasma is the most abundant form of visible matter in the universe: stars, for examples, are plasmas confined into spherical structures by their own gravitational force. On Earth, producing fusion in a laboratory first requires to confine plasma. Two main approaches are being developed: inertial and magnetic confinement.

Inertial confinement uses high-energy lasers or ion beams to compress and hit a small fuel target (e.g. D-T). The implosion of the target determines the increase in temperature and density up to the state at which fusion reactions are triggered. Inertia of D-T nuclei sustains the reaction long enough to achieve a net energy gain, until when the compression phase ends. The National Ignition Facility (NIF) [5] in the United States, a large public-funded project, has achieved significant progress on this research field. Private startups, as First Light Fusion [6] in the UK, are exploiting the same physics approach on the road to commercial fusion.

Magnetic confinement relies on external magnetic fields to confine a hot plasma into a vacuum vessel of specific geometry, such as e.g. tokamak or stellarator. The tokamak configuration is the most researched. It consists of a doughnut-shaped reactor that combines external field coils together with a central solenoid to confine the plasma in a helical magnetic field. In particular, looking at figure 1.4: toroidal magnetic field coils wrap the tokamak structure producing a magnetic field in the toroidal direction; a central solenoid induces a plasma current that generates a magnetic field poloidally directed; poloidal and toroidal magnetic fields combine to form the helical lines; poloidal magnetic field coils, and other particularly shaped coils, control the final confining magnetic field and the stabilization of the plasma itself. Notable tokamaks studied in this thesis are the Joint European Torus (JET) [7], the Divertor Tokamak Test (DTT) [8] and the international project ITER [9], and will be presented later in chapter 3. Stellarators, instead, have complex twisted magnetic coils to directly produce a helical magnetic field configurations, without the use of a central solenoid. The most advance realizations of this concept are the Large Helical Device (LHD) [10] and Wendelstein 7-X [11].

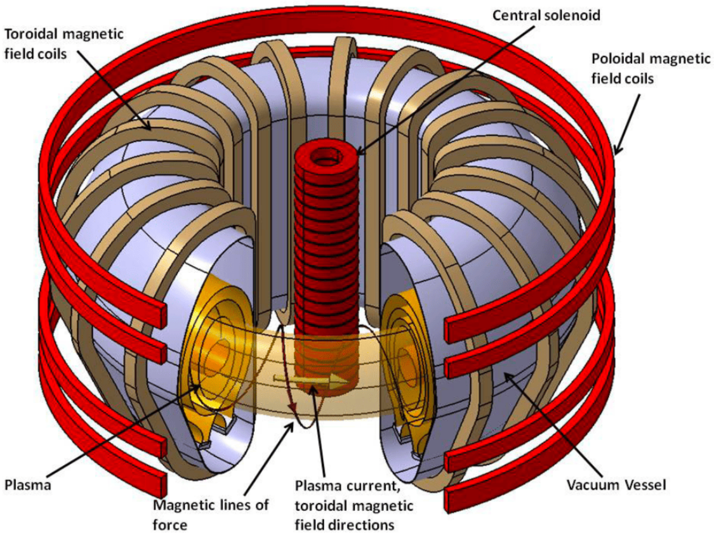

Figure 1.4: Scheme of tokamak magnetic coil systems [12].

Confining the plasma is only one of the essential requirements for achieving controlled fusion. Indeed, a fusion reactor must also be capable of reaching and sustaining fusion-relevant temperatures. Initially, these temperatures are obtained through ohmic heating induced by the current in a tokamak and auxiliary heating systems. Such systems are indispensable because the plasma's intrinsic self-heating mechanism, i.e. the ohmic heating arising from the toroidal current flowing through the plasma's finite resistivity, can increase the temperature only to few keV. While the plasma is heating up, the resistivity decreases, thereby reducing the effectiveness of ohmic heating. The most commonly used auxiliary heating systems include Electron Cyclotron Resonance Heating (ECRH), Ion Cyclotron Resonance Heating (ICRH), the Neutral Beam Injection (NBI) and the Lower Hybrid wave (LH) systems. ECRH, ICRH and LH are based on launching electromagnetic waves into the plasma and exploiting the wave-particle resonance to exchange their power with the plasma and accelerate thermal electrons and ions; NBI, instead, involves the injection of energetic neutral particles that become ionized inside the plasma and transfer their energy to the plasma by Coulomb collisions. A more detailed explanation of ICRH and NBI systems will be provided in chapter 2.

The goal of a fusion reactor is to maintain fusion relevant temperature without relying on continuous external heating, thereby producing the so-called self-sustaining burning plasma. In this regime, the plasma is primarily heated by the energy carried by alpha particles, generated by the fusion reactions themselves. This condition, known as ignition, is formally described by the Lawson criteria, that relates three keys parameters: the plasma density and temperature n, T and the energy confinement time τ_E:

$$n T \tau_E \ \geq \ 3 \times 10^{21} \ \frac{\mathrm{keVs}}{\mathrm{m}^3} \tag{1.5}$$

The alpha particles, and the particles obtained through the NBI and ICRH systems, are known as Energetic Particles (EPs). Indeed, all of them have an energy significantly larger than the plasma temperature, usually defined in keV (1 KeV $\approx 1.16 \times 10^7$ K) [13]. Considering a fusion plasma with a temperature in the core of 10 keV, alpha particles have indeed an energy of 3.5 MeV, beam ions are in a range of 20 keV to 1 MeV (expected in ITER) and IC-accelerated ions can reach energy in the MeV range too. Electrons that propagate through the plasma at relativistic velocities, commonly referred to as runaway electrons, are also classified within the EP group [13].

Alpha particles carry approximately 1/5 of the total fusion power released in D-T fusion reactions. The remaining power is carried by neutrons, whose kinetic energy should be predominantly deposited as heat in the blankets surrounding the reactor [14]. This thermal energy is then converted into electricity by producing mechanical work in a turbine that drives an electric generator. The goal of a commercial fusion reactor is to produce significantly more energy than is required to initiate and sustain fusion. This performance is quantified by the amplification factor Q, defined as $Q = \frac{P_{fus}}{P_{aux}}$, where P_{fus} and P_{aux} are the fusion power output and the external heating power supplied to the plasma respectively. At ignition, when $P_{aux} = 0$, $Q \to \infty$. The optimal operating regime for future fusion plant is within $Q \in [30; \infty]$ [15]. A crucial step towards this objective is ITER, the international project under construction in Cadarache, France. ITER indeed should demonstrate the feasibility of a burning plasma by achieving a fusion gain of Q = 10. The following section briefly outlines the roadmap leading to ITER, ultimately towards DEMO, the DEMOnstration fusion power plant prototype under designed for Europe [16].

1.3 The path towards nuclear fusion reactors

From this brief introduction, it may be difficult to fully appreciate the complexity involved in the realization of the first fusion power plant. However, the vast number of experiments and research laboratories involved in this field, from both public and private sectors, clearly demonstrate the scale (and interest) of this challenge. The roadmap leading to the realization of a power plant, such as DEMO in Europe, indeed is strongly populated by experimental projects all over the world, each contributing piece by piece to the scientific knowledge and technological expertise required for its realization.

The Joint European Torus (JET) experiment was one of the leading world experiments. JET, located in Culham (UK) at the UK Atomic Energy Agency (UKAEA), was operated as a high-performance tokamak, with a primary focus on achieving reactor-relevant plasma conditions, thereby complementing devices such as WEST [17] and EAST [18], which are instead dedicated to the investigation of steady-state and long-duration plasma operation. JET concluded its operation in 2023 after more than 40 years of activity. It was the largest tokamak ever operated until the commissioning of the JT-60SA tokamak [19] in Japan, which happened in 2024. JET was also the only tokamak in operation in the 21st century equipped to conduct D-T experiments. It still holds the record for the highest fusion power peak of 16 MW ever achieved in a magnetic confinement experiment, made in 1997 [20], and it also produced the largest amount of energy in a fusion experiment, reaching 69 MJ of fusion energy production in 2023 [21]. JET experiments validated numerous physics models and operational scenarios that will contribute to ITER operations, i.e. the next D-T fusion experiment in Europe.

The international project ITER is currently under construction in Cadarache (France), and it will be the largest tokamak ever built in the world. ITER is currently scheduled to start operation in the early 2030s, with an initial operation phase in preparation to D-T campaigns, as illustrated in the recent review of the ITER Research Plan [22]. ITER's goals are to achieve $Q \geq 10$, producing approximately 500 MW of fusion power for long plasma pulses, e.g. ~ 400 seconds, and to reach $Q \geq 5$ for 3000 s. Beyond this, ITER will be supported by integrated plasma physics modelling, where advanced theoretical tools within the Integrated Modelling and Analysis Suite (IMAS) are being developed already. ITER is the decisive experiment bridging the gap between plasma physics requirements and technological feasibility of a commercial fusion power plant. However, it cannot cover all the open challenges in plasma physics. For this reason, complementary facilities are being developed.

The Divertor Tokamak Test (DTT) facility, under construction in Frascati (Italy), is one of these. DTT will focus on the power exhaust problem. The divertor, the component which collects the energy and particles flowing out of the plasma, must withstand extreme localized thermal loads (about $10-20$ MW/m^{-2} are expected in DEMO). While ITER will test a conventional divertor configuration, DTT is designed to investigate alternative divertor configurations that may provide more effective solutions for power exhaust mitigation necessary for DEMO.

Although many other experiments contribute to the path towards the first fusion power plant, the presented tokamaks are the main devices of this work. Figure 1.5 shows the design of the cited tokamaks, JET, DTT and ITER, and table 1.1 summarizes their main design and physical parameters for comparison. More detailed descriptions of these devices and their subsystems will be provided when needed throughout this thesis.

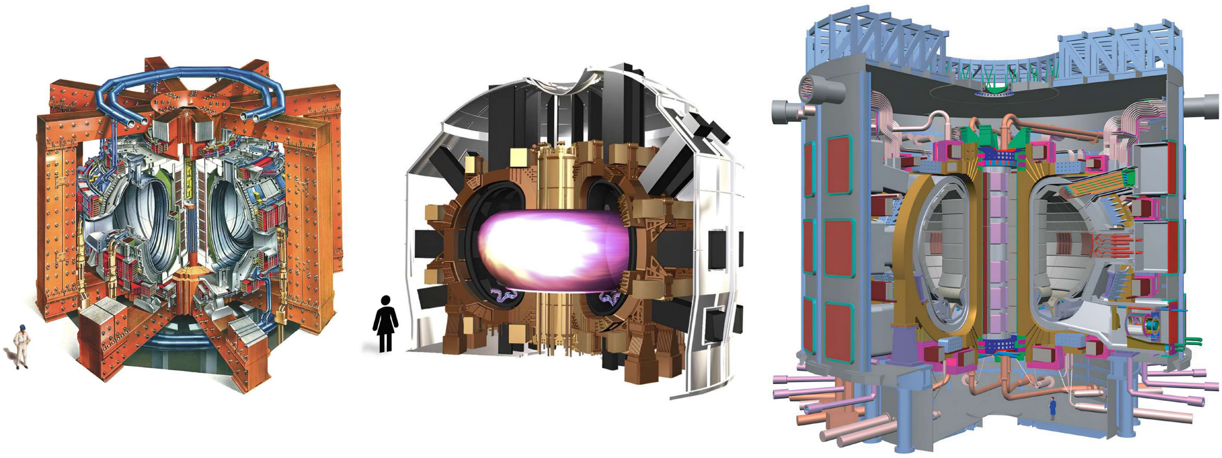

Figure 1.5: From left to right, the representation of JET, DTT and ITER tokamaks. The images are not represented on a comparable scale, but they can be resized by using the people shown in each figure as a reference [7–9].

Finally, DEMO will represent the first true demonstration of a fusion power plant for the European community. DEMO will aim to prove the industrial feasibility of electricity production from fusion reactions, building on the results of ITER and preceding experiments. The expectation is to deliver more than 50 MW of net electrical output. Its design is still under development as many scientific and technological challenges remains, including the development of advanced systems for plasma control, fusion power handling and energy conversion.

Parameter/Tokamak	**JET**	**DTT**	**ITER**
Minor/major radius (a/R_0) [m]	1.25/2.96	0.70/2.19	2.0/6.2
Plasma current (I_p) [MA]	6	5.5	15
Toroidal magnetic field (B_{tor}) [T]	4	6	5.3
Available heating power [MW]	62	45	103 (136.5[2])
Main fuel	He/H/D/DT	H/D	H/D/DT
Electron density (n_e) [10^{20} m^{-3}]	1	1.8	1.2
Electron temperature (T_e) [keV]	10	6.1	36

Table 1.1: Main design parameters of JET, DTT and ITER [23–25].

1.4 Motivation of this thesis

Up to this point, several aspects of fusion physics have been discussed, from plasma confinement and heating methodology, to an introduction of the present experiments significant for this work. It should be clear that the application of auxiliary heating systems, that results in the generation of Energetic Particles (EPs), is essential for reaching fusion temperature. EPs, indeed, play several key roles in fusion plasmas, by contributing to plasma heating, current drive and rotation, and providing valuable information for diagnostic purposes, for example through the observation of their cyclotron radiation and neutron emissions. These particles, however, can also drive instabilities by interacting with waves and other plasma modes, potentially leading to energy losses and degradation of the plasma performance. The characterization of their distribution and dynamics within the plasma is therefore crucial to exploit their potential while avoiding eventual degrading effects.

This thesis aims to characterize the EP behaviour and their distribution functions in magnetically confined fusion plasmas. In particular, the study focuses on EPs generated by the NBI and ICRH systems, as well as through their synergy, using state-of-the-art numerical codes. The main devices investigated are JET, DTT and ITER, for which different techniques and numerical environments were required. JET is considered for a validation activity related to the modelling of ICRH-accelerated energetic particles, simulated through a renewed implementation of the orbit-following Monte Carlo ASCOT code [26, 27] coupled with the RFOF operator to describe the wave-particle interactions [28]. For DTT, the focus is instead placed on NBI energetic particles, which are studied by exploiting the orbit-following Monte Carlo ASCOT code. In ITER, the work addresses both NBI and ICRH energetic particles, with particular attention to their synergistic effects in the context of fusion performance optimization. Part of the work presented in this thesis exploited codes included in the Integrated Modelling and Analysis Suite (IMAS) [29] and contributed to further developments within this framework. The investigations performed within this project contribute to the optimisation of the NBI system in DTT and its impact on the plasma performance, on the definition of the capabilities and limitations of the available modelling tools for ICRH-driven energetic particles under reactor-relevant conditions, and the characterization of synergistic effects of NBI and ICRH in ITER plasmas. The work also contributed to the development of a new IMAS-compatible tool, EPCoM [30], for studying the population and stability of energetic particles in their invariant phase space. Beyond its scientific contributions, this thesis has also served as a valuable opportunity to expand expertise in modelling energetic particles produced by different mechanisms and investigated with diverse approaches.

---

[2] ITER total available heating power considering possible upgrade of the planned auxiliary heating systems.

Before proceeding, a brief outline of the thesis structure is provided. The thesis is organized into three parts. The first, **Theory and Methodology**, introduces the physics of energetic particles in a tokamak (chapter 2) and presents in details the investigated devices and numerical tools applied (chapter 3). This includes section 3.6 dedicated to the IMAS framework and the main IMAS-compatible tools applied in this study. The second part, **Numerical Applications**, contains the numerical studies carried out. It presents the results for NBI EP distribution functions (chapter 4), IC-accelerated EP distribution function (chapter 5) and NBI and ICRH synergy analysis (chapter 6) for the cited devices. The third and final part, called **Conclusions**, summarizes the main findings of the thesis and discusses applications and future perspective.

Part I

THEORY and METHODOLOGY

CHAPTER

2

ENERGETIC PARTICLES IN A TOKAMAK

In fusion plasmas, Energetic Particles (EPs) are ions and electrons whose energies significantly exceed the energy of the thermal plasma background. The EPs generated by the auxiliary heating systems have a central role in plasma performance because they transfer energy (and heat) to the bulk plasma, drive non-inductive currents, provide torque and influence plasma stability. In particular, the suprathermal fast ion populations produced through the NBI and ICRH systems exhibit some characteristics similar to those of alpha particles. Therefore, analysing their behaviour and interaction with the plasma also contributes to the studies of alpha particle physics without the need for burning plasmas. This chapter explores EP physics in section 2.1, presenting a comprehensive theoretical framework for particle motion, orbit drifts, orbit topology and loss mechanisms. The discussion then extends in section 2.2 to a kinetic description, introducing the Fokker-Planck (FP) equation as a fundamental tool for describing the evolution of the EP distribution functions. All relevant terms, such as collisional operator, sources, sinks, and wave–particle interaction, are discussed in detail. Sections 2.3 and 2.4 are dedicated to the two main sources of fast ion populations, namely the NBI and ICRH systems. These sections include detailed descriptions of the systems, as well as the underlying physics governing fast ion generation through each system of interested for this work.

2.1 The single-particle motion

The motion of a charged particle in a uniform magnetic field is governed by Newton's second law, with the Lorentz force included, as expressed in equation 2.1. In a tokamak, where the magnetic field lines follow a helical geometry, the particle velocity can be decomposed in parallel $v_{\parallel}$ and perpendicular $v_{\perp}$ components, defined regarding the magnetic field $\vec{B}$. The motion of a single charged particle can therefore be interpreted as a superposition of two types of motions, as sketched in figure 2.1: the Gyro-Orbit (GO) motion induced by $v_{\perp}$ and the Guiding Center (GC) motion determined by $v_{\parallel}$.

$$m\frac{d\vec{v}}{dt} = q\vec{v} \times \vec{B} \tag{2.1}$$

The GO arises from the component of the Lorentz force perpendicular to the magnetic field, which causes the particle to move in a circular path around magnetic field lines. The corresponding radius of this motion, called Larmor radius r_L, and its characteristic angular frequency, known as gyro- or

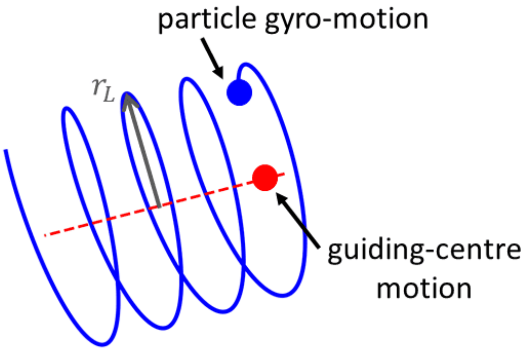

Figure 2.1: Sketch of the superposition of the gyro-orbit motion (solid blue) and guiding centre motion (dashed red) of a charged particle in a plasma.

cyclotron frequency Ω_c, are expressed as:

$$r_L = \frac{mv_\perp}{|q|\mathrm{B}} \qquad\qquad \Omega_c = \frac{|q|\mathrm{B}}{m} \tag{2.2}$$

Its dependence on the $v_\perp$ component indicates that the Larmor radius increases with the particle velocity. For effective plasma confinement, r_L must remain much smaller than the characteristic macroscopic dimensions of the plasma. The gyro-orbit frequency instead does not depend on the particle velocity, but on its charge q and mass m and on the magnetic field strength B. On the other hand, the GC motion arises from the parallel velocity component, $v_\parallel$, which causes the charged particle to move along the magnetic field lines. Since the cyclotron motion around the magnetic field lines is much faster than the overall motion within the tokamak, the particle trajectory can be approximated by the motion of the point, called guiding centre, around which the particle gyrates. The velocity of the guiding centre can be modified by spatial and time variations of $\vec{B}$. Such inhomogeneities give rise to external forces perpendicular to the magnetic fields, which induce a drift velocity v_d in the particle motion such that the guiding centre velocity becomes $\vec{v}_{GC} = v_\parallel \frac{\vec{B}}{B} + \vec{v}_d$. In the worst case, the drifts can lead to particle losses.

2.1.1 Drift terms

The presence of an external force $\vec{F}$ acting on particles moving inside the plasma induces a drift of their guiding centre, which general formula is given by

$$\vec{v}_F = \mathrm{sgn}(q)\frac{\vec{F}\times\vec{B}}{B^2} \tag{2.3}$$

Several drift mechanisms can occur and the total drift velocity v_d experienced by the guiding centre can be expressed as the sum of distinct contributions, the most relevant reported here:

$$\vec{v}_d = \vec{v}_{\nabla B} + \vec{v}_k + \vec{v}_p + \vec{v}_E \tag{2.4}$$

Gradient drift $\mathbf{v}_{\nabla\mathbf{B}}$ A spatial gradient in the magnetic field causes the guiding centre to drift in a direction perpendicular to both $\vec{B}$ and the gradient itself ∇B [31]. In a tokamak, the magnetic field scales as $\sim\ 1/R$, producing a non-zero ∇B and a corresponding drift that depends on the sign of the particle charge:

$$\vec{v}_{\nabla B} = \mathrm{sgn}(q)\frac{v_\perp^2}{2\Omega_c}\frac{\vec{B}\times\nabla B}{B^2} \tag{2.5}$$

Curvature drift $\mathbf{v_k}$ When the magnetic field has a constant radius of curvature $\vec{R}_c$, as in a toroidal geometry, the GC drifts perpendicular to the plane of curvature [31]. This effect arises from the centrifugal force acting on the particle, expressed as $\vec{F}_c = -mv_\parallel^2 \frac{\vec{R}_c}{R_c}$, which produces a drift velocity that depends on the sign of the charge sgn(q) and on the cyclotron frequency Ω_c:

$$\vec{v}_k = \mathrm{sgn}(q) \frac{v_\parallel^2}{\Omega_c} \frac{\vec{R}_c \times \vec{B}}{R_c^2 B} \tag{2.6}$$

Polarization drift $\mathbf{v_p}$ If an electric field is present and varies slowly with time, the particle inertia generates an additional charge-dependent drift known as polarization drift, which modifies the motion of the guiding centre as [31]:

$$\vec{v}_p = \mathrm{sgn}(q) \frac{1}{\Omega_c} \frac{d}{dt} \left(\frac{E_\perp}{B} \right) \tag{2.7}$$

where $E_\perp$ is the perpendicular component of the electric field.

$\mathbf{E} \times \mathbf{B}$ drift $\mathbf{v_E}$ The presence of an electric field $\vec{E}$ perpendicular to the magnetic field $\vec{B}$, that can arises e.g. from the charge separations generated by the above explained drifts, causes the guiding centre to drift in a direction perpendicular to both fields [31]. This drift is independent of the particle charge and mass, meaning that both positive and negative charges moves in the same direction:

$$\vec{v}_E = \frac{\vec{E} \times \vec{B}}{B^2} \tag{2.8}$$

The drift relations 2.5-2.6 depends on $v_\perp$, $v_\parallel$. The magnitude of these drifts therefore increases with the particle energy. Due to the high velocity and energy of energetic particles, the drift effects are amplified in such particles, thereby influencing the types of orbits that EPs can follow.

2.1.2 Orbit topology and losses

Thermal particles can follow mainly passing or trapped orbits. Before introducing these two types of orbits, it is useful to define the pitch angle $\lambda = \frac{v_\parallel}{v}$. Passing particles complete a full toroidal orbit, continuously circulating along the same direction inside the torus. Consequently, the sign of their pitch λ remains constant. Trapped particles, on the other hand, have limited toroidal motion due to the magnetic field gradient and bounce between two poloidal positions, called bounce points. This behaviour, known as mirror effect, arises from the conservation of both particle kinetic energy $E = \frac{1}{2}mv^2$ and magnetic moment $\mu = \frac{1}{2}\frac{mv_\perp^2}{B}$, which is formally an adiabatic invariant due to the slow temporal variations of the magnetic and electric field. In a tokamak, the magnetic field decreases with the major radius ($B \propto 1/R$), meaning that it is stronger in the inner part of the tokamak, also known as High Field Side (HFS). To conserve both the magnetic moment and the energy, a particle in the HFS region must reverse the direction of its parallel motion, leading to periodic changes in the sign of $v_\parallel$ and therefore of λ. The width of the trapped orbits is approximately given by $\delta_b \sim \frac{q(r) r_L}{\sqrt{\epsilon}}$, where ϵ is the inverse aspect ratio and $q(r)$ the safety factor at r, the radius of the magnetic flux surface on which the trapped particle lies. This approximation is valid when $\delta_b \ll r$. Examples of the particle trajectories of passing and trapped orbits in the top view of a tokamak are depicted in figure 2.2.

Beyond passing and trapped orbits, the high energy of EPs can result in non-standard orbits [32], which arise because larger drift effects significantly alter their trajectories. Examples of non-standard orbits include potato and stagnation orbits. Potato orbits are followed by trapped particles for which the width condition $\delta_b \ll r$ is no longer satisfied. The orbit width becomes comparable to the flux surface radius such that $\delta_p \sim r$ with

$$\delta_p = \left(\frac{2 q_0 v_{\perp 0}}{R_0 \Omega_c} \right)^{2/3} R_0 \tag{2.9}$$

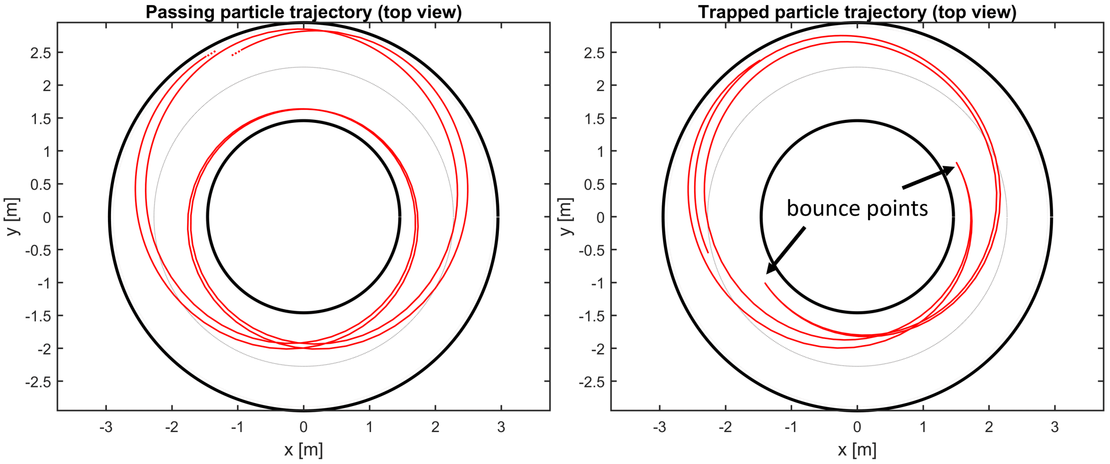

Figure 2.2: Representation of passing and trapped orbit trajectories from the top view: left) passing particle, right) trapped particle.

is the potato width, and the subscript "0" refers to the quantities at magnetic axis [33]. Potato orbits may encircle the magnetic axis (sufficient but not necessary condition to be a potato particle), still showing periodic changes in the sign of the pitch. Stagnation orbits are instead defined by particles that complete a toroidal orbit with minimal poloidal motion and without encircling the magnetic axis. This behaviour arises because the vertical displacement due by gradient and curvature drifts nearly cancels the poloidal component of the parallel motion along the field lines [32]. For stagnation orbits, the sign of the pitch angle, sgn(λ), remains constant. Figure 2.3 shows the poloidal projection of passing (blue), trapped (orange), potato (yellow) and stagnation (purple) orbits on the (R, z) plane, as well as an example of lost particle orbit (green). The trajectory of a trapped particle forms the characteristic banana-shaped path, from which the term "banana particle" originates. Figure 2.4 instead shows the variation of the pitch angle during particle motion for different kind of orbits, using the same colour-coding as in fig. 2.3.

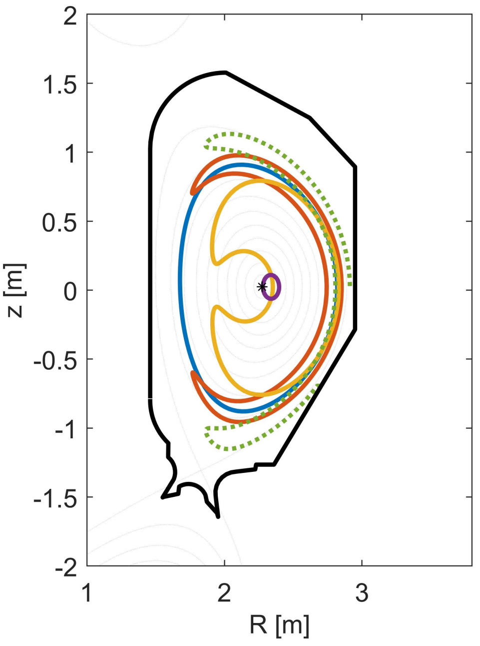

Figure 2.3: Poloidal projections in the (R, z) plane of different particle orbits. The legend is the same as fig. 2.4.

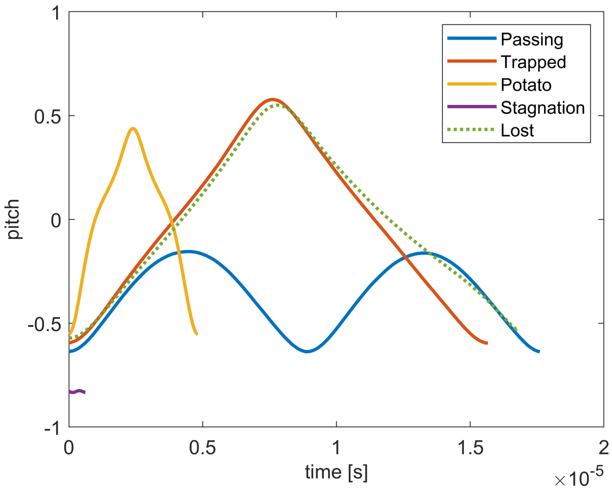

Figure 2.4: Time evolution of the particle pitch angle λ for different particle orbits. While potato and banana orbits show a change in the pitch sign along their orbit, passing and stagnation particles keep their sgn(λ) constant.

When a particle collides with the wall, as in the green example in figure 2.3, it is lost. Multiple mechanisms contribute to the loss of an energetic particle, leading to various types of losses. For energetic particles generated by the NBI, a potentially harmful loss mechanism for the tokamak is the Shine-Through (ST). *Shine-through losses* refer to the fraction of injected neutral particles that do not ionize in the plasma, impacting into the wall. These losses must be minimized to avoid excessive power to the plasma-facing components. If a neutral is instead ionized outside the Last Close Flux Surface (LCFS), where the magnetic field lines are open, the resulting ion is promptly lost to the divertor plates. This mechanism is called *Scrape-Off Layer (SOL) loss*. The presence of neutral atoms, either already in the plasma or introduced by the NBI, can lead to *charge-exchange losses*. In this process, a fast ion undergoes charge exchange with a neutral atom, producing a fast neutral. Unless further re-ionization, the fast neutral travels ballistically until being lost to the wall. Another relevant phenomenon is the *first orbit loss*, which occurs when beam particles are born on non-confined trajectories. This typically happens for ions originating near the LCFS, which drifts carry them towards the wall in timescale shorter than that of collisional processes. Such losses predominantly affect trapped particles. The example depicted in figure 2.3 is indeed a trapped first orbit lost particle. Losses that happen during the collisional processes are known as *collisional orbit losses*, and can originates from EP collisions during their slowing down into the plasma. Finally, inhomogeneities in the magnetic field, e.g. due to the finite number of toroidal field coils, can produce the so-called *ripple losses*. These occur when particles become trapped in a localized region of stronger magnetic field, causing their guiding centre to drift vertically towards the wall. Other phenomena can cause EP losses, such as the resonant magnetic field perturbations due to the edge-localized mode (ELM) control coils. The discussed types of losses are schematically illustrated in figure 2.5. Several strategies exist to mitigate these losses, such as selecting the proper neutral beam injection direction [34], adjusting the beam energy and power according to the plasma scenarios [35] and reducing the magnetic field inhomogeneities through the use of ferromagnetic inserts [36].

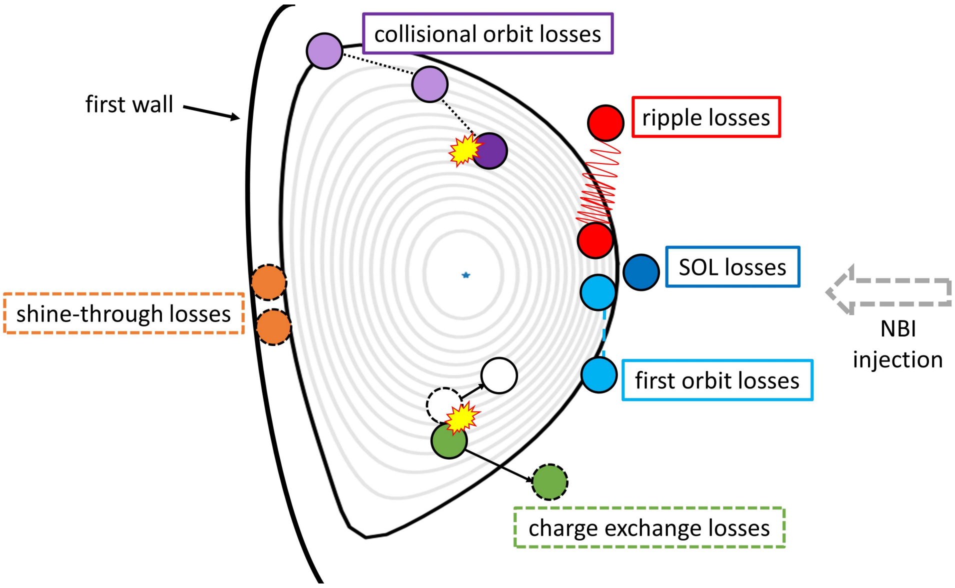

Figure 2.5: Schematic representation of energetic particle loss mechanisms in tokamaks. The dashed and solid particle contours indicate neutral and charged particles, respectively. For *collisional orbit losses*, the lighter colour corresponds to lower particle energy, reflecting the fact that such losses occur during the slowing-down phase.

2.1.3 Constant of motion representation

Directly solving the full equations of motion for all particles is a highly complex task, as it requires solving a 6-dimensional systems of differential equations in spatial and velocity coordinates. The description of particle motion can be simplified by exploiting the existence of three invariants of motion. These are the particle kinetic energy E, the magnetic moment μ and the canonical toroidal angular momentum P_ϕ, respectively defined as

$$E = \frac{1}{2}mv^2 \qquad \mu = \frac{1}{2}\frac{mv_\perp^2}{B} \qquad P_\phi = mRv_\phi + q\Psi \tag{2.10}$$

where Ψ is the poloidal magnetic flux and v_ϕ is the toroidal velocity, that is assumed equal to $v_\parallel$ in the guiding centre approximation [37]. These quantities are conserved over the collisionless timescale, i.e. within a time under which collisions do not impact the plasma dynamics, or in quiescent plasmas, i.e. steady state plasma where fluctuations are negligible. In such regimes, the particle energy is conserved, since no collisions or collective interactions occur to alter it, while the magnetic moment remains an adiabatic invariant. The toroidal canonical angular moment instead is conserved under the assumption of toroidal symmetry, implying that the magnetic field is independent of the toroidal angle.

These invariants are known as Constants of Motion (CoM) and can be used for the classification of the particle orbits, according to the theory developed in [38], which enables the construction of a topological map in the CoM phase space. A detailed description of the construction of the CoM topological map can be found in [39], while here are reported its main features. Orbit classification is typically performed by selecting a fixed particle energy E and representing the corresponding particle population in the phase space defined by the normalized toroidal canonical angular momentum and the magnetic moment, denoted respectively as (Π_ϕ, Λ). These quantities are defined by

$$\Pi_\phi = \frac{P_\phi - q\Psi_0}{q(\Psi_{lcfs} - \Psi_0)} \qquad \Lambda = \frac{\mu B_{tot,0}}{E} = \frac{v_\perp^2 B_{tot,0}}{(v_\perp^2 + v_\parallel^2)B} \tag{2.11}$$

with $B_{tot,0}$ the total magnetic field at R_0, and Ψ_0, Ψ_{lcfs} the poloidal magnetic flux at the magnetic axis and the LCFS respectively. As can be deduced from eq. 2.11, the boundaries of the topological map depend on both the particle energy and the magnetic field strength. An example of this kind of topological map is shown in figure 2.6, obtained for a DTT plasma with $B_{tot,0} \sim 5.8$ T and a particle energy of $E = 510$ keV (DTT beam energy).

Figure 2.6 highlights the boundaries and corresponding domains associated with confined and lost passing orbits, confined and lost trapped orbits, stagnation orbits, and potato orbits. Co-passing and counter-passing particles, respectively defined as particle moving in the parallel or antiparallel direction of the plasma current, can be usually distinguished on the topological map. Since in DTT the beam energetic particles are injected in the co-current direction, opposite to the magnetic field, only co-passing orbit domains, obtained for $\lambda < 0$, are reported in figure 2.6. Figure 2.7 instead reports the changes of orbit boundaries and relative domains while changing E and $|B|$, again considering DTT plasma conditions. Similar variations will be observed in section 4.2, for changes in both energy and magnetic field strength, as well as in sections 4.3.1 and 4.3.2, where CoM distribution functions of ITER ions are analysed at different energies.

When the CoM are well-preserved, the plasma confinement is good. However, strong perturbations, e.g. symmetry field breaking, or fast changes in the energetic particle dynamics due to Coulomb collisions, can violate the system invariance destroying the conservation of one or more of the CoM variables [13]. Describing the steady-state condition of the plasma through the CoM invariants provides valuable inputs for plasma transport and stability studies, as those given by the EPCoM tool [40]. This is an IMAS-based tool built on the CoM formalism that will be presented in more details in chapter 3.

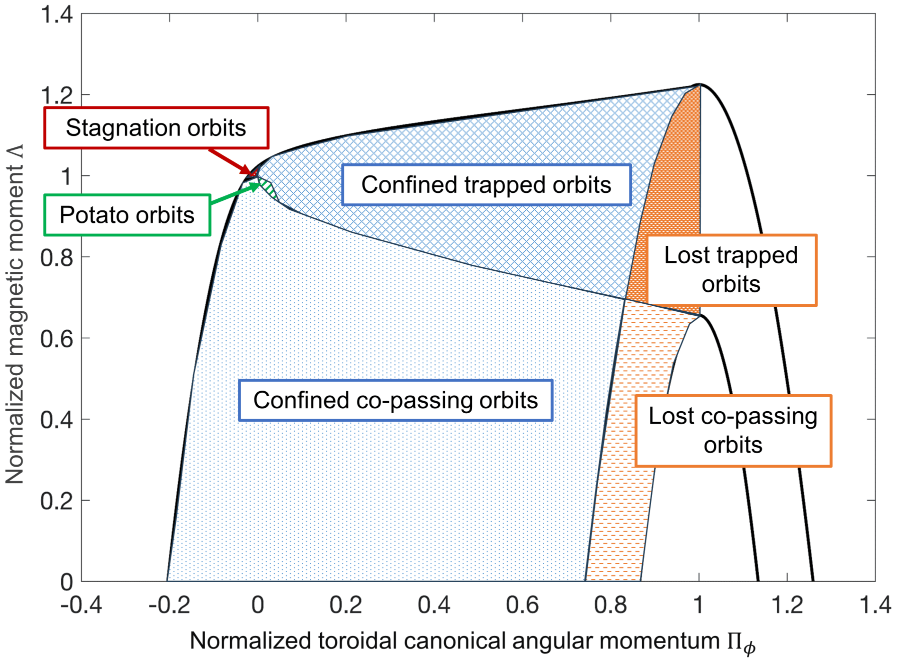

Figure 2.6: EP orbit domains defined through the topological map in the normalized CoM phase space obtained for particle energy $E = 510$ keV and $B_{tot,0} \sim 5.8$ T. Only co-passing orbits domains are cited in this map since the DTT newly born fast ion population follows co-current orbits because of the particle negative pitch.

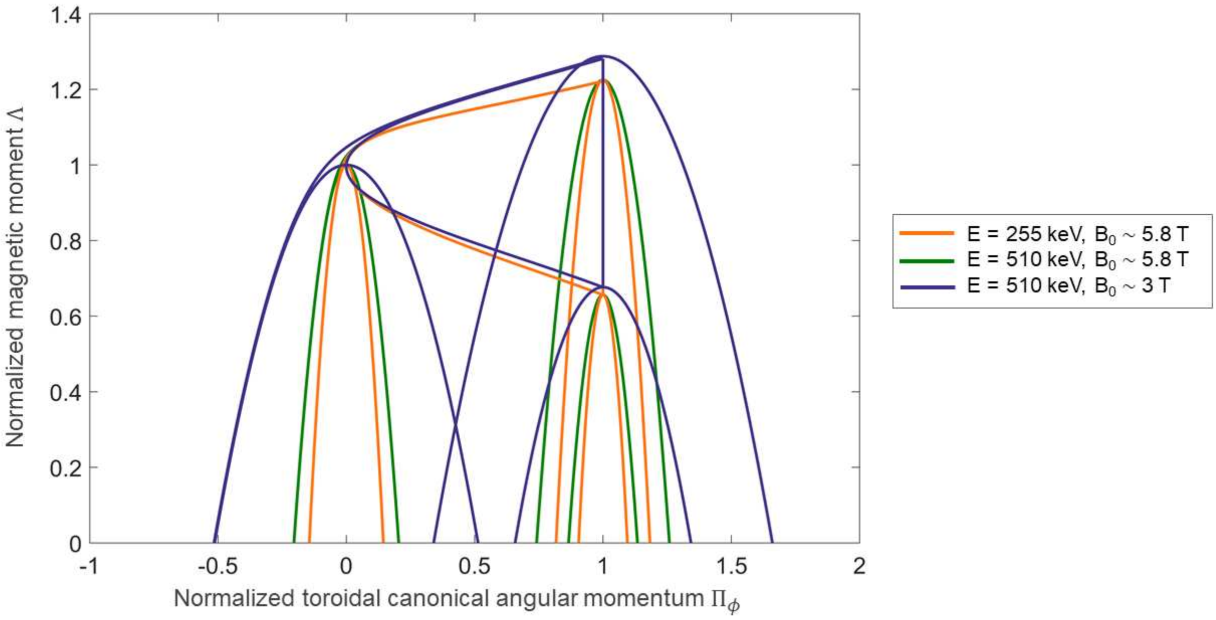

Figure 2.7: Topological maps in the normalized CoM phase space built considering different energies and toroidal fields at the magnetic axis.

2.2 The kinetic theory

The motion of a single charged particle in a plasma provides the fundamental basis for understanding the orbit confinement and loss processes of energetic particles (EPs). However, the collective properties of a plasma cannot be captured by considering single-particle dynamics alone. The kinetic theory, based on statistical model, is the proper approach to describe the dynamics of many particles and their interactions. This is done studying the evolution of a distribution function f which represents the density of particles in a phase space. Depending on the chosen coordinates, different distribution functions f may be used, e.g. $f(\vec{r},\vec{v},t)$ in Cartesian phase space, or $f(E,\mu,P_\phi)$ in the constant of motion reference. From f all relevant macroscopic quantities like particle density, averaged velocity, pressure, can be derived through velocity-space moments. In the absence of collisions, the evolution of f is governed by the Vlasov equation

$$\frac{Df}{Dt} = \frac{\partial f}{\partial t} + \frac{\partial f}{\partial \vec{r}} \cdot \vec{v} + \frac{\partial f}{\partial \vec{v}} \cdot \frac{q}{m}(\vec{E} + \vec{v} \times \vec{B}) = 0 \tag{2.12}$$

where $f = f_\alpha(\vec{r},\vec{v},t)$ identifies the distribution function of the particle species α, which stands for electrons or ions, and D/Dt is the total derivative [41]. Equation 2.12 describes the deterministic collisionless evolution of the plasma, determining that the distribution function is constant along its characteristics ($d\vec{r}/dt$ and $d\vec{v}/dt$) [42]. Coulomb collisions, however, cannot be neglected in real plasma: even if they produce a small angle interaction, they induce a cumulative effect in the whole plasma [43]. The collision contribution is usually expressed as

$$\left(\frac{\partial f}{\partial t}\right)_{coll} = \frac{\partial}{\partial \vec{v}}\left(-A_\alpha f + \frac{\partial}{\partial \vec{v}}(D_{\alpha\beta} f)\right) \tag{2.13}$$

where A_α and $D_{\alpha\beta}$ are respectively the friction and diffusion coefficients [27, 43]. Including this operator in the time evolution of f, the resulting equation is known as Fokker-Planck equation:

$$\frac{\partial f}{\partial t} + \vec{v} \cdot \frac{\partial f}{\partial \vec{r}} + \frac{q}{m}(\vec{E} + \vec{v} \times \vec{B}) \cdot \frac{\partial f}{\partial \vec{v}} = \left(\frac{\partial f}{\partial t}\right)_{coll} \tag{2.14}$$

In the absence of sources and external perturbations, the distribution consistent with the collisional Fokker-Planck equation 2.14 is almost Maxwellian. However, when treating energetic particles, additional effects such as wave-particle interaction, external particle injection and particle losses must be considered into the Fokker-Planck equation, leading to a more complex solution. The collisional operator (eq. 2.13) is simplified when considering the energetic particles. Indeed, due to the high velocity of energetic particles, i.e. $v_{fast} \gg v_{th,i}$, the energy diffusion contribution can be neglected, and the collisional operator $C(f) = \left(\frac{\partial f}{\partial t}\right)_{coll}$ is therefore defined by a slowing down term $C_{sd}(f)$ and a pitch angle scattering term $C_{pas}(f)$ [44, 45]

$$C(f) = C_{sd}(f) + C_{pas}(f) = \frac{1}{v^2}\frac{\partial}{\partial v}\left[\frac{v^3 + v_c^3}{t_s} f\right] + \frac{\partial}{\partial \eta}\left[\frac{v_\gamma^3}{t_s v^3}(1-\eta^2)\frac{\partial f}{\partial \eta}\right] \tag{2.15}$$

where $\eta = v_\parallel / v$, t_s is the Spitzer slowing down time and v_c, v_γ are, respectively, the characteristic velocity associated with the pitch angle scattering and the critical velocity. The first term in the bracket of the slowing down operator $C_{sd}(f)$ represents ion-electron collisions and the second ion-ion collisions. The Spitzer slowing down time [46] is instead defined the ion-electron slowing down time, expressed as

$$t_s = 6.28 \times 10^8 \left(\frac{A_{\text{fast}}(T_e[eV])^{3/2}}{Z_{\text{fast}}^2 n_e[m^{-3}] \ln\Lambda}\right) \tag{2.16}$$

with $A_{\text{fast}}, Z_{\text{fast}}$ referring to the energetic ion interacting with the plasma background and $\ln\Lambda$ the Coulomb logarithm (typically in the range 10-20 [47]). The critical energy E_c is the energy at which thermal electrons and ions receive the same amount of energy when they interact instantaneously with an energetic particle. It depends linearly on the electron temperature T_e as expressed in equation 2.17, where A, Z are the mass and atomic number, with fast, i subscripts representing respectively the fast and thermal ions, n_e, n_i the electron and ion plasma densities:

$$E_c = \frac{1}{2}mv_c^2 = 14.8\ A_{\text{fast}}T_e\left(\sum_i \frac{n_i}{n_e}\frac{Z_i^2}{A_i}\right)^{2/3} \tag{2.17}$$

Finally, the characteristic energy of the pitch angle scattering is expressed as

$$E_\gamma = \frac{1}{2}mv_\gamma^2 = 14.8\ T_e\left[2A_{\text{fast}}^{1/2}Z_{eff}\right]^{2/3} \tag{2.18}$$

with Z_{eff} the effective charge. From the slowing down contribution $C_{sd}(f)$ in equation 2.15, which describes the power transfer between energetic particles and the background plasma, it turns out that EP transfer power preferentially to electrons when their kinetic energy exceeds the critical energy E_c. The $C_{pas}(f)$ term instead, that represents the diffusion of energetic particles associated to collisions with background ions, shows that the pitch angle scattering weakens rapidly with EP velocity $\left(\propto v_{fast}^{-3}\right)$, being therefore more important for energetic particles close to the thermalization. Another characteristic of the energetic particles is that their bounce time τ_b, i.e. the time a particle takes to complete a poloidal orbit, is smaller than the typical collisional time τ_c. Consequently, the distribution function can be expanded in the small parameter τ_b/τ_c as $f = f_0 + \tau_b/\tau_c f_1 + ...$ On the slow collisional time scale, the distribution function f_0 can be shown to be a function of three invariants of the unperturbed orbits $\left(I^1, I^2, I^3\right)$ [45], such as the Constants of Motion introduced in section 2.1.3 for axisymmetric equilibrium, $f_0 = f_0\left(E, \Lambda, P_\phi\right)$. The evolution of f_0 under these assumptions is governed by the orbit-averaged Fokker-Planck equation

$$\frac{\partial f_0}{\partial t} = \langle C(f_0)\rangle + \langle Q(f_0)\rangle + \langle S\rangle - \langle L\rangle \tag{2.19}$$

where the orbit averaging is given by $\langle ...\rangle = \frac{1}{\tau_b}\int_0^{\tau_b} ...d\tau$. Here $C(f_0)$ is the collisional operator, $Q(f_0)$ is the quasi-linear operator describing wave-particle interaction, S is the source term, which can include e.g. NBI injected ions, and L is the loss term, to be accounted for when a source term is present to control the particle density in a simulation. In the orbit averaged formulation, the slowing down collision operator is expressed as

$$\begin{aligned}\langle C_{sd}\left(f_0\right)\rangle = \frac{1}{J_{CoM}}\frac{\partial}{\partial E}&\left[J_{CoM}\left\langle 2E\frac{1+\frac{E_c^{3/2}}{E^{3/2}}}{t_s}\right\rangle f_0\right] + \\ \frac{1}{J_{CoM}}\frac{\partial}{\partial P_\varphi}&\left[J_{CoM}\left\langle (P_\phi - Ze\psi)\frac{1+\frac{E_c^{3/2}}{E^{3/2}}}{t_s}\right\rangle f_0\right]\end{aligned} \tag{2.20}$$

where

$$J_{CoM} = \frac{4\pi^2 E}{ZeB_0 m^2}\tau_b(E, \Lambda, P_\phi) \tag{2.21}$$

is the Jacobian of the transformation to the invariant CoM variables (E, Λ, P_ϕ). Regarding the quasi-linear operator $\langle Q(f_0)\rangle$, instead, its definition can be written as [45]

$$\langle Q(f_0)\rangle = \frac{1}{J_{CoM}}\frac{\partial}{\partial I^i}\left[J_{CoM}D_{RF}^{ij}\frac{\partial f_0}{\partial I^j}\right] \tag{2.22}$$

with D^{ij}_{RF} being the quasi-linear diffusion tensor, discussed more in detail in section 2.4.2.

To summarize, kinetic theory provides the fundamental basis for describing the dynamics of the particles in a plasma. The Fokker–Planck formalism allows characterizing the distribution functions of energetic particles, combining in one formula the theory of collisions, wave–particle interactions, external sources and losses. This treatment enables to study the impact of energetic particle population in view of the optimization of plasma performance, stability and transport. In the present work, analytical and orbit-following Monte Carlo codes are employed to solve the kinetic equation 2.19 and to model the interaction between beam fast ions and ICRH waves with the background plasma. The NBI and the ICRH systems will be presented in details in the following two sections.

2.3 Neutral Beam Injection physics and beam fast ions

The Neutral Beam Injection (NBI) is a widely used auxiliary heating system. This system is primarily applied to heat the plasma, and, under appropriate configurations, can also drive current, provide torque and fuelling. The NBI operates by injecting high energy neutral particles into the plasma, which subsequently become ionised through the interaction with the plasma background. After the ionization, the generated fast ions transfer their energy by Coulomb collisions to the bulk plasma, during the so-called slowing down phase. In the following, a brief description of how neutrals beam are produced and ionised is provided, as well as how beam and plasma interactions occur.

2.3.1 The Neutral Beam Injection system

The NBI system is structured in four main components: the ion source, the accelerator grids, the neutralizer and the residual ion dump. These are sketched in figure 2.8.

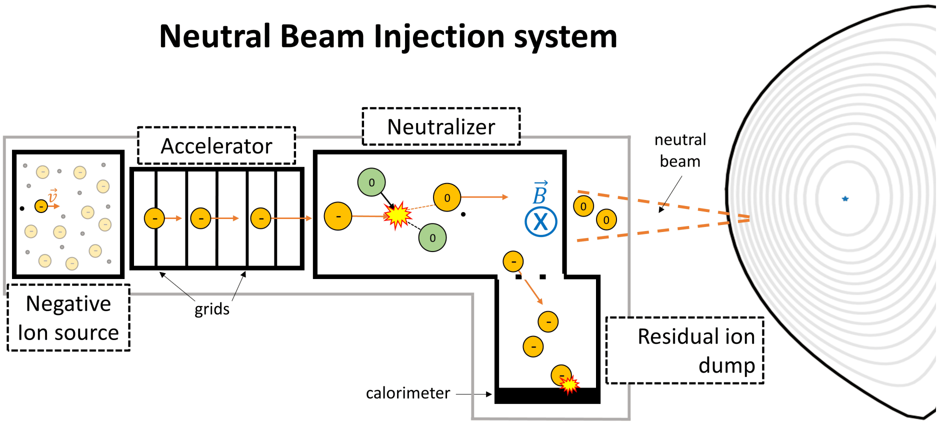

Figure 2.8: Schematic design of a neutral beam injection system characterized by a negative ion source.

- The **ion source** is selected to produce either low-energy positive or negative ions, depending on the device geometry, NBI configuration and physics requirements. Positive ions can be easily extracted from a low-temperature plasma. However, molecular ions may also be generated during the process. For example, when starting from a Deuterium (D) plasma, the extracted ions species can include D^+, D_2^+ and D_3^+. The fraction of molecular ions must be minimized since during the acceleration phase, their higher mass produces neutrals with lower energy than required, reducing beam penetration into the plasma. Positive ion source NBI (P-NBI) systems are typically used for low-energy injection, e.g. up to 100 keV, as their neutralization efficiency decreases significantly at higher energy. High-energy injection therefore requires negative ion sources, as planned for the NBI systems of DTT and ITER. Although the production of negative ions is more complex, their neutralization efficiency remains around 60% also at the energy required by the ITER NBI system (1 MeV in Deuterium beam). This improved efficiency arises from the weak binding of the extra electron, which can be easily stripped away [2].

- The acceleration to high energy is achieved through a series of grids forming the **accelerator**. These grids are held at different voltages (positive or negative depending on the ion source type), which establish potential differences that accelerate the ions as they pass through. During this phase, the most of the input electrical power is consumed.
- The **neutralizer** is a crucial component of the NBI system in a tokamak. The accelerated ions indeed must be neutralized before the injection, otherwise they would be deflected by the confining magnetic fields and subsequently lost. The neutralization occurs through collisions with a background gas, typically of the same species of the ion source. Figure 2.9 shows the neutralisation efficiency for hydrogen (H) and deuterium (D) beams, originating from positive and negative ion sources, clearly illustrating why negative ion sources are preferred for high-energy injection.

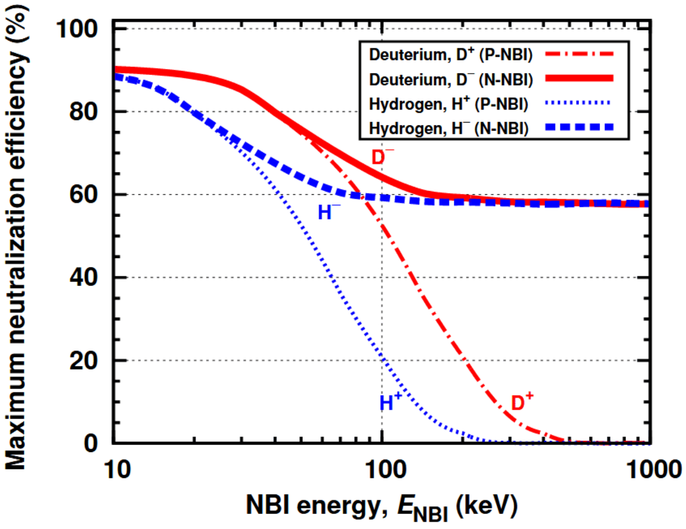

Figure 2.9: Neutralization efficiency for D and H atomic ions as a function of beam energy E_{NBI} [48].

- The **residual ion dump**, the last components of the beam-line, acts as a filter before the injection. Indeed, it collects the ions that are not neutralized in the previous stage by deflecting them through magnetic or electrostatic fields. The deviated ions are directed to the beam dump, e.g. a calorimeter, while the neutrals continue along their injection trajectories towards the tokamak plasma.

2.3.2 Neutral ionization and beam-plasma interactions

When neutral particles are injected into the plasma, they interact with the bulk plasma particles, becoming ionised and subsequently transferring their energy to the background plasma through Coulomb collisions. The ionization with the plasma occurs through three different mechanisms: charge exchange, ionization by ions (both main plasma ions and impurities) or ionization by electrons. As shown in figure 2.10, the charge-exchange process (CX) dominates at low injection energies, while ionization by ions and electrons becomes prevalent at higher injection energies. The cross-section of the ionization through impurities (Z) is significant, but impurity concentration in the plasma is small, determining a lower, though not negligible, effect on the total ionization of the beam. At high injection energies, moreover, the ionization cross-section must be corrected to account for the multistep ionization process [49], which occurs when a neutral atom is excited to a higher energy state through successive collisions before being ionized. Therefore, the total beam-stopping cross-section becomes:

$$\sigma = \sigma_0(1+\delta_{ms}) \qquad \text{with} \quad \sigma_0 = \sigma_p + \sigma_{CX} + \sigma_e + \sum \frac{n_Z}{n_e}\sigma_Z \tag{2.23}$$

where δ_{ms} is the multistep correction factor, n_Z and n_e are the impurity and electron density respectively. An additional effect that is not considered here, but could contribute to an enhancement of the beam-stopping cross-section, is the beam population self-interaction [50]. In this mechanism, neutral beam particles are ionized through interactions with beam energetic ions and its contribution may become non-negligible in low-density plasmas or when the fast-ion population is sufficiently large.

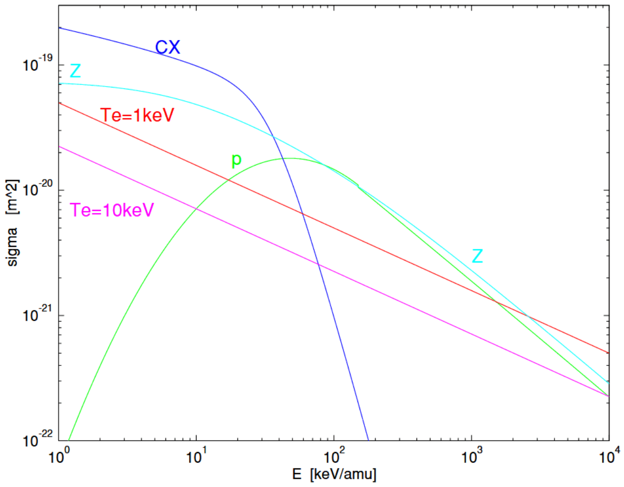

Figure 2.10: Cross-sections (sigma) of charge exchange (CX), electrons (Te lines), proton (p) and impurities (Z) ionizations of the injected neutral beams in the plasma. [49].

The ionization processes determine the attenuation of the neutral beam along its trajectory, which is commonly described by the beam penetration length. In a plasma with density n_e, this is defined as $\lambda = \frac{1}{n_e\sigma} \sim \frac{E_{\mathrm{NBI}}}{n_e}$, where the latter approximation is obtained since the ionization cross-section scales inversely with the beam injection energy E_{NBI} [2].

Once ionized, the beam particles interact with the background plasma through Coulomb interactions, transferring energy, current and torque. The beam particles are represented by a source term in equation 2.19, here assumed as a delta function $\langle S\rangle \propto \delta(E - E_{\mathrm{NBI}})$. Neglecting finite orbit width effects, assuming a static background plasma and no wave-particle interactions, a solution of the Fokker-Planck equation including the source of EP coming from the NBI can be obtained from 2.19 further integrating over the pitch angle, resulting finally in

$$f(E) = \frac{s_0 t_s m^{3/2}}{8\sqrt{2}\pi}\frac{\sigma\left(E_{\mathrm{NBI}} - E\right)\sigma\left(E - E_{min}(t)\right)}{E^{3/2} + E_c^{3/2}} \tag{2.24}$$

$$\text{with} \qquad E_{min}(t) = \left[\left(E_{\mathrm{NBI}}^{3/2} + E_c^{3/2}\right)e^{-\frac{3t}{t_s}} - E_c^{3/2}\right]^{2/3} \tag{2.25}$$

where s_0 is the number of NBI particles ionized on a flux surface per unit time and unit volume, E_c is the critical energy (eq. 2.17) and t_s the Spitzer slowing down time (eq. 2.16). Equation 2.24 represents the classical slowing down distribution function and it is valid for EP with energies much higher than the background temperature. The steady state solution is reached after a time denoted as slowing down time τ_s

$$\tau_s = \frac{t_s}{3}\ln\left(1 + \left(\frac{E_{\mathrm{NBI}}}{E_c}\right)^{3/2}\right) \tag{2.26}$$

The power deposited on each species ($P_{dep,i}$, $P_{dep,e}$) can be determined by integrating the energy transferred to the ions and electrons by collisions over the entire slowing down process [48], from the injection energy E_{NBI} to thermal energies, as

$$P_{dep,i}(E_{\mathrm{NBI}}) = P_{\mathrm{NBI}} \frac{E_c}{E_{\mathrm{NBI}}} \int_0^{E_{\mathrm{NBI}}/E_c} \frac{dy}{1+y^{3/2}} \qquad P_{dep,e}(E_{\mathrm{NBI}}) = P_{\mathrm{NBI}}\left(1 - p_i(E_{\mathrm{NBI}})\right) \tag{2.27}$$

The integral appearing on equation 2.27 can be carried out analytically, speeding up integrated modelling of NBI heated plasmas. The fraction of the deposited power density redistributed among electrons and ions as a function of E_0/E_c, with $E_0 = E_{\mathrm{NBI}}$, is shown in figure 2.11, illustrating in particular the case of injected beam energy of JET and ITER and the energy of alpha particles. From figure 2.11, it is possible to note that, considering the entire slowing down phase, the same energy transferred to ions and electrons is reached at $E_0/E_c \sim 2.4$ [48].

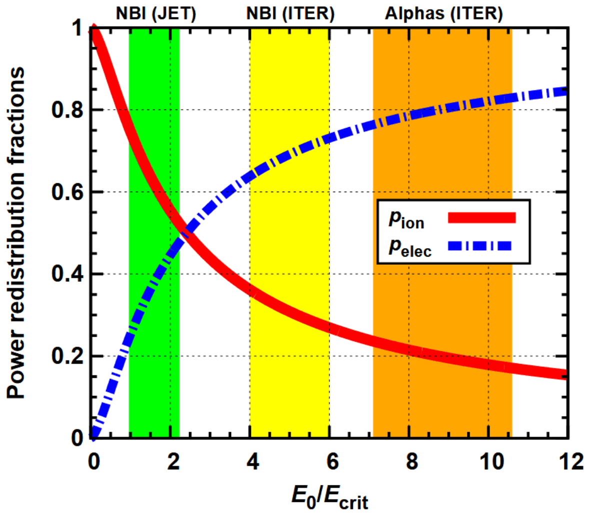

Figure 2.11: Power redistribution fraction from the energetic ions, showing examples of the NBI operation in JET (green) and ITER (yellow) and the case of alphas in ITER (in orange). E_0, E_{crit} stand for the beam injection and critical energy respectively [48].

Depending on the injection direction of the neutral beams, the fast ions may also drive plasma current and inject momentum. Two main configurations are distinguished: tangential and perpendicular injection (left fig. 2.12). The tangential injection can occur either in the co-current or counter-current directions and may be applied on-axis, i.e. aiming at the magnetic axis, or off-axis, i.e. aiming at different vertical and/or horizontal positions (right fig. 2.12). Counter-current tangential injections are affected by significant first orbit losses, previously discussed in subsection 2.1.2. Counter-current injection indeed generates trapped particles that close their orbits towards the outer part of the plasma, being more subjected therefore to losses on the wall when born on flux surfaces close to the plasma edge. Normal injection also presents a larger fraction of first orbit losses, compared to the tangential injection, since the generated beam particles are characterized by an higher perpendicular particle velocity and therefore the population of trapped particles is large. The Shine-Through (ST) losses can occur for both normal and tangential beams, in particular when the beam penetration is too large with respect to particle accessible path. For machine safety, it is essential to evaluate the acceptable limit of ST power deposited on the wall. A recent study [35] on ITER scenarios has performed this evaluation, considering not only the effect of E_{NBI}, and line-averaged n_e on the shine-through loss fraction but including also other parameters influencing the beam penetration (e.g. the density peaking factor and the electron temperature).

The normal injection configuration is mainly used to heat the plasma core, while the tangential injection can simultaneously heat, drive current and torque into the plasma. The injected ions carry toroidal momentum and as a result a fast ion current density is established, j_{NBI}. The magnitude of this fast current density depends on several factors such as the injection energy, the injection angle, the deposition profile of the injected ions and the strength of the collisions. Calculations of j_{NBI}

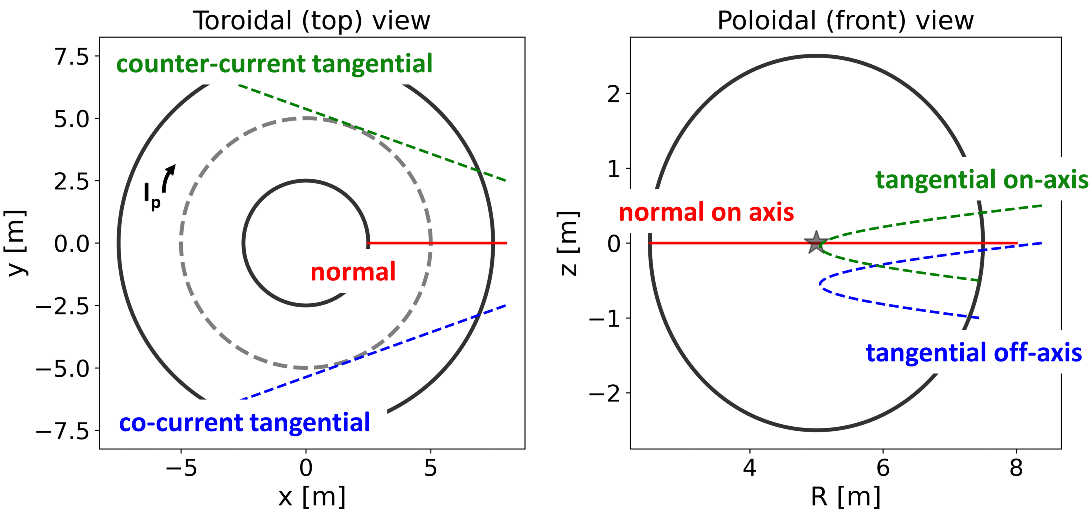

Figure 2.12: Schematic views of the possible NBI configurations in a tokamak. The toroidal view (left plot) shows normal (red), co-current tangential (blue), and counter-current tangential (green) injection directions. The dashed grey line represents the magnetic axis and the plasma current sign is reported too. The poloidal view of a circular plasma (right plot) shows on-axis normal (red) and tangential (green) injection and off-axis tangential beam (blue). The grey star represents the magnetic axis.

require solving at least a 2D Fokker-Planck equation in which trapping effects are taken into account. The situation is further complicated by the fact that the fast ion momentum drags the electrons along, establishing an electron back current density [31]. In the large aspect ratio approximation and in the low collisionality banana regime, the expression for the total driven current density j_{NBCD} can be expressed as:

$$j_{NBCD} = j_{\mathrm{NBI}} \left(1 - \frac{Z_{\mathrm{NBI}}}{Z_i} + 1.46\sqrt{\epsilon}\frac{Z_{\mathrm{NBI}}}{Z_{eff}} A(Z_{eff}) \right) \tag{2.28}$$

where ϵ the inverse aspect ratio and $A(Z_{eff})$ a function which depends on the effective charge Z_{eff} [31]. The second term on the right-hand side of equation 2.28 is the electron current contribution in absence of trapped electrons, which counteracts the beam ion current. The third term instead accounts for the trapped electrons, which reduce the impact of the electron current on the final driven j_{NBCD} [31]. The efficiency of the Neutral Beam Current Drive (NBCD) can be quantified as

$$\eta_{CD} = \frac{I_{NBCD}}{P_{NBI}} R_0 n_e = \gamma_{CD} R_0 n_e \tag{2.29}$$

with I_{NBCD} the total current driven by the NBI, obtained integrating the current density j_{NBCD} over the plasma surface, and it measures the capability of a neutral beam system to drive current, independently of device size and density scaling effects. The quantity γ_{CD} presents the engineering current-drive efficiency, expressing the driven current per unit injected power. The η_{CD} efficiency, incorporating the explicit dependence on n_e and R_0, allows meaningful comparisons across different machines and plasma scenarios.

Additionally, neutral beam injection provides a toroidal torque on the plasma, which can cause plasmas to rotate with rather high angular velocities. Plasma rotation has beneficial effects, e.g. in stabilising resistive wall modes [51]. The total torque provided by the beam ions is approximately given by

$$T_{\mathrm{NBI}} = \frac{P_{\mathrm{NBI}}}{E_{\mathrm{NBI}}} L_{\phi} = \frac{P_{\mathrm{NBI}}}{E_{\mathrm{NBI}}} R_0 A_{\mathrm{NBI}} m_p v_{NBI} = \frac{\sqrt{2 A_{\mathrm{NBI}} m_p}}{\sqrt{E_{\mathrm{NBI}}}} P_{\mathrm{NBI}} R_0 \tag{2.30}$$

where $\frac{P_{\mathrm{NBI}}}{E_{\mathrm{NBI}}}$ represents the particle injection rate and $L_\phi = R_0 m_i v_\|$ is the toroidal angular momentum carried by each injected ion, with $m_i = A_{\mathrm{NBI}} m_p$ and $v_\| \approx v_{\mathrm{NBI}}$ for tangential beam injection. This torque is transferred to the background plasma through two different mechanisms: one involves collisions (the collisional torque T_{coll}) while the other the radial current originated from the beam EPs (the electromagnetic torque T_{em}). The density of these two contributions can be formally expressed respectively as

$$T_{coll} = \left\langle Rm \int v_\| C(f) d^3v \right\rangle_\psi \tag{2.31}$$

with $\langle ... \rangle_\psi$ describing the flux surface average,

$$T_{em} = R(\vec{j}_r \times B_p)_\phi \tag{2.32}$$

where j_r is the radial current arising from the thermal bulk plasma to respond to the radial motion of energetic ions and maintain the quasi-neutrality of the plasma, such that $j_r + j_{EP,r} \approx 0$ [52–54]. The major source of radial current during the NBI is provided by particle ionised into trapped orbits, while the collisional mechanism is mainly related to passing particles. An import feature of these two torques is the characteristic time scale for transferring the injected momentum: indeed, while the collisional torque is obtained throughout the slowing down time, the electromagnetic torque develops over the orbit bounce period. An experimental evidence for this difference in time scales is shown in [55].

2.4 Ion Cyclotron Resonance Heating physics and IC-accelerated ions

The Ion Cyclotron Resonance Heating (ICRH) system is another widely used auxiliary heating method in present fusion experiments, and planned for future machines, including ITER and DTT. The ability to directly heat ions makes it an efficient tool for e.g. enhancing and controlling plasma fusion reactivity [56]. Beyond heating, the ICRH system can also be applied for current drive, wall conditioning and plasma initiation, during plasma breakdown and ramp up phases. The underlying physical principle relies on the generation of electromagnetic waves which resonate with the natural frequencies of the plasma ions, leading to a large transfer of power via particle acceleration. The accelerated particles then thermalize through Coulomb collisions, redistributing the absorbed wave power to the plasma. The following sections provide a concise overview of the ICRH system design and the fundamental physics of wave-particle resonances. For a detailed treatment of the wave physics, the reader is referred to the following works: [42, 56–58].

2.4.1 The Ion Cyclotron Resonance Heating system

The ICRH system is composed by three main elements, schematically illustrated in figure 2.13.

- Powered by a dedicated **supply system**, the ICRH **wave source** generates electromagnetic waves in the ion cyclotron frequency range (typically radio-frequency, in the range 20-100 MHz). The source is usually based on high-power vacuum tubes, which can operate across a broad frequency range, in contrast with gyrotrons (the wave source used in the electron cyclotron resonance heating), which are usually designed to operate at a fixed frequency [48].
- The waves produced by the source are then conveyed to the launching structure via the **transmission lines** system. In an ICRH system, conventional coaxial transmission lines are typically employed [59].
- The launching structure is usually an **antenna**, capable of coupling the waves power into the plasma [59]. The antenna consists of several metallic conductors, known as straps, positioned inside the vacuum chamber near the plasma edge. A current flows through the straps, with

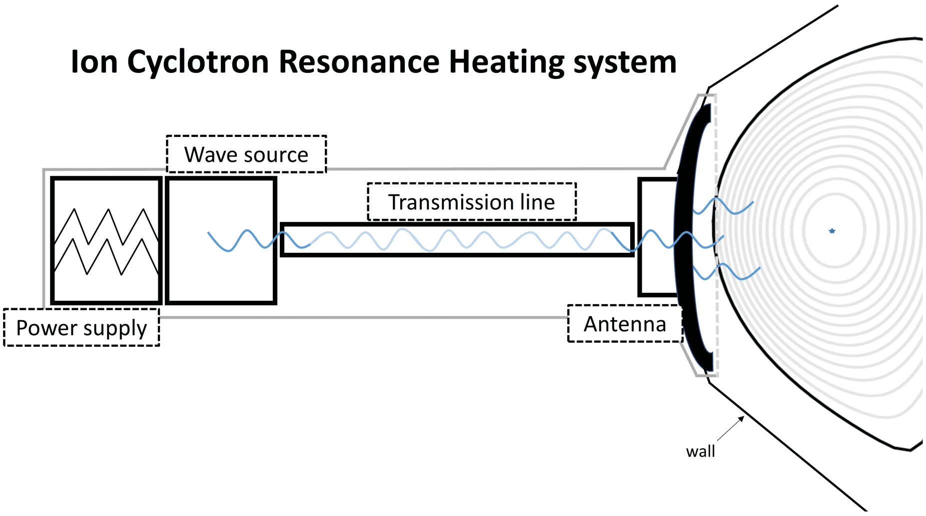

Figure 2.13: Schematic design of an ion cyclotron resonance heating system.

a frequency imposed by the source, and a phase dictated by the transmission lines. The antenna phasing, i.e. the phase difference between adjacent straps, determines the wave spectrum launched into the plasma. By adjusting this phasing, the propagation characteristics and power absorption profiles of the waves can be controlled [60]. An asymmetric spectrum is used to drive plasma current [59]. Careful optimisation of the antenna-plasma coupling is crucial to maximise power transfer efficiently and to avoid potential issues e.g. regarding the impurity release due to plasma-antenna interactions.

The operation of the ICRH system is characterized by two key parameters: the wave frequency ω, selected within the available range of frequencies of the source, and the parallel wave number $k_{||}$, defined with respect to the magnetic field, approximated for large toroidal mode number N_ϕ to $k_{||} \approx \frac{N_\phi}{R}$. The N_ϕ parameter is optimised to maximise the wave power spectrum according to the strap phasing. These quantities play a central role in determining wave propagation and resonance conditions, discussed in the following section.

2.4.2 Propagation of waves in the ion cyclotron range of frequencies and the effect of their absorption on resonating ions

The combination of the Maxwell's equations and the plasma particle equation of motion leads to the wave equation, which governs the evolution of the wave electric field $\vec{E}$ as

$$\nabla \times \nabla \times \vec{E} + \frac{\omega^2}{c^2} \overset{\leftrightarrow}{\epsilon} \cdot \vec{E} = i\mu_0 \omega \vec{j}_{ext} \tag{2.33}$$

where $\vec{j}_{ext}$ is the externally imposed current and $\overset{\leftrightarrow}{\epsilon}$ is the dielectric tensor, which accounts for the response of the plasma particles to the electric field. To provide some basic properties of equation 2.33 a planar geometry is assumed, despite full wave codes, such as CYRANO used in this thesis (see chapter 3), solve this wave equation in a toroidal tokamak geometry. The perturbation considered has the form $exp[i(\vec{k} \cdot \vec{r} - \omega t)]$. The propagation of the waves therefore results in the following dispersion relation [57]:

$$\vec{n} \times \vec{n} \times \vec{E} = \overset{\leftrightarrow}{\epsilon} \cdot \vec{E} \tag{2.34}$$

where $\vec{n} = \frac{\vec{k}c}{\omega}$ is the refractive index. The explicit form of the dielectric tensor depends on the chosen plasma model. In the cold plasma approximation, where thermal effects are neglected, $\overset{\leftrightarrow}{\epsilon}$ can be expressed as [57]:

$$\overleftrightarrow{\epsilon} = \begin{bmatrix} S & -iD & 0 \\ +iD & S & 0 \\ 0 & 0 & P \end{bmatrix} \tag{2.35}$$

with

$$S = \frac{1}{2}(R+L) \qquad D = \frac{1}{2}(R-L) \qquad P = 1 - \sum_s \frac{\omega_{ps}^2}{\omega^2} \tag{2.36}$$

and

$$R = 1 - \sum_s \frac{\omega_{ps}^2}{\omega(\omega+\Omega_s)} \qquad L = 1 - \sum_s \frac{\omega_{ps}^2}{\omega(\omega-\Omega_s)} \tag{2.37}$$

Here, $\omega_{ps} = \sqrt{\frac{n_s q_s^2}{m_s \epsilon_0}}$ is the plasma frequency and $\Omega_s = \frac{q_s B_0}{m_s}$ the cyclotron frequency for species s (ions or electrons), with n_s, q_s, m_s denoting their density, charge and mass respectively. In the ICRH system, the parallel component of the refractive index $n_\parallel$ is imposed by the antenna properties, meaning that the dispersion relation defines a constraint only on the perpendicular component $n_\perp$. Equations 2.34-2.37 give rise to two distinct dispersion relations, which are approximately given by

$$n_\perp^2 \simeq -\frac{\omega_{pe}^2}{\Omega_i^2} \quad \text{(slow wave)} \qquad n_\perp^2 \simeq \frac{(R-n_\parallel^2)(L-n_\parallel^2)}{S-n_\parallel^2} \quad \text{(fast wave)} \tag{2.38}$$

The fast magneto-sonic wave can easily access the centre of high-density plasmas and is therefore the main vehicle used for ICRF heating of fusion plasmas. However, it requires a finite density to propagate (typically $n_e \sim 1 \times 10^{18} m^{-3}$) [13]), being therefore evanescent at the plasma edge. For this reason, ICRF antennas need to be close to the plasma to minimise the distance the wave has to tunnel.

To describe the wave-particle resonances, a warm plasma model that includes the thermal and kinetic effects of the plasma is needed [42]. Within this description, which modifies the dielectric tensor defined in equation 2.35, wave power absorption occurs through resonant damping mechanisms. For the ICRH, the dominant damping arises when waves resonate with plasma ions satisfying the cyclotron resonance condition[1]:

$$\omega = N\Omega_i - k_\parallel v_\parallel \tag{2.39}$$

where $N = 0, 1, 2, ...$ is the harmonic number and $k_\parallel$, $v_\parallel$ are the parallel wave vector and parallel velocity of the resonant ions. The last term on the right-hand side of eq. 2.39 represents the Doppler shift, which becomes more significant for energetic ions that have a larger $v_\parallel$, broadening and shifting the resonance layer in the velocity space. The resonant region, located in the vicinity of $\omega = N\Omega_i$, depends on the harmonic number (N), the ion species (Z_i, A_i), and magnetic configuration, in particular on the major radius (R_0) and the magnetic field (B_0) at the magnetic axis. Assuming $B(R) = \frac{R_0 B_0}{R}$, the location of the resonant layer can be computed as [48]:

$$R_{IC} = 15.2\ R_0[\text{m}] B_0[\text{T}] \frac{N Z_i}{A_i} \frac{2\pi}{\omega[\text{MHz}]} \tag{2.40}$$

Due to the Doppler shift seen in eq. 2.39, ions with sufficiently high $v_\parallel$ experience the resonance away from the nominal layer R_{IC}, with a spatial correction proportional to $\frac{v_\parallel n_\parallel}{\omega[MHz]}$. Figures 2.14a and 2.14b illustrate, respectively, the dependence of the resonance layer on ion species and harmonic number, and the impact of the Doppler shift for an ITER-like plasma with $B_0 = 5.3$ T, $R_0 = 6.2$ m. In this case, the antenna phasing has $N_\phi = \pm\ 35$.

The wave electric field E, appearing in eq. 2.34, can be decomposed into a perpendicular and a parallel components. For the fast waves, while the parallel electric field is weak and can therefore

---

[1] The wave frequency ω is defined in rad/s if not opportunely specified

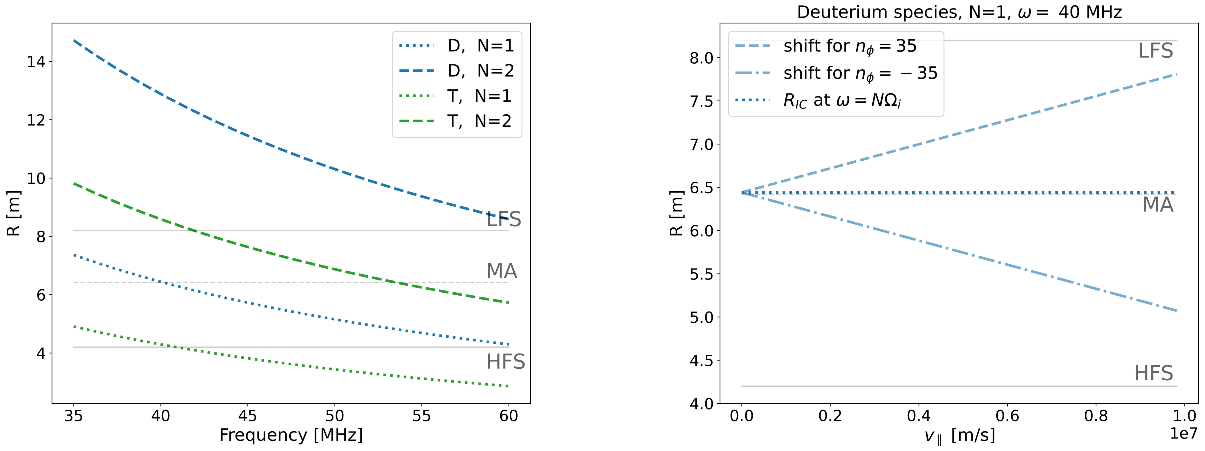

(a) Location of the ion cyclotron resonance layers for Deuterium and Tritium ions at fundamental (N=1) and second (N=2) harmonics, shown respectively by dotted and dashed lines. The grey lines indicate the plasma boundaries, marking the limits of the low-field side (LFS) and high-field side (HFS), as well as the position of the magnetic axis (MA).

(b) Shift of the resonance layer from the nominal condition, where $\omega = N\Omega_i$ (dotted line), due to Doppler shift effects for deuterium ions heated at the fundamental scheme with $\omega = 40$ MHz and $n_\phi = \pm 35$. Increasing ion parallel velocity $v_\parallel$ leads to a larger displacement from the nominal resonance position R_{IC} [61]. Plasma boundaries and magnetic axis are indicated as in 2.14a.

Figure 2.14: Dependence of the resonance layer on ion species, harmonic number and on the Doppler shift.

be neglected when analysing the interaction with resonant ions, the perpendicular component can be further decomposed into the left-hand E_+ and right-hand E_- rotating components. Ions rotate in the same direction of the left-hand E_+ electric field component, being therefore responsible for the acceleration of resonating ions. The ratio between the two rotating components, in the cold plasma approximation, result in [62]

$$\frac{E_+}{E_-} = \frac{\frac{\Omega_i}{\omega+\Omega_i} - N_\parallel^2}{\frac{\Omega_i}{\omega-\Omega_i} + N_\parallel^2} \propto \frac{\omega - \Omega_i}{\omega + \Omega_i} \tag{2.41}$$

where $N_\parallel$ is the Alfvén refractive index, defined as the parallel phase velocity normalized to the Alfvén velocity [62]. Close to the resonance ($\omega = \Omega_i$), the fast wave is predominantly right-handed polarized (E_-), with $E_+ \to 0$ for a plasma composed of a single ion species. As consequence, the ion acceleration is inefficient. A common solution is the introduction of a minority species in the plasma (two-species plasma), which becomes the resonant species. In this way, the majority species control the wave polarisation E_+/E_-, while the minority ions absorb the RF power at their cyclotron resonance frequency [61]. The optimal concentration of the minority species is typically in the range of 1-10% [63]. A more comprehensive discussion of wave power absorption should include both the appearance of the so called ion-ion hybrid resonance layer and the possibility of mode conversion to shower wavelength waves in the vicinity of the minority cyclotron resonance [57]. However, in this thesis, only warm plasmas and high toroidal mode numbers are considered, for which mode conversion is generally not important. Classical fundamental minority heating schemes are hydrogen minority in deuterium plasmas (H)D, helium-3 minority in deuterium plasmas (He3)D and deuterium minority in majority tritium plasmas (D)T. ICRF wave absorption can also be achieved through second harmonic ion cyclotron resonances. In this case, the absorption mechanism is a Finite Larmor Radius (FLR) effect. During second harmonic interaction, a resonant ion is accelerated during half of its Larmor orbit and de-accelerated during the other half. However, owing to the finite perpendicular wave number, the electric field strength is not uniform along the Larmor orbit and as a consequence there is a finite change of energy of the resonant ions. For thermal ions, the Larmor radius is small, and the interaction is therefore relatively weak, leading a low damping rate of the ICRF waves in cold plasmas. On the other hand, if an energetic ion population develops, e.g. through the neutral beam injection or through prior-ICRH application, the absorption efficiency increases. This behaviour is exploited for example in the combined application of NBI and ICRH, which determines the appearance of a significant energetic tail on the distribution function, beyond the injection energy, as represented by a schematic representation in figure 2.15. Combining NBI and ICRH together can contribute to increase the neutron reaction rate [64], and a study of their synergy in ITER is presented in chapter 6.

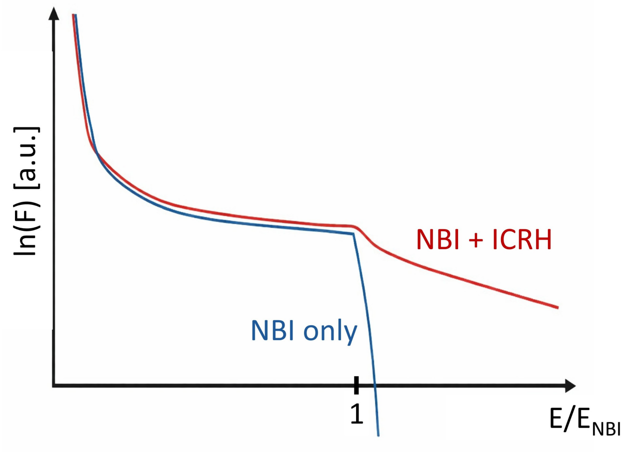

Figure 2.15: Illustrative scheme to represent the effect of combined neutral beam injection and absorption of ICRH waves by the ionized particles.

It should be noted that FLR effects are not restricted to second harmonic only, but can also influence fundamental resonance absorption when energetic ions are present. An additional efficient heating scheme configuration is the three-ion scheme [58]. This method introduces a third ion species such that $min(Z_1,\ Z_2) < Z_3 < max(Z_1,\ Z_2)$, which benefits from the enhanced left-hand polarization near the $(L - n_{\|}^2)$ cut-off of the fast wave solution (eq. 2.38) [58]. Indeed, if the resonance layer of this third species lies near this cut-off region, substantial power can be absorbed even at very low concentrations ($< 5\%$). This approach can exploit the presence of impurity ions, when of suitable species, to act as effective power absorbers, producing energetic ions beneficial for plasma heating [60]. The efficiency of this scheme has been successfully demonstrated in several experiments [58].

Despite the considered heating scheme, as result of an interaction, the resonant ion gets a kick, mainly on its perpendicular velocity, according to the wave electric field preferential direction. The magnitude of this kick depends on the local wave fields and on the relative phase α between the ion cyclotron motion and the wave. Efficient absorption due to wave-particle interaction relies on the fact that successive kicks at the resonance are decorrelated, i.e. the phase α is random. Such assumption is valid because of collisions and non-linear diffusive effects [65]. The sequence of uncorrelated energy kicks can therefore be interpreted as a random walk process in invariant space, leading to the quasi-linear diffusion tensor D_{RF}^{ij} appearing in equation 2.22. The energy diffusion term, D_{RF}^{EE}, can be written as [45], [66]

$$D_{RF}^{EE} = \sum_{N_\phi} \sum_{i_{res}} \frac{\left\langle (\Delta E)^2_{N_\phi, i_{res}} \right\rangle_\alpha}{2\tau_b} \tag{2.42}$$

where i_{res} indicates the number of resonance points along a particle orbit (e.g. four for a trapped particle), for a given toroidal mode number N_ϕ and ΔE is the energy kick. Within a stationary phase approximation, the $\left\langle (\Delta E)^2 \right\rangle_\alpha$ contribution, averaged over the phase angle α, can be expressed as

$$\left\langle (\Delta E)^2 \right\rangle_\alpha \approx \frac{\pi (Ze)^2 v_\perp^2}{|N\dot{\Omega}|} \left| E_+ J_{n-1}\left(\frac{k_\perp v_\perp}{\Omega}\right) + E_- J_{n+1}\left(\frac{k_\perp v_\perp}{\Omega}\right) \right|^2 \tag{2.43}$$

where $J_{n-1},\ J_{n+1}$ are Bessel functions of order $n \pm 1$ ($J_m(x) \sim \frac{(x/2)^m}{m!}$) which show a dependence on the perpendicular wave-vector $k_\perp$ and on the Larmor radius $\rho_L = \frac{v_\perp}{\Omega}$. The kick in energy is related to the kicks a particle receives in the other invariants of motion Λ and P_ϕ as [66]

$$\Delta\Lambda = \frac{N\Omega - \Lambda\omega}{E}\Delta E \tag{2.44}$$

$$\Delta P_\phi = \frac{N_\phi}{\omega}\Delta E \tag{2.45}$$

Relation 2.44 shows that $\Lambda = \frac{n\Omega}{\omega}$ is a stable fixed point of the dynamics: as resonant ions gain energy, their normalized magnetic moment Λ approaches $n\Omega/\omega$. For trapped ions this condition corresponds to having their orbit turning point located at the resonance layer ($n\Omega = \omega$). Equation 2.45, instead, can be particularly important for asymmetric toroidal mode number spectra. For a trapped ion, whose turning point is located at $\psi_p = P_\phi/Ze$, a change in the toroidal canonical angular momentum P_ϕ, due to the absorption of wave momentum, results in a radial displacement of the turning point. If the wave spectrum is asymmetric (i.e. dominated by positive or negative N_ϕ) the turning point can shift outward or inward. A detailed analysis shows that resonant ions are driven outward by counter-current propagating waves and inward by co-current propagating waves, a behaviour that has also been observed experimentally [67]. There exists a set of invariants of motion where only one variable is affected by the resonant kick. This set, used in RFOF library [28] (see chapter 3), foresees:

$$\begin{aligned} I_\perp &= \frac{\omega}{N\Omega}\Lambda E \\ I_\parallel &= E - I_\perp \\ I_\phi &= P_\phi - E \end{aligned} \tag{2.46}$$

In this invariant set, only $I_\perp$ changes after a resonant interaction. In RFOF, a Monte Carlo operator updates the variable $I_\perp$ after an interaction occurs and translates this change into variation of the perpendicular and parallel particle velocities.

All the physics basis described in this chapter are essential to understand the models of the numerical codes that will be presented in the following chapter, as well as the analysis performed and presented from chapter 4 to characterize the distribution functions of the energetic particles generated by the NBI and the ICRH systems.

CHAPTER

3

INVESTIGATED FUSION DEVICES AND APPLIED NUMERICAL TOOLS

The fusion devices considered in this work are here presented, going deeper into their description after having already mentioned them in section 1.3. In particular, the tokamaks JET, DTT, and ITER are presented in this order, describing their achieved or planned scientific objectives. Moreover, the key characteristics of each device, and the configurations of the NBI and ICRH systems simulated in this work, are summarized. The second part of this chapter describes the numerical tools used for the modelling activities. It starts with the codes applied to model the sources of energetic particles and waves, following then the solvers used for the Fokker-Planck equation, either in analytical form or via Monte Carlo orbit following method. Finally, the IMAS modelling framework, which allows the different codes described to be linked in a workflow, is described, as well as a dedicated tool that enables to study the EP stability after slowing down simulations.

3.1 The Joint European Torus (JET)

The Joint European Torus (JET) [68] was the largest operating tokamak in the world until 2023, when started the decommissioning phase. Located at the Culham site in the UK, JET has been the leading experimental facility of the European fusion programme. Its primary mission was to explore plasma physics in reactor-relevant conditions, studying in particular plasma-wall interaction, plasma heating and EP physics, including alphas thanks to D-T operations. For this scope, JET underwent several upgrades of its vessel and plasma facing components, it was equipped with auxiliary heating systems capable to provide more than 60 MW of input power in the plasma, and was designed to operate with Deuterium-Tritium (DT) plasma mixtures.

JET was designed with a major radius of $R_0 = 2.96$ m and a minor radius $a = 1.25$ m, making it the largest tokamak of its time. It achieved toroidal magnetic field up to $B_{tor} = 4$ T at R_0 and high-plasma current up to $I_p = 6$ MA [23], allowing improved confinement of energetic particles. It was also the first tokamak having a D-shaped poloidal cross-section [23]. In the last decade of its operations, JET was equipped with a full-metal wall, consisting of beryllium in the main chamber and tungsten in the divertor, allowing experiments under conditions very similar to those foreseen for ITER's original first wall design, which has now evolved towards full tungsten wall. Several auxiliary heating systems were installed on JET. These included NBI systems with positive ion sources having energies up to

120 keV, an ICRH system operating in the 23–57 MHz range, and a LHCD system for off-axis current drive [69]. This flexible heating mix also enabled the development of advanced scenarios. Moreover, the synergy between the NBI and ICRH systems played a central role in achieving the record of the highest fusion energy produced during the last JET campaign in 2023 [21]. Figure 3.1 shows the two NBI lines, the four installed ICRH antennas and the LHCD system in the torus top view.

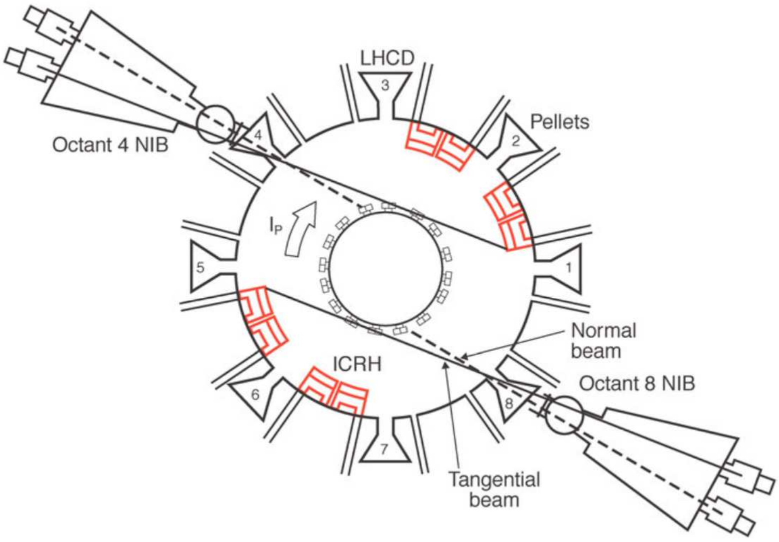

Figure 3.1: Top view of the available NBI lines, ICRH antennas and LHCD system in JET since 2000 [70].

The JET ICRH was designed to operate in the 23-57 MHz frequency range and could couple up to 22 MW of power to the plasma through several antenna configurations. Over the years, the system evolved significantly [70]. After the divertor upgrade in 1992-94 [23], the ICRH system was composed by four antennas with multiple phasing options. These configurations, listed in table 3.1, contribute in different ways to the ICRH exploitation, enabling different waves spectrum and applications. In 2005, an additional upgrade was implemented to address performance limitations in ELMy (Edge-Localised Mode) H-mode plasmas [71] and to introduce a new antenna concept for the ITER-Like Antenna (ILA) project [72], which offered an opportunity to test one of the main concepts that has been proposed for ITER ICRH system. Figure 3.2 shows two of the standard JET antennas and the ILA, installed in 2008 and commissioned in 2009 [73]. Its worth noting that the design of the ITER ICRH antenna has been substantially revised [74], therefore, the JET ILA antenna can no longer be considered ITER-like.

Strap phasing	$\lvert \mathbf{N}_\phi \rvert$	**Types of waves**
$(0,\ \pi,\ 0,\ \pi)$	27	waves with a symmetric spectrum
$(0,\ \pi/2,\ \pi\ 3,\ \pi/2)$	14	waves in the co-current direction
$(0,\ -\pi/2,\ -\pi\ 3,\ -\pi/2)$	14	waves in the counter-current direction

Table 3.1: Possible strap phasing, and relative toroidal wave mode N_ϕ, of the four straps in the JET antenna [70].

JET's data has been crucial for validating transport and fast-ion models, assessing alpha-particle physics and studying operational regimes for future reactor-scale devices. Its unique DT capability provides the closest experimental conditions to those expected in ITER, making it the only operating facility in the last 20 years capable of handling DT plasma experiments before ITER operations. Even if JET ended its experimental activity in 2023, the extensive data collected during its experimental campaigns play a crucial role in the validation of models in support of the forthcoming JT-60SA experimental campaign and ITER operations.

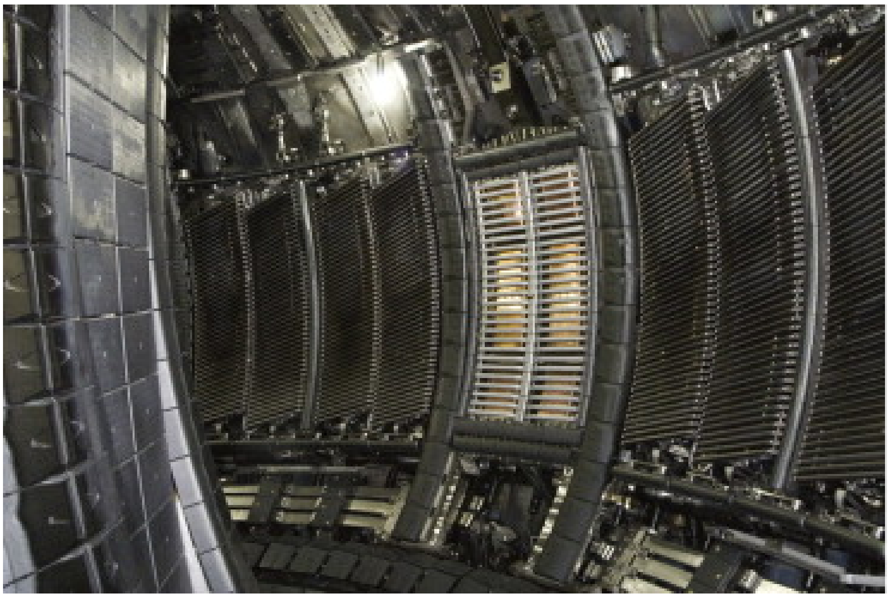

Figure 3.2: Picture of the ITER-Like Antenna installed between two of the four antennas available since 1994 in JET [73].

3.2 The Divertor Tokamak Test (DTT) facility

The Divertor Tokamak Test (DTT) facility [75] is a tokamak project currently under construction in Frascati, Italy, proposed in line with the objectives of the European Roadmap [76] for the realization of fusion energy. The primary objective of DTT is to investigate the power exhaust problem by evaluating different plasma shapes at different tokamak magnetic fields and divertor configurations, under conditions relevant for ITER and DEMO. DTT is a tokamak with superconducting coils, led by ENEA and ENI consortium and the participation of important Italian research centres and universities, including Consorzio RFX.

The design of DTT has been optimized for specific plasma parameters, such as the normalized beta factor, the plasma collisionality and the normalized Larmor radius, to replicate plasma conditions similar to those in ITER and DEMO. The machine features a major and minor radius of $R_0 = 2.19$ m and $a = 0.70$ m [75]. The current design foresees a toroidal magnetic field of $B_{tor} \sim 6$ T at R_0 and a plasma current of I_p up to 5.5 MA. The total auxiliary heating power is up to 45 MW, distributed among ECRH (29 MW), ICRH (6 MW) and NBI (10 MW) systems [75]. All plasma facing components and the first wall are made of Tungsten (W), the same material planned for ITER as stated in the recent released research plan [22, 77]. Therefore, DTT will be exploited to investigate advanced confinement scenarios in a full W environment, operating in parallel with ITER, supporting experiments and addressing potential issues before DEMO realization. The first plasma is expected at the end of this decade, with three distinct operation phases at increasing auxiliary heating power [75].

DTT will be equipped with a Negative-ion sourced NBI (N-NBI) [78], capable of injecting deuterium and hydrogen neutrals up to 510 keV. Such injection energy is needed due to the high plasma volume-averaged density foreseen in DTT, approximatively $n_e \sim 1.5 \times 10^{20}\ m^{-3}$ for the baseline full power scenario, which requires a high-energy NBI for core heating. The DTT NBI system would represent the second-highest beam energy after ITER operation, similar to the JT-60SA N-NBI system, which will soon operate in the experimental campaign, foreseen at the end of 2026/early 2027. Moreover, DTT NBI will be the only other system apart from ITER NBI with a N-NBI applied in a high magnetic field device with a full metal wall. The beam energy can be modulated with an almost linear decrease in power due to beam optics requirements, within the range 250-510 keV. The NBI system will inject slightly below the magnetic axis as foreseen for the DTT reference plasma scenario and in the co-current tangential direction ($R_{tang} \sim 1.95$ m). This choice minimizes the first orbit losses, enabling current drive and torque injection. The trajectories of some of the 1360 sub-beams, or beamlets, composing the beam are illustrated in figure 3.3, from torus top and poloidal views. The nominal power injected in the torus is 10 MW, but the effect of the so-called stray field, which results in beam duct losses, slightly reduced it by about 3.8% at full plasma current [79]. The NBI system is expected to be installed and operational from phase 2 of DTT operation, starting in mid 2030s [75].

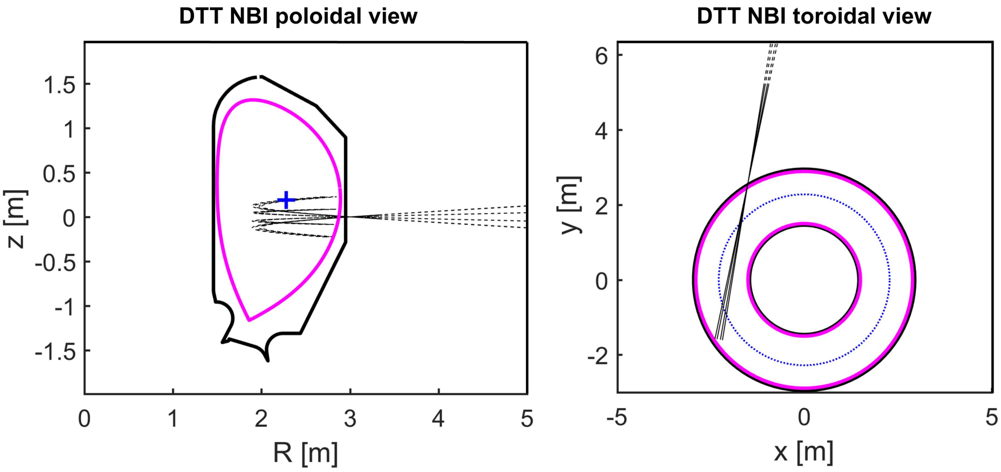

Figure 3.3: Poloidal and toroidal views of neutral beam injection lines of DTT NBI system [79].

3.3 ITER

ITER is the first-of-a-kind reactor-scale superconductive tokamak being constructed in Cadarache, France, by an international collaboration that involves Europe, USA, China, Japan, Korea, India and Russia. ITER represents the first attempt to integrate reactor-relevant technologies and burning-plasma physics within a single device, to demonstrate the scientific and technological feasibility of fusion energy at reactor scale. It is a large-scale tokamak with a major radius of $R_0 = 6.2$ m and a minor radius $a = 2.0$ m, designed to reach a toroidal magnetic field of 5.3 T and a high-plasma current up to 15 MA. Its large size and strong magnetic field allow operations at low collisionality and dimensionless parameters comparable to those expected in future reactors. Its primary objectives is to achieve high-Q, long-duration plasmas, with a target fusion gain of Q $\geq$ 10 sustained for $\sim$ 400 s and Q $\geq$ 5 for $\sim$ 3000 s, while addressing key challenges in plasma control, alpha-particle confinement and power exhaust. To achieve ITER scientific goals, the research plan, recently updated [22, 77, 80], defines three main operational phase:

- the **Start of Research Operation (SRO) phase** aims at commissioning the device auxiliary systems and at developing the operational basis for the plasma scenarios realized in the following phases. This is achieved by operating in low confinement mode at high plasma current (15 MA) in hydrogen plasmas and high confinement mode in deuterium plasmas at low magnetic field ($B_{tor} = 2.65$ T at R_0);
- the **first Deuterium-Tritium phase (DT-1)** will demonstrate plasma confinement with Q $\geq$ 10, for a duration of about 400 s in D-T plasmas;
- the **second DT phase (DT-2)** will test the feasibility of long pulses and steady state operations with Q $\geq$ 5.

Thanks to these ambitious objectives, ITER offers the unique opportunity to obtain unprecedented results that will directly impact the design and realisation of future fusion power plants.

More than 100 MW of auxiliary heating power will be available, including two Deuterium Negative NBI systems operating at the highest injection energy to date (1 MeV in Deuterium, or 870 keV in Hydrogen), delivering 33 MW of power, an ICRH system capable of operating in the 40–55 MHz frequency range (10 MW initially planned), and an ECRH system at 170 GHz delivering up to 60 or 67 MW. A detailed partition of the auxiliary power across the planned operational phases is shown in figure 3.4, including possible power upgrades for all the mentioned systems.

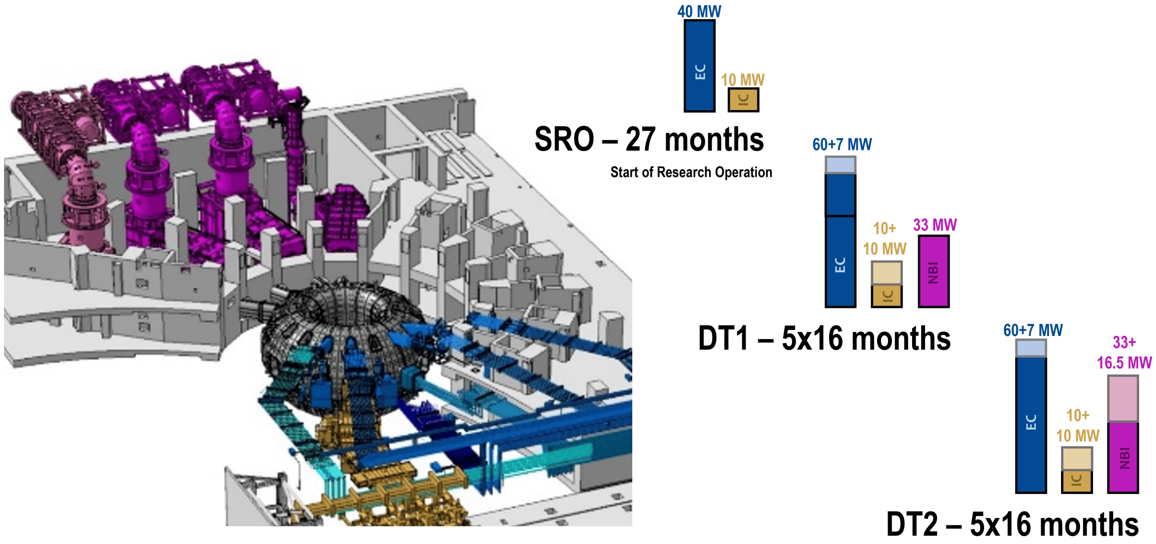

Figure 3.4: Design of the three auxiliary heating systems available in ITER: the NBIs are coloured in purple (with the third negative beam planned for an upgrade in pink, and the diagnostic one on the right side), the ICRH line is coloured in gold and the ECRH in blue [74]. The block diagrams on the right side represent the injected power available in the various operational phases of ITER, according to the colour coding of the figure on the left. The total time allocated for the experimental campaigns of each phase is reported, according to the current research plan [22].

The ITER NBI system foresees two Heating Neutral Beam (HNB) injectors, with a third one to be considered for installation at the later stage of operations [81], for heating and current drive purposes. In addition, a Diagnostic Neutral Beam (DNB) will be equipped to support charge exchange recombination spectroscopy measurements; this beam is based on a low-energy (100 keV) negative hydrogen ion source [82]. The choice of a negative ion source for the DNB is driven by considerations related to cost reduction. The HNB system are designed to inject hydrogen and deuterium neutrals into the plasma at energies of 870 keV and 1 MeV, respectively. The technological requirements of the deuterium beam, achieved through an extraction current of 40 A of negative ions, allow the hydrogen beam to use the same beam optics at lower injection energy and higher extracted current, namely 870 keV and 46 A. The beam energy can be modulated, guaranteeing an optimised beam optic down to 500 keV. Each injector delivers 16.5 MW of power, for a total of ~33 MW coupled to the plasma. The injected power depends on the beam energy following the scaling $\mathrm{P}_{\mathrm{NBI}} \propto \mathrm{E}_{\mathrm{NBI}}^{2.5}$, ensuring an acceptable beam perveance, in terms of focal broadening within the design limits [81]. The beams are injected in the co-current tangential direction, with a tangential radius of $R_{tang} = 5.3$ m. Their poloidal position can be modified by tilting the injector by ±10 mrad relative to the neutral beam axis, which is tilted by -49.2 mrad with respect to z = 0 plane. A downward tilt corresponds to the extreme off-axis configuration (-10 mrad), while a full upward tilt defines the extreme on-axis configuration (+10 mrad) [83]. The standard ITER NBI geometry uses one off-axis and one on-axis beam (OFF-ON configuration), tilted of ±9 mrad. In the analysis presented in chapters 4 and 6, the impact of varying the NBI tilt on fast-ion orbit topology is examined in detail.

Regarding the ICRH system, the updated ITER research plan includes a single antenna operating in the 40-55 MHz frequency range. The antenna will couple 10 MW of power, with a possible upgrade to 20 MW during the DT-1 phase. In SRO phase, the ICRH system will primarily support wall conditioning and will investigate possible tungsten accumulation due to its use, an effect currently examined through extensive modelling efforts [84]. The ITER antenna is composed by 24 straps, arranged in eight triplets, which enable multiple excitation configurations. Toroidal and poloidal phasing refer respectively to the phase differences between straps in the toroidal and poloidal directions. ITER foresees five toroidal phasing: three dipole heating configurations $(0, \pi, \pi, 0)$, $(0, \pi, 0, \pi)$, $(0, 0, \pi, \pi)$, and two current-drive configurations $\pm(0, \pi/2, \pi, 3\pi/2)$ [85]. Four poloidal phasing are available: $(0, 0), (0, \pi), \pm(0, \pi/2)$. In terms of power coupling capability and load resistance, the reference phasing scheme adapted is $(0, \pi, \pi, 0)$, with poloidal configuration $\pm(0, \pi/2)$ [86]. This configuration produces a symmetric spectrum peaked at $k_{\|} \sim 4\ m^{-1}$, with the antenna located at $R_{ant} \sim 8.45$ m and a toroidal mode number of $|N_\phi| = 35$. This is the phase scenario considered in the ICRH modelling studies presented in chapter 5.

3.4 Codes for energetic particle sources in plasmas

After the introduction of the fusion devices investigated in this work, it is now appropriate to present the numerical tools used to characterize the distribution functions of the energetic particles generated by the previously presented NBI and ICRH systems. Modelling energetic particle behaviour in a plasma requires two classes of numerical codes: EP source codes and slowing down solvers. While the latter are discussed in section 3.5, the present section focuses on the source codes, which provide information on the origin of energetic particles, such as beam ions or ICRH-accelerated populations. In the case of ICRH, it is necessary to model both the energetic particle sources that interact with the waves, e.g. thermal and beam particles, and the waves themselves. This section therefore describes the BBNBI code for modelling the beam ion source and the CYRANO code used to compute the electromagnetic fields associated with ion-cyclotron heating. Thermal particles also need to be modelled for ICRH interaction studies; however, no suitable tool was available for this purpose. A dedicated thermal-particle generator was therefore developed as part of this project and is presented in detail in section 5.1.2, along with its implementation and validation.

3.4.1 BBNBI

BBNBI (Beamlet-Based Neutral Beam Injection) [87] is a Monte Carlo beam deposition code based on a beamlet representation of the neutral beam injection system. It computes neutral-beam ionization, including ionization outside the Last Closed Flux Surface (LCFS), and estimates the fraction of shine-through particles reaching the wall. The code follows neutral particles, represented by an ensemble of markers injected per second, from the grounded grid, i.e. the last accelerator grid of the NBI system, until they are ionized in the plasma. The stopping cross-section is determined according to the Suzuki model [88] but ADAS ionization cross-section can also be used if available. Markers that exit the plasma hitting the wall without being ionized are counted as shine-through losses. In BBNBI, the beam is modelled beamlets by beamlets The origin and injection direction of each beamlet, as well as the beamlet horizontal and vertical divergence, can be independently specified. The total injected power, particle species and the full beam energy of the beam can be set, and the usual fraction energy components (E, E/2, E/3), used in positive-ion NBI modelling, can also be considered. Several NBI geometries are already implemented in BBNBI, including e.g. those of JET, DTT and ITER. A list of typical BBNBI inputs is reported in table 3.2. BBNBI can also be used in the Integrated Modelling and Analysis Suite (IMAS) framework [89]. BBNBI has been already benchmarked with NUBEAM, PENCIL and NEMO beam ionization codes, showing a good quantitative agreement [87, 90].

3.4.2 CYRANO

Modelling wave propagation and absorption in hot plasmas requires different levels of approximations due to the complexity of the physics problem reflected in the dielectric tensor. Full-waves codes provide the most complete description, since they solve directly the wave equation, using finite elements or finite difference methods combined with the poloidal Fourier decomposition [56, 91]. CYRANO (for CYclotron Resonance Analysis with No Obfuscation) is one of these: a full-wave code that solves the full Maxwell's equations in a tokamak in the ion-cyclotron frequency range [92]. It uses the finite-element method (FEM) for the radial discretization and the Fourier decomposition in the poloidal and toroidal directions for the electromagnetic fields [61]. Users may specify parameters such as the radial resolution (number of finite elements) and poloidal resolution (number of Fourier modes). CYRANO handles both Maxwellian and non-Maxwellian distribution functions and includes finite Larmor radius effects up to the second order: the lowest order in Larmor radius describes the fundamental cyclotron damping and Landau damping; while the second order describes the Bernstein waves, TTMP and second harmonic cyclotron absorption [92]. The code requires equilibrium magnetic field and plasma kinetic profiles as input. Its output includes the three components of the wave fields (the left-hand E_+, right-hand E_- polarization and the parallel $E_\parallel$ components) as well as the power absorption resolved for all the species considered, including the beam ions and impurities, if present. Such outputs are essential inputs for Fokker-Planck solvers incorporating the quasi-linear operator. All required inputs and available outputs for CYRANO are listed in tables 3.2 and 3.3 respectively. CYRANO is widely used for modelling in JET [93, 94], WEST [95] and ITER [89], and is also available within the IMAS framework [89].

3.5 Codes for slowing down distribution functions

Distribution functions of energetic particles enclose essential information regarding the EPs' behaviour. To obtain the slowed-down EP distribution functions, two main approaches are used to solve the Fokker-Planck (FP) equation: the analytical solution or the orbit following method. The FP equation, reported in its general form in eq. 2.19, governs the time evolution of the distribution functions. However, its analytical solution is non-trivial and relies on several assumptions and approximations which inevitably limit the accuracy of the resulting distributions. In the orbit following approach, the FP equation is solved statistically by tracking an ensemble of markers and integrating their trajectories according to their equations of motion. The particle phase-space, denoted by the 6D vector $\vec{z} = (\vec{x}, \vec{v})$, where $\vec{x}$ and $\vec{v}$ are the particle position and velocity respectively, can be evolved in time through a Langevin equation

$$d\vec{z} = \left[\dot{\vec{z}} + \vec{a}(\vec{z}, t)\right] dt + \vec{\sigma}(\vec{z}, t) \cdot d\vec{W} \tag{3.1}$$

where $\dot{\vec{z}}$ represents the deterministic evolution of the particle along its orbit in the absence of collisions and $\vec{W}$ is a vector of independent Wiener processes modelling stochastic effects [27]. The effects of Coulomb collisions and wave-particle interactions on particle trajectories are included in eq. 3.1 through $\vec{a}$ and $\vec{\sigma}$ coefficients, which represent the drift and diffusion coefficients [96]. Solving a large number of Langevin equations provides an accurate approximation of the distribution function and naturally includes physical effects often neglected in analytical FP treatments, such as pitch-angle scattering and the finite orbit width effects. The following subsections introduce two codes that apply these approaches: FOPLA, an analytical Fokker-Planck solver, and ASCOT, an orbit-following Monte Carlo code.

3.5.1 FOPLA

FOPLA [97] is a simplified model used to solve the slowing down process of energetic particles. It computes analytically the steady-state solutions of coupled one-dimensional (1D) Fokker-Planck equations in the velocity space. By focusing on time-independent and pitch angle averaged distribution functions $f(v)$, FOPLA provides computationally efficient evaluations of energetic particle behaviour in a fusion plasma. FOPLA is designed to handle non-Maxwellian populations, such as minority ions populations, e.g. generated by neutral injection through NBI systems or heated by ICRH, and fusion-born alpha particles. It can also include majority ion population in the plasma, considering self-collisions and interspecies Coulomb collisional interactions. The form of the Fokker-Planck equations implemented in FOPLA includes collisions, quasi-linear diffusion, particle loss and source terms. Defining f_0 as the 1D distribution function, the detailed equation is the following:

$$\frac{1}{v^2}\frac{\partial}{\partial v}\left[v^2\left((D_{RF}+D_{coll})\frac{\partial f_0}{\partial v}+(B_{coll}+B_{loss})f_0\right)\right]+S-\frac{f_0}{\tau_p}=0 \qquad (3.2)$$

where D_{coll} and B_{coll} are the collision contributions, D_{RF} is the quasi-linear diffusion term, B_{loss} and S are the loss and source terms and τ_p is the particle loss time. More details on this equation can be found in [97]. The 1D approximation implies that the magnetic surfaces are decoupled. Therefore, radial transport effects, such as neoclassical diffusion, RF induced transport or finite orbit width effect, are not considered. The anisotropy of the distribution function is not treated. FOPLA requires the inputs (see table 3.2) of a wave solver, e.g. the parallel component of the wave vector $k_{\|}$, the ratio between the left-hand and right-hand components of the electric field E_+/E_-, and the power absorbed by each species in the plasma. Indeed it is tightly integrated with the CYRANO wave solver, which provides all these necessary waves field information. As it will be discussed later, within the IMAS framework, this coupling can be extended also to other wave solver codes available. Due to its simplified nature, FOPLA is conceived to be used as a fast tool for assessing the qualitative behaviour of energetic particles in a plasma, including synergistic effects between different heating mechanisms. More detailed investigations need a more sophisticated solver, as e.g. orbit following codes.

3.5.2 ASCOT

ASCOT (Accelerated Simulation of Charged Particle Orbits in a Tokamak) is a fully three-dimensional (3D) orbit following Monte Carlo code used to study the behaviour of minority species in a toroidal fusion device [26,27]. The "accelerated" term in its name refers to the code capability of running in an accelerated mode, where one calculated orbit represents many in reality (such mode is not exploited in the present project). ASCOT provides the distribution functions of the minority species by solving the Fokker-Planck equation through the use of Langevin equations (see equation 3.1). More details on the algorithm used within the code to solve these equations are reported in [27]. To accurately solve the Fokker-Planck equations with a statistical approach, ASCOT needs to follow a large number of markers, that represent the source of minority species of interest, such as beam energetic particles, fusion alphas particles or ICRH-accelerated fast ions. To describe the particle motion, three different references could be used in ASCOT: the gyro-orbit (GO), the guiding-centre (GC) or the hybrid reference, which combines both GO and GC references together. The GO reference requires a huge computational effort since particles are followed for millions of oscillation periods in their gyro-orbit motion. In the GC approach, the computational demand is reduced: only the particle guiding centre is followed by ASCOT and GC variations have a larger timescale than that of the full GO case. Both approaches can be used together in the so-called hybrid reference. Here, markers are followed in their GC motion, but when they pass close enough to the wall. i.e. closer than a Larmor radius r_L, ASCOT changes to the GO reference to better evaluate the particle location [26]. This approach is time-saving and allows a better estimation of the power load to the wall, since it reduce the uncertainties due to the GC reference. To obtain a steady state solution, markers are followed from their original location until they fulfil an end-condition, e.g. thermalization or lost conditions [27]. An example of thermalization end-condition in ASCOT is when a particle reaches a multiple (e.g. 1.5x) of the local plasma temperature. A lost particle instead is observed when the particle trajectory crosses the surface representing the wall of the device. ASCOT supports both 2D and 3D magnetic equilibria and machine first wall description and operates by utilizing the same inputs as the BBNBI code, to which are added the input of the markers to follow and a specific option file (details in table 3.2). The marker input is provided by a source code, e.g. BBNBI for beam EPs. The option file instead is a user-defined file that allows to customize ASCOT parameters such as the orbit reference method, the end-condition criteria, and the distribution phase space limits. ASCOT provides as outputs N-dimensional histograms referred to as distributions from which it is possible to retrieve 2D, 1D and

0D quantities of interest, such as the energy-pitch distribution function, the profiles and integrated values for e.g. the deposited power, the injected torque and current (see table 3.3). Two common dimensions across all available distributions are time and marker species, while the others can involve energy, pitch, R and z coordinates, parallel and perpendicular particle velocity, etc. The most detailed distributions are 6-D histograms. Distribution functions in the constant of motion phase space are available too. ASCOT can be used as a stand-alone tool or integrated within transport suites like JINTRAC [98]. ASCOT includes other codes such as BBNBI as beam source code, AFSI as alpha particle source code [99] and RFOF library for handling the wave-particle interaction phenomena. Within the integrated modelling frameworks, the ASCOT suite of codes is fully available within IMAS and other codes can be used coupled to it [89].

3.5.3 RFOF library

RFOF (Radio Frequency interactions in Orbit Following code) [28] is a library that can be coupled to orbit following codes like ASCOT to model the wave-particle resonant interactions. It incorporates the diffusion operator Q, defined according to the quasi-linear model, into the particle equation of motion (eq. 2.19). RFOF evaluates the resonance condition, both spatially and on frequency, and periodically applies Monte Carlo operators to account for RF-induced effects when the condition is fulfilled [96]. Wave-particle interaction occurs only at discrete points along the orbit where the resonance condition (eq. 2.39) is satisfied. RFOF determines the precise resonance location, including the Doppler shift correction, and checks whether a marker lies sufficiently close to it. This requirement is met when the distance between the markers and the resonance point is smaller than $10^{-3}L_c$ with $L_c = \frac{1}{|\nabla \log B|}$ the characteristics scale length of the system. Once the condition is satisfied, the particle receives a "kick". The algorithm used in the RFOF starts from the quasi-linear wave particle diffusion operator, discussed in section 2.4, formulated in terms of the invariants $I_\perp$, $I_\parallel$, I_ϕ. The resulting Monte Carlo operator determines the update of $I_\perp$ when a resonance is passed (the other two invariants are unaffected). RFOF assumes $I_\perp = \frac{m\omega}{qN}\mu$ and describes the stochastic interaction between waves and particles through the equation

$$\begin{aligned} &\frac{dI_\perp}{dt} = AN_{acc}dt + \sqrt{2D_{I_\perp}N_{acc}}dW \\ \Rightarrow \qquad &\Delta I_\perp = \int \frac{\partial D_{I_\perp}}{\partial I_\perp}dt + \int \sqrt{2D_{I_\perp}}dW \end{aligned} \tag{3.3}$$

where A and $D_{I_\perp}$ are the deterministic and diffusion coefficients, while N_{acc} is a time acceleration factor (here assumed $N_{acc} = 1$). The diffusion coefficient for $I_\perp$ is defined as

$$D_{I_\perp} = (qv_\perp E_{eff}\tau)^2 \tag{3.4}$$

with E_{eff} and τ are respectively the effective RF electric field amplitude and the effective resonance interaction time [28]. The change in $I_\perp$ is then translated into updates of the local parallel and perpendicular velocities after which the orbit following resumes. A complete description of the underlying formalism is given in [28, 96], and a detailed overview of the RFOF model coupled with ASCOT (in the following called ASCOT-RFOF) is provided in section 5.1. ASCOT-RFOF requires the standard ASCOT inputs, plus an RF-specific option file, containing e.g. the normalisation factor and the resonance layer width, and the waves electromagnetic fields information. The latter are typically retrieved by full-waves code such as CYRANO. These data allow RFOF to compute the wave-field intensity self-consistently: a normalization factor is derived so that the absorbed wave power for the species of interest matches at the end of the simulation the input value provided by the full-waves code. About the ensemble of markers, ASCOT-RFOF can simulate both thermal particles and beam energetic particles, but only one species at a time. Thermal particles are treated as a population, i.e. all markers have a weight that correspond to a certain number of real particles, whereas beam EPs are obtained from BBNBI code as a source of particles, with each marker representing a number of injected particles per second. A dedicated tool for generating the thermal marker populations, THED-G (THErmal

Distribution-Generator), has been developed as part of this thesis and is described in chapter 5.1.2. The outputs of ASCOT-RFOF are identical to those of ASCOT. However, when starting from a population, all distribution functions must be normalized to the total simulation time. RFOF has already been applied for modelling on ASDEX Upgrade [100] and JET [101]. Its integration and revitalization within the IMAS framework formed part of this Ph.D. work and is detailed in chapter 5.

Input type	**Codes**	**Description**
Injector geometry	BBNBI	Beamlet geometry in three dimensions
Magnetic field	BBNBI / CYRANO / FOPLA / ASCOT / ASCOT-RFOF	Toroidal and poloidal magnetic field data (2D or 3D)
Plasma kinetic profiles	BBNBI / CYRANO / FOPLA / ASCOT / ASCOT-RFOF	Plasma scenario including density and temperature profiles of electrons, ions, and impurities
First wall geometry	BBNBI / FOPLA / ASCOT / ASCOT-RFOF	Tokamak first-wall geometry used to detect particle–wall interactions (2D or 3D)
Distribution functions	CYRANO / FOPLA	Fast-particle distribution functions used to model NBI–ICRH synergy
Wave equation solutions and wave power absorption	FOPLA / ASCOT-RFOF	Electromagnetic field components and computed wave power absorption per species
Markers	ASCOT / ASCOT-RFOF	Marker information (inistate) generated e.g. by BBNBI and used as input for orbit-following simulations
Option file	CYRANO / FOPLA / ASCOT / ASCOT-RFOF	User-defined simulation parameters that depends on the code

Table 3.2: Main inputs required by the numerical codes used in this thesis.

Output type	**Codes**	**Description**
Markers (inistate)	BBNBI	Ensemble of markers used as initial state for slowing-down simulations. Position, energy, pitch and other characteristics are defined for each marker of the ensemble
Markers (endstate)	ASCOT / ASCOT-RFOF	Final marker states after the simulation that include position, energy, pitch, and constants of motion information
Shine-through	BBNBI	Fraction of particles and power lost by shine-through
Waves electromagnetic field information	CYRANO	Left-hand, right-hand, and parallel components of the electromagnetic wave field and wave vector components
Power absorption by species	CYRANO	Power absorbed by each plasma species, including impurities
Fast ion density	FOPLA / ASCOT / ASCOT-RFOF	Radial profiles and volume-integrated fast-ion density in the plasma
Power deposition to electrons and ions	FOPLA / ASCOT / ASCOT-RFOF	Radial profiles and integrated quantities derived from distribution functions; FOPLA considers self-collisions, whereas ASCOT does not
Current drive and torque	ASCOT / ASCOT-RFOF	Radial profiles and integrated quantities of driven current and torque: the current includes electron shielding current correction; both $\mathbf{j} \times \mathbf{B}$ and collisional torques are evaluated
Distribution functions	FOPLA / ASCOT / ASCOT-RFOF	Distribution functions in different phase spaces: 1D velocity space in FOPLA, and 5D–6D phase space, including velocity, energy, and pitch, in ASCOT and ASCOT-RFOF

Table 3.3: Main outputs produced by the codes used in this thesis.

3.6 IMAS framework

The Integrated Modelling and Analysis Suite (IMAS) [29] is the framework developed to support ITER modelling and plasma operations. Strongly influenced by the European Integrated Modelling Task Force (EU-ITM), IMAS is built around a standardized data model which allows storing inputs and outputs in a uniform format, independent of the code or the experimental device producing them. This standardization allows the coupling of different physics codes together and the development of integrated modelling workflows, as e.g. the Heating & Current Drive (H&CD) workflow [89] and the Energetic Particle stability workflow [102]. The data are stored in the so-called Interface Data Structures (IDSs), which form the data dictionary of the framework. Table 3.4 lists several IDSs used in this work. The data dictionary is evolving together with the new physical phenomena modelled and code requirements, creating a standardized and shared language for the fusion community. A full machine description, stored in the Machine Description data, allows the modelling of machine-generic components. Within IMAS, tools for accessing, reading and writing IDS-based data are provided. Each physics codes integrated to IMAS is associated with a dedicated "physics actor", i.e. a wrapper or interface that handles data exchange between the code and the IMAS formats. During a code or workflow execution, actors retrieve input data from relevant IDSs and write simulation results back in the same standardized format. This approach enables codes written in different languages and using different I/O conventions to interact efficiently. All the modelling codes introduced earlier in this chapter have their corresponding IMAS actors, supporting NBI-ICRH synergistic studies, as such discussed in chapter 6. Among the tools available in IMAS, the EPCOM (Energetic Particle Constant of Motion) code has been used in this thesis and is therefore introduced below.

IDS	**Description**
equilibrium	Profiles and global quantities describing the magnetohydrodynamic equilibrium of the plasma
core_profiles	Profiles and global quantities of the core plasma
distribution_sources	Particle sources used as input to kinetic equations, such as newly born beam fast ions or fusion reaction products
distributions	Distribution functions of different particle species in several phase-space dimensions
nbi	Neutral Beam Injector geometry
waves	Quantities describing wave propagation and absorption, as well as antenna geometry
wall	Geometry of the tokamak first wall and divertor

Table 3.4: Interface Data Structures (IDSs) frequently used in the following chapters [103].

3.6.1 EPCoM

EPCoM is an IMAS-compatible tool designed to provide realistic energetic particle distribution functions to study the stability and non-linear dynamic of EP-driven modes. Its main function is to transform EP distributions from common numerical representations, e.g. (R, z, E, λ) to the Constant of Motion phase space (E, μ, P_ϕ), obtaining realistic and continuous EP distribution functions suitable for kinetic-MHD and gyrokinetic applications [40]. To achieve this, EPCoM constructs a Cartesian CoM grid in $(E, \mu, P_\phi; \sigma)$ coordinates, where σ represents the sign of the pitch angle. The introduction of σ removes the orbit degeneracy of passing particles, since co- and counter- passing particles indeed share identical values of the invariants (E, μ, P_ϕ). The parameter σ distinguishes the direction of particle motion along the magnetic field, with e.g. $\sigma = +1$ corresponding to co-passing orbit and $\sigma = -1$

to counter-passing orbits. Within this representation, trapped particles appear as two branches with $\sigma = \pm 1$, corresponding to the two legs of poloidal trajectory. This formulation allows to remove the singularity on the trapped-passing boundary where the bounce time τ_b diverges as $v_\parallel \to 0$. For every point of the grid, XTOR-K [30] is used to trace the full 6D particle orbits, allowing to evaluate the CoM Jacobian, the orbit topology and the characteristic particle frequencies, such as the bounce and precession frequencies (ω_b, ω_d). The CoM grid and the associated orbit database generated through XTOR-K depend exclusively on the provided magnetic equilibrium. EPCoM indeed requires as input the magnetic equilibrium and the initial EP marker distribution, which, within IMAS, are provided through the *equilibrium* and *distributions* IDSs. Once the database is generated, EPCoM projects the input EP distribution, given e.g. in (R, z, E, λ) space, onto the CoM phase space, through high-order binning and spline interpolation ensuring a smooth CoM distribution. This enables the computation of quantities crucial for full-F and δf simulations, such as the gradient in terms of CoM variables, as well as enabling resonance analysis. The obtained CoM representation can also be mapped back to (R, z, E, λ). In this thesis, EPCoM is used to analyse the orbit topologies of beam-driven energetic particles in ITER, as described in chapter 4.

Part II

NUMERICAL APPLICATIONS

CHAPTER

4

DISTRIBUTION FUNCTION CHARACTERIZATION OF NEUTRAL BEAM ENERGETIC PARTICLES

High-fidelity modelling of NBI energetic particle confinement and beam–plasma interaction is essential to guarantee reliable operation of current and future fusion devices, such as DTT and ITER. These processes have indeed a direct impact on the plasma performance, influencing heating, current drive and plasma rotation sources, as well as driving EP instabilities. A detailed assessment of shine-through, power deposition, fast-ion slowing-down behaviour and fast ion distribution functions across realistic plasma scenarios is therefore crucial to define a robust NBI operability space and to support the development of auxiliary heating systems and applications. This chapter presents two complementary investigations. The first, presented in section 4.1, explores the NBI operability in DTT plasma scenarios through a numerical analysis of beam-plasma interaction in future machine operations, including low-density scenarios where NBI application is particularly challenging because of shine-through losses. The study evaluates shine-through losses and beam deposition by varying key plasma and NBI parameters, such as the electron plasma density and the energy (sections 4.1.1 and 4.1.2). Moreover, it includes an analysis of newly born fast ion orbit topology using the CoM phase space representation (section 4.2). The work described in this section has been published in the Frontiers in Physics journal [79]. This publication also features an extended assessment of the power-density heat load on the Plasma Facing Components (PFCs). The second part of the study, discussed in section 4.3, examines beam EP confinement and beam–plasma interaction in two ITER scenarios, with particular emphasis on orbit-topology classification through the EPCoM tool [40]. Initially, the ITER scenario adopted as a test case for EPCoM development and validation is introduced (section 4.3.1). It shows the importance of using high-statistic simulations for this scope. The second part (section 4.3.2) investigates the impact of NBI geometry on orbit topology, and its implications for heating, current drive and torque deposition in a half-field ITER configuration, relevant for the initial part of the DT-1 phase.

4.1 EP confinement and beam-plasma interaction in DTT plasmas

Regarding the assessment of the DTT NBI operability, this section presents the three scenarios used for the numerical analysis of beam EP confinement and beam-plasma interaction. The scenarios correspond to H-mode DTT D plasmas at the stationary flat-top phase, all characterized by a single null divertor configuration with positive triangularity. The three selected scenarios (called “A”, “C” and “E”) have different plasma current, vacuum magnetic field and auxiliary heating power, as reported in table 4.1. A detailed description of “A” and “C” plasmas can be found in [104] where JINTRAC [98] and ASTRA [105] simulation settings, defined according a mixed iterative approach discussed in [106], are also described. “E” plasma scenario is instead described in [107]. All plasmas have a seeding impurity, that is varied among the scenarios, and a smaller concentration of tungsten (W), added to simulate the source from the DTT First Wall (FW). The plasma composition and effective charge values Z_{eff} of each flat-top plasma are summarized in table 4.1. The axis-symmetric magnetic equilibria used as input of the numerical simulations of this work are calculated by the CREATE-NL code [108]. In the present work, only 2D axis-symmetric magnetic equilibria are considered. The effects of the 3D magnetic perturbations due to toroidal field ripple have been investigated in e.g. [109, 110].

Scenario	$\mathbf{I_p}$ **[MA]**	**Vacuum** $\mathbf{B_{tor}}$ **[T]**	**Auxiliary power (ECRH, ICRH, NBI) [MW]**	**Composition -** $\mathbf{Z_{eff}}$
“A”	2.0	3.00	8, 0, 0	D, N, W - 2.5
“C”	4.0	5.85	16, 4, 0	D, Ne, W - 1.4
“E”	5.5	5.85	32, 9.5, 10	D, Ar, W - 1.8

Table 4.1: Main parameters of the analysed DTT plasmas.

Scenario “E” represents the DTT reference scenario reaching the full machine performance. Scenarios “A” and “C” instead refer to early-operation configurations that do not include NBI heating. However, neutral beam injection is here simulated for these cases, that are from now on denoted as “A*” and “C*” since they are representative cases of half-field/reduced-current scenarios on which NBI may be operated in later phases, once the system will be available. ASCOT is run stand-alone, i.e. the beam source calculated is not used here as input to re-calculate the plasma kinetic profiles and equilibria[1]. For all scenarios, the volume averaged electron and ion densities and temperatures are reported in table 4.2, together with the corresponding volume-averaged critical energy $\langle \mathrm{E_c} \rangle_{\mathrm{vol}}$. For completeness, the radial profiles of electron temperature $\mathrm{T_e}$, ion temperature $\mathrm{T_i}$, electron density $\mathrm{n_e}$ and deuterium (main) ion density $\mathrm{n_D}$ are shown in figure 4.1.

Scen.	$\langle n_e \rangle_{\mathrm{vol}}$ **[m^{-3}]**	$\langle T_e \rangle_{\mathrm{vol}}$ **[keV]**	$\langle n_i \rangle_{\mathrm{vol}}$ **[m^{-3}]**	$\langle T_i \rangle_{\mathrm{vol}}$ **[keV]**	$\langle E_c \rangle_{\mathrm{vol}}$ **[keV]**
“A”	0.59×10^{20}	3.39	0.45×10^{20}	1.98	63.18
“C”	1.36×10^{20}	4.93	1.31×10^{20}	3.80	91.58
“E”	1.83×10^{20}	5.07	1.75×10^{20}	3.61	94.01

Table 4.2: Plasma properties of the analysed DTT scenarios.

Preliminary studies on beam shine-through losses for the DTT full power scenario have already shown that shine-through (ST) losses are negligible at the reference “E” density [111]. The present work extends the analysis to the up-to-date scenario “E”, characterized by an upward-shifted equilibrium with respect to the NBI line, and to low-density, low-current/magnetic field scenarios (“A*”, “C*”). Simulations are performed through the ASCOT suite of codes. Beam ionization is modelled using

---

[1] The input kinetic profiles and equilibrium include the beam effects as modelled by simplified codes, supporting the validity of applying ASCOT independently to study energetic particle physics.

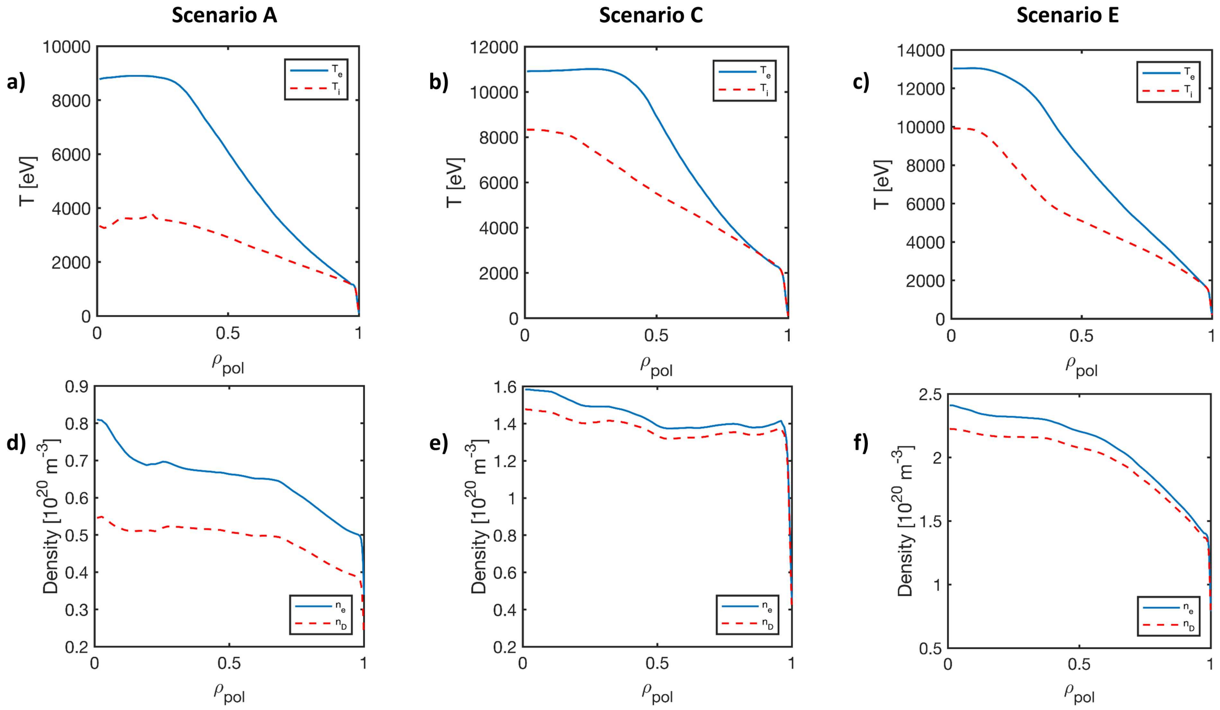

Figure 4.1: Kinetic profiles for all the analysed scenarios [104]: a), b), c) represent plasma temperature profiles of electrons (blue solid) and ions (red dashed); d), e), f) show the plasma density profiles of electron (blue solid) and Deuterium (red dashed) species

BBNBI, while ASCOT is used as orbit-following Monte Carlo code for slowing down characterization (see chapter 3 for more details on the codes). Each simulation injects 50,000 markers (or test particles) representing the source of neutral beam EPs. The ionization outside the LCFS is negligible due to the low-density in the SOL, which BBNBI models as an exponential decay of the density kinetic profiles. ASCOT simulations are then performed using the initial fast-ion distributions provided by BBNBI. The hybrid method is considered as orbit-following approach, enabling an accurate evaluation of orbit losses with significantly reduced computational time. Beam EPs are followed until they are lost or thermalized. Thermalization condition is full-filled when beam particles reach an energy equal to $1.5T_i$, with T_i the local ion thermal energy. These conditions are usually assumed in all the ASCOT studies in this thesis.

4.1.1 Beam ionization and shine-through losses

A wide-range parameter scan has been carried out to estimate the shine-through fractions under different plasma conditions and beam energies. For each scenario (“A*”, “C*” and “E”), four different beam energies have been simulated covering the range from 255 to 510 keV. The injected beam power $\mathrm{P_{NBI}}$ is set to decrease linearly with the energy (see section 3.2). For each beam energy, the plasma density is varied from the scenario reference value to lower densities. Shine-through losses indeed become relevant at low-densities or high injection energy. Although other plasma parameters affect the shine-through, such as plasma temperature, injection geometry (which determine the actual local density/temperature seen by beam particles), beam particle species (here only D is considered), plasma composition, impurity concentration and though almost negligible, magnetic field [88], the dominant dependences are the beam energy and plasma density. In this analysis, the focus is therefore placed on these two main parameters, while BBNBI naturally accounts for all relevant physical effects in the ionization model [87]. Figure 4.2 represents the plasma density profiles used in the parameter scan and table 4.3 reports the corresponding line-averaged plasma electron densities $\langle \mathrm{n_e} \rangle_{\mathrm{line}}$.

Scenario	**"A*"**	**"C*"**	**"E"**
$\langle \mathbf{n_e} \rangle_{\mathbf{line}}$ $[\mathbf{10^{20}\ m^{-3}}]$	**0.62**	**1.39**	**1.97**
	0.46	1.04	1.48
	0.31	0.70	0.98
	0.25	0.49	0.69
	0.22	0.35	0.49
		0.28	0.39
			0.30

Table 4.3: Line-averaged electron densities of the performed parameter scan for "A*", "C*" and "E" scenarios. The values in bold represent the reference density of each scenario.

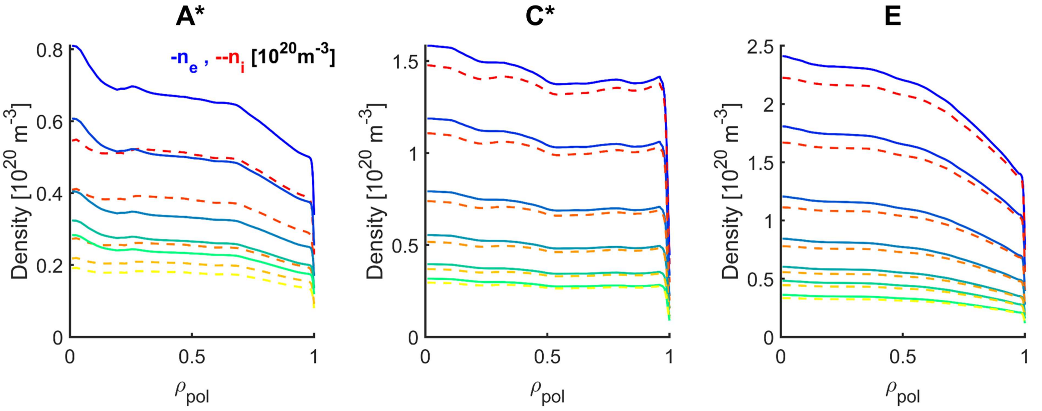

Figure 4.2: Rescaled density profiles used for the shine-through study. Solid blue and dashed red lines represent respectively the reference electron and main ion density for each scenario. The other profiles are obtained with scaling factors, that resulted in the line-average densities shown in tab. 4.3.

The reference DTT scenario "E" foresees a line-averaged plasma electron density of $\langle \mathrm{n_e} \rangle_{\mathrm{line}} = 1.97 \times 10^{20}\ \mathrm{m^{-3}}$, which is sufficient to ionize all energetic beam neutrals inside the plasma, without shine-through losses. At full beam energy and power, the neutrals ionization for scenario "E" extends from the outer part of the plasma, corresponding to the injection region, up to the magnetic axis. This is shown in the beam ionization flux, which describes where neutrals are ionized in the plasma, represented from the toroidal top view in fig. 4.3a. Decreasing the plasma density, the beam penetrates progressively deeper and part of the energetic neutrals start to cross the whole plasma, eventually reaching the opposite wall. This behaviour is illustrated in figure 4.3b, for a lower plasma density of $\langle \mathrm{n_e} \rangle_{\mathrm{line}} = 0.30 \times 10^{20}\mathrm{m^{-3}}$ and the same nominal injection energy of 510 keV considered in figure 4.3a. Keeping fixed the plasma density and decreasing the beam injection energy, a reduction of the beam penetration, and consequent shine-through losses, is observed, as can be seen in fig. 4.3c where $\mathrm{E_{NBI}} = 255$ keV and the plasma density is kept at $\langle \mathrm{n_e} \rangle_{\mathrm{line}} = 0.30 \times 10^{20}\mathrm{m^{-3}}$. Table 4.4 reports the shine-through fractions obtained with the BBNBI code as a function of density and energy for all scenarios. These results shows that decreasing the electron plasma density or increasing the injection energy, the shine through fraction increases, as expected from the theory. Shine-through fractions reported in table 4.4 have been used to estimate the power loads on the Plasma-Facing Components (PFCs) and to subsequently identify operational limits for the DTT NBI system [79]. Despite nominal power load limits on the FW and PFCs of DTT have not yet been formally defined, the analysis in [79] indicates that peak power densities of approximately 46 $\mathrm{MWm^{-2}}$ and 52 $\mathrm{MWm^{-2}}$ are expected on the ICRH components and FW, respectively, located in front of the beam injection port.

To extend the applicability of this study to any DTT SN plasma with characteristics similar to the cases analysed here but with different plasma density/beam energy, a heuristic formula (eq. 4.1) is retrieved similarly to what was done for ITER [112] and DEMO [113]. This formula takes into account the exponential dependencies on plasma density (in 10^{20} m^{-3}) and beam energy (in keV), and can be used to rapidly estimate NBI shine-through (ST):

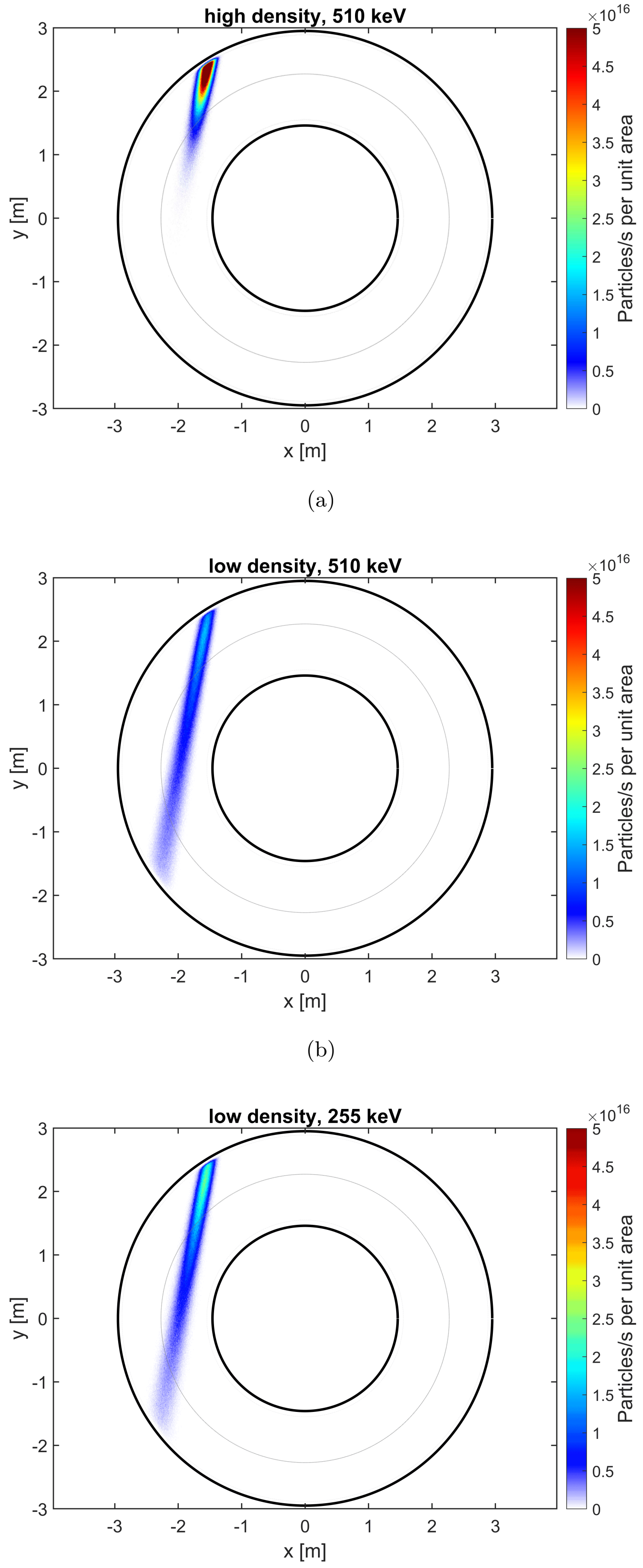

(a)

(b)

(c)

Figure 4.3: Toroidal top view of the beam particle ionization flux for the reference target scenario “E” at different plasma densities and energies. From fig. 4.3a to 4.3c: high energy and density case (510 keV, $n_e \sim 1.97 \times 10^{20}\mathrm{m}^{-3}$), high-energy and low density case (510 keV, $n_e \sim 0.30 \times 10^{20}\mathrm{m}^{-3}$), low-energy and high plasma density case (255 keV, $n_e \sim 0.30 \times 10^{20}\mathrm{m}^{-3}$).

Shine-through power fraction [%]					
Scenario	**Line density [10^{20} m^{-3}]**	**510 keV**	**400 keV**	**300 keV**	**255 keV**
"A*"	**0.62**	**2.74**	**1.43**	**0.62**	**0.35**
	0.46	7.14	4.54	2.66	1.73
	0.31	18.26	13.86	9.08	7.06
	0.25	26.01	20.55	15.27	12.41
	0.22	31.36	25.26	19.39	16.18
"C*"	**1.39**	**0.08**	**0.01**	**0.00**	**0.00**
	1.04	0.58	0.16	0.05	0.02
	0.70	3.71	2.01	0.84	0.51
	0.49	10.61	6.99	4.05	2.66
	0.35	21.02	15.89	10.58	8.15
	0.28	29.59	23.40	16.89	13.85
"E"	**1.97**	**0.00**	**0.00**	**0.00**	**0.00**
	1.48	0.03	0.00	0.00	0.00
	0.98	0.52	0.22	0.08	0.02
	0.69	3.02	1.56	0.69	0.35
	0.49	9.07	5.66	3.09	2.13
	0.39	14.92	10.55	6.71	4.66
	0.30	24.85	18.97	13.37	10.60

Table 4.4: Estimates of shine-through power fraction [%] obtained through the injection energy and plasma density scans.

$$ST = exp\left(-\frac{\langle \mathrm{n_e}[10^{20}\mathrm{m}^{-3}]\rangle_{\mathrm{line}}^{\alpha}\mathrm{E_{NBI}}[\mathrm{keV}]^{\beta}}{D}\right) \tag{4.1}$$

Coefficients $\alpha, \beta, \mathrm{D}$ are obtained from a multilinear regression, using the log(log()) of shine-through fractions computed by the BBNBI code (see eq. (3) in [112]) and reported in table 4.4. Due to differences in plasma density shape, clearly shown in fig. 4.1, but with too few points to include the density peaking factor $\mathrm{n_{pf}}$ in the regression, a different fit for each scenario is performed, and the results are reported in table 4.5.

DTT SN scenarios	**E-like**	**C*-like**	**A*-like**
Density peaking factor	1.32	1.16	1.37
RMSE	0.21 %	0.44	0.48
α	1.089 ± 4.19e-07	1.116 ± 6.41e-07	1.07 ± 1.08e-06
β	-0.678 ± 1.24e-06	-0.692 ± 2.60e-06	-0.636 ± 2.34e-06
D	2.77e–03 ± 1.22e-07	2.65e–03 ± 2.43e-07	3.13e–03 ± 2.56e-07

Table 4.5: Regression coefficients α, β, D for eq. 4.1 for each plasma case analysed. The density peaking factor $\mathrm{n_{pf}}$ is stated, as well as the root-mean-square error (RMSE) of the regression, reported as percentage.

Eq. 4.1 well describes the shine-through dependencies, as proved by the low RMSE reported in tab. 4.5 and by the good agreement between shine-through values calculated by BBNBI and those obtained with eq. 4.1 shown in figure 4.4. Equation 4.1 is used to fit shine-through fractions calculate by BBNBI as a function of the line-averaged plasma electron densities for all the analysed scenarios, considering both injection energies $\mathrm{E_{NBI}} = 510$ keV and $\mathrm{E_{NBI}} = 255$ keV. The resulting fits are shown in figure 4.5 where it can be observed that shine-through fractions at identical values of line-averaged density and beam injection energy are not the same across scenarios. Since beam injection geometry, plasma volumes and flux surfaces topology are almost identical, the beam path inside the plasma is almost equal in all cases. The observed differences in shine-through must therefore arise from the different plasma density profile shapes. Because beam ionization is a local process, variations in the density profile shape affect the ionization rate even when the line-averaged density is the same. The fraction of shine-through is always lower in the A*-like plasmas, which present the highest density peaking factor, defined as the ratio of the core density to the volume-averaged density $\mathrm{n_{pf}} = \frac{\mathrm{n_{e,0}}}{\langle \mathrm{n} \rangle_{\mathrm{vol}}} \sim 1.37$. A larger peaking factor implies a larger core density, and since DTT NBI aims at the plasma core region, the ionization results more efficient. In contrast, the peaking factor of scenario "C*" is the smallest ($\mathrm{n_{pf}} \sim 1.16$), resulting in the highest shine-through fraction at equal energy and density. The values of $\mathrm{n_{pf}}$ for the three scenarios is listed in tab. 4.5.

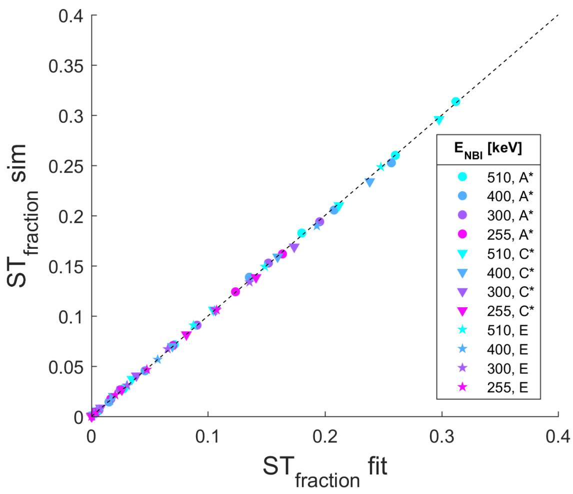

Figure 4.4: Comparison of DTT NBI shine-through values obtained by Monte Carlo BBNBI simulations ($\mathrm{ST_{fraction}}$ sim) and by eq. 4.1 ($\mathrm{ST_{fraction}}$ fit), for all the plasmas considered in this work.

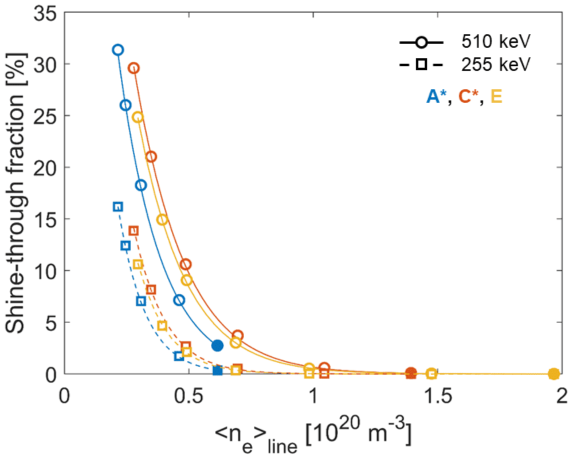

Figure 4.5: DTT NBI shine-through fractions for the "A*", "C*", "E" plasmas as function of plasma density $\langle \mathrm{n_e} \rangle_{\mathrm{line}}$. BBNBI results and fitted values through eq. 4.1 are shown for $\mathrm{E_{NBI}} = 510$ keV (circles, solid lines) and $\mathrm{E_{NBI}} = 255$ keV (squares, dashed lines). Filled symbols indicate reference density.

The results presented so far neglect the effects of stray magnetic fields acting on the neutral beam trajectory prior to plasma injection [114]. Such fields lead to a reduction of the effective injected NBI power as a consequence of beam particle collisions involving beam line components before they enter the plasma. The magnitude of this effect depends on the specific scenario and is computed in [79]. The shine-through fractions reported in table 4.4 can be easily rescaled once the injected power corrected for stray-field effects is known. For this reason, stray magnetic field effects are neglected in the results presented here for the beam ionization while are accounted for during post-processing for the ASCOT slowing-down result discussion.

4.1.2 Distribution functions and EP confinement from collisional slowing down

Beam fast ions interact with the plasma particles through Coulomb collisions, providing heat, current and torque to the plasma. Collisions are indeed responsible for energy and momentum transfer, which may also result in fast ion losses due to e.g. pitch-angle scattering into unconfined orbits. In this study, charge-exchange fast ion losses with background neutrals are neglected. This loss mechanism is difficult to model due to the lack of both experimental measurements and reliable modelling of the cold neutral density. In ITER and DTT, however, the high plasma density and temperature prevent the penetration of cold neutrals, therefore ensuring negligible losses due to charge-exchange process. ASCOT slowing down results are here presented for the three analysed scenarios, taking into account the stray field effects which reduce the total beam injected power into the plasmas. The corresponding injected $\mathrm{P_{NBI}}$ values are reported in table 4.6, together with the volume-integrated quantities for scenarios "A*", "C*" and "E" of power deposition, current drive, torque and losses. Both full and half injection energy cases are shown. All these quantities, as well as the radial profiles and distribution functions presented later, are representing the steady-state description of beam energetic particles.

	$\mathrm{E_{NBI}}$	**255 keV**			**510 keV**		
	Injected $\mathrm{P_{NBI}}$ [MW] considering stray field losses	**4.45**	**4.35**	**3.80**	**9.76**	**9.72**	**9.62**
	Scenario	**"A*"**	**"C*"**	**"E"**	**"A*"**	**"C*"**	**"E"**
$\mathbf{P_{dep}}$ [%]	By electrons	44.05	44.03	46.74	60.60	56.94	58.49
	By ions	55.95	55.97	53.26	39.40	43.06	41.51
	Total	99.57	99.98	99.91	97.12	99.92	99.99
$\mathbf{P_{loss}}$ [%]	Shine-through	0.36	0.00	0.00	2.74	0.08	0.00
	Orbit	0.07	0.02	0.09	0.14	0.00	0.01
	Total	0.43	0.02	0.09	2.88	0.08	0.01
Current Drive	I_{NBCD} [MA]	0.29	0.09	0.04	1.09	0.46	0.24
	$\eta_{CD}[10^{20}\ \mathrm{A/Wm^2}]$	0.10	0.075	0.05	0.15	0.14	0.11
	$\gamma_{CD} = \frac{I_{NBCD}}{P_{NBI}}$ [MA/MW]	0.065	0.020	0.013	0.11	0.047	0.025
Torque [Nm]	Collisional	2.47	1.33	0.80	4.39	3.04	2.30
	$j \times B$	0.75	1.77	1.79	0.55	1.96	2.42
	Total	3.22	3.10	2.59	4.94	5.00	4.72

Table 4.6: DTT NBI power deposition and losses, current drive and torques due to beam slowing down process modelled by the ASCOT code.

For all scenarios, approximately 99% of the injected beam power is deposited through collisions, except for low-density scenario "A*" at 510 keV, where shine-through losses (2.74%) and orbit losses (0.14%) cause a slightly reduced beam power deposition. Co-current injection prevents unfavourable fast ion orbits (e.g. "outward banana"), resulting in negligible prompt losses in all scenarios. Orbit losses due to scattering processes also remains minimal. Regarding the power transferred to plasma species, electron heating at $\mathrm{E_{NBI}}$= 510 keV is ∼ 55–60% of the power deposited for all scenarios, still with considerable power coupling to plasma ions. Ion heating is larger at 255 keV (up to ∼55%). The beam particle energy is indeed closer to the critical energy and a larger ion heating is observed during the slowing down, as well as an increased ion-beam collision frequency ($\nu_{ib} \propto v_{beam}^{-3}$, where v_{beam} is the beam particle velocity) [31]. In absolute terms, NBI can drive up to $I_{NBCD} = 1.1$ MA, in the low-density plasma (scenario "A*") when the highest injection energy is considered. The dependence of the beam-driven current on the injected power $\mathrm{P_{NBI}}$, beam energy $\mathrm{E_{NBI}}$ and plasma density and temperature, accounted through the slowing down time included in the I_{NBCD} formulation (see equation 2.28), are clearly reflected in tab. 4.6. In particular, I_{NBCD} shows significant variations both across different plasma scenarios (i.e. varying n_e, T_e) and with changes in injection parameters (i.e. $\mathrm{P_{NBI}}$, $\mathrm{E_{NBI}}$). The current drive efficiency η_{CD}, computed as in equation 2.29, results in the range $\sim$ 0.5–0.15 × $10^{20}\mathrm{A/Wm^2}$, again demonstrating a clear sensitivity to plasma conditions and beam energy. ASCOT also computes the torque contributions arising from both collisions and the electromagnetic ($j \times B$) force [52]. Collisional torque scales proportionally to the ratio $\frac{\mathrm{P_{NBI}}}{\sqrt{\mathrm{E_{NBI}}}}$, which is larger for the $\mathrm{E_{NBI}}$ = 510 keV case (see tab. 4.6). Electromagnetic, or $j \times B$, torque instead is mainly localized at the plasma edge, where banana orbits are predominantly formed. Figure 4.6 shows the radial profiles of the collisional and $j \times B$ torque density, normalized to the beam injected power, for scenario “E” at half and full injection energies. It is clearly shown that collisional torque is provided mainly in the plasma core, and it is higher for the $\mathrm{E_{NBI}} = 510$ keV energy case, while the $j \times B$ torque is peaked at the edge and dominant at lower injection energy.

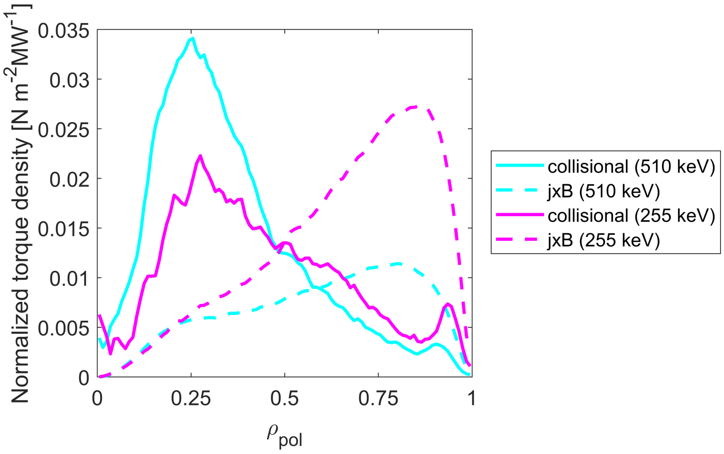

Figure 4.6: Radial profiles of collisional (solid) and $j \times B$ (dashed) torque density, normalized over the injected power, for the full (cyan) and half (purple) injection energies of scenario “E”. The injected powers used for the normalization are respectively 9.62 MW and 3.80 MW.

Figure 4.7 presents the radial profiles of the deposited power, toroidal driven current and torque densities as a function of the normalized poloidal flux ρ_{pol}. Decreasing the beam energy modifies both the absolute magnitude and radial behaviour of these quantities (see table 4.6). In high-density scenario such as “C*” and “E”, power deposition shifts toward the outer plasma region, still showing a central peaked deposition around $\rho_{\mathrm{pol}} \sim 0.25$. The off-axis peak observed in all the profiles is due to a different vertical position of the plasma magnetic axis. The driven current and torque also exhibit peaks around $\rho_{\mathrm{pol}} \sim 0.25$ for the same reasons.

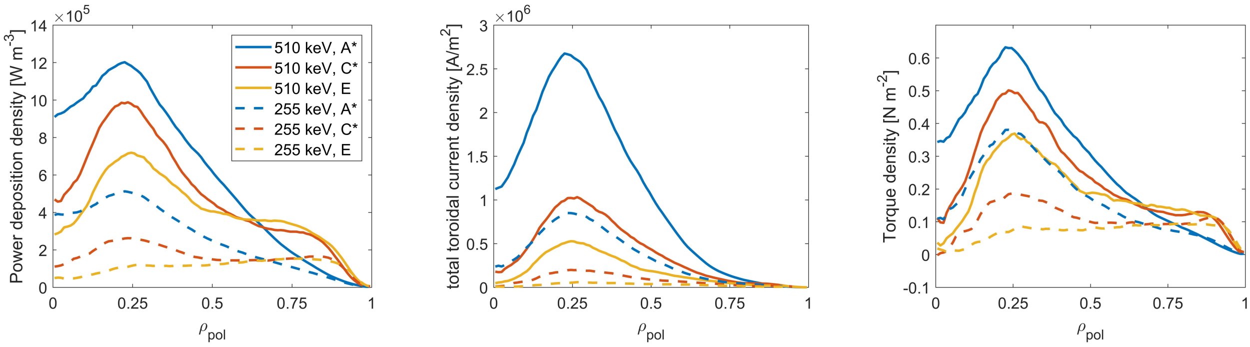

Figure 4.7: From left to right: radial profiles of the power deposition density, total toroidal current density and total torque density for the analysed DTT scenarios. Solid lines represent the results of ASCOT simulations with a beam injection energy of 510 keV, while dashed lines the results those for injection energy of 255 keV.

Figure 4.8 shows the energy-pitch distribution functions for the steady state scenarios at 510 keV (top) and 255 keV (bottom). These distributions are affected both by plasma parameters and EP initial energy. The source of EPs, originated by the NBI, has a negative pitch (peaked at $\lambda \sim -0.69$ for the DTT reference scenario “E”). Differences across scenarios reflect variations in the ionization location of newly born fast ions: lower plasma density leads to deeper beam penetration and more tangential ionization, i.e. $|\lambda| \sim 1$). Each distribution spreads towards positive pitch values when the fast ion energy decreases, due to the pitch-angle scattering effect that becomes progressively relevant when particle energy approaches the critical energy $\mathrm{E_c}$ (see table 4.2). Even if $\mathrm{E_c}$ varies with local plasma parameters, the volume-averaged values reported in table 4.2 and plotted in figure 4.8, can already highlight the significant effect of the pitch angle-scattering at $\mathrm{E} \sim \langle \mathrm{E_c} \rangle$.

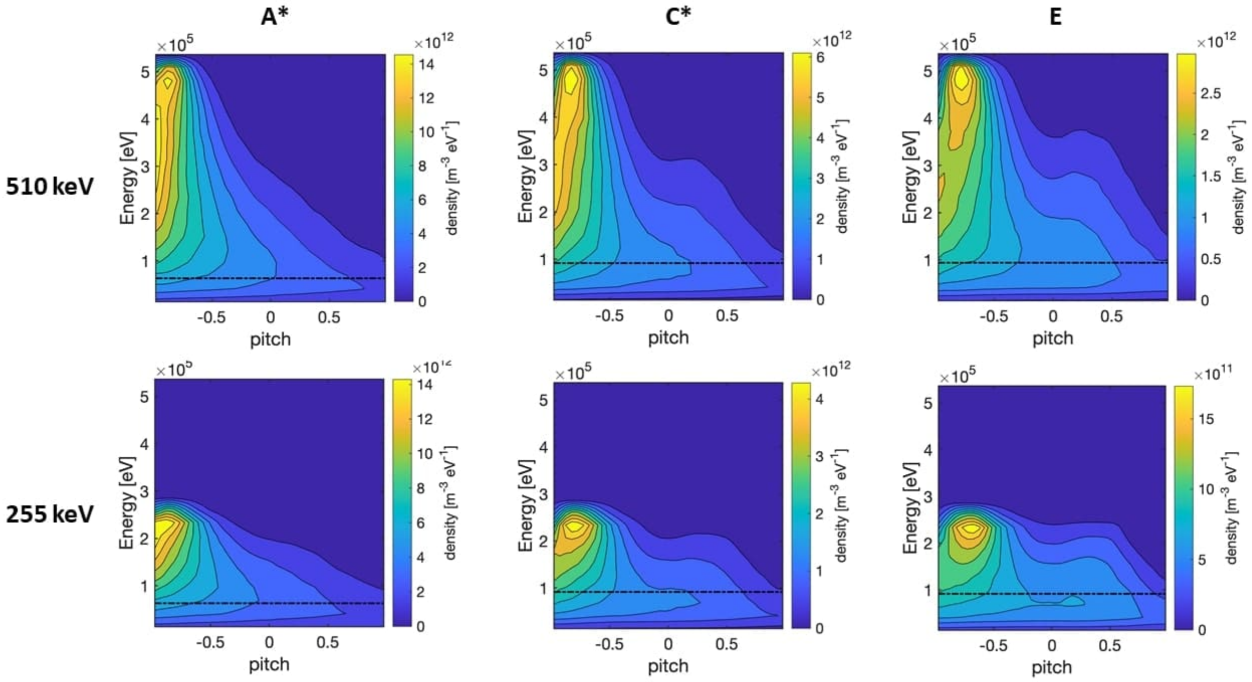

Figure 4.8: DTT beam EP energy-pitch distributions for “A*”, “C*”, “E” scenarios, considering an injection energy of 510 keV (top) and 255 keV (bottom). The black dashed lines represent the critical energy E_c.

4.2 Orbit classification of DTT newly born beam energetic particles

While the previous section focused on fast-ion confinement and slowing down, the present section applies an alternative analytical method to analyse the beam EP orbits immediately after the ionisation. This method, based on the Constants of Motion phase space (see section 2.1.3), is capable to predict orbit topology and prompt losses, and can also be used on slowing down particle population, as applied to ITER in section 4.3. After the ionization, fast ions typically perform several toroidal turns before experiencing a Coulomb collision with the background plasma particles. During this collisionless phase, their motion is governed by the magnetic field and can be described in terms of the three constants of motion: energy E, toroidal canonical angular momentum P_ϕ, and magnetic moment μ, already introduced in chapter 2. In this section, a classification of the orbits of newly born fast ions for DTT scenarios “A*”, “C*” and “E”, introduced in section 4.1, is performed through the definition of the topological map in the CoM phase space (see section 2.1.3). The analysis examines the influence of the plasma density (which determines the fast-ion birth position) and beam injection energy (affecting both ionization location and EP velocity) on the orbit topology. Only co-passing orbits, i.e., orbits defined by particles moving in the same direction as the plasma current, are relevant for DTT because the NBI geometry produces fast ions moving in the co-current direction exclusively (with pitch $\lambda = \frac{v_\parallel}{v} < 0$, defined with respect to the toroidal magnetic field, opposite to I_p in DTT). By combining CoM boundaries, shown in figure 2.6 of chapter 2, and the BBNBI ionization results from section 4.1.1, the collisionless orbit classification of newly born fast ions in scenarios “A*”, “C*” and “E” is obtained in figure 4.9. Figure 4.9 shows 2D histograms of the newly born fast-ion distributions in CoM space for all cases, showing clearly that both particle energies and scenario properties significantly affect the fast ion orbit topology. Quantitative fractions of each orbit class are summarized in table 4.7.

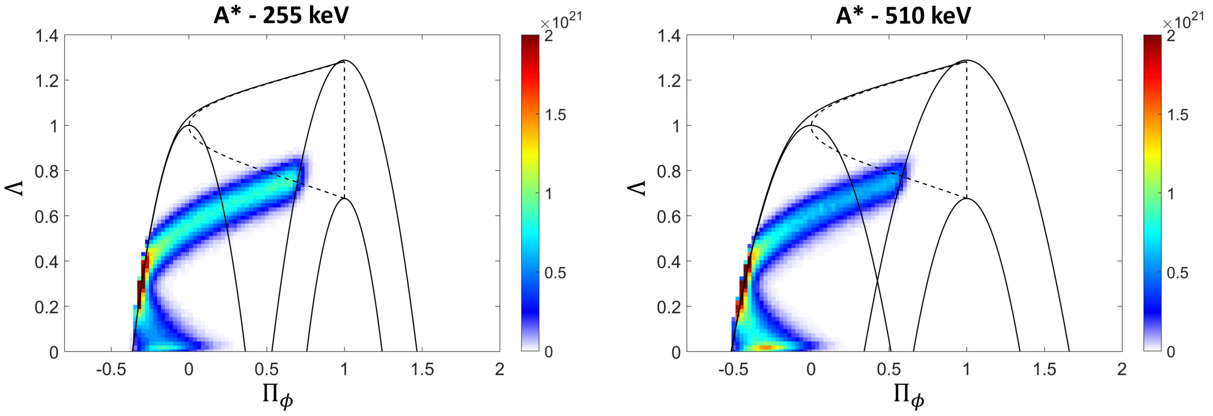

(a) Histograms for scenario "A*".

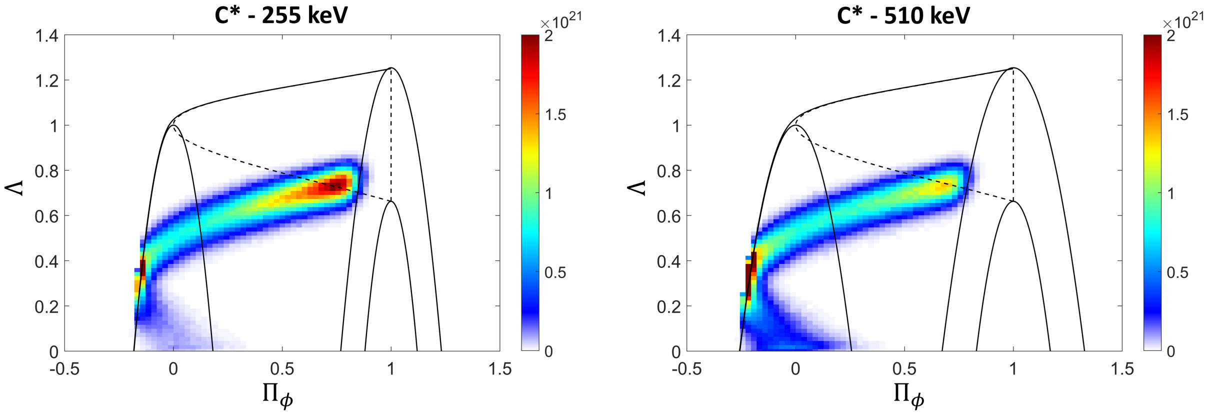

(b) Histograms for scenario "C*".

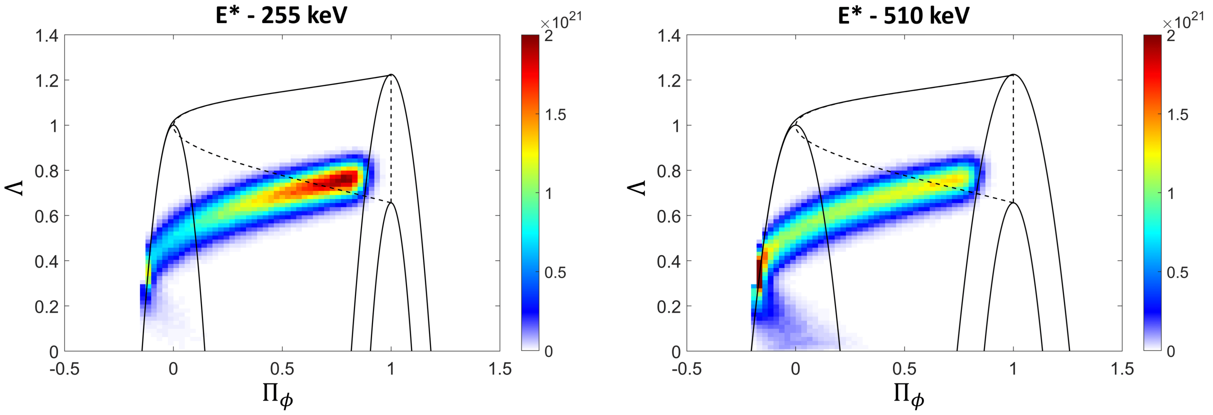

(c) Histograms for scenario "E".

Figure 4.9: Histograms in the CoM phase space of newly born fast ions (particle rate density [1/s]). Two beam injection energies are shown for each DTT scenario: 255 keV (left column) and 510 keV (right column). The normalized toroidal canonical angular momentum Π_ϕ and magnetic moment Λ are considered for the CoM representation (see eq. 2.11).

E_{NBI}	**255 keV**			**510 keV**		
Scenario	**“A*”**	**“C*”**	**“E”**	**“A*”**	**“C*”**	**“E”**
Confined orbits [%]						
Co-passing	92.80	84.94	74.24	92.93	90.36	84.26
Trapped	3.79	13.29	24.85	1.29	6.46	14.50
Stagnation	2.25	1.09	0.25	5.00	2.78	0.79
Total	**98.84**	**99.33**	**99.34**	**99.22**	**99.60**	**99.55**
Lost orbits [%]						
Co-passing	0.39	0.11	0.04	0.41	0.11	0.03
Trapped	0.77	0.57	0.62	0.37	0.29	0.42
Total	**1.16**	**0.68**	**0.66**	**0.78**	**0.40**	**0.45**

Table 4.7: Fractions of newly born fast ion orbits for DTT scenarios “A*”, “C*”, “E” at two different injection energy.

Confined passing orbits characterize the large majority of the DTT beam EPs. The number of newly born fast ions with confined co-passing orbits decreases when the injection energy is reduced. This decrease is evident for high density scenario, high B_{tor} “E” ($\sim$ 84% at 510 keV versus $\sim$ 74% at 255 keV) and almost negligible for low density, low B_{tor} scenario “A*” (92.93% at 510 keV versus 92.80% at 255 keV). At the same magnetic field and the same injection energy (scenarios “C*” and “E”), the percentage of passing orbits increases when decreasing the plasma density. A decrease of EP energy determines an increase in trapped orbits. These effects depend on the penetration of the beam into the plasma. Passing particles are likely to form close to the plasma centre, where the ions are born with a larger parallel particle velocity. Trapped particles instead are likely to form at the edge of the plasma due to a larger perpendicular velocity component resulting for geometrical reasons. Therefore, the larger the beam penetration (e.g. due to a higher beam energy or lower plasma density), the higher the fraction of confined passing particles. EP non-standard orbits, such as potato or stagnation orbits, will not significantly characterize DTT scenarios. However, a modest fraction ($\sim$ 0.8-5%) of stagnation orbits is present (potato orbits are not predicted at all). For all the analysed cases, lost (or unconfined) orbits contribute up to $\sim$1% (“prompt losses”). Although in the CoM phase space analysis a particle is considered lost when it crosses the LCFS, in reality a fast ion that crosses the separatrix can re-enter the plasma without being lost, especially if the LCFS is far enough from the FW as in DTT. The lost particle fractions reported in tab. 4.7 are therefore an overestimate, representing the case of a loss boundary at the LCFS and not at the machine FW. Indeed, the orbit-following Monte Carlo ASCOT code shows that prompt losses, in absence of collisions, are negligible when considering a simulation domain up to DTT FW.

Passing from the histogram representation, as in fig. 2.6, to the final Constants of Motion distribution function F_{CoM} requires the computation of the Jacobian J_{CoM} (eq. 2.21). This transformation is essential to obtain realistic EP distribution functions (details in sec. 3.6.1). However, computing the transit/bounce time τ_b, which appears in J_{CoM} definition, is non-trivial. The IMAS-compatible tool EPCoM can perform this calculation through the integration with the XTOR-K orbit tracing code, enabling the reconstruction of the full distribution function $F_{CoM} = \frac{H_{CoM}}{J_{CoM}}$. In the following section, EPCoM is applied to ITER scenarios, presenting examples of the Jacobian and the resulting CoM distribution functions. For DTT, only the CoM histograms H_{CoM} are presented. Although the IMAS infrastructure for DTT has recently become available, its implementation was still evolving during this work and the EPCoM-based analysis was therefore not pursued here.

4.3 Confinement and losses of ITER beam energetic particles in the Constant of Motion phase space through EPCoM

NBI EP confinement, beam-plasma interaction and orbit topology classifications are now presented for two different ITER plasma scenarios, a hydrogen plasma and a deuterium plasma, in which hydrogen (H) beam injection is applied. In particular, the hydrogen scenario was used as a reference case for the test and validation of the EPCoM tool [40]. Section 4.3.1 presents for this scenario the physics interpretation of the steady-state beam EP distributions used as input for EPCoM application and the resulting orbit classification obtained at different particle energies. The deuterium scenario instead is considered to study the impact of different NBI geometries using the EPCoM workflow. The corresponding results are shown in section 4.3.2. Details of these scenarios are provided in the following sections.

4.3.1 Distribution functions of ITER beam particles supporting EPCoM development

The EPCoM tool [40], introduced in chapter 3, can compute the CoM distribution function F_{CoM}, the Jacobian J_{CoM} and spatial-velocity F_{EpRz} distribution function from an initial set of markers. Such input can be obtained through ASCOT, available within IMAS as EPCoM, which is capable to generate a discrete ensemble of markers sampled in the (E, λ, R, z) phase space, as needed by EPCoM. Reliable reconstruction of EPCoM distribution functions, however, requires high-statistics input to avoid significant statistical noise and poorly populated regions in the CoM phase space, which could introduce reconstruction artifacts. To efficiently increase statistics, an additional IMAS actor, called *markersampler*, is used together with ASCOT. Indeed ASCOT simulations with millions of markers become expensive in terms of CPU time, even when adopting the guiding-centre approximation, as in this study. The *markersampler* actor samples markers from an existing distribution function, e.g. that produced by ASCOT, to generate a larger ensemble consistent with the initial distribution. This section presents the beam ionization and beam-plasma interaction results of the ASCOT+*markersampler* application, evaluating the capability of *markersampler* of reproducing ASCOT results while decreasing the numerical noise. Moreover, the steady-state CoM distribution functions obtained through EPCoM for the high-resolution simulations are shown for different particle energies, enabling orbit classification and physical interpretation of the interaction phenomena.

The scenario considered for this application is a Hydrogen plasma (shot/run = 100015/1) at one-third magnetic field (1.8 T, I_p= 5 MA). Such scenario was still considered in ITER operations at the time of the study for the second Pre-Fusion Operation Phase (PFPO-2) [89]. However, the recent updates of the ITER research plan [22] do not foresee any scenario at B_T = 1.8 T. The injection of two H neutral beams is simulated considering the standard beam injection configuration (OFF-ON), and an injection energy of 744 keV, selected to deliver 23 MW of total power, according to tolerable limits of ST losses [112]. Additional 30 MW of wave power coming from ICRH (10 MW) and ECRH (20 MW) systems are considered in the scenario. The plasma for this scenario was produced using the METIS 0.5D fast transport solver [115] and kinetic profiles are reported in figure 4.10. The CHEASE equilibrium code [108] was applied to the METIS output to obtain the final 2D axisymmetric equilibrium for the BBNBI and ASCOT simulations.

NBI simulations have been performed with the BBNBI code, showing that $\sim$ 10% of the injected power is lost by shine-through, according to the theoretical ST prediction of the heuristic formula for H NBI in H plasma presented in [112]. In this scenario, a line averaged electron density $\langle \mathrm{n_e} \rangle_{\mathrm{line}} \sim 3.55 \times 10^{19}$ m^{-3} and a density peaking factor $\mathrm{n_{pf}} \sim 1.3$ are considered. This shine-through power remains within the acceptable limit for the first wall [35]. The ASCOT simulation shows that the beam primarily heats electrons, depositing about 81% of the injected power to the electron population. This is expected since the volume-averaged critical energy is $\langle \mathrm{E}_c \rangle_{\mathrm{vol}} \sim 152$ keV, significantly lower than the injection energy. The radial profiles of the power deposition, the total toroidal current driven by fast ions, that

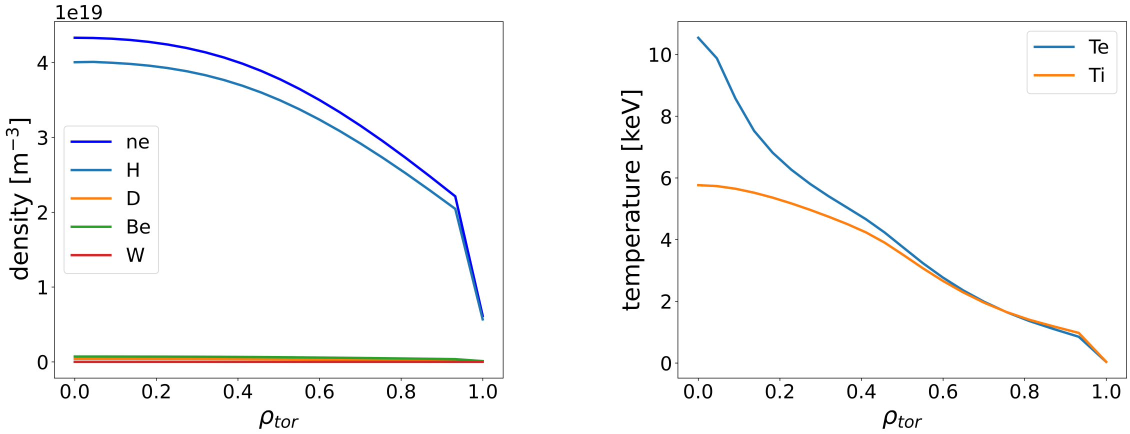

Figure 4.10: Plasma density and plasma temperature radial profiles in the normalized toroidal coordinate ρ_{tor} of Hydrogen scenario (shot/run = 100015/1).

includes the electron back-current correction, and the total injected torque are reported respectively in figures 4.11a, 4.11b, 4.11c. These figures show a central contribution due to the beam in terms of heat, current and momentum delivered to the plasma. The beam-driven current is estimated to be about $I_{NBCD} = 0.66$ MA, with an efficiency of $\eta_{CD} \sim 0.08 \times 10^{20}\mathrm{A/Wm}^2$, comparable to the current drive efficiency observed for DTT reference scenario ($\eta_{CD,DTT} \sim 0.11 \times 10^{20}\mathrm{A/Wm}^2$). The torque is mainly collisional, with the integrated values of collisional and electromagnetic torques respectively of $\mathrm{T_{coll}} = 13.71$ Nm and $\mathrm{T_{EM}} = 2.71$ Nm. This result is due to dominant passing-orbit nature of beam fast ions in ITER, as also evident from the CoM distribution functions presented below.

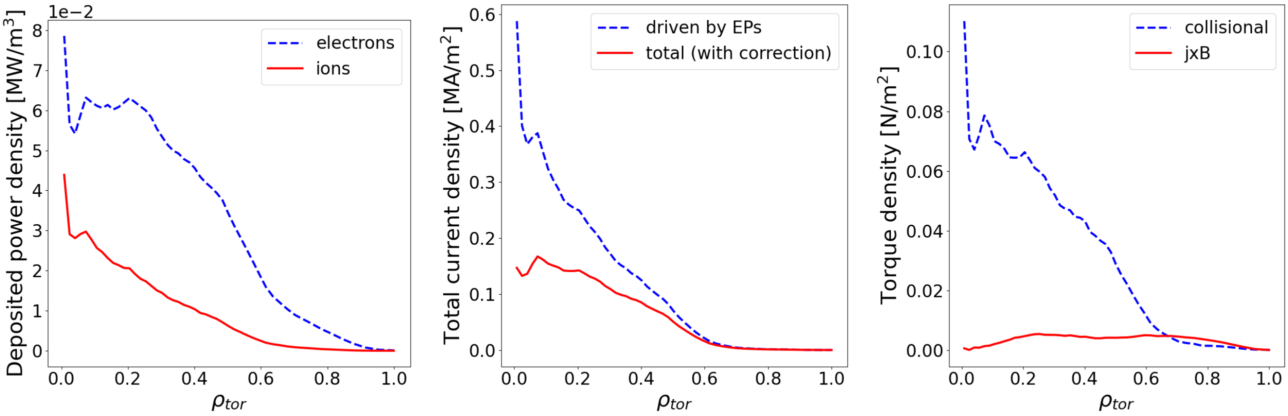

(a) Radial profiles of the deposited power density, divided among electrons (dashed, blue) and ions (solid, red).

(b) Radial profiles of the toroidal fast ion driven current I_{NBI} density (blue) and the total current I_{NBCD} density (red).

(c) Radial profiles of collisional T_{coll}(blue) and electromagnetic T_{em} (blue) torque density.

Figure 4.11: Radial profiles of power deposition, driven current, and torque density for shot #100015 obtained with the *markersampler*+ASCOT code.

The marker end-states of the ASCOT simulation describe the steady-state EP distribution. The corresponding energy histogram is compared in figure 4.12 with the analytical steady-state distribution f(E) at steady state, computed as in [27]. While the overall agreement is satisfactory, some discrepancies are observed, as ASCOT accounts for physical processes that are not included in the analytical model, such as the presence of a small population of particles with energies exceeding the injection energy (i.e. at $E/E_{beam} > 1.0$ in fig. 4.12). Although such events are rare, collisions between fast and background ions can produce particles with energies higher than the initial injection energy E_{beam}.

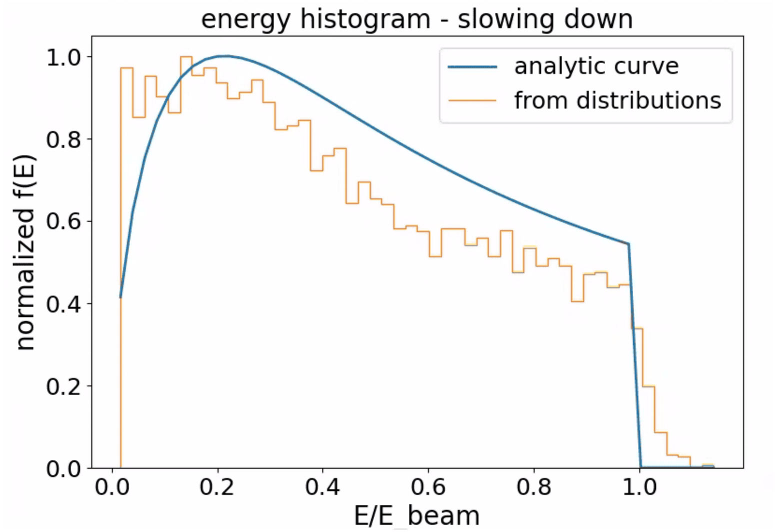

Figure 4.12: Comparison between the energy histogram from the marker end-states of ASCOT simulation and the analytical curve describing the energy distribution function f(E) at the steady state (eq. 2.24).

Using the ASCOT+*markersampler* approach, inputs containing 5×10^6 and 3×10^7 markers were generated from the initial 5×10^5-marker ASCOT slowing-down simulation. Figure 4.13 shows that fast-ion density and power deposition profiles are in good agreement among the 5×10^5, $\times 10^6$ and 3×10^7 marker cases, verifying the capability of *markersampler* actor to reproduce the properties of the initial ASCOT distribution. The simulation noise, already minimal with 5×10^5 markers, being 5×10^5 markers enough to describe the beam slowing down physics for this ITER plasma, is further reduced while increasing the statistics through *markersampler*.

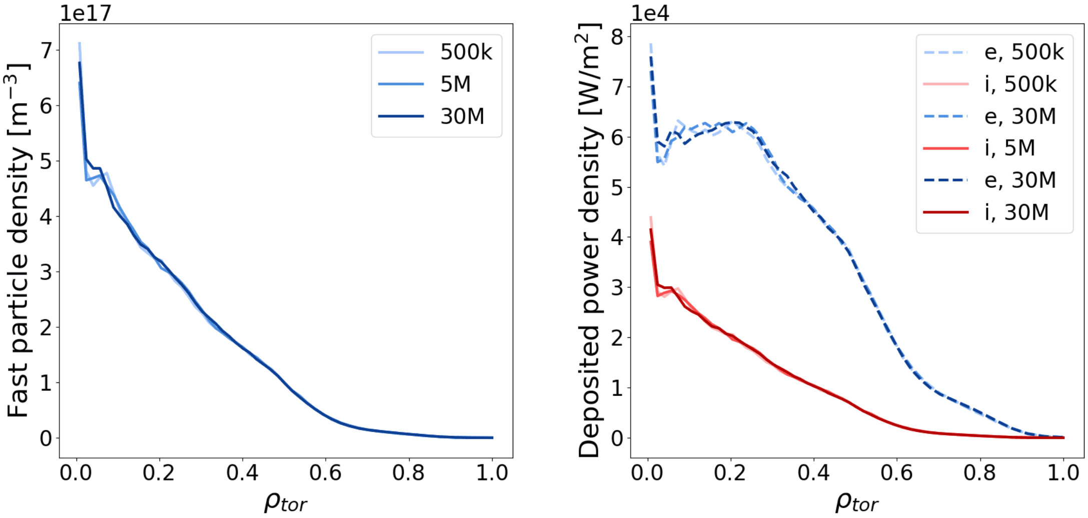

Figure 4.13: Comparison of the radial profiles for the fast ion density (left) and deposited power density (right) of ASCOT simulations with different statistics: 5×10^5, 5×10^6 and 3×10^7 markers.

High-statistics impact becomes evident when examining the two-dimensional distributions. The 2D plots representing the energy-pitch and (R, z) histograms reported in figures 4.14 and 4.15 show that smoother results are obtained as the number of markers increases. For this reason, the 3×10^7-marker end-states was used as EPCoM input. EPCoM produces the histograms of F_{Ep} and F_{Rz} distribution functions, shown in figure 4.16, which are in good agreement with the histograms represented in figures 4.14 and 4.15.

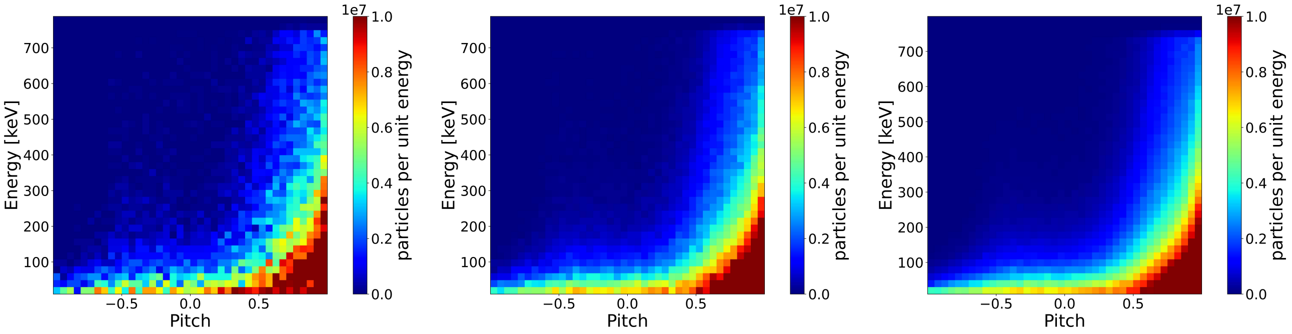

Figure 4.14: 2D energy-pitch histograms obtained by ASCOT simulations performed considering different numbers of markers as input: 5×10^5, 5×10^6 and 3×10^7 markers from left to right.

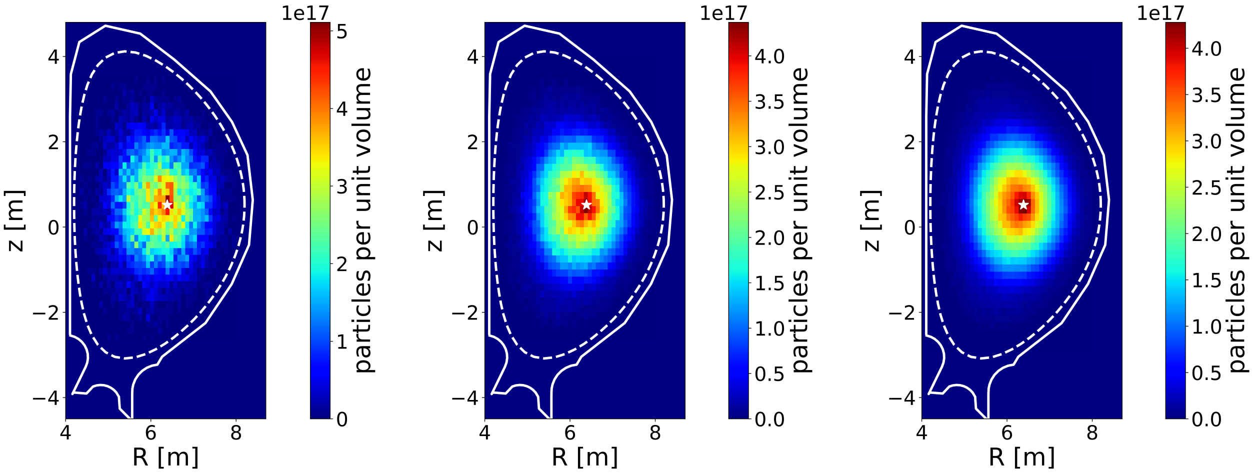

Figure 4.15: 2D R, z histograms obtained by ASCOT simulations performed considering different numbers of markers as input: 5×10^5, 5×10^6 and 3×10^7 markers from left to right. Solid and dashed lines represent respectively the ITER first wall and LCFS of the considered plasma.

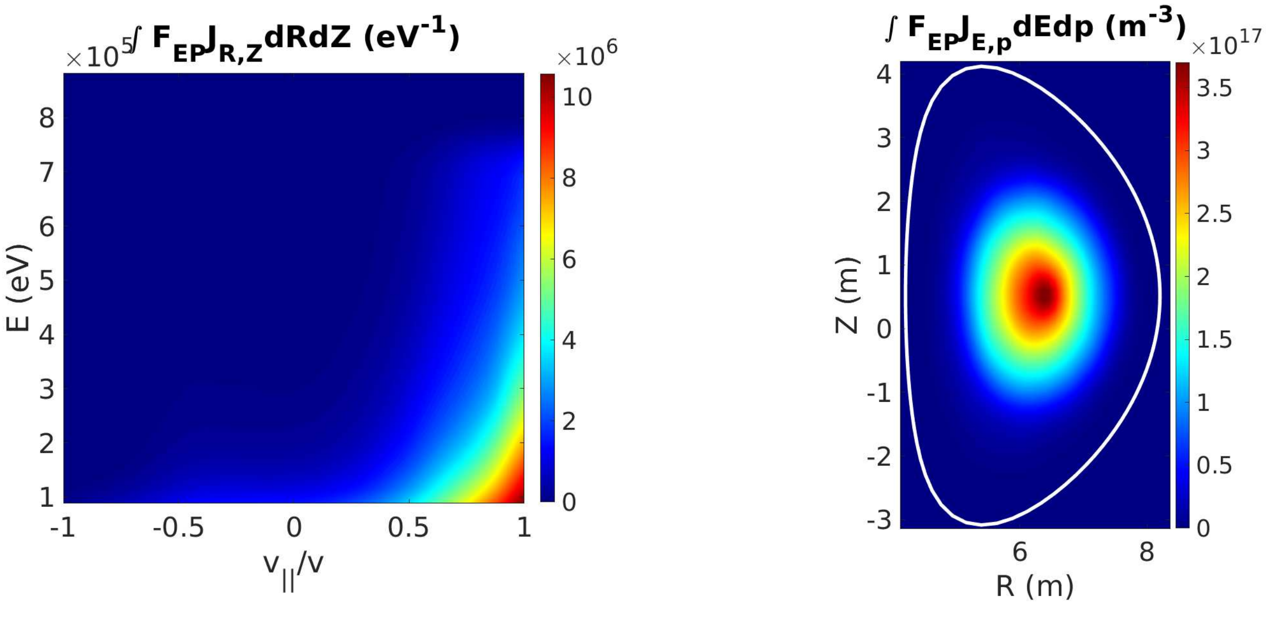

Figure 4.16: 2D energy-pitch and R, z histograms obtained through EPCoM using 3×10^7 marker as input [40].

The computation of the CoM distribution function F_{CoM} requires the Jacobian J_{CoM} evaluation, according to equation 2.21. EPCoM enables the computation of the transit/bounce time required for such calculation, showing that J_{CoM} becomes particularly large near the trapped–passing boundary due to the particle velocity approaching to zero ($\tau_b \to \infty$), especially at high EP energies ($J_{CoM} \propto E$). This is clearly seen in figures 4.17 and 4.18, which show steady-state CoM distribution functions at the injection energy (744 keV) and at the available energy in the distribution closest to thermalization (∼88 keV), together with their corresponding Jacobians J_{CoM} for the $\sigma = +1$ case (co-passing orbits). As discussed in section 3.6.1, EPCoM distinguishes coordinate $\sigma = \pm 1$ to resolve singularities near the trapped–passing boundaries, associating σ values to co- or counter- passing orbits, depending on the plasma current and magnetic field orientation. In ITER, since plasma current and toroidal magnetic field are oriented in the same direction, co- and counter-passing orbits are respectively associated to $\sigma = +1$ and $\sigma = -1$.

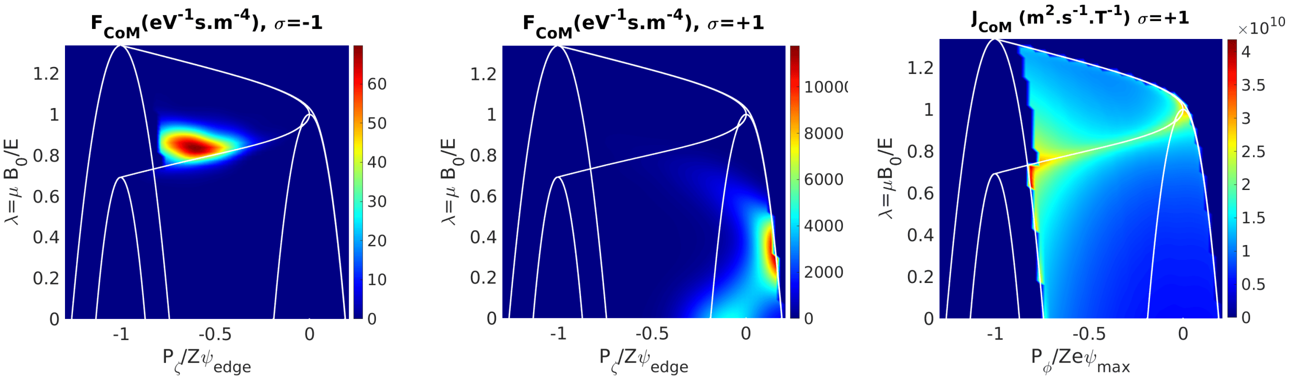

(a) (b) (c)

Figure 4.17: CoM distribution functions F_{CoM} for $\sigma = \pm 1$ particles, and CoM Jacobian J_{CoM} for the $\sigma = +1$ case. The energy considered for these plot corresponds to the injection energy of ∼ 744 keV.

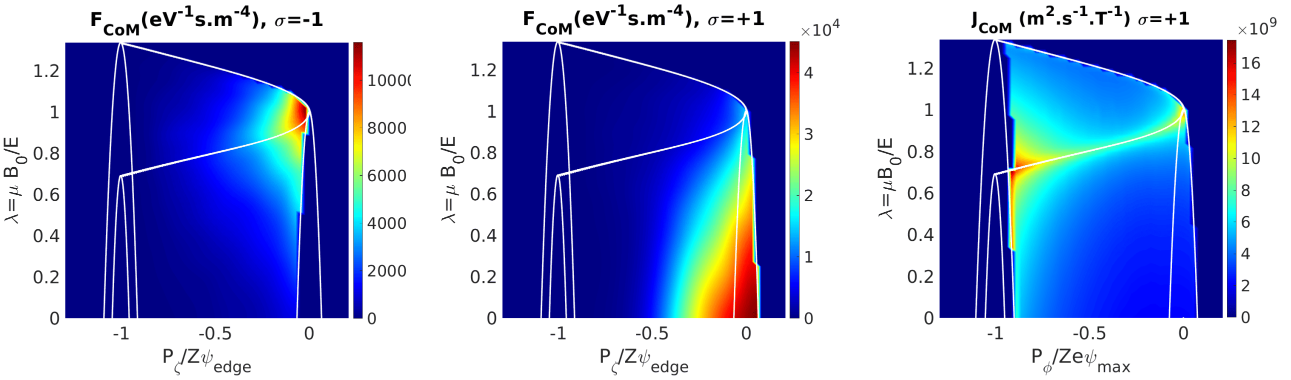

(a) (b) (c)

Figure 4.18: CoM distribution functions F_{CoM} for $\sigma = \pm 1$ particles, and the Jacobian J_{CoM} for the $\sigma = +1$ case. The energy considered for these plot corresponds to ∼ 88 keV, the closest available in the energy grid to the thermalisation value.

In this scenario, beam energetic particles predominantly follow co-moving passing orbits (figures 4.17b and 4.18b), consistently with the injection geometry and I_p and B_{tor} convention. Trapped particles can be observed in both σ domains (figures 4.17a, 4.17b for distributions at the injection energy, figures 4.18a, 4.18b at 88 keV), since their motion alternates between co- (outer leg) and counter-moving (inner leg) orbits [40]. At lower energies, during slowing down, (figure 4.18), beam particles exhibit a broader variety of orbits than newly born energetic particles, including trapped and counter-moving passing particles. This is an effect due to collisions, which modify the initial distribution functions in both spatial and velocity space, determining therefore a change also of the CoM phase space itself.

The significant presence of passing particles at different energies could explain why the collisional torque contribution, associated with passing particles, dominates over the electromagnetic torque (see figure 4.11c).

Unlike the DTT CoM analysis (section 4.2), where the newly born beam energetic particles were topologically classified to evaluate first orbit losses and the trapped/passing ratio of EPs immediately after the ionization, the steady-state (after beam collisional slowing down) CoM distributions obtained here allow describing the orbit topology of beam particles when collisions take place. In the next chapter, the EPCoM workflow is employed to a different scenario to analyse how variations in NBI geometry influence the resulting energetic-particle populations. By resolving the associated orbit topologies in the Constants of Motion space, the impact of NBI geometry on slowing-down dynamics and EP confinement characteristics is assessed.

4.3.2 The impact of ITER NBI geometries on the beam particle distributions through EPCoM

The ITER NBI system allows neutral beams to be injected at different vertical angles with respect to the nominal NBI axis (details in chapter 3). The two reference configurations for ITER are referred to as ON- and OFF- axis injection, corresponding respectively to a +9 mrad or -9 mrad tilt relative to the standard NBI axis. The ITER baseline configuration combines one OFF-axis and one ON-axis injector, a choice motivated by its mitigating effect on Alfvén activity driven by fast ions, through the spreading of the fast ion density in the plasma [83]. This section investigates how different NBI geometries impact the steady-state energetic-particle distribution functions and, consequently, the integrated and radial quantities such as power deposition, current drive and torque. The considered scenario is a Deuterium plasma (shot/run = 53301/3) at half field (2.65 T, I_p= 7.5 MA) with a small concentration of Hydrogen (5%). The injection of H NBI beam at 600 keV is used, delivering 13 MW of NBI power in total. These beam parameters were chosen to satisfy the shine-through limit for this plasma configuration [112]. This scenario is representative of those planned for the early part of the DT-1 operational phase of the updated ITER research plan. As the previous scenario, the plasma is produced using the METIS 0.5D fast transport solver [115] and the kinetic profiles are represented in figure 4.19. The CHEASE equilibrium code [108] was instead applied to compute the 2D axial-symmetric equilibrium for the ASCOT simulations. Three ASCOT simulations were carried out considering three possible beam injection configurations: OFF–OFF, OFF–ON, and ON–ON geometries. EPCoM was subsequently used to compute the CoM distribution functions F_{CoM} and to classify the resulting orbit populations.

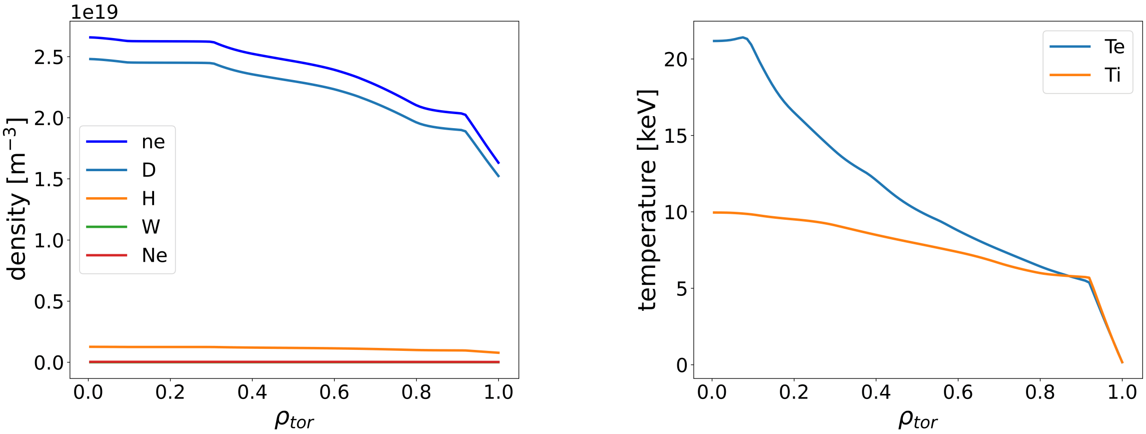

Figure 4.19: Plasma density and plasma temperature radial profiles in the normalized toroidal coordinate ρ_{tor} of the deuterium ITER scenario (shot/run = 53301/3).

The initial ionization fluxes associated with the three NBI geometries considered, obtained from 5×10^5-marker BBNBI simulations, are represented in figure 4.20. The OFF–ON configuration produces a broader vertical spread than the OFF–OFF or ON–ON cases. ASCOT guiding-centre simulations were then performed, and the resulting volume-integrated deposited power, driven current and injected torque for the three geometries are reported in table 4.8. The integrated quantities are similar across the cases, with variations of only $3-4\%$. The OFF-OFF axis configurations yields the highest power deposition to electrons ($\sim 69\%$) and the highest shine-through power loss (~ 2.83 MW). The ON-ON axis case instead has the highest current drive efficiency, reaching $\eta_{CD} = 0.2 \times 10^{20}$ A/Wm^2, doubled with respect to the DTT reference scenario.

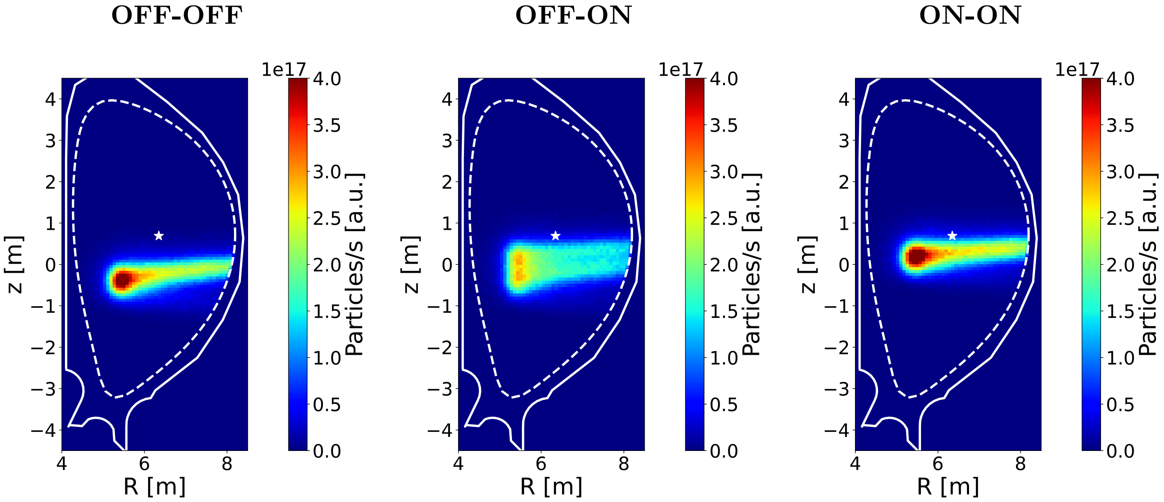

Figure 4.20: Beam energetic particle ionization fluxes for the three NBI geometries.

E_{NBI}, P_{NBI}		600 keV, 13 MW		
NBI configuration		OFF-OFF	OFF-ON	ON-ON
$\mathbf{P_{dep}}$ [%]	on electrons	68.87	68.45	66.88
	on ions	31.13	31.55	33.12
$\mathbf{P_{loss}}$ [%]	Shine-through [MW]	2.83	2.72	2.63
Current Drive	I_{NBCD} [MA]	1.44	1.47	1.57
	η_{CD} [10^{20} A/Wm^2]	0.186	0.191	0.204
	γ_{CD} [MA/MW]	0.14	0.14	0.15
Torque [Nm]	Collisional	6.87	6.77	7.16
	$j \times B$	2.51	2.16	1.96
	Total	9.38	8.93	9.12

Table 4.8: ITER NBI power deposition, losses, current drive and torques due to beam slowing down process estimated by ASCOT code for Deuterium plasma 53301/3.

Regarding the torque, while ON-ON configuration presents the highest collisional torque contribution ($T_{coll} \sim 7.16$ Nm), the OFF-OFF axis shows the highest electromagnetic torque estimate ($T_{em} \sim 2.51$ Nm), providing the largest contribution in total among the three analysed cases ($T_{tot} = 9.38$ Nm). A reasonable explanation for the current drive and torque estimates observed could be related to the orbit population: OFF-OFF is likely presenting the higher fraction of trapped particles, which contributes to the $j \times B$ torque; whereas ON-ON configuration has a larger population of particles following passing orbits, contributing to current drive and collisional torque too. This will be better observed later on when EPCoM F_{CoM} distribution functions will be analysed. Figure 4.21 compares the radial profiles of the deposited power density, total driven current and torque of the three NBI geometries. The spikes observed for the radial profiles at $\rho_{tor} = 0$ are a numerical effect due to the small volume at that such ρ_{tor}. OFF-OFF axis injection deposits power in the region $\rho_{tor} \in [0.25, 0.6]$, while the ON-ON axis deposition is concentrated closer to the core ($\rho_{tor} \in [0, 0.3]$). The OFF–ON configuration produces the broadest radial profiles. Similar trends are observed for the current drive and torque. These results are in agreement with earlier studies presented in [83].

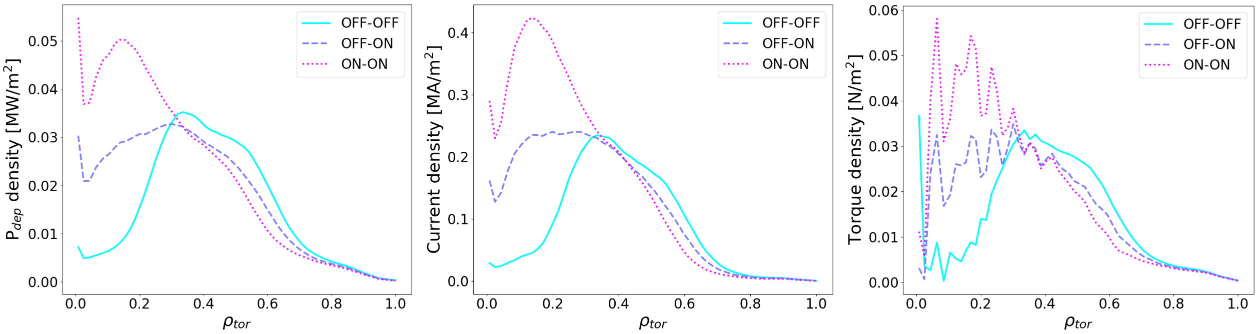

Figure 4.21: Comparison of the radial profiles for the deposited power (P_{dep}) density, total injected current and total torque densities of ASCOT simulations performed considering beam energetic particles generated with different NBI geometries (OFF-OFF cyan solid, OFF-ON purple dashed, ON-ON pink dotted).

As for the analysis presented in section 4.3.1, the *markersampler* actor was used to increase the statistics from the initial $\sim 5 \times 10^5$ markers to 2×10^6 markers before EPCoM execution. The steady state distributions in the R, z phase space resulting from EPCoM for the three analysed cases are shown in figure 4.22. Clear differences between injection geometries are visible. In the OFF–OFF configuration, energetic particles accumulate predominantly on the high-field side (HFS) of the torus, leaving the core less populated. This HFS accumulation could be explainable with a larger trapped-particle fraction, whose banana tips lie on the HFS where particle motion is slowest. The ON–ON configuration produces a distribution centred near the magnetic axis, likely characterized by a predominance of passing orbits and a smaller trapped fraction. The OFF–ON configuration displays an intermediate behaviour, with HFS accumulation (as in OFF–OFF) combined with a populated core region (due to the ON-axis beam). All these qualitative observations are confirmed by the CoM distribution functions F_{CoM} obtained with EPCoM. Figure 4.23 presents the CoM distribution functions at the injection energy (600 keV) and at near-thermal energy (73 keV).

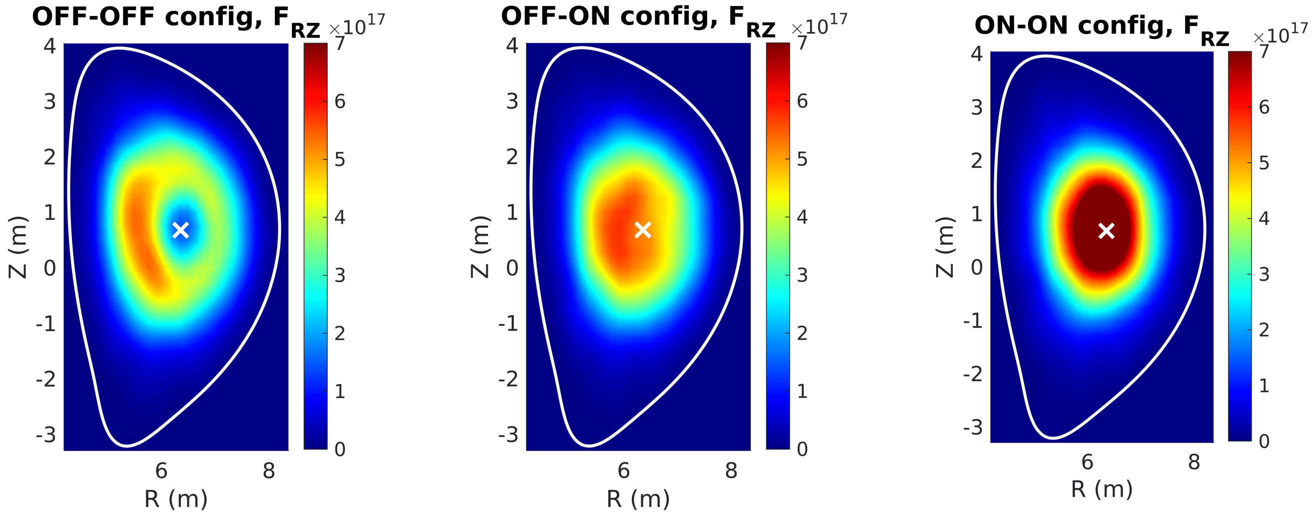

Figure 4.22: Steady state distribution functions in the R, z phase space computed by EPCoM for the three analysed injection geometries.

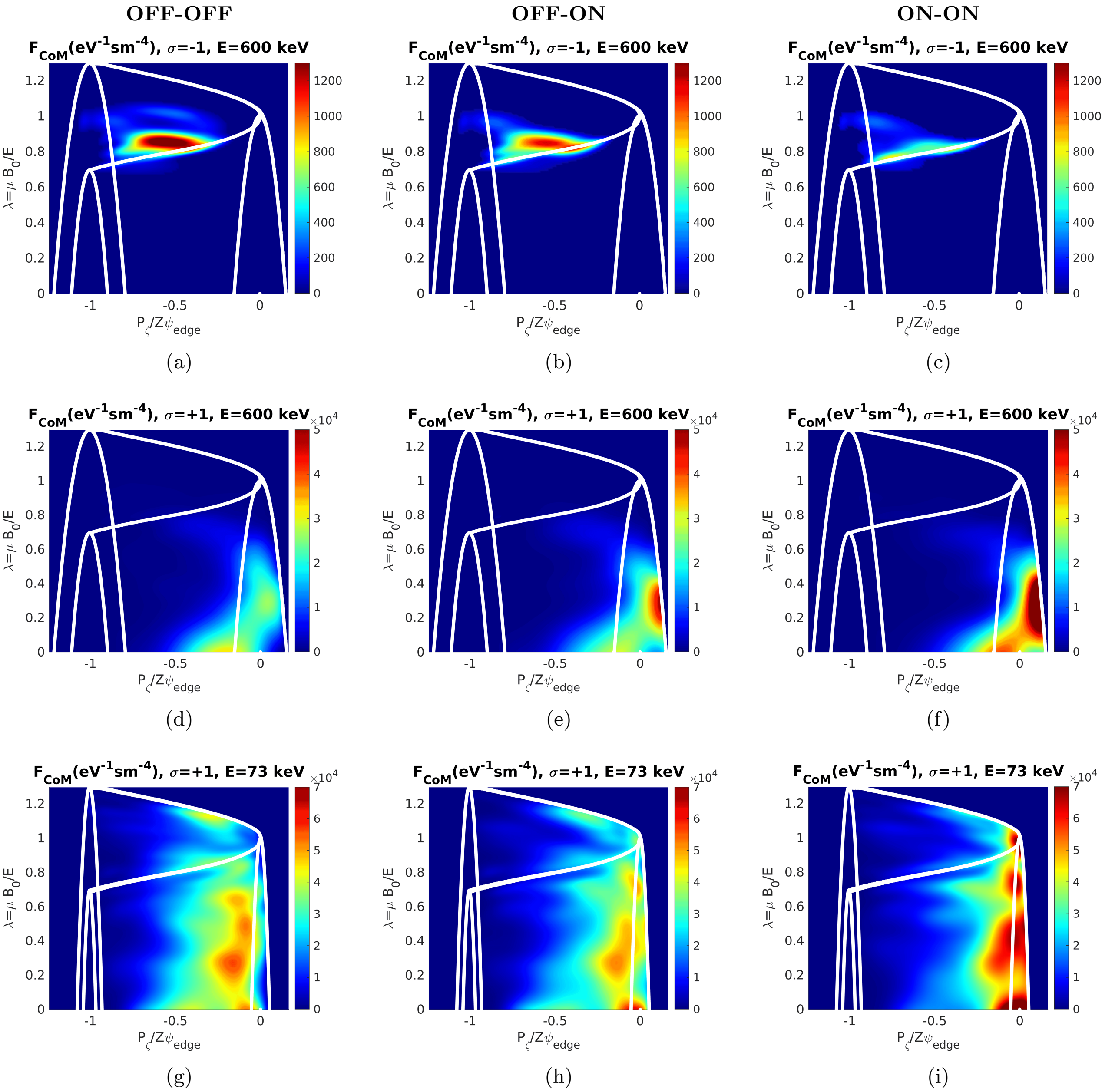

(a) (b) (c)

(d) (e) (f)

(g) (h) (i)

Figure 4.23: CoM distribution functions F_{CoM} for all the NBI configurations analysed at two different energy slices and σ values. Figures a), d), g) are related to OFF-OFF injection geometry, b), e), h) to OFF-ON configuration and c), f), i) to ON-ON case. The first row represents the $\sigma = -1$ population at E = 600 keV, which is mainly formed by trapped particles; the second row shows $\sigma = +1$ the population at E = 600 keV, which is mainly due to co-moving passing particles; the third row presents the trapped and co-moving passing populations ($\sigma = +1$) at E = 73 keV. All rows present the plots with the same colorbar, making the plots of each row easily comparable.

For the injection energy case (E = 600 keV), both $\sigma = \pm 1$ populations are shown in the first and second row of figure 4.23. The OFF–OFF configuration (fig. 4.23a) exhibits a denser trapped-particle population than the ON–ON case (fig. 4.23c), that instead shows a larger co-passing population ($\sigma = +1$) with markers concentrated near the magnetic-axis boundary (fig. 4.23f). The behaviour of lower-energy particles (73 keV) in the slowing down steady state solution is shown in the third row of figure 4.23. Only $\sigma = +1$ case is reported since no significant differences are observed with respect to the $\sigma = -1$ case. Counter-moving passing particles indeed arise during the slowing down phases, likely due to the collision effects, e.g. pitch angle scattering. Also on the ON–ON case at E=73 keV (fig. 4.23i), passing particles remain strongly concentrated near the magnetic axis, consistent with the R, z distribution functions commented above (fig. 4.22), while the OFF-OFF beam geometry presents a magnetic axis region emptier than the other beam geometry cases (fig. 4.23g). The OFF–ON configuration (fig. 4.23b, 4.23e, 4.23h) again exhibits an intermediate behaviour. Particles crossing the LCFS (clearly visible in the first row of 4.23) may represent first orbit losses. However, ASCOT simulations show that prompt losses in ITER are negligible, as well as orbit losses. Markers in the lost-orbit domains therefore may be potential lost particles that however re-enter the plasma and stay confined. The F_{CoM} distribution functions obtained from the EPCoM analysis offer an interpretation of the behaviour of the radial profiles and integrated quantities observed in the previously discussed ASCOT results (see tab. 4.8). In particular, the ON–ON injection configuration shows the largest collisional torque to its higher fraction of passing particles at both at injection and thermal energies. This explains also the higher current drive efficiency observed in such configuration. In contrast, the OFF–OFF injection geometry produces the strongest electromagnetic torque because of its larger trapped-particle population.

Figures 4.24 and 4.25 show representative trapped orbits at injection energy and near thermal energy, respectively, with the following CoM coordinates: $(E, P_\phi, \lambda) = (600\ \text{keV}, -2.81, 0.82)$ in figure 4.24 and $(E, P_\phi, \lambda) = (73\ \text{keV}, -0.077, 0.98)$ in figure 4.25. The orbit in figure 4.24, related to the OFF-OFF configuration, exhibits the banana tips on the HFS, while that in fig. 4.25, coming from ON-ON configuration, has banana tips closer to the magnetic axis. The corresponding pitch evolution illustrates a slower motion along the inner leg of the orbit (blue curve), where the magnetic field is stronger, for both orbits. As expected, the bounce period increases with magnetic-field strength [31].

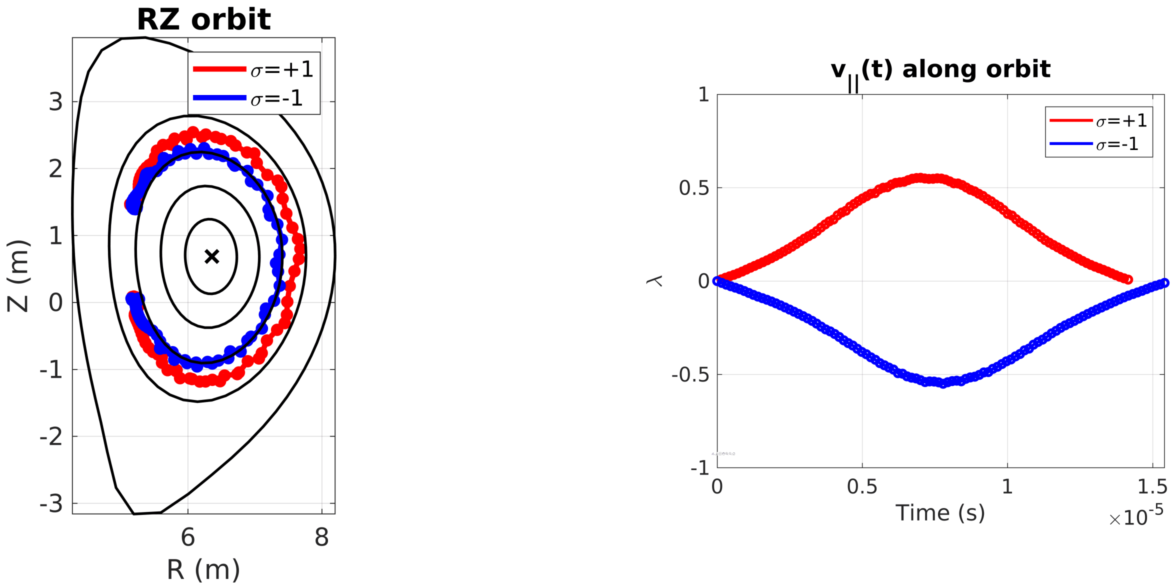

Figure 4.24: Example of trapped orbit for a particle with energy E = 600 keV for the OFF-OFF axis injection configuration and the relative time evolution of the pitch $\lambda = v_{\parallel}/v$ for the outer ($\sigma = +1$, red) and inner ($\sigma = -1$, blue) leg of the trapped particle orbit.

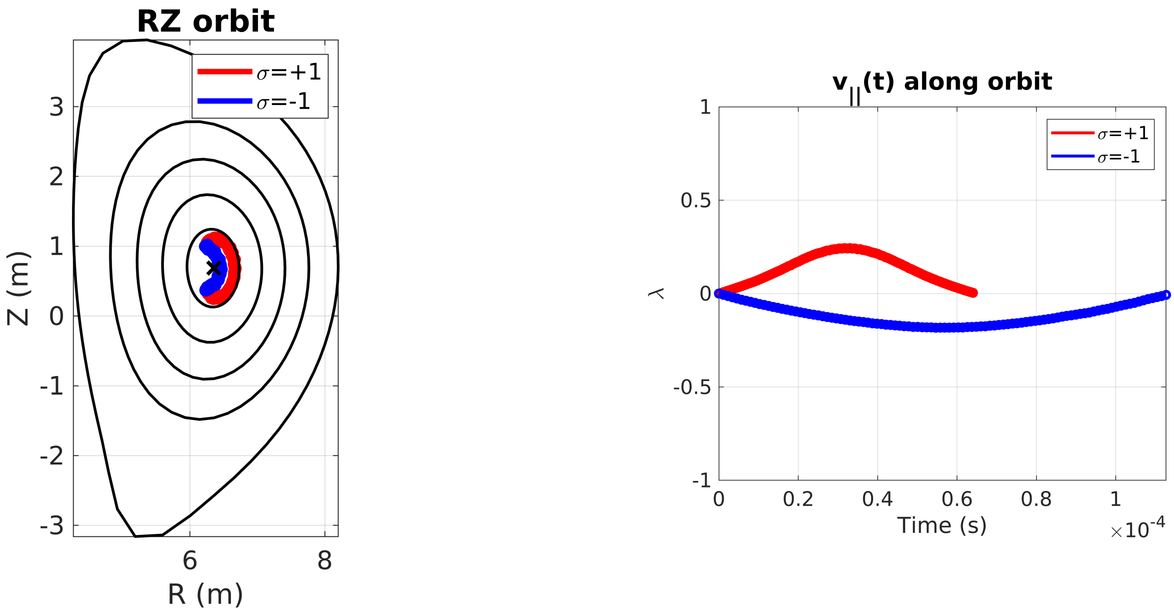

Figure 4.25: Example of trapped orbit for a particle with energy E = 73 keV for the ON-ON axis injection configuration and the relative time evolution of the pitch $\lambda = v_{\parallel}/v$ for the outer ($\sigma = +1$, red) and inner ($\sigma = -1$, blue) leg of the trapped particle orbit.

4.4 Conclusions of the chapter

This chapter presented the NBI modelling activities for both DTT and ITER plasma scenarios, characterizing beam ionisation and slowing down physics through numerical simulations performed primarily with the ASCOT suite of codes.

For DTT, the impact of NBI application is investigated across several plasma scenarios, spanning different B_{tor}/I_p configurations, plasma densities, and beam injection energies. A detailed analysis of shine-through losses is performed, including the definition of an analytical ST estimate formula, according to [112]. This study contributes to the evaluation of beam power loads on plasma-facing components and first wall in DTT [79]. Efficient beam ionisation is observed at high plasma density, while low-density scenarios require reduced beam energy and power due to increased shine-through losses. Heating, current drive, and torque contributions during the slowing-down phase are quantified, showing efficient beam–plasma coupling in all analysed cases, with higher collisional fast-ion losses at low density and high injection energy. Electron and ion heating depend on beam energy and plasma temperature, and cases of electron-dominated or ion-dominated heating are both observed. Finally, the use of the Constants of Motion phase space enables the classification of newly born fast-ion orbit populations in DTT.

ITER NBI studies are supported by both ASCOT and EPCoM workflow simulations. A first analysis introduces the scenario utilised to contribute in EPCoM development, demonstrating a methodology to enhance marker statistics through the *markersampler* actor, that leads to reduced numerical noise and improved resolution of ASCOT distribution functions in 2D space. High-statistics simulations enable accurate reconstruction of Constants of Motion distributions from EPCoM, which support the interpretation of beam–plasma interaction effects at different energies. A second ITER study investigates the influence of beam injection geometry on beam-plasma interactions and orbit populations, showing that while global volume-integrated quantities vary modestly ($\sim 3-4\%$), significant differences arise in radial profiles of deposited power, current drive, torque, and orbit topology. Variations in trapped and passing populations identified through EPCoM provide a consistent explanation for the observed radial distributions and integrated quantity trends.

A comparison between DTT and ITER scenarios highlights both common features and device-specific differences. In both machines, electron heating dominates. The higher density of the DTT reference plasma strongly reduces shine-through losses, whereas in the ITER scenario analysed, characterized by a lower plasma density, ST losses are present but within acceptable limits. Current-drive efficiency is higher in the ITER Deuterium plasma, consistent with its higher electron temperature and therefore lower collisionality regime. Torque injection is also larger in ITER, mainly due to the significantly higher injected power compared to DTT NBI capabilities.

The orbit-topology analysis performed for both devices confirms a strong correlation between energetic-particle orbits and macroscopic NBI-driven quantities. An increased trapped-particle population is associated with enhanced electromagnetic $j \times B$ torque, while passing particles mainly contribute to current drive and collisional torque. EPCoM further demonstrates how collisions progressively modify the initially anisotropic, co-passing beam population during slowing down, redistributing particles across the Constants of Motion phase space through pitch-angle scattering. Beyond its role in stability-oriented analyses, EPCoM thus proves to be a valuable tool for interpreting orbit topology and its impact on EP-driven physics.

CHAPTER

5

DISTRIBUTION FUNCTION CHARACTERIZATION FOR ICRH-ACCELERATED ENERGETIC PARTICLES

Ion Cyclotron Resonance Heating (ICRH) is a standard auxiliary heating technique used in magnetically confined plasmas. Its modelling is intrinsically complex, as it involves physics processes on different time scales [116]. Various numerical models have been developed to consistently address these mechanisms, with different levels of approximations. Reduced and one-dimensional approaches are unable to capture finite orbit width effects and radial drifts, that can potentially lead to particle losses, since the Fokker-Planck equation could e.g. be solved for each magnetic flux surface. The finite orbit width effects and radial drifts, however, become increasingly relevant for energetic particles generated in e.g. fusion-relevant plasmas. Orbit-following approaches are therefore essential to obtain a more complete description of ICRH-driven energetic particle dynamics. This chapter presents initial numerical application of the revitalizing version of the orbit-following ASCOT-RFOF code within the IMAS framework. This work includes both methodological developments and ICRH modelling exercises in experimental and reactor-relevant plasmas. Only the acceleration through ICRH of thermal particle population is considered in this chapter, whereas the synergy between beam particles and IC waves is discussed in chapter 6. While ASCOT–RFOF has previously been applied to ICRH modelling on ASDEX Upgrade [100] and JET [117], the present work addresses a substantially different implementation, integrated into IMAS and with revised routines to improve several modelling aspects. First, the chapter introduces the ASCOT–RFOF computational workflow in section 5.1. A dedicated tool for generating four-dimensional thermal marker distributions, required as input, has been developed and presented in section 5.1.2. Two different applications of ASCOT–RFOF are then discussed. The first, presented in section 5.2, focuses on a JET ICRH scenario and includes a sensitivity analysis of key ASCOT–RFOF parameters (see 5.2.1) as well as the comparison of the IMAS ASCOT-RFOF actor against established modelling tools, reported in 5.2.2). The second analysis, discussed in section 5.3, is an exploratory application of ASCOT-RFOF to ITER ICRH scenario performed evaluating the temporal evolution of ICRH-driven distribution functions (section 5.3.1) and the differences of considering positive and negative toroidal wave spectrum components (see 5.3.2). The observed modelling limitations emerging when applying the current available IMAS ASCOT-RFOF actor to high-performance plasmas are openly discussed in section 5.3.3.

5.1 ASCOT-RFOF workflow and developments

The revitalization of the ASCOT–RFOF code within the IMAS environment required a significant amount of computational development, which is partially summarized in appendix A. Here the RFOF workflow is presented to provide a synthetic overview of the overall code structure and execution logic. Then, since no tools were available to generate the initial thermal marker population required for the present ICRH modelling within IMAS, a new tool dedicated to this purpose has been developed within this project. Its detailed description and validation is presented in detail.

5.1.1 Overview of the ASCOT-RFOF model

As introduced in chapter 3, the Radio-Frequency Orbit-Following (RFOF) module library [28] is utilized by orbit-following codes, e.g. ASCOT, to model the interaction between waves and particles. A schematic overview of the ASCOT-RFOF model is shown in figure 5.1. The diagram illustrates the steps followed by a marker during an ASCOT-RFOF simulation. The principal stages of the RFOF algorithm that occur throughout marker lifetime, such as the evaluation of the resonance condition, the Monte Carlo treatment of RF-induced acceleration, and the normalization of the electric field, are described. The overall RFOF simulation is structured in a main block, or ensemble time loop, and in a set of nested time-integration levels. The loop controls the evolution of the entire marker group and the IC wave electric fields over a user-defined ensemble time (in the following referred as $\mathrm{t_{glob}}$). The nested loops instead resolve the orbit dynamics, the collisions and wave-particle interactions for each marker over a smaller time step *dt*, finally modifying the marker parameters (e.g. energy, velocity, radial position). This separation of time handling represents a non-trivial intrinsic modelling choice, which may affect the interpretation of the time evolution and of the overall power balance. In the present ASCOT-RFOF implementation within IMAS, $\mathrm{t_{glob}}$ should correspond to the maximum allowed orbit-following time of the markers, the *TMAX* parameter as called in the following. In this work, the code is applied to a fixed particle population instead of a continuous particle source. This choice is motivated by the focus, in the initial modelling phase, on the impact of ICRF waves on thermal particles, which are not appropriately represented as an external source. As a consequence, quantities derived from time integration, such as the deposited power, must be interpreted with caution within the ASCOT-RFOF time-handling strategy.

When the ensemble time loop begins, a set of ion markers is initialised following the marker properties of the input population. The simulation then enters the nested time-integration phase. One marker at a time is advanced in time by *dt*, during which collisional processes and/or wave-particle interactions may occur. The marker orbit integration proceeds in time until an end condition is reached. Typical end conditions for ASCOT-RFOF simulations are `TMAX`, corresponding to the achievement of the user-defined simulation time ($TMAX = \mathrm{t_{glob}}$), and `WALL`, indicating a particle loss due to a collision with the machine first wall. During the orbit integration, RF resonances are treated as discrete and time localized events. At every time step *dt*, the marker trajectory is advanced and the condition for crossing an RF resonance layer is evaluated. If no resonance layer is encountered, the orbit integration proceeds uninterrupted evaluating collisions and possible end conditions. When a crossing is detected, instead, the location condition of the resonance is checked such that the time step can be adjusted to guarantee that the marker actually experiences the resonance. At this point, the Monte Carlo acceleration is applied through a quasi-linear RF kick. More specifically, the wave-particle resonance condition is evaluated through the resonance frequency ω_{res} function (see also 2.39)

$$\omega_{\mathrm{res}} = \omega - n\Omega_c - k_{\parallel}v_{\parallel} - \vec{k}_{\perp} \cdot \vec{v}_d = 0 \tag{5.1}$$

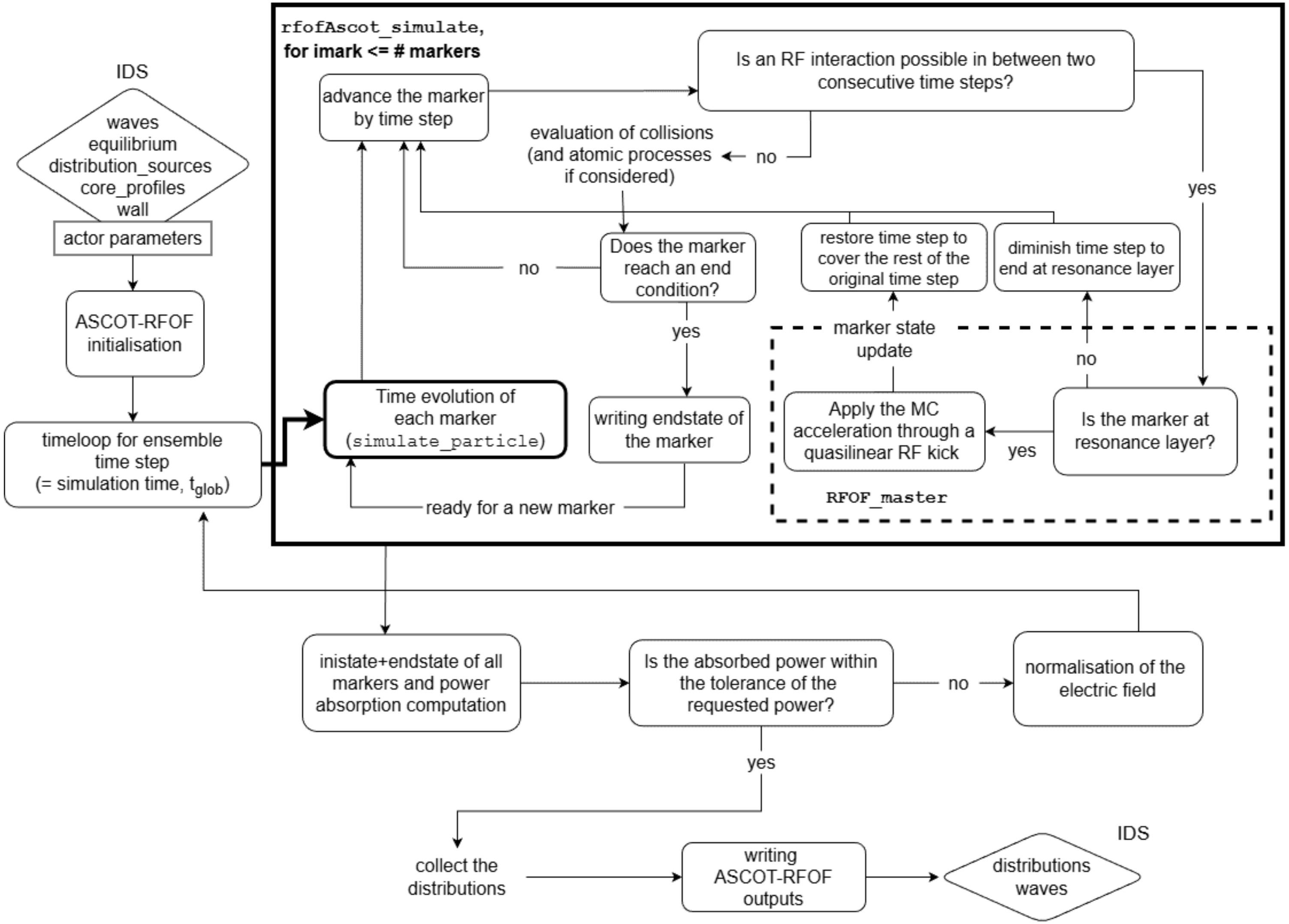

Figure 5.1: Flowchart of the ASCOT-RFOF workflow [28]. The bold black box encloses the set of nested time integration levels, where the particle is advanced over time step *dt*. In the dashed black box the two main functions of RFOF are performed: the resonance detection and quasilinear Monte Carlo RF acceleration. Inputs and outputs are reported in the diamond-shape boxes.

where ω is the angular frequency of the waves, n is the harmonic number, Ω_c is the particle cyclotron frequency, $k_{\|}, \vec{k}_{\perp}$ the parallel and perpendicular wave number defined according to the toroidal magnetic field, and $v_{\|}$ and $\vec{v}_d$ the parallel and drift velocities of the marker.

The time t_{res} at which $\omega_{\mathrm{res}} = 0$, as well as the corresponding spatial resonance location $(R_{\mathrm{res}}, z_{\mathrm{res}})$, are then estimated. For an interaction to occur, the marker must lie sufficiently close to the resonance in both time and space. These conditions are expressed as

$$(R - R_{\mathrm{res}})^2 + (z - z_{\mathrm{res}})^2 < \Delta R_{\mathrm{res}}^2 \qquad |t_{\mathrm{res}} - t| < \Delta t_{res} \tag{5.2}$$

where the ΔR_{res} is the radial width of the resonance layer, and the Δt_{res} is the temporal tolerance for resonance layer crossing. If the conditions in eq. 5.1 and eq. 5.2 are satisfied, a stochastic Monte Carlo procedure computes the consequent acceleration. This approach follows the theory described in [96], parametrizing the interaction in terms of the perpendicular invariant $I_{\perp}$, as described by equations 3.3 and 3.4. The resulting change in $I_{\perp}$ induces deterministic changes in marker variables such as the parallel velocity $v_{\|}$ and magnetic moment μ. Consequently, energy, pitch and canonical momentum are updated consistently. In particular, the kick in energy for a marker can be computed through

$$\Delta E = E(I_{\perp}^{old} + \Delta I_{\perp}) - E(I_{\perp}^{old}) \tag{5.3}$$

where $I_{\perp}^{old}$ is the value of the invariant before the particle receives the kick. This energy increment is then checked to avoid unphysical large kicks by the following condition

$$\frac{\Delta E}{E} < \bar{E}_{max} \tag{5.4}$$

where $\bar{E}_{max}$ is the maximum normalized relative energy. Both ΔR_{res}, present in eq. 5.2, and $\bar{E}_{max}$, in eq. 5.4, are related to user-defined parameters that will be explained in detail in section 5.2.1. After the evaluation of the wave-particle interaction, collisional and atomic processes are applied, if enabled in the simulation by the user, and the end conditions are checked. If no end condition is matched, the time integration of the marker continues. Otherwise, the final marker state is recorded, and the simulation passes to the next marker.

After all markers have been simulated, the code exits the ensemble time loop. The total energy absorbed by the marker population through the wave-particle interactions is used to evaluate the absorbed wave power $\mathrm{P_{abs}}$ by dividing it by the $\mathrm{t_{glob}}$ considered[1]

$$\mathrm{P_{abs}} = \frac{E_{tot,abs}}{\mathrm{t_{glob}}} \qquad \text{with} \quad E_{tot,abs} = \sum_{markers} \sum_{res} \Delta E = \sum_i w_i \sum_j \Delta E_{ij} \tag{5.5}$$

where $\sum_{markers}$, $\sum_{res}$ are the sums over all markers and resonances present in the simulations and w_i is the weight associated to each marker. This value of power is then compared with the reference absorbed wave power $\mathrm{P_{req}}$, provided in this work by the full-wave code CYRANO (see chapter 3). This comparison is necessary to check if the electric field recomputed by ASCOT-RFOF, starting from the CYRANO electric field input, provides the same amount of power expected by CYRANO to the particle population investigated. If this is not happening, i.e. if the difference between $\mathrm{P_{abs}}$ and $\mathrm{P_{req}}$ exceeds the code-defined tolerance of 5%, the amplitude of the RF electric field is adjusted through a normalization factor and the ensemble time loop is repeated. The normalization factor depends on the ratio between $\mathrm{P_{abs}}$ and $\mathrm{P_{req}}$ and ensures the convergence toward the target value $\mathrm{P_{req}}$. The procedure continues until wave power convergence is achieved within the tolerance. Once the power convergence is reached, the results are saved as outputs. The framework described and schematized

---

[1] Throughout the text, *absorbed power* $\mathrm{P_{abs}}$ refers to the power that thermal or energetic particles absorbed during their interaction with the ICRF waves (also called *absorbed wave power*), whereas *deposited power* $\mathrm{P_{dep}}$ refers to the power transferred from the energetic particles to the the background plasma via Coulomb collisions, also referred to as *collisional power*.

in figure 5.1 is thought to enable the self-consistent evaluation of RF power absorption and particle dynamics, making ASCOT–RFOF suitable for modelling ICRH-accelerated energetic particles within the IMAS framework. Applications to JET and ITER plasma scenarios, discussed in the following sections, show some limitations of the current workflow. These limitations highlight the needs for further tests and developments to provide a reliable predictive model within the IMAS framework to describe detailed ICRH induced dynamics in all plasma conditions. These aspects will be discussed in detail in the sections 5.2 and 5.3.

5.1.2 THED-G: a thermal marker generator for ICRH modelling in ASCOT–RFOF

Most of the inputs required by ASCOT-RFOF can be obtained either from the IMAS ITER scenario and machine database (e.g. *core_profiles*, *wall* IDSs) or from numerical codes already available within the IMAS framework (e.g. *equilibrium* IDS from CHEASE [108], and *waves* IDS from CYRANO [92]). Regarding the *distribution_sources* IDS, the development of a proper tool is required when simulating the application of ICRH to a thermal particle population. Indeed, while ASCOT provides dedicated tools within the IMAS framework to model beam fast ions (BBNBI) or fusion-products (AFSI [99]), no tool was available at the start of this activity to generate marker distributions representing a thermal particle population. To address this gap, the THermal 4D Distribution Generator (THED-G) was developed[2]. THED-G produces four-dimensional thermal marker distribution functions in (R, z, E, λ) phase space as required by ASCOT-RFOF, where R, z are the toroidal coordinates (assuming toroidal symmetry), E denotes the particle energy and the pitch parameter is λ. A description of THED-G is provided below.

THED-G is a python program [118] developed to be used in IMAS to generate the thermal markers starting from given kinetic profiles. The four-dimensional (4D) distribution in (R, z, E, λ) is stored in the *distribution_sources* IDS. The normalized poloidal flux coordinates, ρ_{pol} as well as the toroidal angle ϕ, are included within the IDS marker properties, as they are required for the proper initialization of ASCOT–RFOF markers. The normalized poloidal flux coordinates $\rho_{pol} = \sqrt{(\psi - \psi_0)/(\psi_{ax} - \psi_0)}$, with ψ the poloidal flux surface, is computed at the relative R, z coordinates of the marker, while the toroidal angle ϕ is sampled from a uniform distribution in the interval [0, 2π], consistent with the assumption of axisymmetry adopted in the present applications. The same method is used for the marker pitch parameter, which is sampled from a uniform distribution in the interval [-1, 1], according to the isotropic properties of thermal particles in a non-rotating plasma. The spatial and energetic coordinates of the markers are instead generated using a Monte Carlo (MC) technique, selecting them according to the density and temperature radial profiles of the species of interest, stored in the *core_profiles* IDS. The accuracy of the Monte Carlo sampling procedure is then checked by reconstructing the kinetic profiles from the MC markers. More specifically, the normalized density function $f(\rho)$, with $\rho = \rho_{pol}$, and max[$f(\rho)$] normalized to 1, is used as a probability density for the spatial selection of markers. To generate N markers, a larger set of $(R, z)_{MC}$ candidates, typically ten times larger (Nx10), is sampled uniformly choosing the coordinates within the LCFS and FW limits of the plasma considered. From each $(R, z)_{MC}$ candidate, the corresponding ρ_{MC} coordinate is computed and the values of $f(\rho_{MC})$ is compared with a uniformly distributed random number ξ in the interval [0, 1]. If $\xi < f(\rho_{MC})$ then the marker is selected; otherwise, it is rejected. Initial application of this spatial sampling procedure revealed an artificial accumulation of markers near the last closed flux surface. This behaviour was attributed to a numerical issue arising when allowing the maximum normalized poloidal flux to reach $max(\rho_{pol}) = 1.0$ during the spatial sampling. To mitigate this artifact, an artificial limit on ρ_{pol}, denoted in the following as ρ_{max}, was introduced and a dedicated scan was performed to evaluate the appropriate value. The reconstructed density profiles obtained for different values of $\rho_{max} = [0.90, 0.95, 0.99, 0.999, 0.999, 1.0]$ are shown in figure 5.2.

For $\rho_{max} = 1.0$ a clear accumulation of markers at the plasma edge is observed, while values of

---

[2] THED-G was developed by the author of this Ph.D. thesis and is now available as an open-access tool

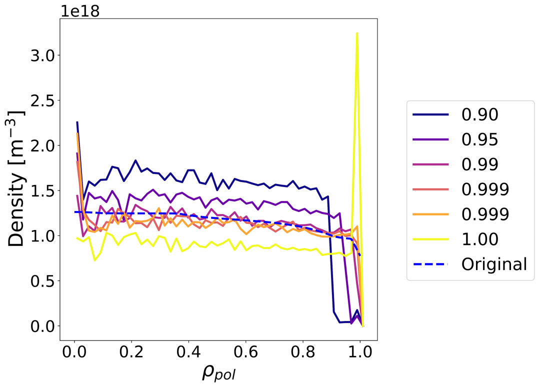

Figure 5.2: Scan on the upper limit ρ_{max} of the normalized poloidal flux coordinate. The dashed curve represents the original reference density profile stored in the *core_profiles* IDS.

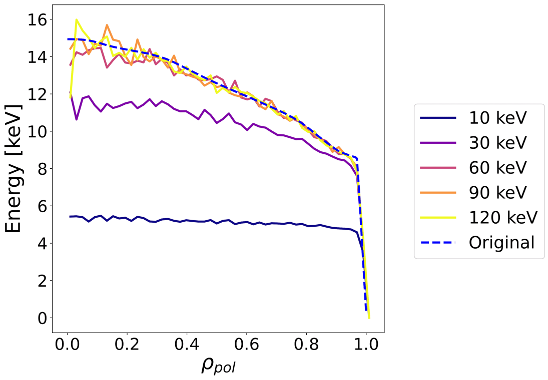

Figure 5.3: Scan on the maximum energy limit E_{lim}. The dashed curve represents the original reference energy profile obtained from the temperature profile stored in the *core_profiles* IDS.

$\rho_{max} = 0.90$ or $\rho_{max} = 0.95$ lead to an artificial emptying of the edge region. At $\rho_{max} = 0.99$, no accumulation occurs and the integral of the reconstructed density curve is the closest to the original density profile. Therefore, this value has been selected as the maximum normalized poloidal flux in THED-G.

Once the spatial coordinates of the selected markers are determined, their relative energies can be computed according to a Maxwellian velocity distribution $f(v)$, defined as 5.6, with m the mass of the interested species

$$f(v) = \sqrt{\frac{2}{\pi}} \left[\frac{m}{T}\right]^{3/2} v^2 exp\left(-\frac{mv^2}{2T}\right) \tag{5.6}$$

T = T(ρ) corresponds to the local temperature obtained from the ion temperature profile at the marker location. The marker energy is then given by $E = mv^2/2$. The marker velocity is selected using a Monte Carlo method analogous to the one applied for the spatial sampling. In this case, the maximum velocity used for sampling, or equivalently the maximum energy E_{lim}, must be selected with particular attention to avoid truncating the Maxwellian hot tail in a way that biases the reconstructed energy profile. A scan on the maximum energy limit E_{lim} is therefore performed considering $E_{lim} = [10, 30, 60, 90, 120]$ keV and assessing its impact on the reconstructed energy profile, shown in figure 5.3.

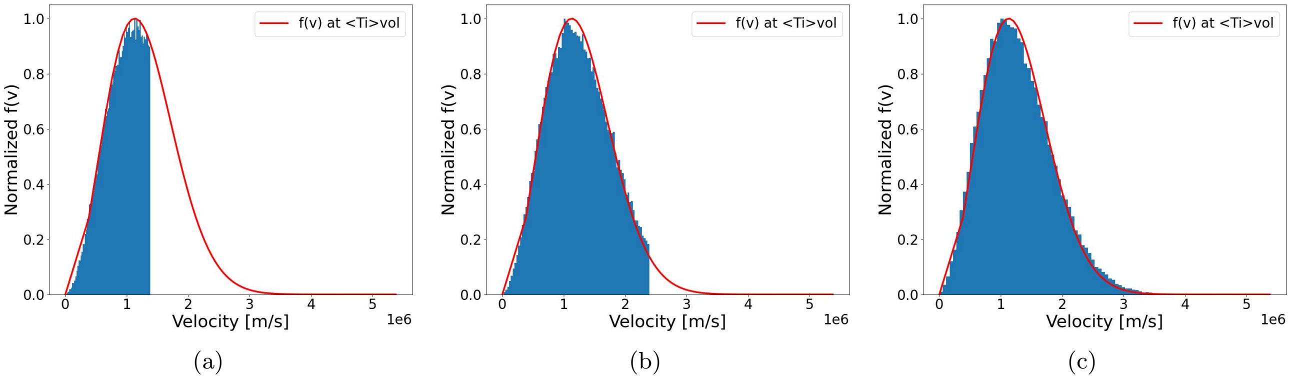

(a) (b) (c)

Figure 5.4: Analytical distribution functions $f(v)$ (red curve) and velocity histograms from the marker distributions (in blue) obtained considering $E_{lim} = 10$ keV (a), $E_{lim} = 30$ keV (b) and $E_{lim} = 120$ keV (c) as maximum energy limit. The temperature assumed for the Maxwellian distribution is the volume-averaged plasma ion temperature $\langle T_i \rangle_{\text{vol}} \sim 4.3$ keV.

The reference energy profile is derived from the plasma temperature radial profiles as $E = 3T/2$.

For low values of E_{lim}, the Maxwellian tail is artificially truncated, leading to an underestimation of overall marker population energy. For $E_{lim} = 120$ keV, the reconstructed energy profile is in good agreement with the reference distribution. At such energy limit and for the current reference energy profile, the tail population is estimated as $\sim exp(-E_{lim}/T_i) = exp(-8)$, being the core ion temperature $T_i \sim 15$ KeV. The truncation effects therefore are negligible. Figure 5.4 further illustrates this effect by comparing the analytical Maxwellian distribution f(v) with the THED-G generated energy histograms. Based on these results, $E_{lim} = 120$ keV is adopted in THED-G for the scenarios analysed in this work.

The quality of the reconstructed distributions depends on the number of generated markers. The results presented in figures 5.2 and 5.3 are obtained generating N = 10^5 MC markers. A scan over the number of generated marker is performed to assess convergence of the reconstructed profiles with the reference ones, considering N = 10^3, 10^4, 10^5, 10^6. The reconstructed density and energy profiles corresponding to these cases are shown in figure 5.5. The spikes observed in the core for the density reconstruction are a numerical effect due to the small volume at $\rho_{pol} = 0$. While the distributions obtained with 10^3 and 10^4 markers exhibit significant statistical noise, the cases with 10^5 and 10^6 markers show good agreement with the original profiles, both in shape and in their integrated value. Therefore, 10^5 markers are considered sufficient for the present applications.

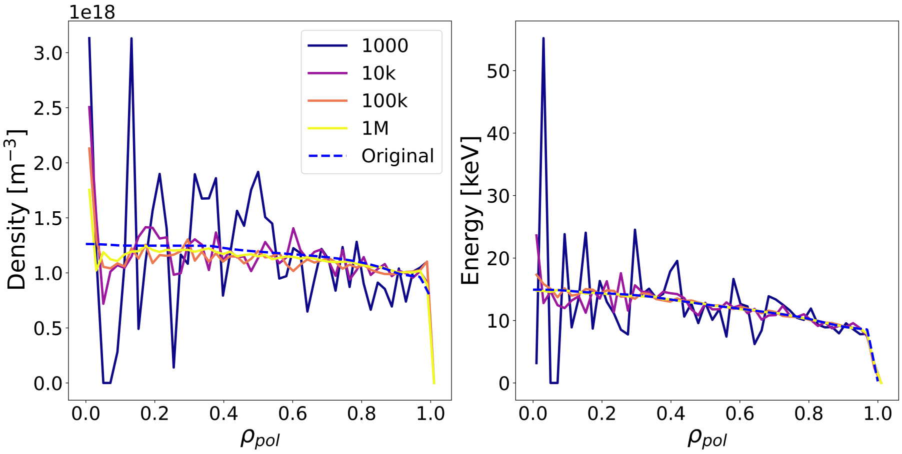

Figure 5.5: Scan on the number of markers N generated through THED-G to assess the accuracy of the initial thermal population of the selected species with respect to the original kinetic profiles (dashed blue curves). The same legend is applied for both plots.

THED-G has been validated across different ITER scenarios, characterized by different shapes and gradients of the kinetic profiles. Representative examples are shown in figure 5.6, where good agreement is observed in both density and energy reconstructions for all considered cases. The reconstruction error is quantified using the root-mean-square error (RMSE) to evaluate how far the reconstructed profiles are from the original ones. The differences observed at the edge ($\rho_{pol} \sim 1.0$) between the THED-G density profile and the reference is attributed to the low number of bins used for the reconstruction of the density profiles.

During the development and validation of THED-G, an IMAS actor capable of producing four-dimensional distributions in R, z, energy, and pitch space, called *thermalPitchE*, has been made available. THED-G was therefore compared against the output of this actor, as shown in figure 5.7. The comparison shows that both tools well reproduce the original density and energy profiles with comparable accuracy. However, since THED-G directly produces the *distribution_sources* IDS required by ASCOT-RFOF, while *thermalPitchE* actor writes the *distributions* IDS and requires an additional conversion step to sample markers from it in the present simulations, THED-G is adopted in this work to generate the thermal marker populations used as input for ASCOT–RFOF simulations.

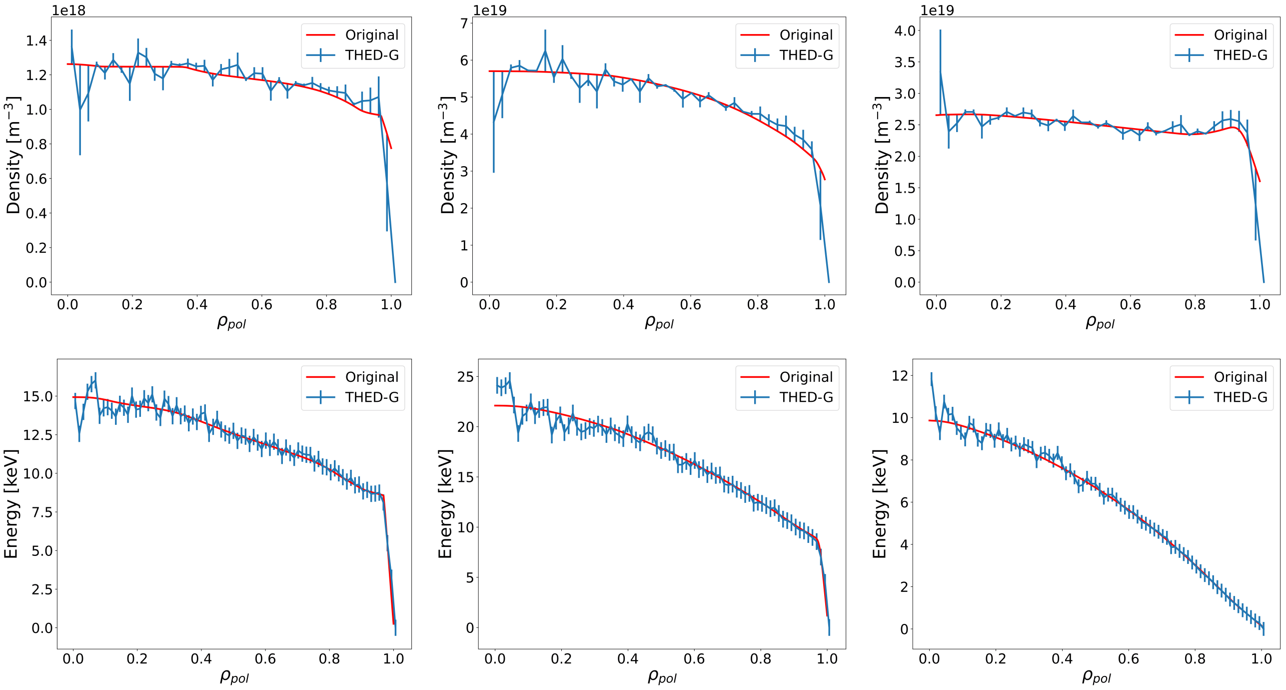

(a) (b) (c)

Figure 5.6: Density (top) and energy (bottom) radial profiles reconstruction (in blue) of three different scenarios (fig. 5.6a-5.6c), which present different shapes and gradients of the radial profiles. In particular, 5.6a D plasma with H minority heating (modelled species) at $I_p = 7.5$ MA and $B_{T,0} = 2.65$ T (magnetic toroidal field at R_0); 5.6b DT H-mode plasma with D as the modelled species at $I_p = 15$ MA and $B_T, 0 = 5.3$ T; 5.6c high-density DT L-mode plasma with D as the modelled species at $I_p = 15$ MA and $B_T, 0 = 5.3$ T. The reconstruction error is quantified using the root-mean-square Error (RMSE). The reference kinetic profiles are reported with red curves.

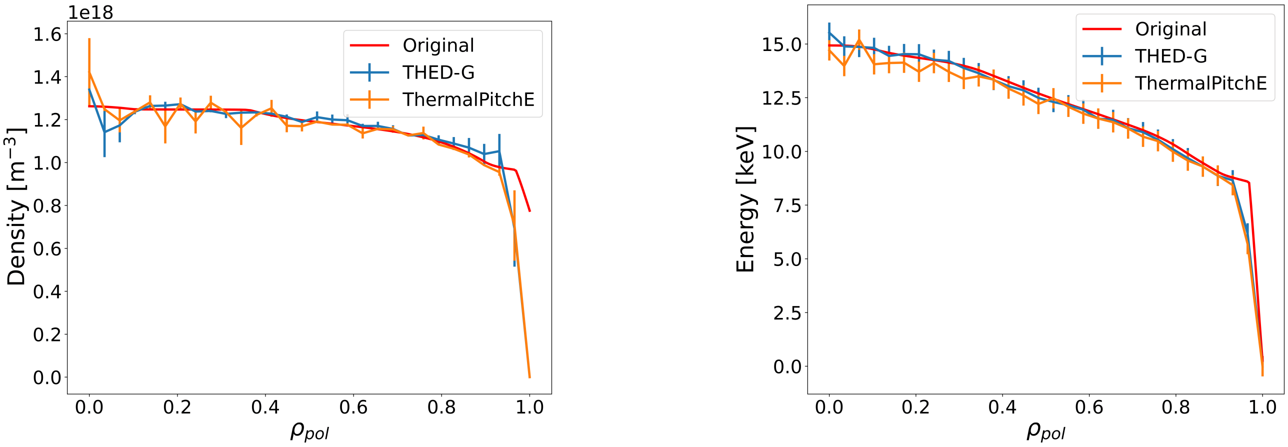

Figure 5.7: Comparison between *thermalPitchE* (orange) and THED-G (blue) reconstructed profiles and the reference kinetic profiles (red), relative to a D plasma with H minority heating (modelled species) at $I_p = 7.5$ MA and $B_{tor,0} = 2.65$ T. The reconstruction errors are quantified using the Root Mean Square Error (RMSE), comparing the actor results with the original profile.

5.2 ICRH modelling validation on a JET D-T plasma

This section presents an application of ASCOT-RFOF and a validation of the code against previous modelling results for JET tokamak. JET provides a particularly suitable testbed for this purpose, due to the extensive use of ICRH in recent experimental campaigns and the availability of several simulation results. The aim of this section is to assess the capability of ASCOT–RFOF, coupled to CYRANO within IMAS, to model ICRH interactions in realistic JET scenarios and identify potential limitations of the workflow. This is done through systematic comparison with established reduced models such as FOPLA code. In particular, the following analysis is based on a combination of simulations performed in this work, such as those for ASCOT-RFOF, and pre-existing simulations made available by collaborators (e.g. CYRANO-FOPLA results).

The validation activity focuses on a JET plasma (discharge #104522) from the DTE3 campaign. Since the original JET data for this discharge were available in the Consistent Physical Objects (CPO) format rather than in IMAS IDSs, an initial data conversion was required. In particular, the following data have been converted into IDSs: the kinetic profiles, stored in the *core_profiles*, the magnetic equilibrium, stored in the *equilibrium* IDS, and the results from CYRANO and FOPLA simulations, that are respectively stored in *waves* and *distributions* IDSs. Plasma in shot #104522 corresponds to a deuterium–tritium plasma with a hydrogen minority, characterized by a toroidal magnetic field of $B_{tor} = 3.77$ T at R_0 and a plasma current of $I_p = 2.4$ MA. The kinetic profiles are shown in figure 5.8. The two-dimensional, axisymmetric magnetic equilibrium is reconstructed using the CHEASE actor within IMAS starting from an equilibrium generated by TRANSP modelling [119]. Reference values of key plasma parameters, including electron and ion densities and temperatures at the magnetic axis, are reported in table 5.1.

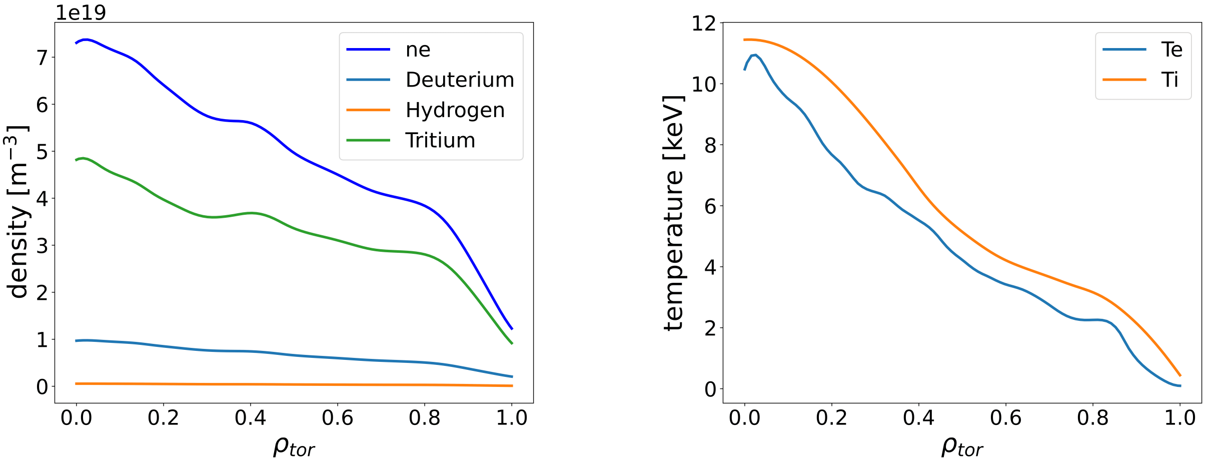

Figure 5.8: Kinetic profiles in the radial ρ_{tor} coordinate for JET DT plasma (discharge #104522 of the JET DTE3 campaign).

$n_{e,0}$ [m^{-3}]	$T_{e,0}$ [keV]	$n_{T,0}$ [m^{-3}]	$n_{D,0}$ [m^{-3}]	$n_{H,0}$ [m^{-3}]	$T_{i,0}$ [keV]	$E_{c,0}$ [keV]
7.31e19	10.5	4.82e19	0.97e19	5.41e17	11.4	136

Table 5.1: Plasma properties of analysed JET plasma (#104522). Subscript "0" refers to quantities at the magnetic axis.

Both ICRH and NBI systems are applied in this JET shot. IC heating is applied using the deuterium fundamental minority scheme to deliver 5.50 MW of power, at a frequency of 28.75 MHz with a toroidal mode number $n_\phi = 27$. Such scheme, that ensures the resonance located close to the magnetic axis, was selected to accelerate deuterium beam energetic particles. Indeed, two deuterium neutral beams with a nominal injection energy of 120 keV, are applied to provide approximately 30 MW of auxiliary power. In principle, both thermal and NBI particle populations can resonate with the IC waves in this scenario. However, even if the main target of the scheme are D beam EPs, in the present application of ASCOT–RFOF, only the thermal particle population is modelled, using THED-G to generate the ensemble of thermal markers for ASCOT-RFOF, as explained in section 5.1.2. Modelling the thermal particle population represents indeed the first stage of the validation strategy for ASCOT–RFOF before extending the analysis to NBI–ICRH synergistic effects. The resonance location of all the possible heating schemes for this plasma are illustrated in figure 5.9, computed according to equation 2.40. For the deuterium fundamental scheme (denoted as D1 in figure 5.9), the electric field components E_+ and E_- calculated by the full-wave CYRANO code, and used as input for ASCOT-RFOF simulations, are shown in figure 5.10.

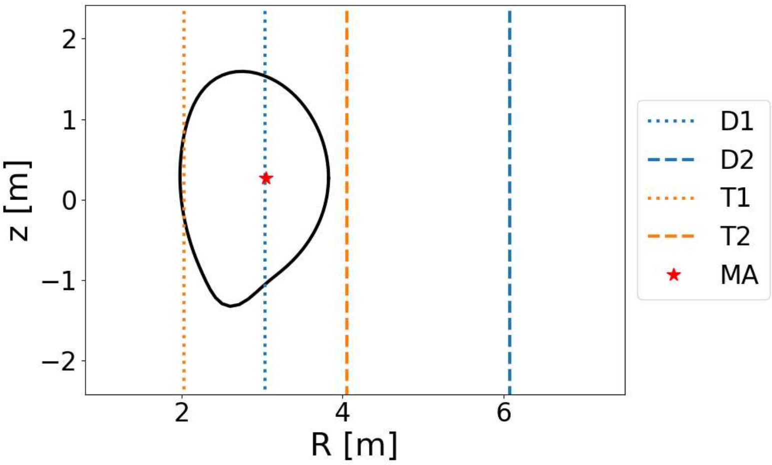

Figure 5.9: Resonance locations of different heating schemes available for the JET shot #104522 at a wave frequency of 29 MHz. The fundamental deuterium (D1) scheme (dotted blue) is the one adopted for this scenario. The red star represents the magnetic axis, while the black line is the last closed flux surface of this JET plasma. D1, D2, T1 and T2 represent the heating scheme, where D and T define the species and 1, 2 the harmonic numbers.

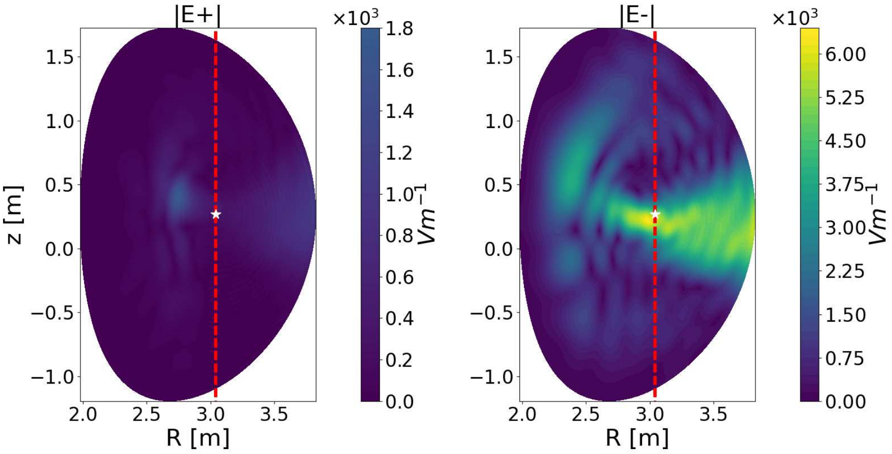

Figure 5.10: Left-hand $|E_+|$ and right-hand $|E_-|$ electric field components provided by CYRANO simulation for the D1 scheme adopted in the JET shot #104522. The red dashed line represents the resonance location of D1 and the white star the magnetic axis.

5.2.1 Sensitivity parameter scans on JET

Before comparing ASCOT–RFOF results with those obtained from CYRANO and FOPLA, an appropriate setup of the ASCOT–RFOF simulations is required. The code indeed relies on a set of user-defined parameters, specified in a RFOF-specific actor parameter file, that influence the simulation results. Some of these parameters have a clear physics interpretation, e.g. *TMAX*, while others must be adjusted according to the specific simulation setup, such as *EfieldNormalisation*, *MAX_relative_energy_kick* and *Width_of_rf_resonance_layer*. For some of these parameters, dedicated parametric scans were performed to evaluate the sensitivity of the results. A detailed discussion of these parameters and the corresponding scans are provided below.

EfieldNormalisation defines the scaling factor used to normalise the wave electric field components. Such normalization maintains the consistency between the wave power absorbed by the ion population computed by ASCOT–RFOF (P_{abs}) and the reference absorbed wave power provided by CYRANO (P_{req}), which is used as input. A preliminary simulation with a reduced number of markers (typically of the order of 10^4) is sufficient to determine an appropriate value of *EfieldNormalisation* parameter. This approach significantly reduces the computational cost of subsequent large-scale simulations, as the ensemble time loop can be limited to a single iteration if the proper normalisation factor is set. The computation of *EfieldNormalisation* is internally handled by ASCOT-RFOF and is returned as an output quantity. The default value, *EfieldNormalisation* $= 0.1$, is then replaced by the user in the actor parameters with the ASCOT-RFOF computed value before running a larger simulation. *EfieldNormalisation* parameter does not have a unique value for a given device. Indeed, it is specific to each simulation and must be recomputed whenever the simulation configuration is modified.

TMAX specifies the particle tracking time. It must be sufficiently long to allow the energetic particle population generated by ICRH to reach a steady state condition, i.e where the collisional slowing down and acceleration by IC waves are in balance. Therefore, *TMAX* is typically chosen to be comparable to the slowing down time of energetic ions. In the current IMAS implementation of ASCOT-RFOF, it represents the t_{glob} presented in section 5.1. In this work, a reference particle energy of 1 MeV is assumed to estimate the slowing down time in JET and ITER applications. According to equation 2.26, the corresponding slowing down time are therefore $\tau_{s,\mathrm{JET}} \sim 1.0\ s$ and $\tau_{s,\mathrm{ITER}} \sim 3.0\ s$. Accordingly, *TMAX* is set to 1.0 s for JET simulations. A dedicated scan on *TMAX* has been performed on JET to check whether the 1.0 s estimate is sufficient to observe the stabilization of the high-energy tail due to IC wave absorption. The particle tracking time is explored within the range [0.1, 2.0] s. The result is represented in figure 5.11, where the energetic hot tail is observed to evolve significantly with *TMAX*. At *TMAX* $= 0.02$, the energetic tail has not yet developed. As *TMAX* is increased, particles can reach progressively higher energies, leading to an enhancement of the distribution function $f(E)$ at high energy. The energy hot tail stabilization occurs around *TMAX* $= 0.5$ s, confirming *TMAX* $= 1.0$ s to be long enough to reach a steady state condition. The fluctuations observed in each curve are consistent with statistical noise due to limited marker sampling. A similar scan will be presented in section 5.3 for the analysed ITER scenarios.

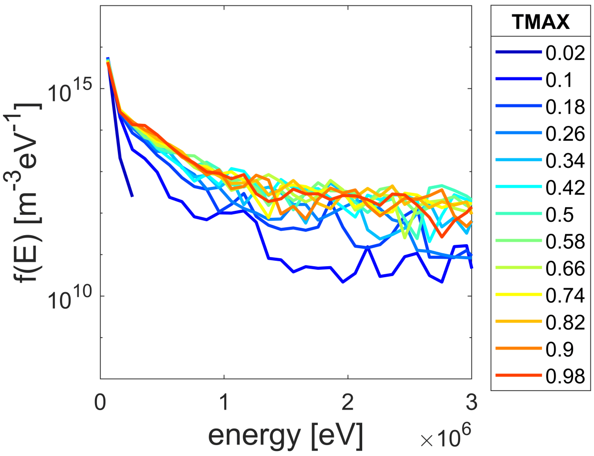

Figure 5.11: Energy distribution functions f(E) in logarithmic scale representing the energetic hot tails generated by wave-particle interactions at different *TMAX*. The stabilization of the hot tail is observed around *TMAX* $= 0.5$ s.

MAX_relative_energy_kick defines the maximum allowed fraction of energy that a particle can receive from an RF-kick. It is introduced to prevent unphysical large energy increments that may arise when markers remain in resonance with the RF wave for extended periods, and applied as reported in eq. 5.4 where $\bar{E}_{max} = MAX\_relative\_energy\_kick$. Its careful selection is therefore essential to avoid non-physical results. Since no specific information was available to set this parameter, a value of 0.07 is adopted for the studied JET and ITER cases, based on previous ASCOT-RFOF simulations performed for ASDEX-Upgrade [100]. There is no a-priori justification that this values is appropriate. This motivated a dedicated sensitivity study, carried out for the currently analysed JET plasma, to evaluate the effect of *MAX_relative_energy_kick* on the results and eventually to identify a suitable range of the parameter. *MAX_relative_energy_kick* is varied over the range [0.01, 1.0]. The resulting radial profiles of the absorbed wave power (P_{abs}) density computed by ASCOT-RFOF are reported in figure 5.12 and compared with the corresponding CYRANO input. Within the explored range, a negligible variation of the absorbed wave power density profiles is observed. This apparent insensitivity should not be interpreted as evidence that the parameter has no physics impact. A more conclusive assessment would require significantly higher marker statistics (here only 10^4 markers are considered) to exclude statistical noise effects, since this parameter impacts mainly on rare high-energy particles during the wave-particle interaction. In the present study *MAX_relative_energy_kick* is therefore kept at the initial value of 0.07, for both JET and ITER.

Width_of_rf_resonance_layer controls the effective width of the resonance layer, entering in the definition of ΔR used in eq. 5.2. In principle, this width should be smaller than $10^{-3}L_c$ with $L_c = \frac{1}{|\nabla \log B|}$ the characteristics magnetic field length of the system. This condition ensures that particles are sufficiently close to the resonance location to be considered resonant. For JET and ITER plasmas, the corresponding values of $10^{-3}L_c$ are approximately 0.002 m and 0.006 m, respectively. However, previous studies [120] suggest that the effective resonance layer may include the Doppler-broadening, with a characteristic width of several centimetres for keV-range thermal ions. In light of this discrepancy, an exploratory scan of this parameter is performed for JET plasmas to assess the *Width_of_rf_resonance_layer* impact on the simulation results and to identify an appropriate value for the device. The explored range covers from 0.002 m to 0.2 m. Results presented in figure 5.13 show that, conversely to *MAX_relative_energy_kick* parameter, the $\mathrm{P_{abs}}$ density radial profile is strongly affected by *Width_of_rf_resonance_layer*. However, none of the explored values leads to a satisfactory agreement with the absorption profile provided by CYRANO, for a reason that will be explained in section 5.2.2. In the absence of a physically motivated criterion, the initial value computed as in [28] (0.002 m for JET), is assumed for following ASCOT-RFOF simulations.

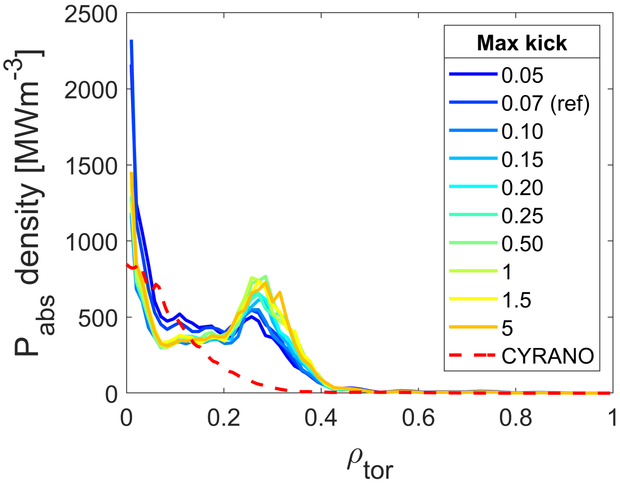

Figure 5.12: Radial profiles in ρ_{tor} of the absorbed wave power $\mathrm{P_{abs}}$ density obtained from ASCOT-RFOF at different *MAX_relative_energy_kick* (max kick) input values. The red dashed curve is CYRANO $\mathrm{P_{abs}}$ profile. The selected value is indicated by "ref" in the legend.

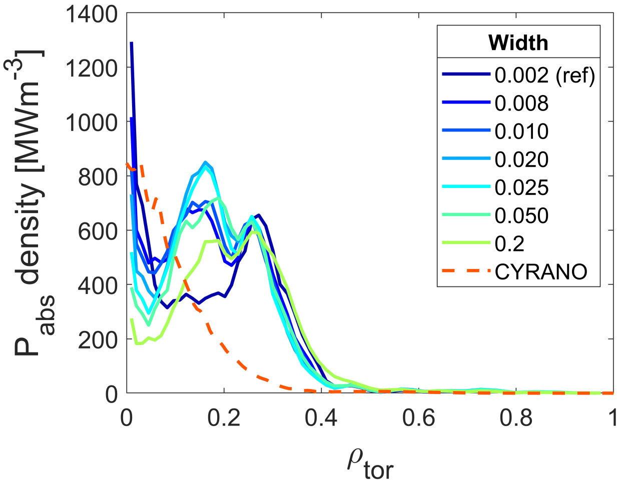

Figure 5.13: Radial profiles in ρ_{tor} of the absorbed wave power $\mathrm{P_{abs}}$ density obtained from ASCOT-RFOF at different *Width_of_rf_resonance_layer* (width) input values [in m]. The orange dashed curve is CYRANO $\mathrm{P_{abs}}$ profile. The selected value is indicated by "ref" in the legend.

5.2.2 ASCOT-RFOF versus FOPLA: physical interpretation of the discrepancies

The results presented so far on the wave power absorption on thermal particles (fig. 5.12 and 5.13) show a noticeable discrepancy with the CYRANO input available for the analysed JET case. ASCOT-RFOF predicts an absorption peak at $\rho_{tor} = 0.28$, shifted outward compared to CYRANO results. This discrepancy has been later discovered to be related to a mismatch in the (R, z) grids used for the evaluation of wave–particle absorption and the magnetic equilibrium. While the equilibrium reconstructed with CHEASE correctly accounts for the vertical shift of the magnetic axis at $z_{ax} \approx 0.27$ m with respect to the geometrical axis (z = 0), CYRANO generates and stores the wave RF fields in a grid with an axis at $z_{ax} = 0$ m. Since ASCOT–RFOF reconstructs the RF electric fields from CYRANO wave-field information but on a grid defined according to CHEASE equilibrium, the mismatch with CYRANO grid in the z-coordinate introduces a vertical shift in the wave-field mapping, leading to a displacement in the toroidal flux coordinate. Correcting the shift in the CYRANO *waves* IDS, the wave power absorption profiles show a significantly improved agreement, as shown in figure 5.14. The correction applied here is a workaround adopted for this study, but a general solution for the integrated modelling involving an equilibrium code, a full-wave solver and a slowing down model should be considered to avoid this kind of issue in future applications. The integrated absorbed wave power matches the tolerance of 5% set in ASCOT-RFOF, with $\mathrm{P_{abs,CYRANO}} = 1.84$ MW and $\mathrm{P_{abs,ASCOT}} = 1.75$ MW, corresponding to a relative difference of 4.9%.

The deposition power $\mathrm{P_{dep}}$ density profiles, which describe the transfer of absorbed RF power to ions and electrons through Coulomb collisions, reveal a larger discrepancy between ASCOT–RFOF and FOPLA. Figure 5.15 and table 5.2 show that even if both models locate the main deposition region within the inner half of the plasma, FOPLA predicts a large fraction of power deposited to ions, whereas ASCOT–RFOF predicts broader profiles and a dominant electron heating. The prediction of broader power deposition profiles by ASCOT–RFOF is physically reasonable, as the model accounts for finite orbit width effects. In contrast, since such effects are not captured by FOPLA, the wave power absorbed in a given region, as predicted by CYRANO, is deposited locally in the same region by FOPLA, as clearly shown looking at figures 5.14 and 5.15. However, ASCOT results are inconsistent with the experimental evidence observed at JET, where ion heating is found to be dominant. The incorrect partition of the absorbed wave power in favour of electrons points to the presence of high-energy ions, which locally satisfy the condition $\mathrm{E_{fast}} > \mathrm{E_c}$, where $\mathrm{E_c}$ denotes the critical energy.

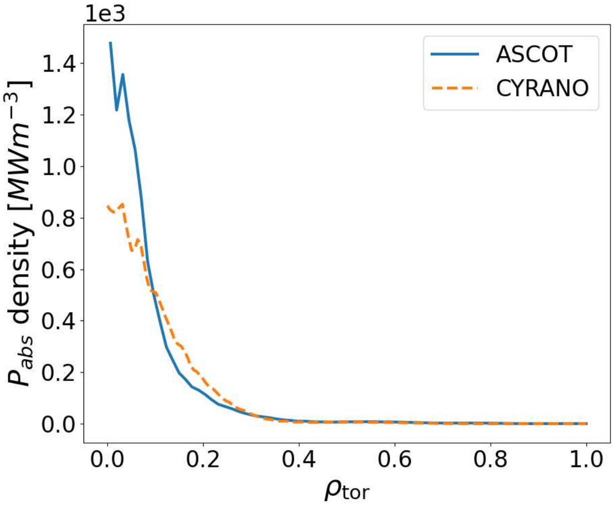

Figure 5.14: Radial profiles in ρ_{tor} of the absorbed wave power $\mathrm{P_{abs}}$ density by thermal particles obtained from ASCOT-RFOF (labelled as ASCOT with the blue line) and CYRANO (dashed orange curve).

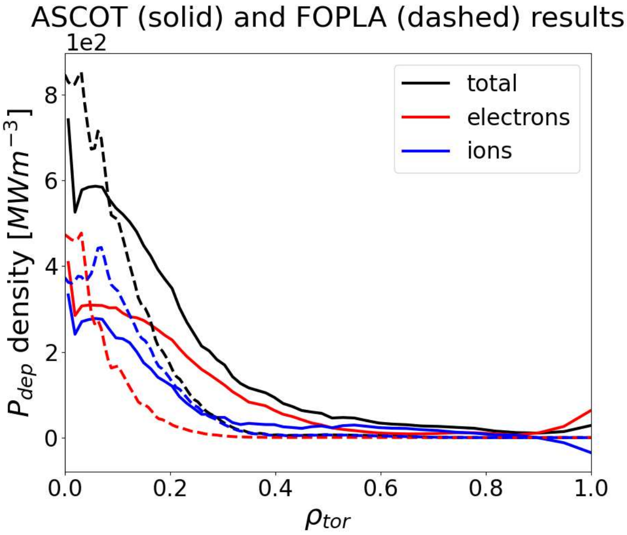

Figure 5.15: Radial profiles in ρ_{tor} of the deposited power $\mathrm{P_{dep}}$ density after the slowing down to electrons (red) and ions (blue) obtained from ASCOT-RFOF (solid lines) and FOPLA (dashed curves).

Species	$P_{\text{dep,FOPLA}}$ [%]	$P_{\text{dep,ASCOT}}$ [%]
Electrons	26.28	68.42
Ions	73.72	31.58

Table 5.2: Fractions of the deposited power to electrons and ions computed by FOPLA and ASCOT-RFOF.

Indeed, when the energy of the IC-accelerated marker is higher than the critical energy E_c, a larger fraction of energy is transferred to electrons. Since the critical energy scales with the electron temperature, its value varies significantly across the plasma, decreasing in this scenario from about 136 keV in the core to about 1.38 keV at the edge. As a result, high-energy ions travelling in outer regions preferentially deposit energy to electrons. In the present scenario, this mechanism is indeed enhanced by the presence of energetic ions with large orbit widths observed in ASCOT-RFOF, consistent with the electron deposition peak at $\rho_{tor} \sim 0.9$ and shown in figure 5.15. Two effects are identified as possible contributors to this discrepancy:

- The limited number of markers used in the present simulations may amplify the contribution of rare, high-energy particles. The energy histogram reported in figure 5.16 shows that ASCOT-RFOF predicts particles with energies above 10 MeV ($\sim$ 2.5% of the population). These are characterized by large orbit widths and can lead to an overestimation of edge electron deposition, as observed in ASCOT-RFOF results (tab. 5.2). A definitive assessment of the relative importance of this effect would require higher-statistics orbit-following simulations to reduce the contribution of rare-high energy events, that is likely due to insufficient particle statistics.

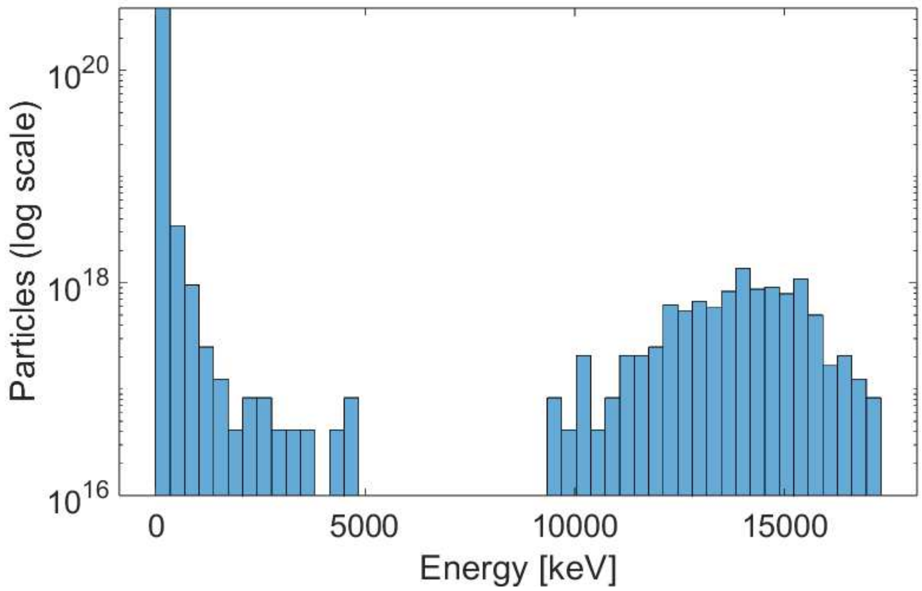

Figure 5.16: Histogram representing the energies of the markers at the end of the ASCOT-RFOF simulation. An ensemble of markers with energies above 10 MeV is predicted.

- The wave-particle interaction is modelled considering a non-symmetric toroidal spectrum, with only $n_\phi = +27$ component included, despite the JET antenna is set on a symmetric spectrum. This decision was made consistently with the input of CYRANO, which had only one toroidal wave number component. For JET, a non-symmetric toroidal spectrum leads to outward drift of resonant ions, as the waves propagate in the counter-current direction. Including the corresponding negative n_ϕ component would introduce an inward drift contribution, balancing the net outward displacement. A symmetric spectrum is therefore expected to limit the accumulation of energetic ions on the low-field side and reduce the associated electron power deposition.

Finally, the integrated deposited power after the slowing down result significantly larger than the absorbed wave power by thermal particles, violating the energy conservation principle. This inconsistency may originates from the interpretation of marker weights. Input markers for ICRH on thermal particles are considered as a population of particles ($[w_i]$ = #particles), while the usual ASCOT model deals with a source of particles ($[w_i]$ = #particles/s) due to e.g. a NBI source. This modelling setting introduces complications in the interpretation of the RF absorbed power and power deposition. Indeed, while RF absorption is normalized using a global time interval (see equation 5.5), collisional processes are accumulated over the actual particle trajectories, contributing to collisional deposition proportionally to their effective lifetime. This mismatch makes the results sensitive to whether markers represent an initial population or a continuous source, potentially leading to apparent violations of energy conservation.
Building on the insights gained from the JET analysis, an exploratory application of ASCOT–RFOF to ITER ICRH scenarios is presented in section 5.3. In this context, increased marker statistics and both positive and negative toroidal mode numbers are considered in the wave–particle interaction.

5.3 Exploratory study of fundamental hydrogen ICRH heating in a ITER plasma at half magnetic field

The revitalized version of ASCOT-RFOF within the IMAS framework is applied here to an ITER plasma to deepen study on the application of orbit-following ICRH modelling to reactor-relevant plasmas. This investigation will not provide reliable quantitative predictions of ICRH power deposition in ITER, but rather aims to investigate the behaviour and limitation of the current IMAS ASCOT-RFOF actor in a regime characterized by long interaction timescale and large orbit effects. The analysis focuses on the time evolution of distribution functions, which is presented in section 5.3.1, and on the application of modelling improvements identified during the work performed for JET (section 5.2.2). This includes the impact of the toroidal wave spectrum setting, which will be discussed in section 5.3.2. The resulting wave power absorption and power deposition profiles are respectively compared with the waves input provided by CYRANO and the slowing down distribution of FOPLA. Contrary to the JET analysis, ITER analysis are based on simulations performed during this work which includes not only ASCOT-RFOF runs but also some CYRANO-FOPLA modelling, combined with pre-existing simulations of CYRANO and FOPLA made available by collaborators. The progresses obtained for the current ASCOT–RFOF code IMAS implementation are finally discussed in section 5.3.3, together with potential strategies to address the observed limitations.

The ITER scenario considered has already been presented in section 4.3.2. It is a deuterium plasma at half field (2.65 T, Ip= 7.5 MA) (shot/run = 53301/3). The kinetic profiles and magnetic equilibria of this plasma discharge are obtained by METIS 0.5D transport code [115]. The profiles, selected at the flat-top time slice t = 355.0 s, are reported in figure 4.19. At the core, the electron density and temperature are respectively $n_{e,0} = 2.6 \times 10^{19}$ m^{-3} and $T_{e,0}$ = 21keV. The ICRH system delivers 10 MW using the hydrogen fundamental heating scheme, being hydrogen present as minority with 5% of concentration. Geometrical design of the ITER ICRH antenna imposes the toroidal wave mode number $|n_\phi| = 35$, and the wave frequency is set to 40 MHz, such that the hydrogen fundamental resonance (N = 1) is close to the magnetic axis. The location of all relevant resonances for this scenario are reported in figure 5.17. The *waves* input IDS containing the electric field used by ASCOT–RFOF is taken from CYRANO, which also provide the absorbed wave power used later for comparison. Larger statistics, as suggested at the end of JET validation activity, for the marker population of thermal hydrogen is used in the present ITER simulations, producing 10^5 thermal markers with THED-G (as described in sec. 5.1.2).

Based on the parameter assessment performed for JET in section 5.2.1, where *Width_of_rf_resonance_layer* and *MAX_relative_energy_kick* parameters have been discussed also for ITER application, these are set to *Width_of_rf_resonance_layer* = 0.01 m and *MAX_relative_energy_kick* = 0.08 for the following

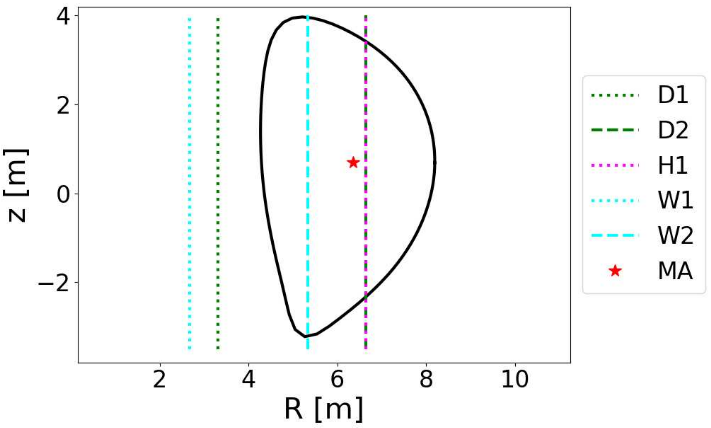

Figure 5.17: Location of the resonance layers at wave frequency of 40 MHz of difference heating schemes available for the ITER plasma modelled in shot #53301. The fundamental hydrogen (H1) scheme (dotted purple line) is the one adopted for this scenario. The red star represents the magnetic axis, whereas the black line is the last close flux surface during flattop. Like in figure 5.9, the legend defines the heating scheme by using the species (D, T, W) and the harmonic numbers (1, 2).

simulations. Even if the slowing down time expected in ITER for a 1 MeV particle is $\tau_{s,ITER} \sim 3s$, the particle tracking time for ITER is assumed to be $TMAX$ = 2.0 s. This choice is dictated by computational constraints, since a simulation with 10^5 markers and $TMAX$ = 2.0 s requires already about ∼ 30 days to be completed in the ITER Scientific Data and Computer Centre (SDCC) cluster. Additional simulations are performed for $TMAX$ = [5e-5, 0.1, 0.5] s to test the sensitivity of this parameter on an ITER case, as discussed in the following section 5.3.1. At $TMAX$ = 5e-5 s, collision effects are negligible, allowing the observation of pure wave absorption effects.

5.3.1 Time evolution of the radial profiles and distribution functions

ASCOT-RFOF results presented in this section are obtained using a wave spectrum with positive toroidal mode number $n_\phi = 35$, in consistency with reference FOPLA simulations[3]. Nevertheless, in ITER the reference ICRH phasing scheme produces a symmetric toroidal wave spectrum. From a modelling perspective, this symmetry should therefore be obtained by simultaneously applying both $n_\phi = \pm 35$. Initially, positive and negative toroidal mode numbers are considered separately, allowing to isolate the effect of the wave propagation direction. This section in particular investigates the time evolution of radial profiles and distribution functions by setting the following $TMAX$ values: [5e-5, 0.1, 0.5, 2.0] s. This type of parametric scan on $TMAX$ parameter allows observing the physical mechanisms of RF wave absorption and collisional relaxation, which are known to happen at different timescales in ICRH-heated plasmas [116]. The integrated absorbed wave power computed by ASCOT-RFOF remains consistent with CYRANO input for all $TMAX$ values, with discrepancies remaining within the imposed 5% tolerance. The wave power absorption profiles instead, compared in figure 5.18 for all the investigated cases, shows some differences with CYRANO predictions. The region of absorption predicted by ASCOT-RFOF, indeed, is consistent with the CYRANO result up to $TMAX$ = 0.1 s. However, as the particle tracking time $TMAX$ increases, the ASCOT-RFOF absorption profile progressively shifts towards the plasma edge. This behaviour could be physically plausible, as particles interacting with the IC waves over longer times can reach higher energies and experience larger Doppler shifts, therefore satisfying the resonance condition at displaced radial locations[4]. Finite orbit width effects, which are absent in CYRANO, could further contribute to this outward displacement visible in ASCOT-RFOF. Nevertheless, such trend on $TMAX$ is expected to eventually saturate. Simulations at larger $TMAX$ values could be used to verify this behaviour but are currently constrained by available computational resources. The absence of saturation would instead suggest the presence of unresolved modelling or numerical issues.

A summary of the deposited power and associated particle losses is provided in table 5.3. A critical outcome of the ITER simulations, as already observed in JET analysis (see sec. 5.2), is the emer-

---

[3] FOPLA does not contain any physics model to account for a symmetric wave spectrum

[4] Figure 2.14b shows the shift of the deuterium fundamental (D1) resonance layer due to the Doppler effect on a deuterium thermal ion, in similar condition to the present case.

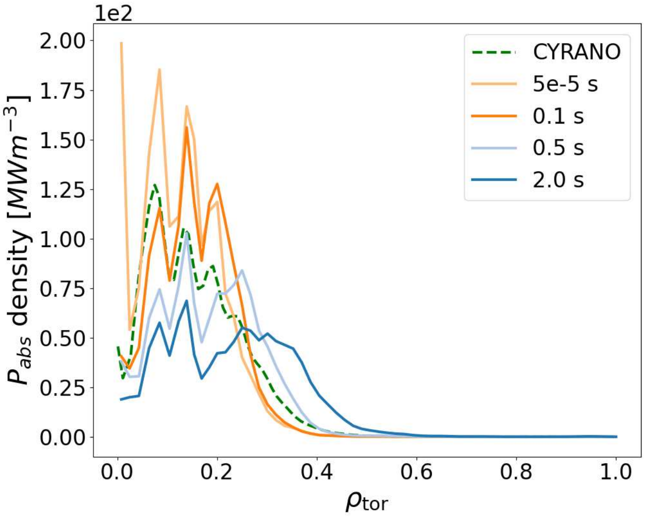

Figure 5.18: Absorption profiles from ASCOT-RFOF (solid lines) with different *TMAX* input parameters, compared to the CYRANO absorption profile (green dashed curve).

gence of a substantial inconsistency between the P_{abs} and P_{dep} power, with cases (in red) where the deposited power significantly exceeds the absorbed RF power, clearly unphysical (this behaviour will be discussed in 5.3.3). Nevertheless, certain aspects of the observed results can still be qualitatively interpreted and discussed in the context of known fast ion physics mechanisms. The deposition profiles normalized to their integral value are shown for FOPLA and ASCOT–RFOF simulations in figure 5.19. The $TMAX$ = 5e-5 s case is not reported, since collisions are not yet effective.

Code	***TMAX*** [s]	$\mathbf{P_{abs}}$ [MW]	$\mathbf{P_{dep}}$ [MW]	$\mathbf{P_{dep,e}}$ [%]	$\mathbf{P_{dep,i}}$ [%]	$\frac{P_{dep,e}}{P_{dep,i}}$	**Losses**[*] [%]
ASCOT	0.1	6.27	3.59	28.28	71.72	0.39	1.97
	0.5	6.13	10.41	71.69	28.31	2.53	5.23
	2.0 (+35)	6.60	21.00	90.24	9.76	9.25	11.75
	2.0 (–35)	6.23	253.29	98.99	1.01	98.0	0
FOPLA	–	6.32	6.32	60.87	39.13	1.56	0

[*] The loss fraction for ASCOT represents the total number of markers that encounter the end condition `WALL`.

Table 5.3: Integrated wave absorbed and deposited power estimated by ASCOT-RFOF, for different *TMAX* simulations, and FOPLA. The P_{dep} values in red are those that exceed the P_{abs} amount. The fraction of power deposited to electrons and ions, respectively $P_{dep,e}$ and $P_{dep,i}$, and particles lost on the wall are reported too. The $TMAX$ = 5e-5 s case is not considered since no collisions happen during this timescale. For $TMAX$ = 2.0 s instead, both $n_\phi = \pm 35$ results are reported for comparison (discussed in sec. 5.3.2).

As *TMAX* increases, collision effects become progressively more important. The outward shift observed in the absorption profiles of ASCOT-RFOF is also seen in the power deposition profiles, deviating substantially from the FOPLA predictions. An interpretation compatible with the results is that, as the thermal particle interaction time with the waves increases, particles can reach higher energies and experience progressively larger orbit widths, giving rise to a broader deposition region. This behaviour, however, produces an increasing fraction of particle losses on the wall when increasing the particle tracking time. In addition, also the power-sharing between electrons and ions is affected. Indeed, the higher is *TMAX*, the higher is the fraction of power deposited to electrons, similarly to the results obtained for JET. At $TMAX$ = 0.5 s, the amount of electron:ion heating predicted from ASCOT-RFOF is the closest to that estimated by FOPLA (60:40 for FOPLA, 71:29 for ASCOT-RFOF).

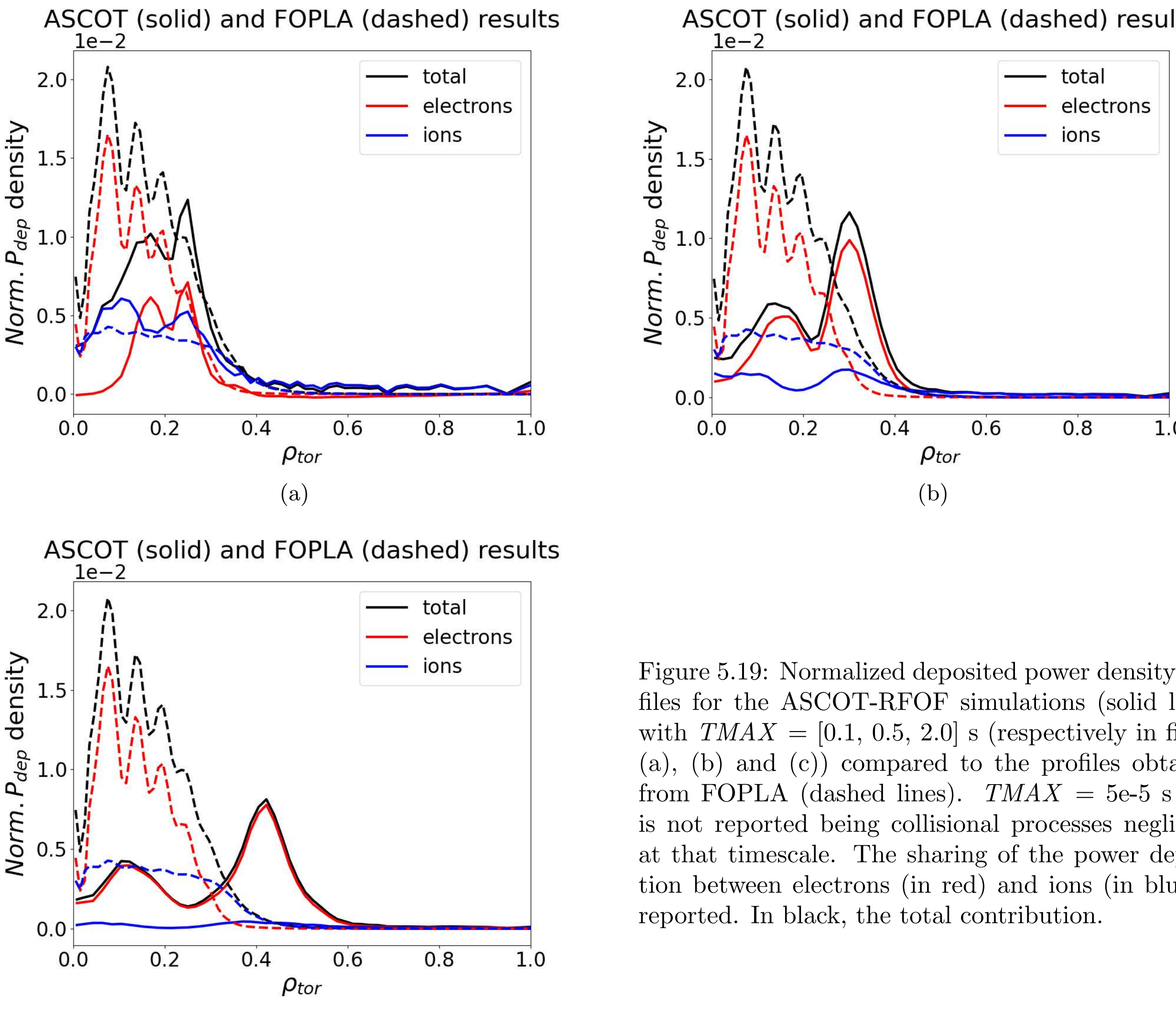

(a)

(b)

(c)

Figure 5.19: Normalized deposited power density profiles for the ASCOT-RFOF simulations (solid lines) with $TMAX = [0.1, 0.5, 2.0]$ s (respectively in figure (a), (b) and (c)) compared to the profiles obtained from FOPLA (dashed lines). $TMAX = 5\text{e-}5$ s case is not reported being collisional processes negligible at that timescale. The sharing of the power deposition between electrons (in red) and ions (in blue) is reported. In black, the total contribution.

Examining the particle, energy, and pitch distribution functions in the R, z phase space for different values of $TMAX$ allows a more detailed characterization of the behaviours discussed above. As shown in figure 5.20, particles are progressively displaced from their initial position as $TMAX$ increases due to wave–particle interactions and collisions with the background. Particles lost in the wall are observed in R $\sim$ 8.3 m, $0 \lesssim z \lesssim 1$ region for $TMAX \geq 0.1$ s. Moreover, a low-density region develops in the plasma core, while particle accumulation is observed both around the magnetic axis and near $R \simeq 7$ m. The resonance seems to trap particles within a region from which they cannot easily escape. The wave–particle interaction provides energy, pushing particles away from the resonance region into larger orbits; once displaced, Coulomb collisions with the background plasma decelerate them, allowing particles to re-enter the resonant condition [121]. This cyclic process repeats continuously. Whether the configuration observed at $TMAX = 2.0$ s predicts a stationary state remains unclear and would require simulations at larger $TMAX$, which were not performed within this work for computational time limits. The corresponding energy distributions in the R, z plane, reported in figure 5.21, shows that the highest energies are in the regions of strong particle accumulation and towards the plasma edge. Energy values exceed 3.5 MeV, reaching energies even above 10 MeV, likely related to rare high-energy particles. The appearance of multi-MeV ions may suggest that the quasilinear RF kick model is being applied beyond its validity range, as will be further discussed in section 5.3.3.

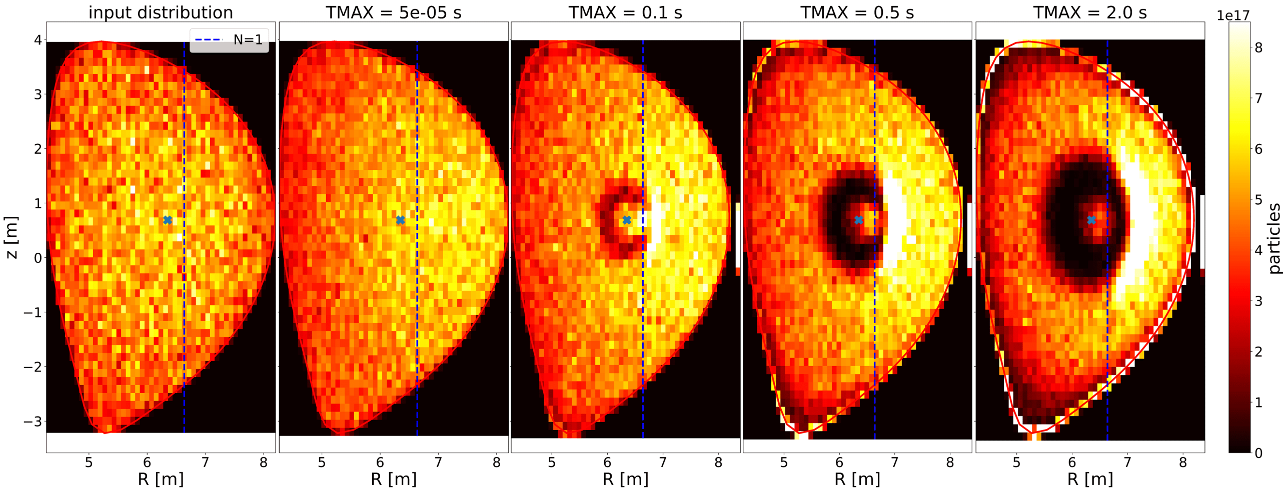

Figure 5.20: Particle distribution of ICRH-accelerated thermal population in the R, z phase space at different *TMAX*. Initial distribution (stored in *distribution_sources* IDS) is represented too. The blue dashed line represents the H1 resonance layer and the blue cross the magnetic axis.

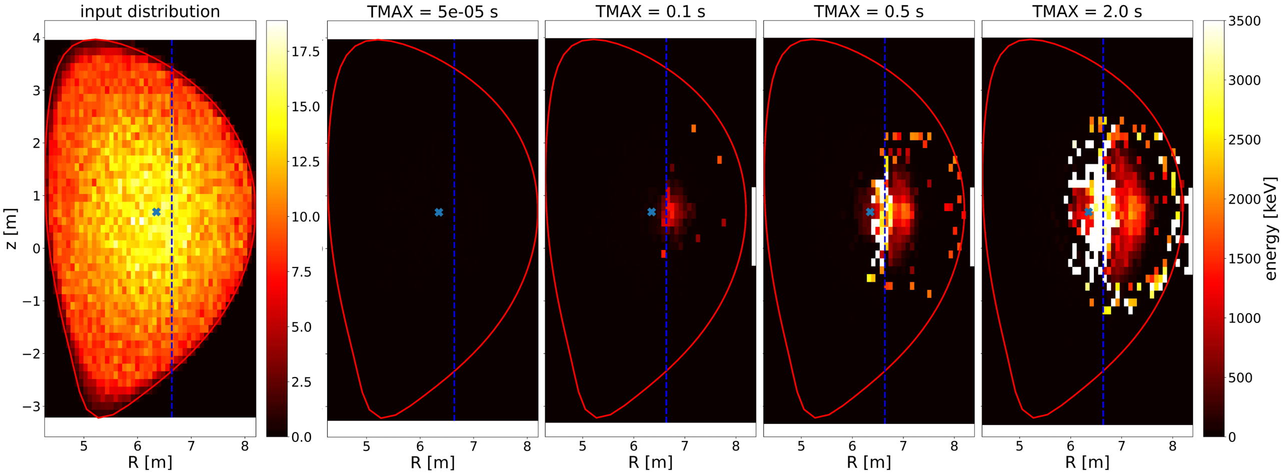

Figure 5.21: Energy distribution of ICRH-accelerated thermal population in the R,z phase space at different *TMAX*. Initial energy distribution (stored in *distribution_sources* IDS) is represented to. Two different scales have been used for the initial energy distribution and those at different *TMAX*. The blue dashed line represents the H1 resonance layer and the blue cross the magnetic axis.

The time evolution of the energy hot tails is shown in figure 5.22. The tails evolve with increasing *TMAX*, in agreement with theoretical expectations, and a tendency towards convergence may be inferred around $TMAX = 2.0$ s. Pitch distributions, reported in figure 5.23, show a peak initially growing with *TMAX* around $\lambda = 0$, corresponding to trapped particles, which represents the effect of the wave-particle interaction. At $TMAX = 2.0$ s, the peak decreases in amplitude and broadens, suggesting that the collisional pitch-angle scattering is smoothing the ICRH-driven anisotropy. This interpretation is supported by the 2D pitch–energy distributions shown in figure 5.24. At *TMAX* = 5e-5 s, the distribution is not already perturbed by the wave absorption. At intermediate times, the progressive formation of energetic tails is observed, indicating the cumulative effect of repeated wave–particle interactions. For $TMAX = 2.0$ s, pitch-angle scattering becomes increasingly relevant, particularly for particles with energies around the critical energy $E_c = 203.44$ keV.

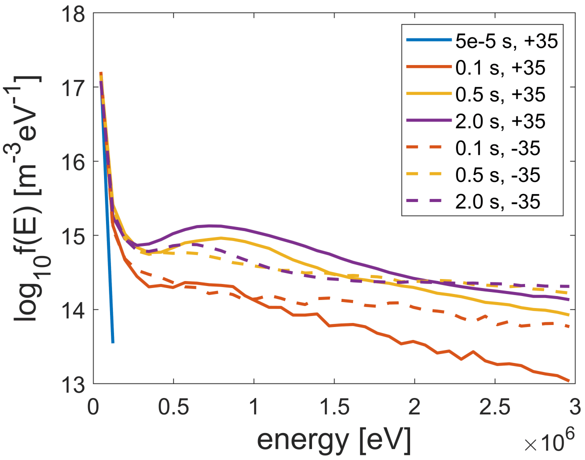

Figure 5.22: Energetic hot tails $log(f(E))$ obtained through wave–particle interaction at different $TMAX$. Both n_ϕ positive and negative cases are represented using respectively solid and dashed curves.

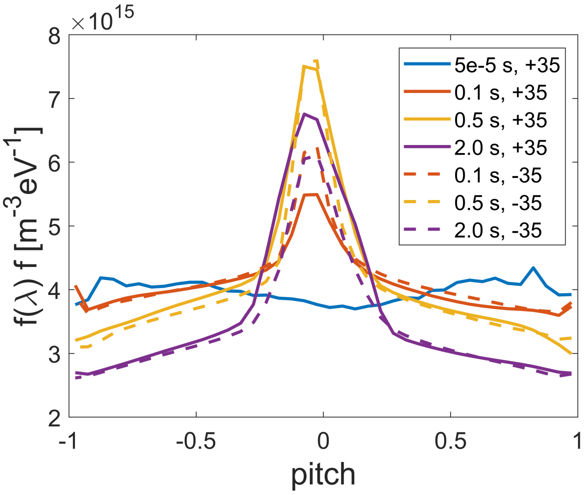

Figure 5.23: Pitch distributions $f(\lambda)$ at different $TMAX$. Both n_ϕ positive and negative cases are represented using respectively solid and dashed curves.

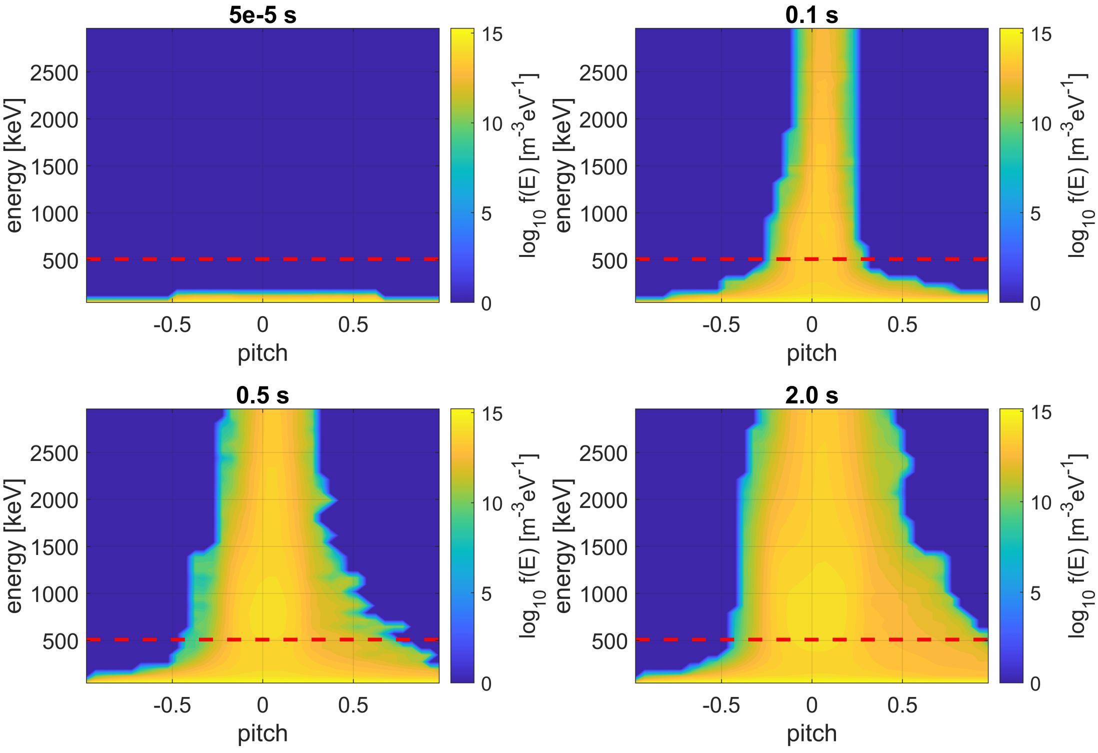

Figure 5.24: Pitch-energy distribution functions at different $TMAX$. The red dashed line represents the value of $2.5E_c$ for this scenario, with $E_c = 203.44$ keV.

The increasing divergence between absorbed and deposited powers observed at large $TMAX$ indicates that the present ASCOT–RFOF implementation does not provide a self-consistent steady-state description. Moreover, increasing the statistics from 10^4 to 10^5 markers, as discussed in section 5.2.2, does not resolve the inconsistency on the power-sharing between electrons and ions while comparing ASCOT-RFOF and FOPLA results, as rare high-energy ions continue to be generated in a non-negligible fraction even when using 10^5 markers. A complete investigation of the effect of marker statistics on high-energy particle generation would require scanning marker numbers up to and beyond the order of millions, in particular for moderate ICRH power and ITER-scale plasmas. However, this analysis requires significantly greater computational resources, necessitating high-performance computing tools that were not available for this work.

5.3.2 Effect of toroidal spectrum symmetry

The impact of wave propagation direction under ITER-relevant conditions in the orbit following Monte Carlo codes is investigated here by comparing the results of ASCOT-RFOF simulations performed considering positive and negative toroidal mode numbers. So far, only results obtained with a positive toroidal spectrum number ($n_\phi = +35$) have been discussed. Additional ASCOT-RFOF and FOPLA simulations are then performed using the negative toroidal component $n_\phi = -35$. For ASCOT-RFOF, different values of $TMAX$ are analysed also with negative n_ϕ, particularly for 0.1 s, 0.5 s and 2.0 s. The results obtained for negative n_ϕ differ substantially from those with a positive toroidal number. In particular, no particle losses are observed in the negative n_ϕ cases. Theoretically, given that ITER has the same plasma current direction as JET, wave propagation with $n_\phi > 0$ corresponds to counter-current propagation and induces outward particle drifts, whereas $n_\phi < 0$ leads to inward drifts (see equation 2.45). As a result, the negative n_ϕ configuration should yield improved confinement and no wall losses, in agreement with the simulation results. The corresponding normalized deposition profiles after collisions obtained for both $n_\phi = \pm 35$ are shown in figure 5.25 (only results at $TMAX$ = 2.0 s are reported). The ASCOT-RFOF profiles are different between the two n_ϕ cases: while for the positive n_ϕ case (see fig. 5.25a) a major peak at $\rho_{\text{tor}} \sim 0.38$ and a smaller one at $\rho_{\text{tor}} \sim 0.18$ are observed, the negative n_ϕ case (see fig. 5.25b) presents two distinct lower peaks, located at $\rho_{\text{tor}} \sim 0.3$ and $\rho_{\text{tor}} \sim 0.6$. For the $n_\phi = -35$ case, the peaks remain stable over the particle tracking time and coincide with regions of increased particle density, as confirmed by the relative R, z particle distributions shown in figure 5.26. The energy distribution for $n_\phi = -35$, reported in the right plot of figure 5.26, strongly exceeds the 3.5 MeV value assumed as the energy limit in the representation.

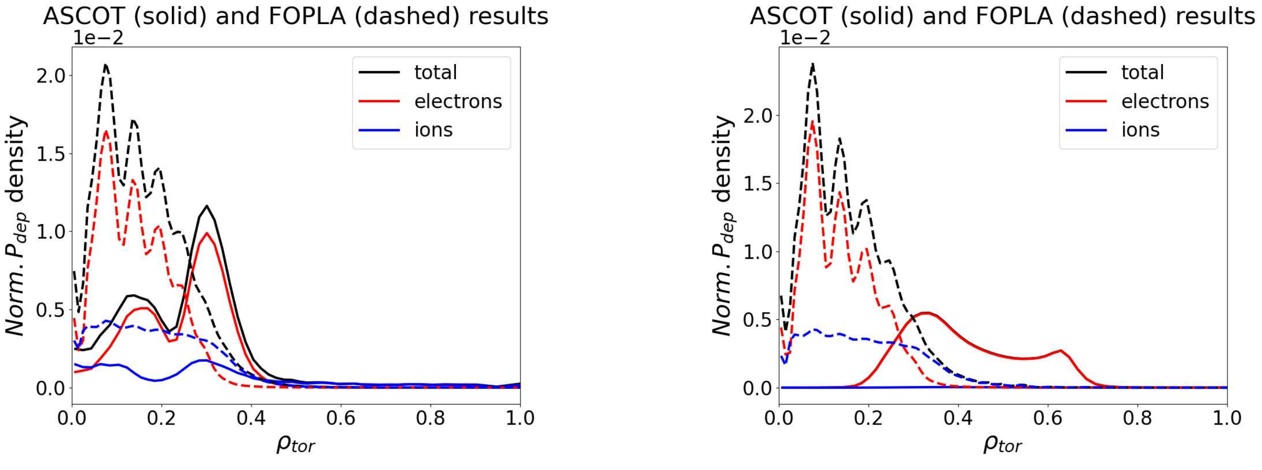

(a) Positive n_ϕ

(b) Negative n_ϕ

Figure 5.25: Normalized deposited power density profiles after energetic particle slowing down computed by ASCOT-RFOF (solid lines) for the positive (a) and negative (b) n_ϕ cases at $TMAX$ = 2.0 s, compared with the relative positive and negative n_ϕ simulations performed with FOPLA (dashed lines). The power deposited to electrons and ions is represented respectively by the red and blue curves, the total contribution instead with the black lines.

In table 5.3, the power fractions between electrons and ions are reported for the ASCOT-RFOF $TMAX$ = 2.0 s case, to be compared with the specular case with positive n_ϕ. The power deposited to electrons and ions is significantly different, presenting a ratio between electron and ion heating of 90:10 for $n_\phi = +35$ against 99:1 for $n_\phi = -35$. However, unlike the positive n_ϕ case, all particles remain confined when using the negative toroidal mode number. This is in agreement with the JET experiment, which proved the different confinement properties when using negative and positive

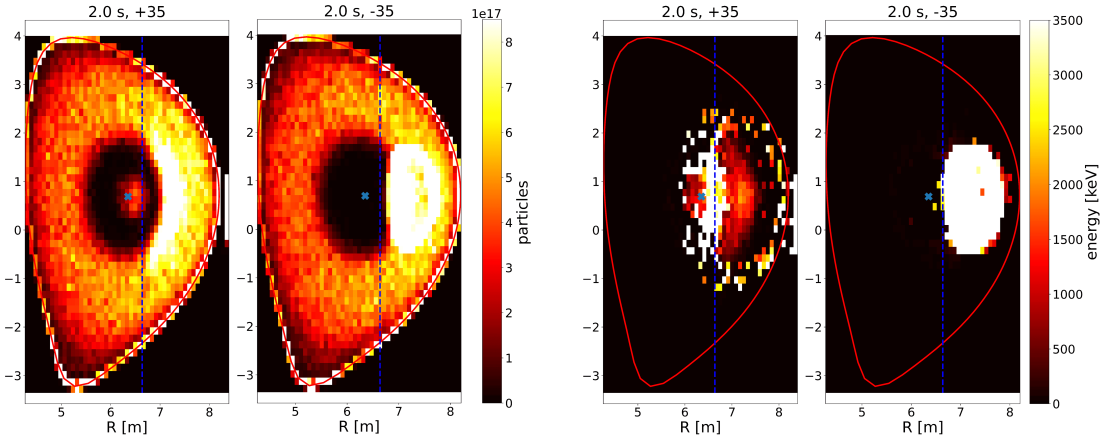

Figure 5.26: Particle (left) and energy (right) distributions from ASCOT-RFOF in the R, z phase space for positive and negative n_ϕ at the same *TMAX* = 2.0 s.

n_ϕ [67]. The energy hot tails obtained for negative n_ϕ are reported by dashed lines in figure 5.22. These tails show a larger population of particles at high energy (> 2 MeV) than the relative positive n_ϕ tails, indicating an improved confinement for highly energetic particles. While the direction of the particle orbit drift and the associated confinement trends are correctly captured, the incorrect magnitude of the response, in terms of integrated power deposition and ratio of power to electrons and ions, suggests that the current ASCOT-RFOF actor implemented in IMAS does not correctly simulate the various steps of ICRH absorption and successive energetic particle slowing down under ITER conditions.

A simulation including both positive and negative toroidal mode numbers simultaneously were also performed. Such simulation combined together the *waves* IDS input obtained by CYRANO simulations, performed separately for the $n_\phi = +35$ and $n_\phi = -35$ cases. Although the electric fields associated with positive and negative toroidal wave numbers can be linearly superposed, the kinetic response of the plasma is non-linear in the distribution function. Therefore, the ASCOT-RFOF simulations already available with single n_ϕ analysis cannot be combined a posteriori. The symmetric simulation, however, do not yield a physically consistent power deposition. Rather than resolving the discrepancies observed in single n_ϕ cases, the symmetric spectrum further increases the sensitivity of the results to modelling assumptions. Despite the limitations discussed in section 5.2 and further analysed in section 5.3.3, alternative *wave* IDS inputs could be explored, for instance, those provided by the TORIC wave code [122], which, differently for FOPLA, includes the physics for simultaneously considering positive and negative n_ϕ. Such a comparison would help separate the issues related to modelling assumptions from potential numerical issues.

5.3.3 Issue of the current IMAS orbit-following ASCOT-RFOF actor

Despite some of the results presented so far are in agreement with the known energetic particle physics, issues of the current ASCOT-RFOF IMAS implementation are now discussed. The most critical one concerns the power deposited through Coulomb collisions, which is found to exceed the absorbed wave power, both when increasing *TMAX* and when considering positive or negative n_ϕ. The integrated values reported in table 5.3, for both absorbed wave power (P_{abs}) and deposited power (P_{dep}), clearly indicate this inconsistency. Two possible explanations, already discussed in JET, are here discussed further and left for future investigation:

- The present study treats the initial set of markers which will be accelerated by the RF wave as a population ($[w_i]$ = #particles) rather than a continuous source ($[w_i]$ = #particles/s). In ASCOT NBI simulations, markers typically represent particles injected per unit time. Although corrections are applied in the post-processing phases, e.g. when calculating distributions by dividing for t_{glob}, this difference may affect the time evolution computation of collisional processes during the simulation and require further revisions of the ASCOT–RFOF code for thermal particle population modelling.

- The very high-energies reached by some particles may play a role in the discrepancy, as already discussed for JET. In the present ITER simulations, a non-negligible fraction of markers reaches energies above 10 MeV (6% in $TMAX = 0.5$ s and 12% in $TMAX = 2.0$ s), where hydrogen ions start to become relativistic, with a velocity close to the speed of light ($\sim 4.3 \times 10^7$ m/s, with $\gamma = \frac{1}{\sqrt{1-\frac{v^2}{c^2}}} = 1.010$). Similar fractions of 10 MeV energetic particles are observed for both positive and negative n_ϕ, but the discrepancy between absorbed wave power and deposited power is significantly larger for the negative n_ϕ case, as well as the power ratio between electrons and ions. This indicates that such energetic ions are unlikely to be the primary cause of the energy conservation issues in ASCOT–RFOF.

The issues identified in this section indicate that the present ASCOT–RFOF IMAS implementation, when applied to thermal population in ITER-relevant ICRH conditions, is not suitable for self-consistent steady-state studies yet. While the orbit-following description correctly captures key physical mechanisms, such as finite orbit width effects and wave–particle resonance dynamics, the combination of the treatment of markers as a particle population, long interaction times, and the generation of very energetic particles leads to fundamental inconsistencies in the interpretation of collisional power deposition. These findings do not invalidate the orbit-following approach itself nor ASCOT-RFOF applications under different modelling framework, but rather highlights that the ASCOT-RFOF actor currently available within IMAS, and coupled to CYRANO full-wave code, requires further attention and development.

5.4 Conclusions of the chapter

This chapter presented the first use and critical discussion of the ASCOT–RFOF orbit-following code within the IMAS environment for modelling the interactions between ICRF waves and thermal particle population. After introducing the computational workflow and the development and validation of the THED-G tool for thermal marker generation, ASCOT–RFOF results have been shown for two different scenarios. A JET discharge was used for parameter sensitivity analyses and validation against established reduced-modelling tools, while an ITER half-field scenario was considered to explore the behaviour of orbit-following ICRH modelling under reactor-relevant plasma conditions. Together, these studies provided a detailed assessment of the capabilities and limitations of the current IMAS ASCOT–RFOF actor available for ICRH modelling.

The validation against JET available modelling and the exploratory ITER study show that ASCOT–RFOF captures the RF absorption mechanisms including finite orbit width effects that are absent in the currently available reduced modelling approaches. In contrast, substantial inconsistencies are instead observed on the collisional power deposition interpretation. These are shown by a lack of energy conservation, in both JET and ITER cases, and as significant discrepancies in the ratio of power between electrons and ions during the collisional relaxation. The inherently differences in modelling approach between analytical solver and orbit-following method do not permit to establish a correct result to aim at, particularly for ITER. Several hypotheses were initially proposed to explain model discrepancies, including the influence of rare high-energy particles arising from limited marker statistics, the use of asymmetric toroidal wave spectra, and the treatment of the initial thermal markers as a particle population rather than as a continuous source. Improved statistics and toroidal mode number effects were explored in the ITER modelling. However, the identified issues were not mitigated and were instead amplified when considering the long wave–particle interaction timescale of ITER plasmas or symmetric spectra. The generation of highly energetic ions approaching relativistic velocities and too large power deposition observed in the ITER simulation suggest that the treatment of the time evolution in population-based simulations may be the main trigger of the discrepancies observed.

The findings of the present ICRH modelling activities indicate that the current ASCOT-RFOF IMAS implementation is not suitable for steady-state predictive studies yet, neither in JET nor ITER. Progress in this direction will require further development of the existing implementation, for instance by reformulating the orbit-following RF algorithm in terms of particle sources rather than particle populations when studying thermal particles. An additional contributing factor may be related to the choice of waves input. Exploring alternative wave codes to provide the required waves input represents a complementary strategy for addressing the present limitations. Moreover, the use of a different Monte Carlo orbit-following code, such as SPOT [101], which is capable to handle distribution functions in time-dependent simulations, could provide another viable solution.

CHAPTER

6

SYNERGY BETWEEN NEUTRAL BEAM IONS AND ICRF WAVES IN ITER-RELEVANT PLASMAS

The wave-particle interaction between IC waves and beam fast ions can lead to the formation of high energy ion tails, with energies exceeding those of injected particles. Under suitable conditions, the generated hot ion energy tail can enhance the fusion reaction rate, as experimentally demonstrated in JET [64] and impact the impurity transport, in particular for tungsten [123]. Previous investigation [89] of NBI–ICRH synergy in ITER for a deuterium–tritium baseline scenario has shown that the synergy between deuterium beams and IC waves operating at the fundamental deuterium resonance is relatively weak in ITER, likely due to the low fast-ion density associated with neutral beam injection at higher energies. Therefore, in ITER, given the large size and the high beam particle energy, NBI–ICRH synergy is expected to affect fast-ion dynamics and power redistribution rather than lead to substantial improvements in plasma fusion performance. The study presented in this chapter evaluates the impact of different beam configurations and wave parameters on the NBI-ICRH synergistic effects in a full field ITER deuterium-tritium scenario, which is presented in sec. 6.2. This scenario is similar to scenarios that will characterize the DT-1 phase of the ITER research plan [22]. The aim is to identify which parameters maximize the interaction between beam particles and waves, investigating the implications on energetic-particle dynamics and possible modifications to fusion performance. The analysis focuses on parameters known to influence the synergy, namely the ICRH frequency and the NBI-to-ICRH input power ratio [124, 125]. In addition, the impact of the NBI geometry is examined, taking advantage of the flexibility in terms of beam line vertical tilt of the ITER NBI system. The modelling framework applied for this investigation is introduced in section 6.1. The parametric scans on wave frequency, beam injection geometry and NBI/ICRH power ratio are respectively presented in sections 6.2.2, 6.2.3 and 6.2.4. Finally, the fusion power is estimated for the most interesting cases observed during the parametric scan, and the results are discussed in section 6.2.5.

6.1 Modelling framework for NBI and ICRH synergy

Accurate simulations of the synergy between the NBI and ICRH require modelling of both beam particles generation and their slowing down as well as the computation of the RF wave fields and their interaction with the plasma and energetic particles. The principle behind the adopted workflow is the following. First, neutral beam injection alone is simulated by employing a NBI source code, and the results is then used in a Fokker-Planck solver to calculate the distribution function of injected ions. This distribution function is subsequently used in a full wave solver to calculate the ICRF wave field and how both fast and background particles interact with the waves. Finally, the wave field is considered as input into a Fokker-Planck solver that calculates the distribution function of the beam and background ions accelerated by the ICRF waves. This approach remains a reasonable approximation, as the wave field is computed without incorporating the full distribution function, i.e. the one including ICRF acceleration. For low to moderate ICRH power levels, reliable results are expected. The same modelling approach for NBI and ICRH synergy is considered in the Heating & Current Drive (H&CD) workflow [89]. While electron cyclotron heating and alpha-particle contributions can also be included within the H&CD workflow, they are here ignored to simplify the modelling case. In the following analysis, the NBI modelling is performed through BBNBI and ASCOT codes, respectively for the beam ionization and slowing down. ASCOT provides the slowing down distributions, stored in the *distributions* IDS, which is needed as input for the wave interaction calculation. The full-wave CYRANO code is applied for evaluating the electric wave field components and their interaction with all plasma species, e.g. thermal and beam particle population. CYRANO gives as output the absorbed wave power per each species and the wave electric field information in the *waves* IDS. These quantities are then used by the Fokker-Planck solver FOPLA to model the slowing down of IC-accelerated particles. FOPLA indeed computes the one-dimensional distribution functions for all ion species and returns the final distributions in the *distributions* IDS. FOPLA ensures energy consistency with CYRANO: the absorbed wave power reported by CYRANO is fully accounted for in the Fokker Planck solver, which then provides information on synergy effects and fusion power estimates. This modelling approach has been successfully applied in previous synergistic studies for both ITER [89] and JET [64, 116]. A schematic representation of the numerical workflow adopted in this analysis is shown in figure 6.1, reporting also the required inputs and outputs within the IMAS framework.

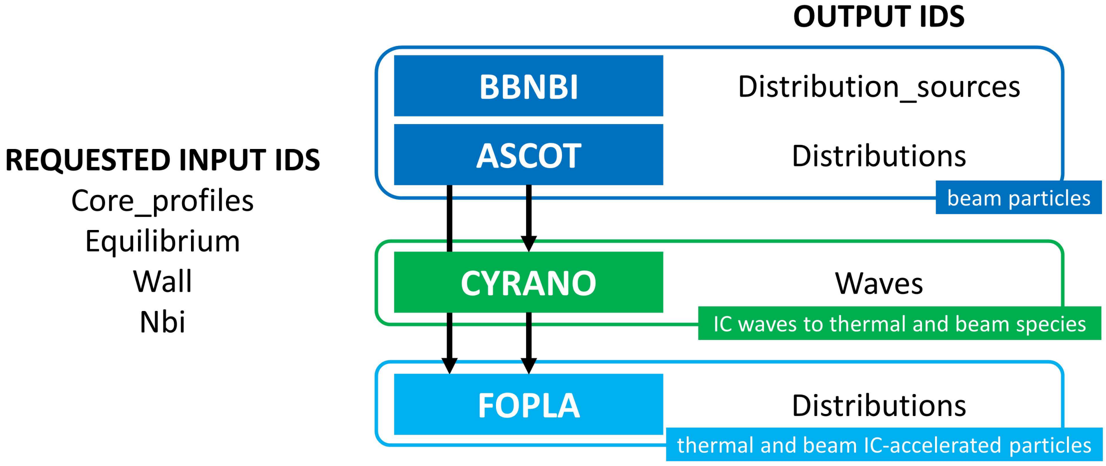

Figure 6.1: Numerical workflow applied for the NBI and ICRH synergy analysis of a DT-1 ITER plasma within the IMAS framework.

The density and temperature profiles, stored in *core_profiles* IDS, are kept unchanged during NBI-ICRH synergy simulations. Nevertheless, the effects of NBI and ICRF heating on the plasma are already incorporated into these profiles. This approach allows to isolate wave–particle interaction effects and power redistribution mechanisms. Achieving a fully self-consistent treatment, e.g. including the feedback of modified heating on turbulent transport, confinement, or current profile evolution, would require additional transport simulations based on the outcomes of the present analysis. Such investigation, however, is beyond the scope of this work. The ASCOT-RFOF code was initially considered computing the final distribution functions of IC-accelerated beam and thermal particles.

This would have allowed to improve the workflow e.g. by including the orbit width effects, which could be significant at the considered EP energies, and thus obtain a more realistic description of the NBI-ICRH synergy in ITER. However, due to the limitations on the current ASCOT-RFOF implementation, discussed in chapter 5, the FOPLA slowing down solver is used. As a consequence, orbit width effects are neglected here.

6.2 Parametric dependence of NBI–ICRH synergy in ITER

This section presents the parametric study performed on an ITER DT baseline plasma [22] to investigate how different beam and wave parameters affect the NBI-ICRH synergy. The strength and characteristics of the beam-wave interactions depend indeed on several factors. The frequency of the launched ion cyclotron waves determines the radial location of the resonance and can therefore have an impact on the efficiency of the wave-beam particle interaction [124]. From a similar perspective, the NBI geometry may modify the spatial overlap between the fast-ion population and the wave absorption region, thereby affecting the resulting synergy. Another important aspect concerns the ratio of deposited power on electrons and ions. This ratio, which has been shown to play a role in e.g. impurity transport phenomena as observed in devices such as ASDEX Upgrade [123], is influenced by the mix of ICRH and NBI auxiliary input power. In particular, the NBI-to-ICRH (NBI/ICRH) power ratio affects the energy and density distributions of the fast-ion population. The plasma composition, in terms of impurities and majority ion concentrations, influences the NBI-ICRH synergy too, as shown in [124, 125].

6.2.1 Reference case

The scenario here analysed corresponds to a baseline ITER full-field deuterium–tritium plasma, characterised by a toroidal magnetic field $B_{\text{tor}} = 5.3$ T and a plasma current $I_{\text{p}} = 15$ MA. The plasma equilibrium and kinetic profiles for the entire discharge are modelled by JETTO 1.5D integrated transport solver [126], coupled to the TGLF quasilinear turbulence model [127]. The present analysis focus on the time slice t = 180 s, corresponding to the scenario flat-top phase with a total auxiliary heating power of 70 MW, which is subsequently reduced to 50 MW in order to meet the Q = 10 operational target. The input kinetic profiles considered are shown in figure 6.2 and the 2D axisymmetric equilibrium is refined by the CHEASE code [108]. The plasma is composed of deuterium and tritium ions with relative concentrations of 56:44, respectively. Tungsten impurity is included to take into account the source from the ITER first-wall, with a concentration of $n_W/n_e \sim 5 \times 10^{-5}$, consistent with the predictions discussed in [128]. The auxiliary heating is provided by a mix of ECRH, ICRH and NBI, with an injected power of 28.5 MW, 8.5 MW and 33 MW respectively. Deuterium beams are injected at an energy of 1 MeV through two NBI systems, set with the reference injection configuration (OFF-ON axis beam [83]), each delivering 16.5 MW of power. For the present plasma conditions, characterized by a line averaged electron density of $\langle n_e \rangle_{\text{line}} = 1.078 \times 10^{20}$ m^{-3} and a density peaking factor of $n_{\text{pf}} = 1.4$, no shine-through losses are expected according to equation (1) of [35]. This is confirmed by a BBNBI simulation, executed with 10^6 markers.

The resulting fast-ion slowing-down distributions, computed using the ASCOT code, provides the energetic particle populations employed in the NBI–ICRH interaction analysis. ASCOT predicts that the 69% of power is transferred to the electrons and 31% to ions, with negligible orbit losses. The deuterium beam particles experience wave-particle interaction when ICRH is applied at the proper resonance. The ICRH system operates here in the fundamental deuterium majority scheme (D1). This scheme is usually inefficient because of the screening effect from the majority background ions [60]. However, its effectiveness increases as the deuterium content is reduced in favour of another main ion species, as in this case, were T is present with 44% of concentration. The toroidal mode number of launched waves is $|n_\phi| = 35$, and the IC wave frequency is 41 MHz, which guarantees a central absorption by the deuterium particles. The locations of the various ion cyclotron resonances for

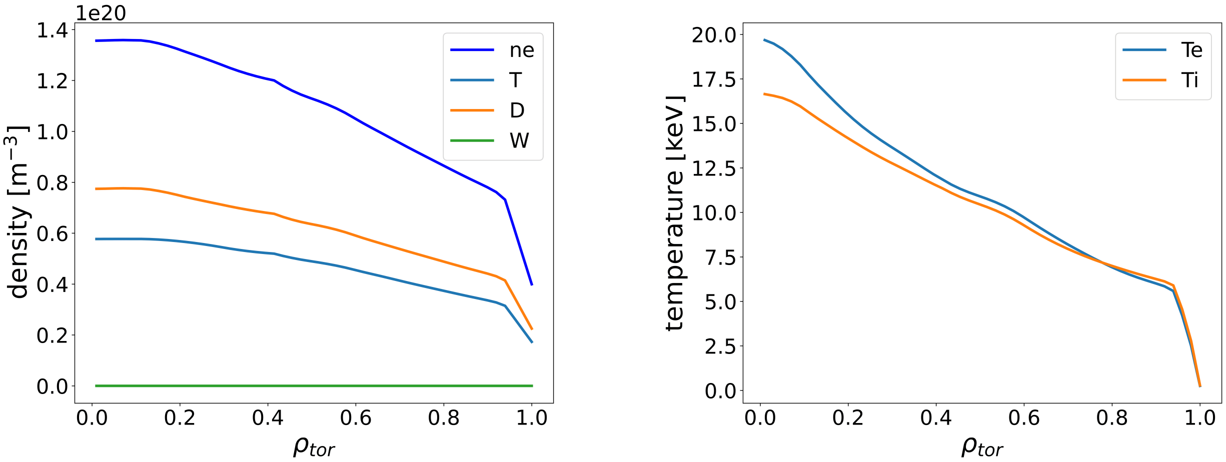

Figure 6.2: Radial kinetic profiles as a function of the toroidal flux coordinate ρ_{tor} for the DT ITER plasma considered in the NBI–ICRH synergy study.

this simulation case are shown in figure 6.3. Due to their energy, beam particles are affected by a higher Doppler shift (see section 2.4.2). As a result, beam ions can satisfy the resonance condition on a broader radial region, represented in figure 6.3 by the shaded area around the D1 resonance, computed considering the Doppler shift affecting a 1 MeV deuterium particle for both $n_\phi = \pm 35$.

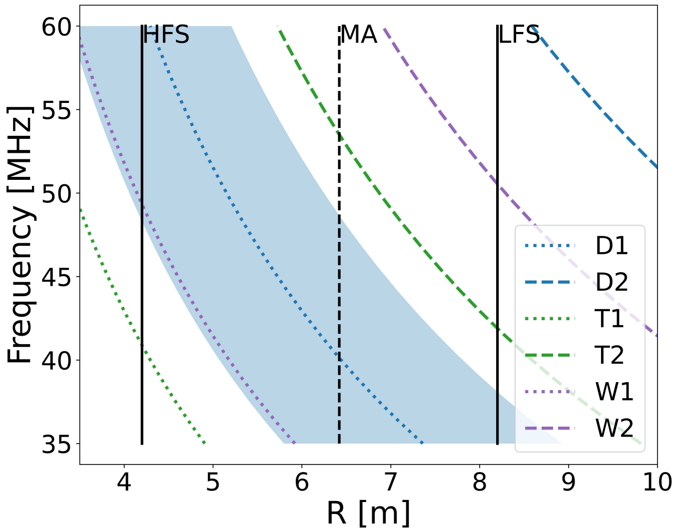

Figure 6.3: Radial locations of the ion cyclotron resonances for the analysed ITER scenario. The D1 scheme is the reference configuration, while at higher frequencies the T2 scheme becomes relevant for central absorption. The shaded region around the D1 resonance indicates the resonance domain accessible to 1 MeV deuterium beam ions due to Doppler-shift effects. Solid black lines denote the low-field-side (LFS) and high-field-side (HFS) boundaries, while the dashed line marks the magnetic axis.

CYRANO predicts that deuterium ions absorb about $\sim 39\%$ of the wave power, including $\sim$2% absorbed by the D beam particles. The remaining power is absorbed by the electrons. Beam wave power absorption is therefore weak, in agreement with results presented in [89] for a similar ITER plasma. Looking at figure 6.3, tungsten (W) ions may, in principle, absorb a fraction of the ICRH power through the fundamental minority scheme (W1) at low IC frequencies. However, the very low tungsten concentration in this plasma, makes W wave power absorption negligible. Tungsten impurity therefore has a smaller impact on ICRH power absorption than Beryllium, which has been shown to account for approximately $\sim 5\%$ of the absorbed power in similar scenarios [89]. In the present case, the considered tungsten charge state is $Z_W = 74$. Given the wide range of tungsten charge states expected in fusion plasmas, the case with $Z_W = 46$ has been simulated too, showing a negligible impact of the W charge state on the wave absorption. No differences are observed also in the power deposition obtained from FOPLA simulations, confirming that tungsten effects remain marginal even considering different charge states in case of concentrations in order of 10^{-5}. For the reference case, FOPLA indicates that 69% of the NBI-ICRH deposited power is deposited to electrons, 31% to ions and about 3.37% of the injected NBI-ICRH auxiliary power is lost.

6.2.2 Role of ion cyclotron wave frequency

As described in equation 2.40, by increasing the IC wave frequency ω, the radial position R_{IC} of the resonance layers is moved towards the HFS of the torus, as seen in figure 6.3. For this scan, the wave frequency is explored within the available range of frequencies of the ITER ICRH antenna, [40; 55] MHz, with values of: [40, 41, 42, 43, 46, 46.5, 47, 47.5, 48, 48.5, 49, 51, 43] MHz. More values around 47 MHz have been simulated because of the appearance of a peak on the D beam absorption around these frequencies. The standard injection geometry of the neutral beams is assumed (OFF-ON), as well as the reference NBI/ICRH power ratio, corresponding to 33 MW of NBI power and 8.5 MW of ICRH power (denoted as 33/8.5). As first result of the scan, figure 6.4 shows the fraction of wave power absorbed by the species composing the plasma, obtained from CYRANO simulations.

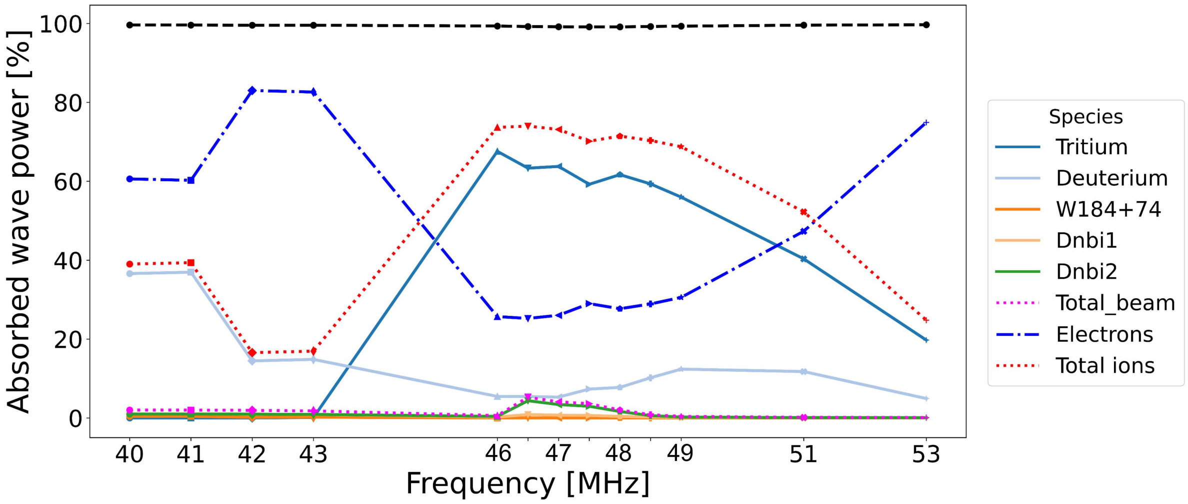

Figure 6.4: Fractions of wave power absorbed by different species computed by CYRANO while changing the frequency of the launched IC waves from 40 to 53 MHz. The dotted red line represents the sum of wave power absorbed by all the ions, while the dotted purple line the total wave power absorbed by the beam EPs, separated by the OFF axis beam (Dnbi1) and ON axis beam (Dnbi2) lines. The dotted-dashed blue line represents the fraction of power absorbed by the electrons.

At maximum Deuterium (D) absorption ($\sim$ 37% at 41 MHz, reference case), D beam ion absorption is about 2% of the total wave power. The two beams absorb the same amount of power. At higher frequencies, the tritium absorption becomes dominant over the ion species ($\sim$ 20% at 53 MHz). At 53 MHz, the heating scheme is the second harmonic of tritium (T2) and the thermal deuterium still absorbs a small fraction of the injected power ($\sim$ 5%), while negligible amount of power is absorbed by D beam ions. For both D1 and T2 schemes, corresponding to 41 and 53 MHz wave frequencies, most of the power is absorbed by electrons ($>$ 60%), but, even if in a smaller fraction, the power absorption from ions is located in the plasma core. At intermediate frequency values, from 46 MHz to 49 MHz, the beam particles increase their absorption, reaching a maximum of about 5% at $\sim$ 46.5 MHz in total. The larger absorption is onto one beam, i.e. the ON axis beam (Dnbi2 in the figure 6.4), reaching 4.4% of the total absorbed wave power. This shift in frequency in the wave absorption from the beam particles is likely due to the larger Doppler shift effect of energetic particles. This changes the spatial location of the resonance, as discussed above (see fig. 6.3). Speaking of the power redistribution after EPs collisional slowing down, the majority of the auxiliary power delivered to the system is deposited to electrons, for all the frequencies analysed. This is clearly shown in figure 6.5, which represents the cumulative deposited power deposited to ions (solid lines) and electrons (dashed lines) for each case. The largest fraction of power deposited to ions is observed in the frequency range that maximize the beam EPs wave power absorption, namely between 46 and 49 MHz. At this frequency range, the tritium absorption plays an important role, reaching its maximum of ∼67% at 46 MHz and dominating the ion power deposition in this frequency range.

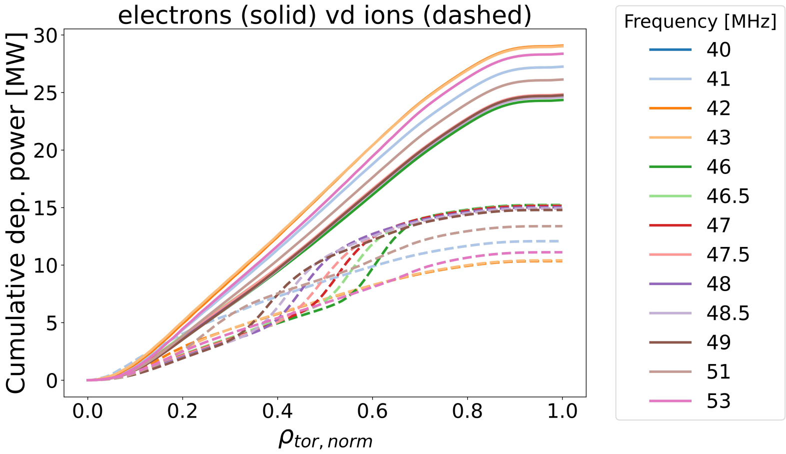

Figure 6.5: Radial profiles of the cumulative power transferred by Coulomb collisions to electrons (solid lines) and ions (dashed lines) for all the RF wave frequencies analysed.

Three representative frequencies are now selected to compare the wave RF absorption and power deposition: 41 MHz, which corresponds to the reference case and central D absorption; 46.5 MHz, that presents the highest D beam EPs absorption; and 53 MHz, which represents the central T2 heating. The radial profiles of power absorption and deposition for these cases are reported in figure 6.6, respectively on plots 6.6a, 6.6b and 6.6c. The histograms reported on the left of figures 6.6a-6.6c represent the 2D particle distribution of the beam EP population at a steady state obtained from ASCOT. The positions of the resonance layers of thermal D, D beam (Dnbi) and thermal T ions at different wave frequencies are also included to be compared with respect to the particle distributions.

41 MHz (fig. 6.6a) Central absorption of deuterium dominates, affecting also the power deposition. The beam particles and thermal tritium are not involved in the absorption mechanism: the beam resonance is in the low field side of the plasma, where the beam particle population is small, while the tritium resonance is outside the tokamak.

46.5 MHz (fig. 6.6b) Both D beam EPs and thermal tritium ions become resonant. The beam population absorbs ∼ 5% of wave power, in a region peaked at $\rho \sim 0.2$, while tritium presents the largest absorption (∼ 63%), localized towards the edge of the plasma. Thermal D absorbs 5.4% in a region peaked at $\rho = 0.4$, likely due to the large population of beam markers close to the resonance D layer. The energy of the beam markers indeed covers a spectrum from thermal to injection energies, explaining why beam markers can still resonate at the D resonance layer. In the power deposition profiles, a central peak appears at $\rho \sim 0.2$ due to the beam ion wave absorption power, while a second, more peripheral peak around $\rho \sim 0.6$ is due the contribution of tritium absorption.

53 MHz (fig. 6.6c) Tritium absorption dominates over the ions in the core (∼ 20%). No beam EP absorption is predicted and a small amount of power absorbed by thermal deuterium is observed on the LFS of the tokamak (5%). Deposition profiles show that the power is distributed over all the plasma, mainly to electrons, with a smoothed peaked central heating on ions.

The presence of modest D beam EP absorption at 46.5 MHz can be explained by the spatial overlap between a strong $|E_+|$ field amplitude region and the resonance layers of D beam ions. The amplitude and spatial structure of the left-hand $|E_+|$ electric field component at the midplane ($z = z_0$) are shown in figure 6.7 for the three selected cases, with the radial locations of the ion cyclotron resonance layers of thermal D, D beam EPs (Dnbi) and thermal T species superimposed to the field profiles. From figure

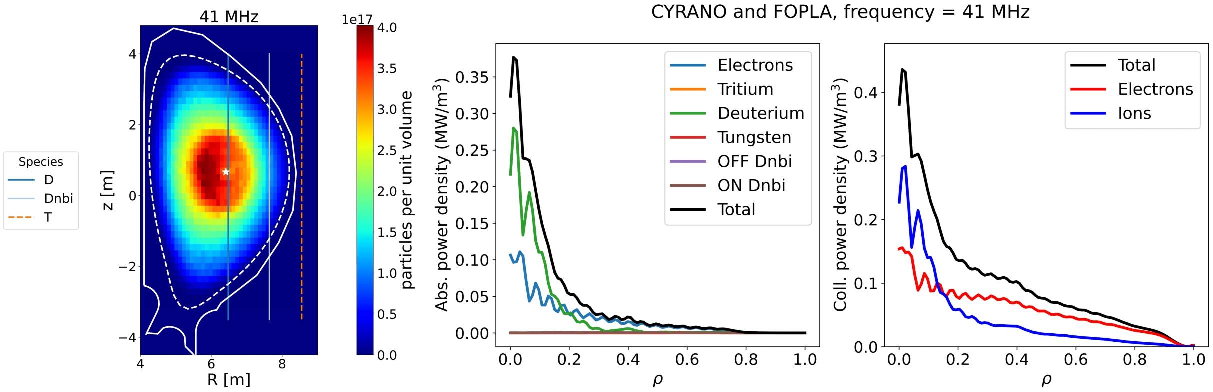

(a) Results for 41 MHz case.

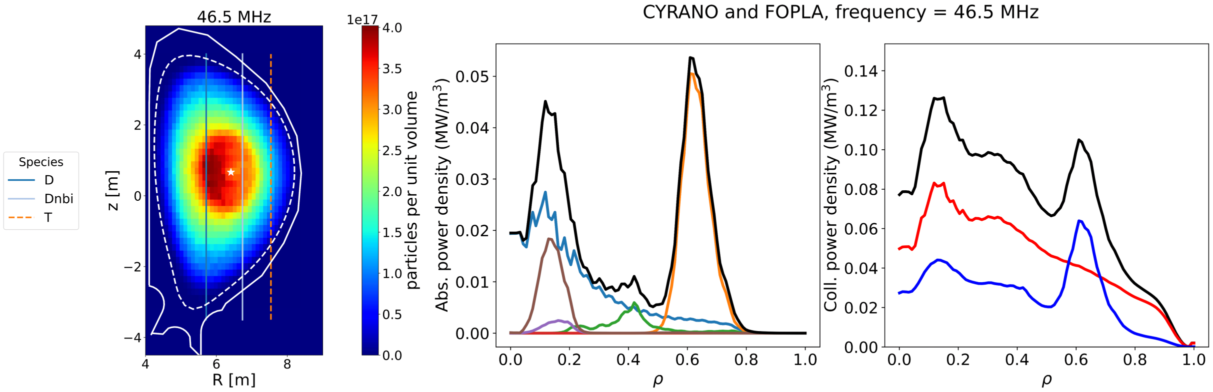

(b) Results for 46.5 MHz case.

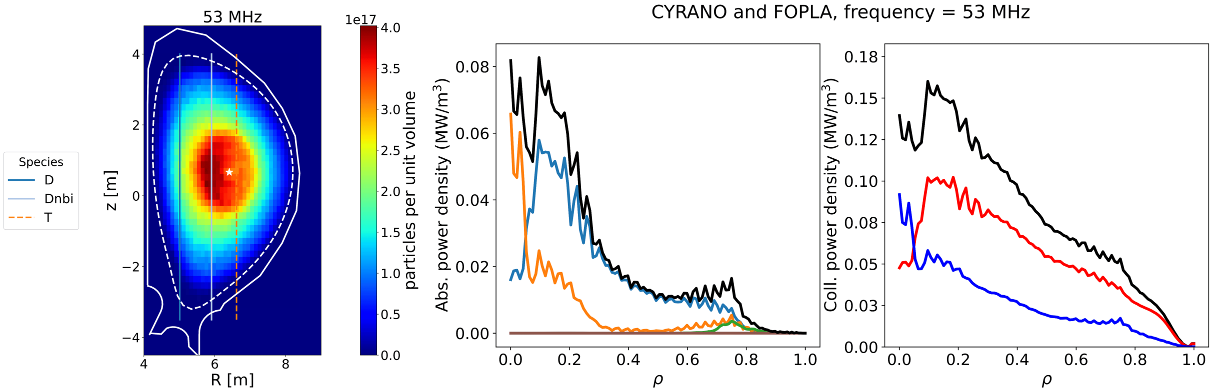

(c) Results for 53 MHz case.

Figure 6.6: Figures 6.6a, 6.6b, 6.6c differ by the RF wave frequency ω. The colour coding of the curves plotted is presented in figure 6.6a (Left) Spatial distributions of the beam energetic particles in R, z phase space obtained from ASCOT simulations before any interaction with the RF wave. The ion cyclotron resonance layers of the main absorbing species (thermal deuterium in solid blue, beam deuterium EPs in solid light blue, and thermal tritium in dashed orange), are also represented. (Central) Radial profiles of absorbed wave power density calculated using CYRANO. The sharing of power among all plasma species is shown. (Right) Radial profiles of deposited power density calculated using FOPLA. The contributions to electrons (red line), ions (blue line), and the total power (black line) are reported.

6.7, it is clear that the $|E_+|$ amplitude for the intermediate frequency case is higher than the other cases and coincides with the D NBI resonance location. This indicates that the acceleration of ions with energies of the order of the injection energy is more effective than that on thermal deuterium. In general, the overlap between the $|E_+|$ field and the resonance layers varies significantly with frequency.

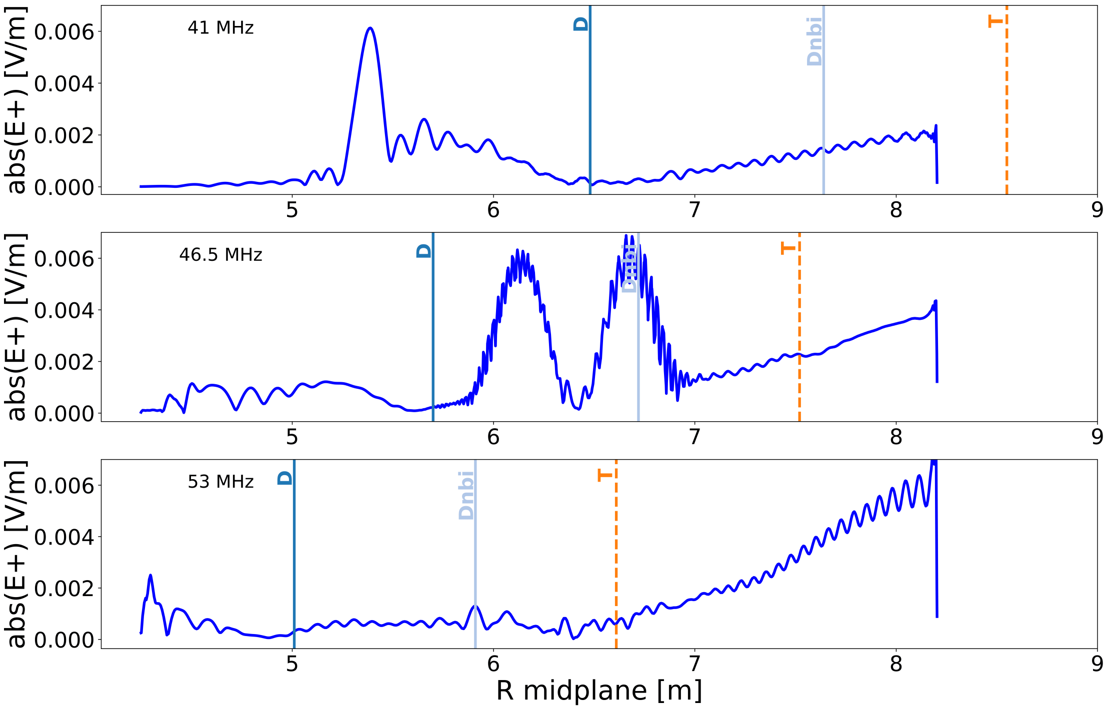

Figure 6.7: Left-hand $|E_+|$ polarized component of the RF wave electric field at the midplane (z = z_0) for three different wave frequencies: 41 MHz (top), 46.5 MHz (middle), 53 MHz (bottom). The resonance layers of thermal deuterium (D), deuterium beam energetic particles at 1 MeV for $n_\phi = +35$ (Dnbi) and thermal Tritium (T) are reported too. Solid lines represent the fundamental resonance locations, while dashed lines the second harmonic scheme.

6.2.3 Influence of neutral beam injection geometry

The wave frequency case with the largest D NBI absorption, i.e. 46.5 MHz, is now considered for the scan on the NBI geometry. As already seen in sec. 4.3.2, the ITER neutral beam injection system offers the flexibility to vertically tilt the injection direction of each beam line between two boundaries called ON-axis and OFF-axis configurations. This capability motivates the interest in assessing the effect of the NBI geometry on NBI–ICRH synergy [83]. As already discussed in chapter 4, where a clear representation of the NBI configurations is reported in figure 4.20 (for a different scenario), changes in the injection geometry lead to modifications of the fast-ion slowing-down distributions. The ASCOT distribution functions used as input for the CYRANO and FOPLA simulations show some variations in energy, pitch, and spatial distributions among the different injection configurations. Figure 6.8 compares the energy (left) and pitch (right) distributions of steady-state beam energetic particles for the ON–ON and OFF–OFF NBI configurations. In both cases, the energy spectrum covers a range from thermal energies up to the injection energy (1 MeV), presenting a peak in particle energy at about $\sim$ 150 keV. The overall spectral shape remains very similar between the two simulations. The pitch distributions in both cases are strongly asymmetric, characterised by a peak at positive pitch values. In the ON-ON configuration, more markers exhibits a positive pitch than OFF-OFF case. Differences among the injection geometries become more evident when examining the spatial distribution of beam ions. Figure 6.9 shows the fast-ion distribution functions in the R, z space for the three configurations considered, together with the ion resonance layers computed at a wave frequency of 46.5 MHz. The overlap between the fast-ion population and the resonance layers varies significantly with the injection geometry, with the ON-ON configuration exhibiting the highest fast-ion density at the deuterium beam resonance layer.

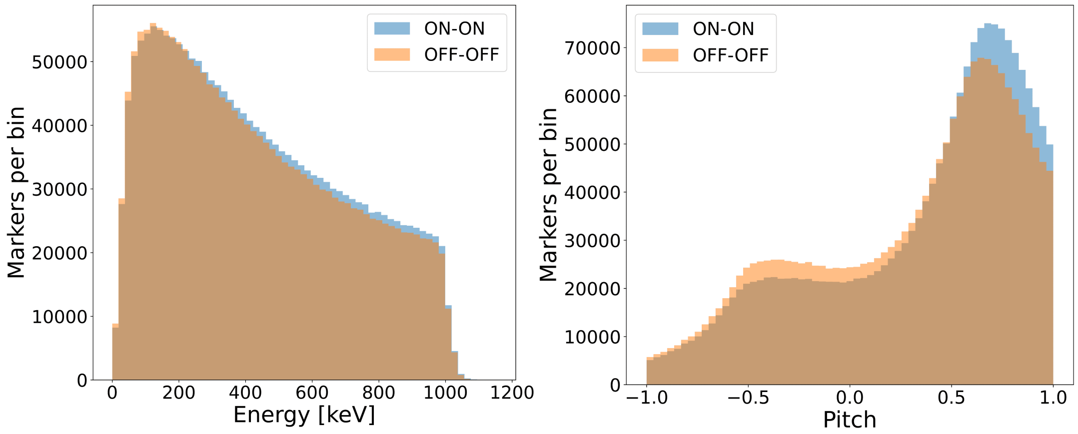

Figure 6.8: Energy (left) and pitch (right) distribution functions of the beam steady state energetic particle population simulated by ASCOT for the ON–ON (blue) and OFF–OFF (orange) NBI configurations.

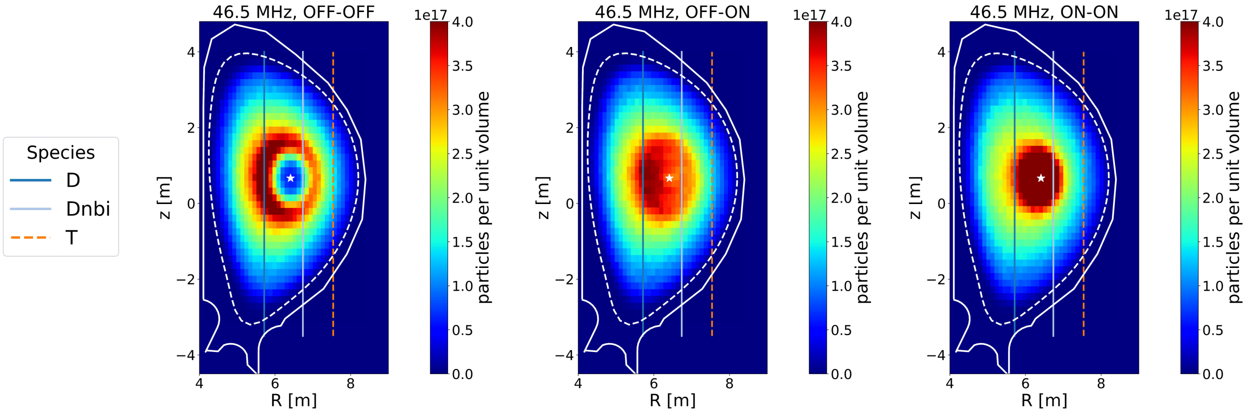

Figure 6.9: Spatial distribution functions of the beam particles in R, z space obtained from ASCOT simulations using the three injection geometries. The ion cyclotron resonance layers of the main absorbing species (thermal deuterium in solid blue, beam EP deuterium in solid light blue, and thermal tritium in dashed orange), computed for an ICRH RF frequency of 46.5 MHz, are reported.

The superposition of beam EP population and RF resonance layers could explain figure 6.10, which reports the fraction of absorbed ICRF power to the plasma species. The observed variations in absorption can be indeed attributed to changes in the fast-ion distributions (figure 6.9). The ON-ON configuration presents the largest D beam EPs absorption, reaching about 10% of absorbed IC power, and a decrease in wave power absorption from thermal D particles. The OFF-OFF configuration shows a much lower beam energetic particle absorption, of the order of 2%, comparable to the reference case at 41 MHz. Finally, the OFF–ON configuration shows an intermediate behaviour. The sharing of deposited power to electrons and ions is not affected by the injection geometry, with approximately 62% of power transferred to electrons and 38% to ions for all the cases. As expected, the ON-ON configuration leads to a more peaked deposition in the plasma core (figure 6.11), because of the high D beam EP absorption. Differences are also observed in the final velocity-space distribution functions f(v) of the beam ions. Figure 6.12 presents the energetic particle density distribution function for one of the two simulated beams (Dnbi2) for the three analysed case.

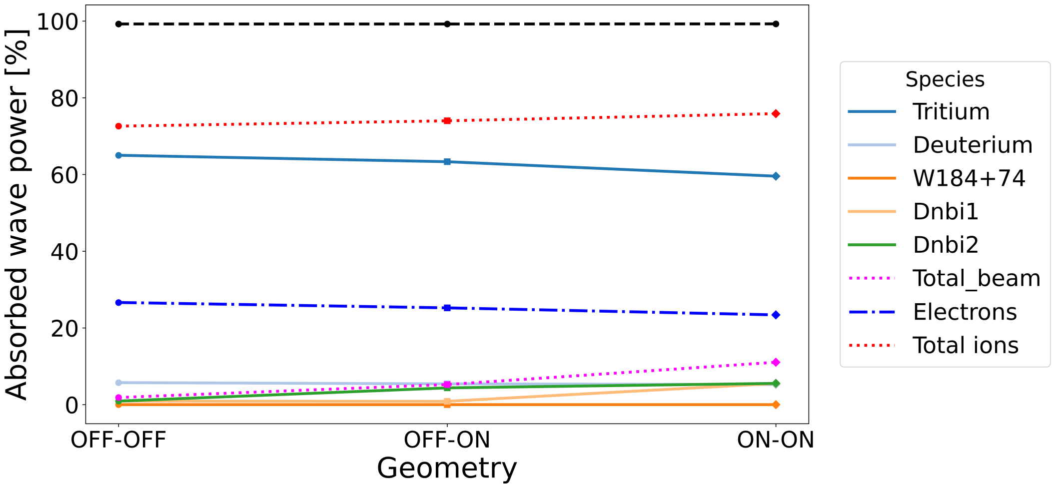

Figure 6.10: Fractions of wave power absorbed by different species, computed by CYRANO considering beam particles originated from different NBI geometries.

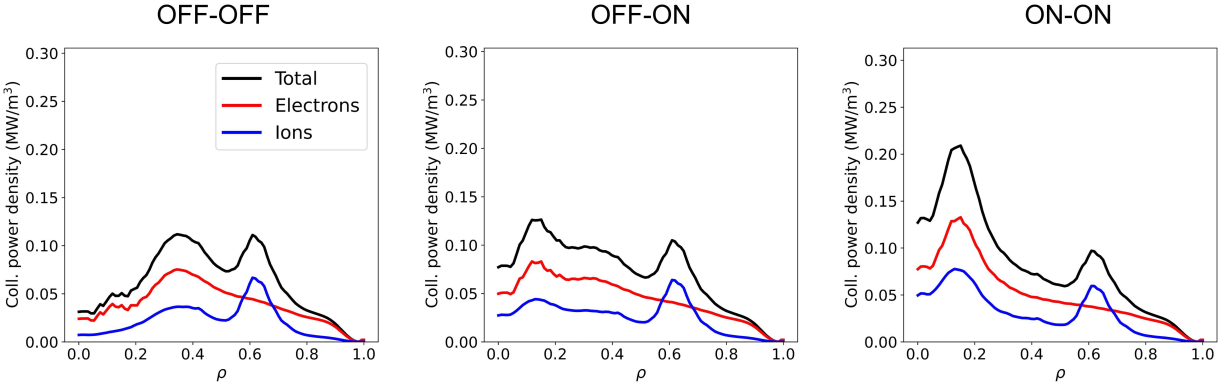

Figure 6.11: Radial profiles of the deposited power densities computed by FOPLA for the three different injection geometries.

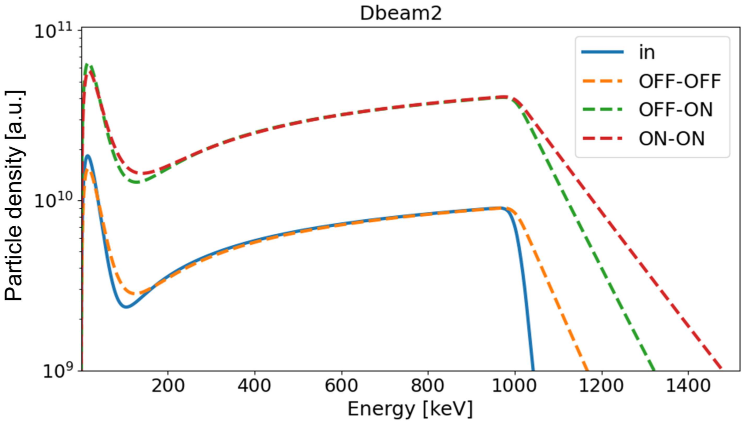

Figure 6.12: Particle density distributions as function of the energy of the deuterium beam ions (Dnbi2) computed by FOPLA for different NBI geometries. The blue curve represents the initial distribution function of beam energetic particles, read from ASCOT for the OFF-ON reference case.

The ON-axis injection consistently results in highest particle density across the energy range, reached through increased IC wave–beam particle interactions, even above the injection energy. The OFF–OFF configuration does not significantly deviate from the initial distribution (in in fig. 6.12). This is consistent with the fact that the RF power absorbed by the beam in this case is very small, and is likely absorbed by already energetic ions, which reach energies above the injection energy.

6.2.4 Effect of the NBI/ICRH power ratio on the energy redistribution

The influence of NBI/ICRH power ratio on NBI-ICRH synergy is investigated by varying the relative power contributions of the two heating systems while keeping the total injected auxiliary power constant. Adjusting this ratio modifies the ratio of the power deposited to electrons and ions. In this study, the redistribution of power between electrons and ions is analysed for three NBI/ICRH power mixes: 27/14.5, 30/11.5, 33/8.5 MW. The total amount of injected power by NBI and ICRH is fixed at 41.5 MW for all cases. The NBI power is progressively increased from 27 MW to 33 MW, with a corresponding decrease of ICRH power from 14.5 MW to 8.5 MW. The NBI energy is increased consistently with the applied power, following the scaling $P_{\mathrm{NBI}} \propto E_{\mathrm{NBI}}^{2.5}$ [81] due to ITER NBI system limitations, injecting therefore 923 keV, 962 keV and 1000 keV, respectively. The results presented in this section are performed considering the standard NBI configuration (OFF-ON) and an ICRH frequency of 46.5 MHz. This wave frequency is selected because it affects more the electron (and ion) power deposition $\mathrm{P}_{\mathrm{dep,e}}$ when varying the NBI/ICRH power ratio compared to e.g. the reference case at 41 MHz, as shown in figure 6.13. In particular, changes in $\mathrm{P}_{\mathrm{dep,e}}$ while varying the NBI/ICRH power mix are approximately of 12% for 46.5 MHz versus about 1% for 41 MHz case. The selection of 46.5 MHz therefore enhances the contrast among the analysed cases and facilitates the interpretation of power redistribution effects. The rapid increase in ion power deposition observed at $\rho \sim 0.6$ is attributed to wave absorption by tritium, as already discussed in section 6.2.2. A no-synergy case is also included in this analysis by summing the power deposited to electrons and ions from independent simulations with only NBI (ASCOT, without waves interactions) and only ICRH (CYRANO and FOPLA without beam ions). This case is reported as a representative case, to show the total contribution to EP dynamics due to separate applications of ICRH and NBI. In the no-synergy case, 59% of the input power is deposited to electrons and 41% to ions, for a total input power equal to 41.5 MW.

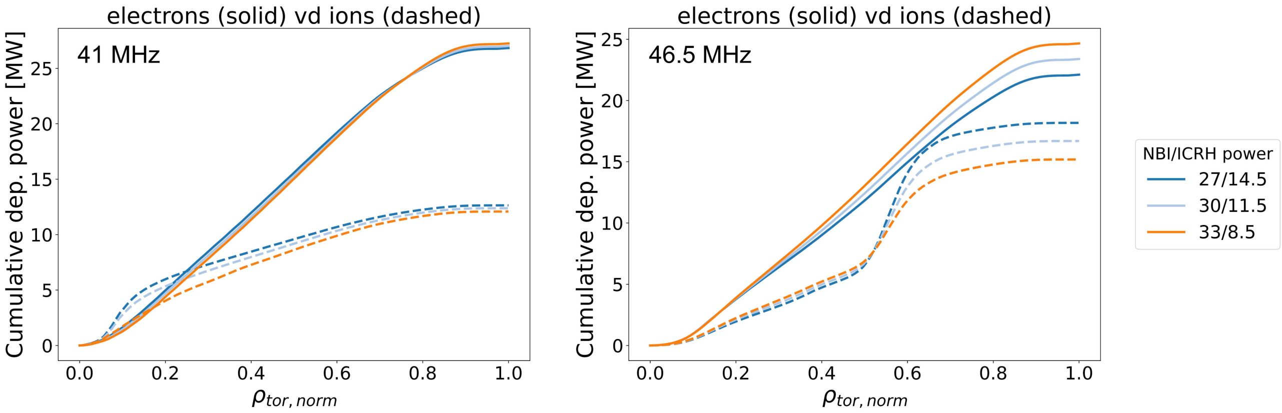

Figure 6.13: Radial profiles of the cumulative deposited power for the parametric scan on the NBI/ICRH power ratio performed considering 41 MHz (left) and 46.5 MHz (right) as IC wave frequencies.

From the wave power absorption perspective, no significant differences are observed, aside from a reduction in the wave power absorbed by the D beam ions when decreasing the NBI power (and corresponding injection energy). This behaviour is expected since lowering the NBI power (and energy) modifies the Doppler shift contribution to the resonance condition, moving the resonance layer in a slightly different position than the one at the observed frequency (46.5 MHz). Moreover, the number of injected fast ions available for the interaction with the IC wave field is reduced when reducing the NBI power, in this case passing from a volume-averaged fast particle density $\langle n_{\mathrm{fast}}\rangle_{\mathrm{vol}} = 1.17 \times 10^{20}$ m^{-3} when injecting 33 MW to $\langle n_{\mathrm{fast}}\rangle_{\mathrm{vol}} = 0.99 \times 10^{20}$ m^{-3} at 27 MW. The impact on beam EP dynamics due to the NBI/ICRH power mix variation is more evident when considering the power deposited after collisions. The integrated power deposited to electrons and ions are reported in figure 6.14 for both synergistic and no-synergy cases.

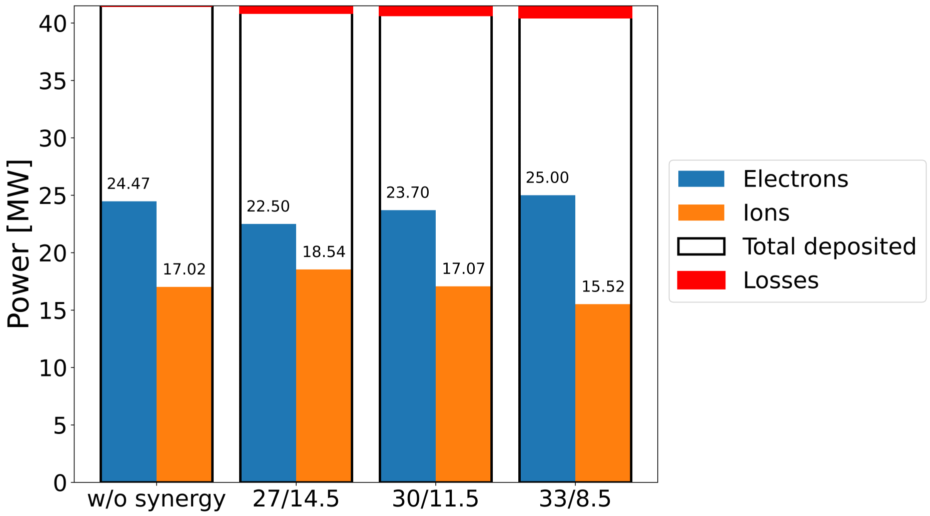

Figure 6.14: Power deposited to electrons and ions for different NBI/ICRH power ratios. A fixed total injected power of 41.5 MW is considered. Power losses are reported in red, on top of the bar representing the total amount of power deposited to the plasma. The no-synergy case /w/o synergy) consider the NBI/ICRH ratio of 33/8.5 MW.

In all the analysed cases, the larger fraction of deposited power is transferred to electrons. Increasing the NBI power, while reducing ICRH, leads to a further enhancement of electron heating. The higher the energy of the beam particles, the higher is the fraction of power deposited on electrons. Higher NBI power, moreover, is associated with a modest increase in power losses to the wall, which nevertheless remain small, for a maximum of $\sim$ 2.5% of the total injected power (NBI+ICRH) obtained for the 33/8.5 case. The no-synergy case presents no losses, thus linking the losses observed in the cases with NBI-ICRH synergy to the beam particles accelerated by the ICRH.

This section completes the parametric investigation of the NBI–ICRH synergy and its effect on energetic-particle dynamics. The impact on fusion performance of the observed wave power absorption and redistribution is discussed in the following section 6.2.5.

6.2.5 Evaluation of resulting fusion power for different NBI-ICRH synergy configurations

The aim of this final section is to assess how the observed changes in NBI-ICRH synergy impact the fusion performance of ITER plasmas, which could be of particular interest for the ITER DT-1 phase goals. In this section, the fusion power is evaluated for five significant cases (A, B, C, D, E*) selected from th parametric scans presented above, together with the no-synergy (NS) case introduced in sec. 6.2.4. Case A is the reference configuration, characterized by a wave frequency of 41 MHz, the reference beam geometry (OFF–ON) and a power ratio of 33/8.5 MW. The difference between cases A and NS is on the heating scheme applications: in case A, ICRF waves interacts with beam energetic particles, while in the NS case NBI and ICRH are apply separately. Cases B, C and D operate at a higher frequency of 46.5 MHz. While B and C consider the same power ratio of case A (33/8.5), case D modify the power balance to 27/14.5. The beam geometry also changes across these cases: B uses the OFF-OFF configuration, case C adopts an ON–ON configuration, while D uses the standard one (OFF-ON). Case E* is a newly introduced configuration that combines the most favourable features identified in the previous scans, i.e those leading to enhanced D NBI absorption in the core region and an higher fraction of power delivered to ions, conditions expected to enhance the fusion power. It consists of an ON-ON injection configuration, an RF wave frequency of 46.5 MHz and a NBI/ICRH power mix of 27/14.5 MW. The main characteristics of all cases are summarized in table 6.1, where the corresponding fusion power values, computed through a tool available within the FOPLA code, are also reported.

	Name	**NS**	**A**	**B**	**C**	**D**	**E***
Scan	**Frequency**	41 MHz	41 MHz	46.5 MHz	46.5 MHz	46.5 MHz	46.5 MHz
	Geometry	OFF-ON	OFF-ON	OFF-OFF	ON-ON	OFF-ON	ON-ON
	Ratio	33+8.5	33/8.5	33/8.5	33/8.5	27/14.5	27/14.5
Fusion Power [MW]	$\mathrm{D_{th}-D_{th}}$	0.49	0.50	0.50	0.49	0.50	0.50
	$\mathrm{D_{th}-D_{beam}}$	0.14	0.14	0.14	0.15	0.11	0.14
	$\mathrm{T_{th}-T_{th}}$	1.98	1.99	1.99	1.99	2.00	2.01
	$\mathrm{D_{th}-T_{th}}$	535.01	535.00	532.77	533.59	536.00	536.68
	$\mathrm{D_{beam}-T_{th}}$	5.55	5.31	5.14	5.53	4.63	5.48
	α	134.18	134.12	133.52	133.83	134.20	134.58
	Total	**677.35**	**677.06**	**674.05**	**675.59**	**677.43**	**679.38**

Table 6.1: Generated fusion power for representative cases collected from the previous sections (A, B, C, D), including the non-synergistic (NS) case where NBI and ICRH contribution are summed from NBI only and ICRH only simulations. E* represents the new configuration considered in this section, which combines the most favourable features identified through the parametric scans. The fusion power is reported distinguishing among the following reactions: $\mathrm{D_{th}-D_{th}}$, $\mathrm{D_{th}-D_{beam}}$, $\mathrm{T_{th}-T_{th}}$, $\mathrm{D_{th}-T_{th}}$, $\mathrm{D_{beam}-T_{th}}$. Alpha power (α), consists of 1/5 of the total fusion power.

As shown in table 6.1, the total fusion power varies weakly across the analysed configurations. The reference case (case A) predicts a total fusion power of approximately 677 MW, very close to that of the no-synergy case. This indicates that, as expected for this scenario, the combined application of ICRH and NBI does not enhance fusion performance. In particular, a small reduction in $\mathrm{D_{beam}-T_{th}}$ reactions is observed. This behaviour can be attributed to the acceleration due to ICRH of a larger fraction of beam ions to energies exceeding the peak of the DT fusion cross section (around 100 keV, fig. 1.3). Among the synergistic cases, the minimum value of fusion power, 674.05 MW, is estimated for case B, likely due to the OFF-OFF configuration which is less favourable for the D NBI absorption. The maximum fusion power instead, 679.38 MW, corresponds to case E*, where the parameters are chosen to maximize NBI–ICRH synergy on purpose. The fusion reactions between deuterium and tritium thermal populations ($\mathrm{D_{th}-T_{th}}$) are the most productive in terms of fusion power. This is consistent with the design of the analysed ITER scenario, which has indeed been designed to obtain a $Q = 10$ factor exploiting the high reactivity from thermal population through high density and high-temperature profiles. The second most significant contribution to fusion power, excluding the alpha power which corresponds to roughly one-fifth of the total fusion power produced [2], arises from $\mathrm{D_{beam}-T_{th}}$ reactions.

Overall, the variations in total fusion power remain below 1%, indicating that the NBI-ICRH synergy, under ITER baseline conditions, does not constitute a primary driver for fusion performance enhancement. nevertheless, parametric analysis as the one performed in this work provides a systematic means to identify which specific parameters (or combination) can enhance, or degrade, the synergy in a given scenario.

6.3 Conclusions of the chapter

This chapter presented a parametric study aimed at assessing the impact of beam and wave parameters on the combined application of NBI and ICRH in an ITER D-T fusion plasma. The NBI-ICRH synergy is evaluated by estimating the fraction of wave power absorbed by the beam ion population and the resulting redistribution of power via collisions to plasma electrons and ions. To evaluate the effect of this synergy on the overall plasma performance, fusion power is computed for a selected set of representative cases.

NBI and ICRH systems will be both employed during DT-1 phase on DT plasmas, aiming at reaching Q = 10 ITER goal. The NBI-ICRH synergy is therefore here evaluated for an ITER representative DT baseline plasma. The effect of tungsten impurities has been examined. While beryllium was found to absorb a non-negligible fraction of the ion cyclotron power (from previous study in [89]), tungsten wave power absorption is shown here to be negligible, independently of the W charge state. Tungsten therefore does not play a significant role in wave power absorption and energetic-particle dynamics in the analysed scenario. The wave frequency scan discussed in section 6.2.2, demonstrates that the ICRH frequency strongly influences wave-particle interactions. Due to Doppler-shift effects, beam ions resonate with the waves at frequencies different from those of thermal ions, with a Doppler shift contribution that increases with particle energy. The strongest NBI-ICRH synergy is obtained in the frequency range between 46 MHz and 49 MHz, where beam EP wave power absorption is localised in the plasma core. Enhanced beam EP wave power absorption leads to an increased EP core power deposition through the collisional relaxation of IC-accelerated deuterium beam ions. Only ON-axis NBI results in a substantial enhancement of beam EP wave power absorption when considering RF frequencies resonant with the beam population, e.g. 46.5 MHz, as observed in sec. 6.2.3. In particular, the ON–ON configuration, with both beams vertically tilted towards the magnetic axis, approximately doubles the deuterium beam absorption of ICRH power compared to the standard beam injection configuration OFF-ON, when instead one beam line is downward tilted to inject off-axis. The ON-ON beam geometry configuration results in a more pronounced central power deposition after EP slowing down. These results indicate that NBI geometry represents a possible control parameter for tailoring the NBI–ICRH synergy. The NBI-to-ICRH power ratio, discussed in section 6.2.4, is seen to have a role in determining the final EP power deposition to different plasma species. Increased plasma ion heating is favoured by reducing the NBI power in favour of ICRH. Larger power loss is instead observed while increasing the NBI power, despite remaining small overall. Finally, fusion plasma performance has been evaluated for representative NBI-ICRH synergy cases (sec. 6.2.5). The variation of the total fusion power among the analysed configurations is small ($< 1\%$), including a no-synergy case where NBI and ICRH contribution are summed without considering possible RF wave interaction with beam particles. The analysed beam and wave parameters (frequency, beam geometry and power ratio) have an effect on the power deposition to plasma electrons and ions, but are not significantly influencing the output fusion power. This behaviour is expected, as the selected scenario assumes that the majority of the fusion power originates from the background plasma. It therefore confirms the role of the heating systems in achieving and maintaining the target scenario.

Part III

CONCLUSIONS

CHAPTER

7

CONCLUSIONS

This thesis has investigated the physics of energetic particles generated by neutral beam injection and ion cyclotron resonance heating in magnetically confined plasmas, with applications to the JET, DTT, and ITER tokamaks. Energetic particles play a central role in fusion plasmas, not only as a source of heating, required to reach and sustain fusion-relevant temperatures, but also because of their contribution to current drive, plasma rotation, and overall confinement properties. Accurate characterization of EP distribution functions and dynamics through numerical modelling is therefore essential to support the optimisation of auxiliary heating systems in present and future devices and to subsequently evaluate their impact on plasma performance, stability, and transport. While detailed conclusions for each performed analysis have been provided at the end of chapters 4, 5, 6, this conclusive chapter offers an integrated perspective of the main outcomes, describing also possible future applications and work.

The NBI modelling studies performed in this thesis are based on the orbit following Monte Carlo ASCOT suite of codes [26, 27, 87] simulations. ASCOT is a state-of-the-art code, widely adopted within the energetic particle physics community, being a validated tool for the analysis and optimisation of neutral beam injection systems. The capability to quantify energetic particle losses in real geometry, power deposition, current drive and torque profiles makes it well suited for predictive applications to both DTT and ITER relevant plasmas presented in this thesis. In the case of DTT, the modelling focused on exploring NBI operation in low-density, high-injection-energy configurations [79], charactering the beam EP behavior through the use of different distribution functions. For ITER, the analysis investigated the impact of different NBI injection configurations on energetic particle orbit populations. The synergy with the EPCoM code [40], an IMAS-compatible tool designed to provide realistic energetic particle distribution functions whose development was partially supported by this work, allows to characterize EP distribution functions in the constants of motion phase space and connect neutral beam application results to the EP orbit populations.

Modelling ICRH wave interactions with the thermal particle population using orbit-following Monte Carlo approaches enables the inclusion of key energetic-particle effects, such as finite orbit width and magnetic drifts. Such effects are not accounted for in simplified or reduced models but are expected to play an increasingly important role in reactor-scale plasmas. At the same time, this modelling highlights the intrinsic complexity of ICRH physics, both conceptually and computationally. This thesis focuses on the ICRH application to JET and ITER devices, modelled through the orbit following

Monte Carlo ASCOT code, coupled with the quasilinear operator RFOF for including wave-particle physics [28], using wave fields computed by the CYRANO full-wave code [92]. The obtained results are qualitatively consistent with the expected wave-particle interaction physics, for example exhibiting broader power deposition profiles associated with finite orbit width effects, as well as variations in the confinement of accelerated EPs when wave spectra with opposite toroidal mode numbers are considered. However, further refinement of the adopted modelling workflow is required to achieve quantitatively reliable predictions for both JET and ITER.

The investigation of NBI–ICRH synergy required both physics comprehension and modelling techniques developed in the modelling of neutral beam injection and ion cyclotron heating, enabling a unified analysis of their combined impact on energetic particle dynamics in ITER plasmas. A dedicated study was carried out to assess how key system parameters influence the NBI–ICRH synergy, exploiting a modelling framework that involved the ASCOT suite of code, the CYRANO full-wave code and the 1D Fokker-Planck solver FOPLA [97]. In particular, the role of ICRH wave frequency, NBI injection geometry, and the combined NBI–ICRH power mix was examined. For specific combinations of these parameters, the NBI-ICRH synergy can be either enhanced or reduced in a controlled manner. While this modulation does not substantially affect fusion power, specifically in a reference scenario designed to maximise fusion reactions from background plasma species interactions, it does alter the dynamics and distribution functions of the energetic particle population. The observed numerical trends motivate future targeted experimental investigations to assess whether synergy effects play a more significant role, also in terms of stability and transport of the EP in ITER.

7.1 Applications and future works

The energetic particle characterisation performed in this thesis can be extended to different plasma conditions and magnetic confinement devices. The modelling strategies applied here can be extended to other scenarios, supporting both present-day experiments and future reactor-relevant studies. In this context, the expertise developed during this work allowed to contribute on integrated modelling activities for scenario development, particularly for the ITER baseline reference scenario [129], and through ongoing collaborations on the development of new plasma scenarios for DTT, e.g. DTT hybrid scenarios [130]. Although NBI-ICRH synergy studies are also planned for DTT, building on the IMAS framework and the workflow established for ITER, further verification of the current ICRH modelling strategy is required before such analyses can be reliably extended to DTT, as discussed below. The results of this thesis are also directly relevant to stability and transport studies, which require realistic energetic-particle distribution functions as input [131], and may also support diagnostic-oriented applications, including the tomographic reconstruction of energetic-particle distributions [132].

The activities carried out within the IMAS framework in this thesis emphasise the importance of integrated modelling frameworks in which multiple codes can operate using a common input–output data structure. Such approach indeed simplified the combined use of different modelling tools, as required for NBI-ICRH synergy studies, and enabled the coupling of energetic particle physics with e.g. plasma stability analyses, through tools such as EPCoM and the energetic particle stability workflow [102]. The same capability is particularly valuable for systematic cross-verification exercises in the context of ICRH modelling, in light of the limitations identified in this work. Disentangling numerical issues from modelling assumptions requires structured benchmarking activities, such as the use of alternative Fokker-Planck solvers, e.g. SPOT-RFOF [101, 117], applied to wave fields computed with the full-wave CYRANO code, or the application of the ASCOT-RFOF orbit-following code to wave field solutions produced by different ICRH codes, e.g. TORIC/SSFPQL [122, 133]. Morevoer, while orbit-following approaches are essential to capture the full complexity of NBI- and ICRH-driven energetic particle physics, their computational cost currently prevent their use in real-time or fast-response integrated modelling frameworks. A particularly promising extension of this work lies in the development of surrogate models capable of reproducing accurate outputs of orbit-following Monte Carlo simulations while reducing the computational cost. Such tools would enable physics-rich energetic particle modelling to be incorporated into transport suites and/or integrated modelling framework for experiment planning and scenario optimisation.

APPENDIX

A

ASCOT-RFOF REVITALISATION

This appendix summarizes part of the work carried out for the revitalization of the ASCOT–RFOF actor within the IMAS framework. This activity has been carried out with the help and supervision of Dr. Sipilä, who worked on the RFOF implementation in IMAS. The developments implemented in the present work are documented in the next sections, with the aim of helping future users or developers in identifying which parts of the code were modified. The appendix is organized according to the issues encountered during the development process. For each issue, the underlying problem is described together with the implemented solution.

A.1 MPI parallelization

Initial IMAS ASCOT–RFOF simulations could not be successfully executed using more than one MPI process. While runs performed with a single MPI process converged correctly within a reasonable computational time, simulations employing two or more MPI processes failed to reach convergence within the expected simulation time. The issue was attributed to the handling of MPI parallelization during the evaluation of the electric field normalization factor.

This normalization factor is computed based on the wave power absorbed by particles in ASCOT–RFOF, here denoted as P_{abs} and compared to the absorbed power stored in the waves IDS (denoted as "absorbed P"), which is provided by CYRANO. The comparison is used to assess whether the electric-field amplitude is consistent with the expected absorbed power or whether a different normalization is required. When running with a single MPI process, P_{abs} and "absorbed P" are in agreement (a snapshot of the output is provided in figure A.1 showing P_{abs} and "absorbed P" on the red squared). However, for simulations using two or more MPI processes, discrepancies between these two quantities were observed, causing the normalization procedure to be repeated multiple times and without reaching a convergence. An examples of such inconsistency is shown in the snapshot of the ASCOT-RFOF output in figure A.2 for $\#MPI \geq 2$.

To resolve this issue, an MPI reduction was introduced using the `mpi_allreduce` function within the subroutine `update_efield_normalisation` located in the Fortran source file `rfof/src/RFOF_Efield_update.F90` as shown in figure A.3. This modification ensures that the absorbed power is correctly summed across all MPI processes before being used in the normalization procedure. Appropriate care was taken to correctly initialize the new variables, evaluate P_{abs} and deallocate memory as required.

With these changes, the discrepancy between P_{abs} and “absorbed P” was resolved, and the execution time of simulations using multiple MPI processes was significantly reduced.

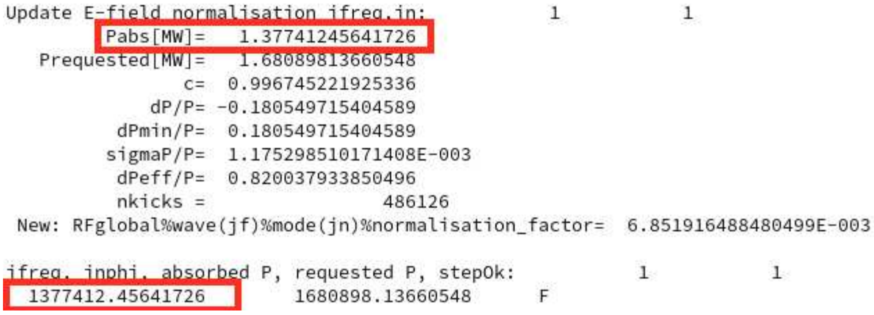

```
Update E-field normalisation ifreq,jn:           1           1
      Pabs[MW]=   1.37741245641726
   Prequested[MW]=   1.68089813660548
                 c=  0.996745221925336
              dP/P= -0.180549715404589
           dPmin/P=  0.180549715404589
          sigmaP/P=  1.175298510171408E-003
           dPeff/P=  0.820037933850496
            nkicks =              486126
 New: RFglobal%wave(jf)%mode(jn)%normalisation_factor=  6.851916488480499E-003

ifreq, inphi, absorbed P, requested P, stepOk:           1           1
  1377412.45641726       1680898.13660548      F
```

Figure A.1: Snapshot of the ASCOT-RFOF output reporting the values of P_{abs} and “absorbed P” for a simulation performed using a single MPI process.

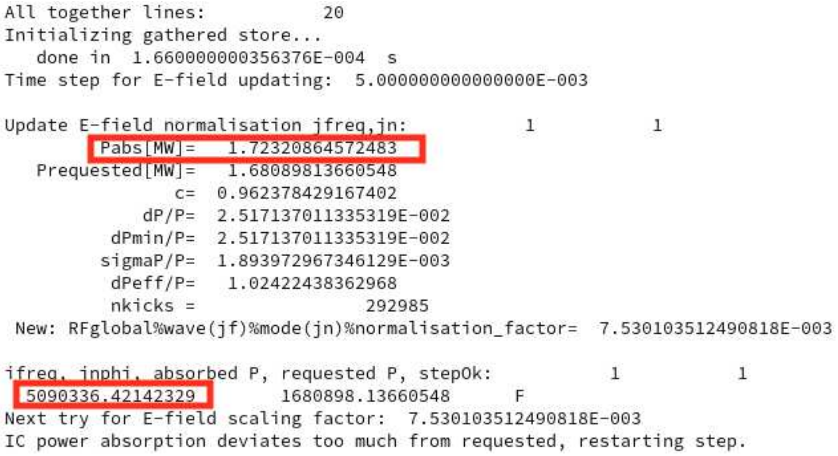

```
All together lines:          20
Initializing gathered store...
   done in  1.660000000356376E-004  s
Time step for E-field updating:  5.000000000000000E-003

Update E-field normalisation ifreq,jn:           1           1
      Pabs[MW]=   1.72320864572483
   Prequested[MW]=   1.68089813660548
                 c=  0.962378429167402
              dP/P=  2.517137011335319E-002
           dPmin/P=  2.517137011335319E-002
          sigmaP/P=  1.893972967346129E-003
           dPeff/P=   1.02422438362968
            nkicks =              292985
 New: RFglobal%wave(jf)%mode(jn)%normalisation_factor=  7.530103512490818E-003

ifreq, inphi, absorbed P, requested P, stepOk:           1           1
  5090336.42142329       1680898.13660548      F
Next try for E-field scaling factor:  7.530103512490818E-003
IC power absorption deviates too much from requested, restarting step.
```

Figure A.2: Snapshot of the ASCOT-RFOF output reporting the values of P_{abs} and “absorbed P” for a simulation performed using a multiple MPI processes.

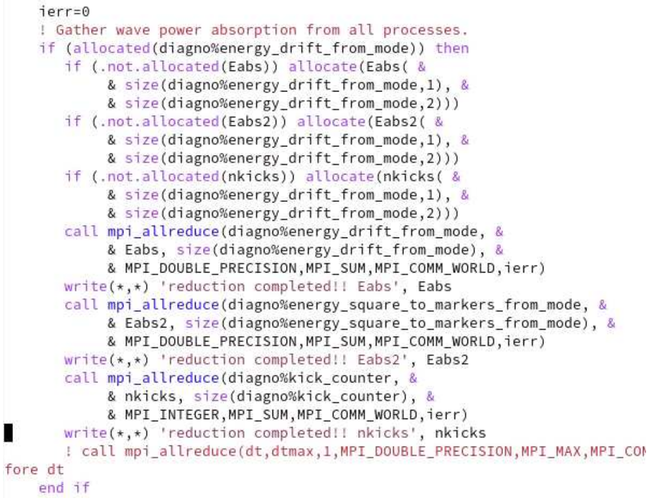

```
    ierr=0
    ! Gather wave power absorption from all processes.
    if (allocated(diagno%energy_drift_from_mode)) then
       if (.not.allocated(Eabs)) allocate(Eabs( &
            & size(diagno%energy_drift_from_mode,1), &
            & size(diagno%energy_drift_from_mode,2)))
       if (.not.allocated(Eabs2)) allocate(Eabs2( &
            & size(diagno%energy_drift_from_mode,1), &
            & size(diagno%energy_drift_from_mode,2)))
       if (.not.allocated(nkicks)) allocate(nkicks( &
            & size(diagno%energy_drift_from_mode,1), &
            & size(diagno%energy_drift_from_mode,2)))
       call mpi_allreduce(diagno%energy_drift_from_mode, &
            & Eabs, size(diagno%energy_drift_from_mode), &
            & MPI_DOUBLE_PRECISION,MPI_SUM,MPI_COMM_WORLD,ierr)
       write(*,*) 'reduction completed!! Eabs', Eabs
       call mpi_allreduce(diagno%energy_square_to_markers_from_mode, &
            & Eabs2, size(diagno%energy_square_to_markers_from_mode), &
            & MPI_DOUBLE_PRECISION,MPI_SUM,MPI_COMM_WORLD,ierr)
       write(*,*) 'reduction completed!! Eabs2', Eabs2
       call mpi_allreduce(diagno%kick_counter, &
            & nkicks, size(diagno%kick_counter), &
            & MPI_INTEGER,MPI_SUM,MPI_COMM_WORLD,ierr)
       write(*,*) 'reduction completed!! nkicks', nkicks
       ! call mpi_allreduce(dt,dtmax,1,MPI_DOUBLE_PRECISION,MPI_MAX,MPI_CO
fore dt
    end if
```

Figure A.3: Snapshot of the changes performed in subroutine `update_efield_normalisation`, defined within Fortran source file `rfof/src/RFOF_Efield_update.F90`.

A.2 Resolution of aborted particles related to wall geometry

Aborted particles were observed in the initial simulations performed with ASCOT–RFOF. Two possible causes were identified: an incomplete or incorrect wall geometry definition, and a magnetic field equilibrium defined on a grid that does not extend up to the physical wall of the tokamak. Both issues were present in the simulations considered here. The first issue is related to the way ASCOT–RFOF interprets the wall geometry from the *wall* IDS, while the second is related to improper CHEASE parameter settings and is therefore not discussed further in this appendix.

The *wall* IDS contains the geometric description of plasma-facing components, including the first wall (FW) and the divertor. The issue encountered in ASCOT–RFOF arises from the fact that the FW and divertor geometries are stored in separate entries of the *wall* IDS (`wall/description_2d/limiter/unit`), whereas ASCOT–RFOF assumes the entire wall geometry to be contained within `wall/description_2d/limiter/unit(1)`. As a result, only the FW boundary is correctly read, while the divertor geometry is effectively truncated. Figure A.4 shows the incomplete wall geometry as interpreted by ASCOT–RFOF at the time the issue was identified.

The adopted solution consisted in making ASCOT aware of the presence of multiple wall geometry units and constructing a single, continuous wall boundary by combining the FW and divertor descriptions. This was achieved by modifying the Fortran routine `ids/ids2wallbkg.F90`. The procedure consists of extracting the FW boundary points and the divertor boundary points, stored respectively in `wall/description_2d/limiter/unit(1)` and `wall/description_2d/limiter/unit(2)`, for both the R and z coordinates. The distance between the initial FW point and all divertor points is computed, and the closest divertor point is identified. The same operation is performed for the final FW point. The FW points and the subset of divertor points enclosed between these two minima are then combined to form a closed wall geometry. The resulting wall definition is shown in figureA.5. This modification partially solved the issue of aborted particles in the simulations.

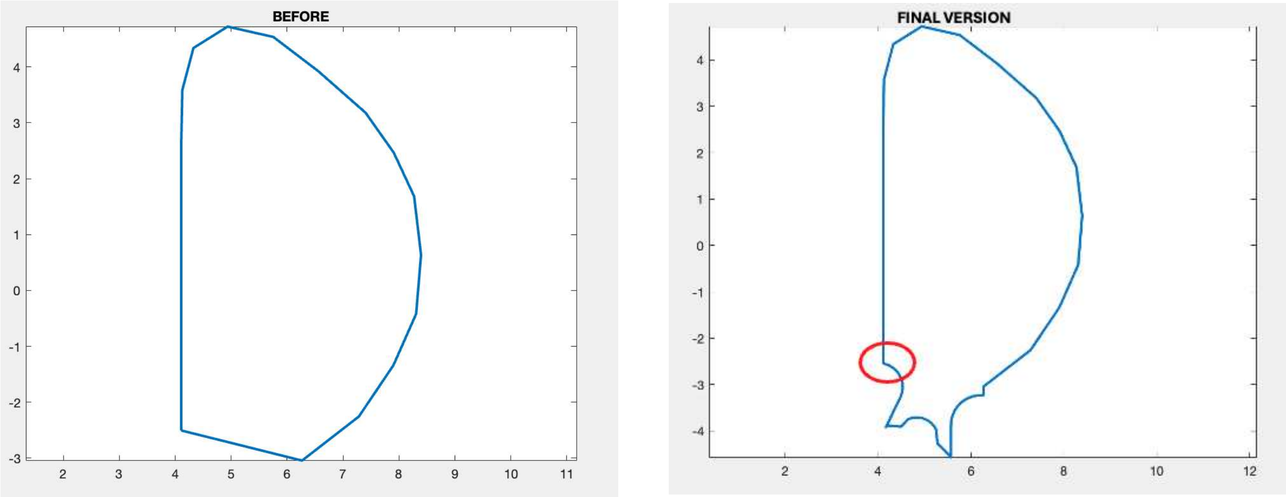

Figure A.4

Figure A.5

Figure A.6: Geometries of the first wall read by ASCOT-RFOF before and after the issue resolution.

A.3 Minor issues

Several minor changes that do not deserve a dedicated section are reported here as a list:

Definition of ”absorbed P” The absorbed power computed by CYRANO (“absorbed P”), used to evaluate the ASCOT–RFOF absorbed wave power (previously denoted as P_{abs}) and to determine the electric-field normalization factor, was found to be incorrectly retrieved from the input. In particular, the absorbed power should correspond to the species of interest for the simulation, which is not necessarily the main plasma species. However, in the initial implementation, ASCOT–RFOF read the absorbed wave power of the first ion species since the parameter for the identification (`use_compositions_ids`) was hard-coded to 1, i.e. the index of the main plasma ion species, in Fortran script `ids/idsRFOFAscot.F90`. In addition, the atomic and mass numbers

(Z, A) used for species identification were not properly initialized and were set to a default value of -999. These issues were resolved through minor code corrections in `ids/idsRFOFAscot.F90`, which are not detailed here.

Maximum and minimum R, z coordinates When applying ASCOT–RFOF to JET, the code stopped because of the generation of markers outside the allowed R and z boundaries. This behaviour was attributed to hard-coded values of R, z limits (R_{min}, R_{max}, z_{min}, z_{max}) for ITER in the Fortran script `RFOF_parameters.F90`. The issues was solved by modifying the Fortran script, allowing user-defined R, z limits in the relative actor parameter files, where R_{min}, R_{max}, z_{min}, z_{max}) are now available.

PAPERS AND CONFERENCE CONTRIBUTIONS

First author

C. De Piccoli, P. Vincenzi, F. Veronese, P. Agostinetti, I. Casiraghi, A. Castaldo, P. Mantica, A. Murari, T. Bolzonella, *Divertor Tokamak Test: Impact of NBI shine-through and beam-plasma interaction on Divertor Tokamak Test facility*, Frontiers in Physics, 12:1492095 (2024).
DOI: https://doi.org/10.3389/fphy.2024.1492095

C. De Piccoli, G. Brochard, E. Lerche, M. Schneider, S. Sipilä, D. Van Eester, P. Vincenzi, T. Bolzonella, *Modelling NBI and ICRH synergy in ITER plasmas* in the 21st European Fusion Theory Conference (2025, Aix-en-Provence).

C. De Piccoli, E. Lerche, M. Schneider, S. Sipilä, D. Van Eester, P. Vincenzi, L.-G. Eriksson, T. Bolzonella, *ASCOT-RFOF modelling of JET and ITER distribution functions of energetic particles accelerated by ion cyclotron heating within the IMAS framework* in the 51st EPS Conference (2025, Vilnius).

C. De Piccoli, M. Schneider, P. Vincenzi, T. Bolzonella, *Exploring the role of auxiliary heating systems in ITER* in the AIV XXVII Conference (2025, Turin).

C. De Piccoli, P. Vincenzi, T. Bolzonella, *NBI energetic particle confinement and orbit characterization for Divertor Tokamak Test plasma scenarios* in the 20th European Fusion Theory Conference (2023, Padova).

C. De Piccoli, T. Bolzonella, P. Vincenzi, M. Cecconello, M. Vallar, *Evaluation of DTT NBI energetic particle confinement and prompt-losses through the constant of motion phase space* in the 49th EPS Conference (2023, Bordeaux).

Co-author

G. Giruzzi et al., *The Divertor Tokamak Test facility research plan*, submitted in Nuclear Fusion (2026)

F. Romanelli et al., *Divertor Tokamak Test facility project: status of design and implementation*, Nuclear Fusion, 64 (2024) 112015.
DOI: `https://doi.org/10.1088/1741-4326/ad5740`

F. Crisanti et al., *Physics basis for the divertor tokamak test facility*, Nuclear Fusion, 64 (2024) 106040.
DOI: `https://doi.org/10.1088/1741-4326/ad6e06`

F. Crisanti, G. Giruzzi, P. Martin et al., *DTT Research Plan*, ENEA editors (2024).
Available at: `https://www.pubblicazioni.enea.it/le-pubblicazioni-enea/edizioni-enea/anno-2024/divertor-tokamak-test-facility-research-plan-version-1-0.html`

P. Vincenzi, P. Agostinetti, R. Ambrosino, T. Bolzonella, I. Casiraghi, A. Castaldo, C. De Piccoli, G. Granucci, P. Mantica, L. Pigatto, A. Snicker, M. Vallar, *Interaction of high-energy neutral beams with Divertor Tokamak Test plasma*, Fusion Engineering and Design, 189 (2023) 113436.
DOI: `https://doi.org/10.1016/j.fusengdes.2023.113436`

G. Brochard, W. W. Heidbrink, M. Van Zeeland, C. De Piccoli, X. Bonnin, A. Bierwage, Z. Lin, M. Schneider, S. D. Pinches, *Method for realistic energetic particle distribution description, and gyrokinetic application for BAE stability in DIII-D plasmas* in the 21st European Fusion Theory Conference (2025, Aix-en-Provence).

C. Bourdelle, F. Koechl, E. Tholerus, M. Schneider, F. Casson, C. De Piccoli, F. Eriksson, D. Fajardo, S.-H. Kim, L. Garzotti, E. Militello-Asp, S. Pinches, A. Polevoi, *ITER* $I_p = 15$ *MA reference cases: sources and profiles in IMAS Data Structure* (2025).

M. Schneider et al., *Integrated modelling activities in support of the ITER re-baseline* in the 30th IAEA Fusion Energy Conference (2025, Chengdu).

G. Brochard, C. De Piccoli, X. Bonnin, M. Schneider, S. D. Pinches, F. Auriemma, A. Bierwage, K. Kirov, M. Fitzgerald, S. Sharapov, *EPCoM: an IMAS-compatible workflow for realistic modelling of energetic particle distributions* in the 50th EPS Conference (2024, Salamanca).

ORIGINAL CONTRIBUTIONS

Within this Ph.D. project, I contributed to deepen the understanding of the Energetic Particle (EP) dynamics and to the improvement of numerical models for simulating different auxiliary heating systems in next-generation fusion devices. This work combines methodological developments, code validation activities and physics investigations on an essential component of present and future fusion experiments, involving state-of-the-art modelling tools. These results support ongoing efforts toward reliable predictive simulations for DTT, ITER and future reactors. The original and main contributions of this work can be summarized as follows:

- I performed a comprehensive characterization of NBI in DTT, considering multiple plasma scenarios representative of plasma operations where the neutral beam system will be exploited. This study in particular provided the estimates of the shine-through fractions for multiple beam energies and plasma parameters, and a heuristic formula to easily estimate the expected shine-through loss fraction for DTT plasmas. Moreover, my work includes an application of the constant of motion phase space to estimate the EP orbit population expected in DTT (see chapter 4). The results of the entire investigation have been published in [79], which includes also the estimation of the power heat loads on the first wall and plasma facing components, made possible through this activity. The work has also been presented at the 49th EPS Conference (2023, Bordeaux) [134] and at the 20th European Fusion Theory Conference (2023, Padova) [135].
- I contributed to the development of EPCoM workflow [30] providing high statistic marker populations obtained by ASCOT. EPCoM workflow was then applied to ITER plasmas to study the orbit topology considering different neutral beam injection geometries and its impact on e.g. current drive and torque contributions, as discussed extensively in section 4.3.2.
- I developed a Monte Carlo tool for generating thermal particle populations based on plasma kinetic profiles. This tool, named THED-G (THErmal Distribution Generator), produces marker distributions in terms of spatial coordinates in the (R, z) plane, particle energy and pitch. The methodology and benchmarking for its development are detailed in section 5.1.2, and THED-G has been successfully employed for ICRH modelling of thermal populations, as discussed in Chapter 5. THED-G application is currently available within the IMAS framework and it is an open-source tool [118].
- I actively contributed to the revitalization of the ASCOT-RFOF code within the IMAS framework. This work involved systematic testing and debugging in collaboration with the developers.

While the code has significant potential for EP modelling in the presence of ICRH, being able to include finite orbit width effects and radial transport usually neglected in simpler analytical fokker-planck code, its complexity and computational requirements pose notable challenges. Appendix A summarizes the main issues I encountered and solved within the project, while remaining limitations, particularly related to coupling with CYRANO code and the time-handling of ASCOT-RFOF, are discussed in chapter 5. Although this effort does not bring to a conclusive and successful revitalization, I highlighted key constraints of the current implementation, suggesting possible directions for future improvements and work. The work has been presented at the 51st EPS Conference (Vilnius,2025) [136].

- I investigated the synergy between NBI and ICRH in plasma scenarios relevant to the DT-1 phase of ITER considering tungsten (W) impurities. I analysed how the wave frequency, the input power ratio (NBI-to-ICRH) and the beam injection geometry influence the synergy between beam particles and RF waves in ITER. The scans result in a moderate synergy, with a negligible effects on the fusion power enhancement. However, the EP dynamics and power deposition profiles can be modified by the synergy significantly exploiting different combinations of parameters, as explained in detail in chapter 6. A preliminary work was presented at the 21st European Fusion Theory Conference (2025, Aix-en-Provence) [137] and a manuscript is planned for submission.

ACKNOWLEDGEMENTS

As conclusions of this work, I would like to express my sincere gratitude to all the people who supported me throughout my PhD journey. I am deeply thankful for the overall guidance and encouragement provided by my supervisors, which, in different ways, contributed significantly to my professional development and to the construction of a solid scientific network. I sincerely hope that the our collaboration will continue in the future. In particular, I would like to thank Dr. Tommaso Bolzonella for his constant guidance and valuable advice during my work at Consorzio RFX, as well as for his continuous encouragement of collaborations with different laboratories. These opportunities allowed me to gain several formative experiences, for which I am truly grateful. I also thank Dr. Pietro Vincenzi, who has guided me through this work, being always present both in joyful moments and in more challenging ones, consistently believing in my capabilities. I am deeply thankful for our teamwork and the shared experiences. A special thanks goes to Dr. Mireille Schneider, who taught me an incredible amount of concepts in fast-ion physics and programming, strongly improving my knowledge and computational skills, and helped me grow within an international research environment.

During my Ph.D., I met many researchers with whom I had the pleasure to share fruitful scientific discussions. In particular, I thank Dr. Ernesto Lerche and Dr. Dirk Van Eester for welcoming me into the ICRH physics team and for always being available for discussions; Dr. Lars-Göran Eriksson for his constant availability for discussion and advice; Dr. Seppo Sipilä for his support with ASCOT and ASCOT-RFOF and for the hospitality at Aalto University; and Guillaume Brochard for involving me in the development of the EPCoM tool and for his continuous support. I also wish to thank the entire ASCOT team, the FS group at Consorzio RFX, particularly our coordinator Dr. David Terranova, and all the researchers I met who contributed to my scientific growth.

I am grateful to my office colleagues, Miriam, Yoana, Monia, Matteo, Pasquale, Jacopo, Edoardo, and Federico, and to my other-office colleagues, Luca, Giulio, Margherita, Alessandro, Leonardo, Nicolò, Umberto & Co, for the many enjoyable moments shared both inside and outside the office.

Finally, I thank my boyfriend Luca and my family for their constant support and encouragement throughout this journey. I am really happy to share this achievement with those who have been by my side since the beginning of my passion in physics!

BIBLIOGRAPHY

[1] M. Mathew, “Nuclear energy: A pathway towards mitigation of global warming,” *Progress in Nuclear Energy*, vol. 143, p. 104080, 2022. [Online]. Available: https://www.sciencedirect.com/science/article/pii/S0149197021004340

[2] J. Freidberg, *Plasma physics and fusion energy.* Cambridge University Press, 2007.

[3] Our World in Data. (2025) Nuclear energy. [Online]. Available: https://ourworldindata.org/nuclear-energy

[4] ——. (2025) Energy mix. [Online]. Available: https://ourworldindata.org/energy-mix

[5] National Ignition Facility and Photon Science. NIF website. [Online]. Available: https://lasers.llnl.gov/

[6] First Light Fusion. FLF website. [Online]. Available: https://firstlightfusion.com/

[7] UK Atomic Energy Authority. JET website. [Online]. Available: https://ccfe.ukaea.uk/programmes/joint-european-torus/

[8] DTT scarl. DTT website. [Online]. Available: https://www.dtt-project.it/

[9] ITER Organization. ITER website. [Online]. Available: https://www.{ITER}.org/

[10] National Institute for Fusion Science. LHD website. [Online]. Available: https://www-lhd.nifs.ac.jp/pub/LHD_Project_en.html

[11] Max Planck Institute for plasma physics. W-7x website. [Online]. Available: https://www.ipp.mpg.de/w7x

[12] M. Kikuchi, K. Lakner, and M. Q. Tran, *Fusion Physics.* IAEA, 2012.

[13] M. Salewski, D. Spong, P. Aleynikov, R. Bilato, B. Breizman, S. Briguglio, H. Cai, L. Chen, W. Chen, V. Duarte, R. Dumont, M. Falessi, M. Fitzgerald, E. Fredrickson, M. García-Muñoz, N. Gorelenkov, T. Hayward-Schneider, W. Heidbrink, M. Hole, Y. Kazakov, V. Kiptily, A. Könies, T. Kurki-Suonio, P. Lauber, S. Lazerson, Z. Lin, A. Mishchenko, D. Moseev, C. Muscatello, M. Nocente, M. Podestà, A. Polevoi, M. Schneider, S. Sharapov, A. Snicker, Y. Todo, Z. Qiu, G. Vlad, X. Wang, D. Zarzoso, M. Van Zeeland, F. Zonca, and S. Pinches, “Energetic particle physics: Chapter 7 of the special issue: on the path to tokamak burning

plasma operation," *Nuclear Fusion*, vol. 65, no. 4, p. 043002, mar 2025. [Online]. Available: https://dx.doi.org/10.1088/1741-4326/adb763

[14] T. Ihli, T. Basu, L. Giancarli, S. Konishi, S. Malang, F. Najmabadi, S. Nishio, A. Raffray, C. Rao, A. Sagara, and Y. Wu, "Review of blanket designs for advanced fusion reactors," *Fusion Engineering and Design*, vol. 83, no. 7, pp. 912–919, 2008, proceedings of the Eight International Symposium of Fusion Nuclear Technology. [Online]. Available: https://www.sciencedirect.com/science/article/pii/S0920379608002391

[15] American Society of Mechanical Engineers, Ed., *Fusion Energy and Future Fusion Power Plants*, ser. Turbo Expo, vol. Volume 5: Cycle Innovations, 06 2024. [Online]. Available: https://doi.org/10.1115/GT2024-126730

[16] EUROfusion. DEMO website. [Online]. Available: https://euro-fusion.org/programme/demo/

[17] J. Bucalossi, M. Missirlian, P. Moreau, F. Samaille, E. Tsitrone, D. Van Houtte, T. Batal, C. Bourdelle, M. Chantant, Y. Corre *et al.*, "The WEST project: Testing ITER divertor high heat flux component technology in a steady state tokamak environment," *Fusion Engineering and Design*, vol. 89, no. 7-8, pp. 907–912, 2014.

[18] B. Wan, Y. Liang, X. Gong, J. Li, N. Xiang, G. Xu, Y. Sun, L. Wang, J. Qian, H. Liu *et al.*, "Overview of EAST experiments on the development of high-performance steady-state scenario," *Nuclear Fusion*, vol. 57, no. 10, p. 102019, 2017.

[19] Broader Approach Satellite Tokamak Program. JT-60SA website. [Online]. Available: https://www.jt60sa.org/wp/

[20] JET Team and others, "Physics of high performance JET plasmas in DT," *Nuclear Fusion*, vol. 39, no. 9Y, p. 1227, 1999.

[21] EUROfusion. (2024) Breaking new ground: JET tokamak's latest fusion energy record shows mastery of fusion processes. [Online]. Available: https://euro-fusion.org/eurofusion-news/dte3record/

[22] A. Loarte, R. A. Pitts, T. Wauters, I. Nunes, P. de Vries, S. H. Kim, F. Köchl, A. Polevoi, M. Lehnen, J. Artola, S. Jachmich, A. Pshenov, X. Bai, I. S. Carvalho, M. Dubrov, Y. Gribov, M. Schneider, L. Zabeo, X. Bonnin, S. D. Pinches, F. Poli, G. S. Lopez, M. Merola, F. Escourbiac, R. Hunt, L. Chen, D. Boilson, P. Veltri, N. Casal, M. Preynas, A. Mukherjee, W. Helou, F. Kazarian, S. Willms, I. Bonnet, R. Michling, L. Giancarli, J. van der Laan, M. Walsh, V. Udintsev, R. Reichle, G. Vayakis, A. Fossen, M. Turnyanskiy, A. Becoulet, Y. Kamada, G. Zhuang, G. Xu, X. Gong, J. Huang, M. Jia, R. Ding, J. Qian, Y. Sun, Q. Yang, L. Zhang, M. Xu, L. Zhang, S. Brezinsek, J. Stober, J. Hobirk, F. Rimini, J. Garcia, S. L. Rao, J. Ghosh, D. Sharma, B. Magesh, R. P. Bhattacharya, G. Matsunaga, H. Urano, T. Hirose, K. Ogawa, G. Motojima, C. K. Sung, H. H. Lee, J. K. Park, M. S. Cheon, Y. M. Jeon, S. Konovalov, S. Lebedev, N. Kirneva, Y. Kashchuk, N. Bakharev, X. Chen, A. Bortolon, L. Casali, R. Maingi, F. Turco, K. Schmid, Y. Liu, J. R. Martín-Solís, C. Angioni, I. Pusztai, D. Fajardo, D. Mateev, E. Lerche, D. van Eester, P. Vincenzi, R. Futtersack, V. Bobkov, and L. Colas, "The new ITER baseline, research plan and open R&D issues," *Plasma Physics and Controlled Fusion*, vol. 67, no. 6, p. 065023, jun 2025. [Online]. Available: https://dx.doi.org/10.1088/1361-6587/add9c9

[23] F. G. Rimini, J. Contributors, and the EUROfusion Tokamak Exploitation Team, "40 years of JET operations: a unique contribution to fusion science," *Plasma Physics and Controlled Fusion*, vol. 67, no. 3, p. 033001, feb 2025. [Online]. Available: https://dx.doi.org/10.1088/1361-6587/adaee5

[24] R. Ambrosino, “DTT - Divertor Tokamak Test facility: a testbed for DEMO,” *Fusion Engineering and Design*, vol. 167, pp. 775–779, 2021.

[25] R. Aymar, P. Barabaschi, and Y. Shimomura, “The ITER design,” *Plasma Physics and Controlled Fusion*, vol. 44, no. 5, p. 519, apr 2002. [Online]. Available: https://dx.doi.org/10.1088/0741-3335/44/5/304

[26] E. Hirvijoki, O. Asunta, T. Koskela, T. Kurki-Suonio, J. Miettunen, S. Sipilä, A. Snicker, and S. Äkäslompolo, “ASCOT: Solving the kinetic equation of minority particle species in tokamak plasmas,” *Computer Physics Communications*, vol. 185, no. 4, pp. 1310–1321, 2014. [Online]. Available: https://www.sciencedirect.com/science/article/pii/S0010465514000277

[27] J. Varje, K. Särkimäki, J. Kontula, P. Ollus, T. Kurki-Suonio, A. Snicker, E. Hirvijoki, and S. Äkäslompolo, “High-performance orbit-following code ASCOT5 for Monte Carlo simulations in fusion plasmas,” *arXiv preprint arXiv:1908.02482*, 2019.

[28] T. Johnson, A. Salmi, G. Steinbrecher, L. Eriksson, T. Hellsten, L. J. Höök, M. Schneider, and I. Contributors, “Library for RF Interactions in Orbit Following Codes,” *AIP Conference Proceedings*, vol. 1406, no. 1, pp. 373–376, 12 2011. [Online]. Available: https://doi.org/10.1063/1.3664996

[29] F. Imbeaux, S. D. Pinches, J. B. Lister, Y. Buravand, T. Casper, B. Duval, B. Guillerminet, M. Hosokawa, W. Houlberg, P. Huynh, S. H. Kim, G. Manduchi, M. Owsiak, B. Palak, M. Plociennik, G. Rouault, O. Sauter, and P. Strand, “Design and first applications of the ITER integrated modelling & analysis suite,” *Nuclear Fusion*, vol. 55, 10 2015.

[30] G. Brochard, C. Liu, X. Wei, W. Heidbrink, Z. Lin, N. Gorelenkov, C. Chrystal, X. Du, J. Bao, A. R. Polevoi, M. Schneider, S. H. Kim, S. D. Pinches, P. Liu, J. H. Nicolau, and H. Lütjens, “Saturation of fishbone instability by self-generated zonal flows in tokamak plasmas,” *Phys. Rev. Lett.*, vol. 132, p. 075101, Feb 2024. [Online]. Available: https://link.aps.org/doi/10.1103/PhysRevLett.132.075101

[31] J. Wesson, *Tokamaks*. Clarendon press, Oxford, 2004.

[32] W. Heidbrink and R. White, “Mechanism of energetic-particle transport in magnetically confined plasmas,” *Physics of Plasmas*, vol. 27, 030901, 2020. [Online]. Available: https://doi.org/10.1063/1.5136237

[33] F. Porcelli, R. Stankiewicz, H. L. Berk, and Y. Z. Zhang, “Internal kink stabilization by high-energy ions with nonstandard orbits,” *Physics of Fluids B: Plasma Physics*, vol. 4, no. 10, pp. 3017–3023, 10 1992. [Online]. Available: https://doi.org/10.1063/1.860461

[34] P. Helander, R. J. Akers, and L.-G. Eriksson, “On neutral-beam injection counter to the plasma current,” *Physics of Plasmas*, vol. 12, no. 11, p. 112503, 11 2005. [Online]. Available: https://doi.org/10.1063/1.2121287

[35] P. Vincenzi, M. Schneider, P. Veltri, J. Artaud, A. Loarte, S. Nicolici, C. Poggi, A. Polevoi, and A. Snicker, “ITER NBI operational window and power availability constraints due to shine-through losses,” *Nuclear Fusion*, vol. 65, no. 3, p. 036009, feb 2025. [Online]. Available: https://doi.org/10.1088/1741-4326/adaf41

[36] K. Tobita, T. Nakayama, S. V. Konovalov, and M. Sato, “Reduction of energetic particle loss by ferritic steel inserts in ITER,” *Plasma Physics and Controlled Fusion*, vol. 45, no. 2, p. 133, jan 2003. [Online]. Available: https://doi.org/10.1088/0741-3335/45/2/305

[37] F. Tenney, “Confinement of Energetic Alphas in TCT and Tritons in PLT,” Princeton Univ., NJ (USA). Plasma Physics Lab., Tech. Rep., 1975.

[38] R. White, *The theory of toroidally confined plasmas (third edition)*. Imperial college press, 2014.

[39] C. De Piccoli, "DTT NBI fast particle modelling with Monte Carlo ASCOT code," Laurea Magistrale thesis, Università degli Studi di Padova, Padova, Italy, 2022. [Online]. Available: https://hdl.handle.net/20.500.12608/41605

[40] G. Brochard, C. De Piccoli, X. Bonnin, M. Schneider, S. Pinches, F. Auriemma, A. Bierwage, K. Kirov, M. Fitzgerald, and S. Sharapov, "EPCoM: an IMAS-compatible workflow for realistic modelling of energetic particle distributions," in *50th EPS Conference on Plasma Physics*. European Physical Society, 2024, poster presentation.

[41] A. Choudhuri, *Physics of Fluids and Plasmas: An Introduction for Astrophysicists*. Cambridge University Press, 1998.

[42] R. Dumont, "Waves in plasma," 2017. [Online]. Available: https://cea.hal.science7cel-01463091v1

[43] J. P. Dougherty, "Model fokker-planck equation for a plasma and its solution," *The Physics of Fluids*, vol. 7, no. 11, pp. 1788–1799, 11 1964. [Online]. Available: https://doi.org/10.1063/1.2746779

[44] J. D. Gaffey, "Energetic ion distribution resulting from neutral beam injection in tokamaks," *Journal of Plasma Physics*, vol. 16, no. 2, p. 149–169, 1976.

[45] L. Eriksson and P. Helander, "Monte Carlo operators for orbit-averaged Fokker–Planck equations," *Physics of Plasmas*, vol. 1, no. 2, pp. 308–314, 02 1994. [Online]. Available: https://doi.org/10.1063/1.870832

[46] L. Spitzer Jr, "Physics of fully ionized gases," 1962.

[47] Naval Research Laboratory, *NRL Plasma Formulary*, Naval Research Laboratory, Washington, DC, 2013, editor: J. D. Huba. [Online]. Available: https://library.psfc.mit.edu/catalog/online_pubs/NRL_FORMULARY_13.pdf

[48] Y. Kazakov, D. Van Eester, and J. Ongena, "Plasma heating in present-day and future fusion machines," *Carolus Magnus School proceedings*, vol. 298, pp. 290–297, 2015. [Online]. Available: www.fz-juelich.de/zb/openaccess

[49] R. Koch, "Plasma heating by neutral beam injection," *Fusion Science and Technology*, vol. 45, no. 2T, pp. 183–192, 2004. [Online]. Available: https://doi.org/10.13182/FST04-A482

[50] K. Okano, "Enhancement of the neutral beam stopping cross-section due to circulating fast ions in a toroidal plasma," *Nuclear Fusion*, vol. 31, no. 7, p. 1349, jul 1991. [Online]. Available: https://doi.org/10.1088/0029-5515/31/7/010

[51] I. Chapman, J. Graves, C. Wahlberg, and the MAST Team, "The effect of plasma profile variation on the stability of the n = 1 internal kink mode in rotating tokamak plasmas," *Nuclear Fusion*, vol. 50, no. 2, p. 025018, jan 2010. [Online]. Available: https://doi.org/10.1088/0029-5515/50/2/025018

[52] F. Hinton and M. Rosenbluth, "The mechanism for toroidal momentum input to tokamak plasmas from neutral beams," *Physics Letters A*, vol. 259, no. 3, pp. 267–275, 1999. [Online]. Available: https://www.sciencedirect.com/science/article/pii/S0375960199004533

[53] K.-D. Zastrow, W. Core, L.-G. Eriksson, M. V. Hellermann, A. Howman, and R. König, "Transfer rates of toroidal angular momentum during neutral beam injection," *Nuclear Fusion*, vol. 38, no. 2, p. 257, feb 1998. [Online]. Available: https://doi.org/10.1088/0029-5515/38/2/309

[54] T. Mazouz, “Numerical characterization of energetic particles generated by NBI and applications to the JT-60SA tokamak,” PhD thesis, Université d’Aix-Marseille, Aix-en-Provence, France, 2025.

[55] K.-D. Zastrow, W. Core, L.-G. Eriksson, M. V. Hellermann, A. Howman, and R. König, “Transfer rates of toroidal angular momentum during neutral beam injection,” *Nuclear Fusion*, vol. 38, no. 2, p. 257, feb 1998. [Online]. Available: https://dx.doi.org/10.1088/0029-5515/38/2/309

[56] ITER Physics Expert Group on Energetic Particles, Heating and Current Drive and ITER Physics Basis Editors, “Chapter 6: Plasma auxiliary heating and current drive,” *Nuclear Fusion*, vol. 39, no. 12, p. 2495, dec 1999. [Online]. Available: https://doi.org/10.1088/0029-5515/39/12/306

[57] T. Stix, *Waves in Plasmas.* American Institute of Physics, 1992.

[58] Y. Kazakov, D. Van Eester, R. Dumont, and J. Ongena, “On resonant ICRF absorption in three-ion component plasmas: a new promising tool for fast ion generation,” *Nuclear Fusion*, vol. 55, no. 3, p. 032001, feb 2015. [Online]. Available: https://doi.org/10.1088/0029-5515/55/3/032001

[59] F. Louche and R. Koch, “The coupling of electromagnetic power to plasmas,” *Carolus Magnus School proceedings*, vol. 298, pp. 298–306, 2015. [Online]. Available: www.fz-juelich.de/zb/openaccess

[60] J. Ongena, A. Messiaen, Y. O. Kazakov, R. Koch, R. Ragona, V. Bobkov, K. Crombé, F. Durodié, M. Goniche, A. Krivska, E. Lerche, F. Louche, A. Lyssoivan, M. Vervier, D. Van Eester, M. Van Schoor, T. Wauters, J. Wright, and S. Wukitch, “Recent advances in physics and technology of ion cyclotron resonance heating in view of future fusion reactors,” *Plasma Physics and Controlled Fusion*, vol. 59, no. 5, p. 054002, mar 2017. [Online]. Available: https://doi.org/10.1088/1361-6587/aa5a62

[61] E. Lerche, D. Van Eester, A. Krasilnikov, J. Ongena, P. Lamalle, and J.-E. contributors, “Modelling of D majority ICRH at JET: impact of absorption at the doppler-shifted resonance,” *Plasma Physics and Controlled Fusion*, vol. 51, no. 4, p. 044006, mar 2009. [Online]. Available: https://doi.org/10.1088/0741-3335/51/4/044006

[62] T. Stix, “Fast-wave heating of a two-component plasma,” *Nuclear Fusion*, vol. 15, no. 5, p. 737, oct 1975. [Online]. Available: https://doi.org/10.1088/0029-5515/15/5/003

[63] E. Lerche, M. Goniche, P. Jacquet, D. Van Eester, V. Bobkov, L. Colas, C. Giroud, I. Monakhov, F. Casson, F. Rimini, C. Angioni, M. Baruzzo, T. Blackman, S. Brezinsek, M. Brix, A. Czarnecka, K. Crombé, C. Challis, R. Dumont, J. Eriksson, N. Fedorczak, M. Graham, J. Graves, G. Gorini, J. Hobirk, E. Joffrin, T. Johnson, Y. Kazakov, V. Kiptily, A. Krivska, M. Lennholm, P. Lomas, C. Maggi, P. Mantica, G. Mathews, M.-L. Mayoral, L. Meneses, J. Mlynar, P. Monier-Garbet, M. Nave, C. Noble, M. Nocente, I. Nunes, J. Ongena, G. Petravich, V. Petrzilka, T. Pütterich, M. Reich, M. Santala, E. Solano, A. Shaw, G. Sips, M. Stamp, M. Tardocchi, M. Tsalas, M. Valisa, and J. Contributors, “Optimization of ICRH for core impurity control in JET-ILW,” *Nuclear Fusion*, vol. 56, no. 3, p. 036022, feb 2016. [Online]. Available: https://doi.org/10.1088/0029-5515/56/3/036022

[64] E. Lerche, M. Maslov, P. Jacquet, I. Monakhov, D. King, D. Keeling, C. D. Challis, D. V. Eester, P. Mantica, C. Maggi, J. Garcia, F. Auriemma, R. Coelho, I. Coffey, A. Chomiczewska, E. Delabie, R. Dumont, P. Dumortier, J. Eriksson, J. Ferreira, M. Fitzgerald, M. Fontana, Z. Ghani, N. Hawkes, J. Hobirk, P. Huynh, T. Johnson, A. Kappatou, Y. Kazakov, V. Kiptily, K. Kirov, M. Lennholm, E. d. l. Luna, J. Mailloux, M. Marin, G. Matthews, S. Menmuir, J. Mitchell, M. Nocente, J. Ongena, A. Patel, G. Pucella, E. Rachlew, D. Rigamonti,

F. Rimini, S. Silburn, P. Siren, M. Salewski, E. Solano, Z. Stancar, M. Tardocchi, M. Valisa, and J. contributors, “Fundamental ICRF heating of deuterium ions in JET-DTE2,” *AIP Conference Proceedings*, vol. 2984, no. 1, p. 030005, 08 2023. [Online]. Available: https://doi.org/10.1063/5.0162554

[65] A. Bécoulet, D. J. Gambier, and A. Samain, “Hamiltonian theory of the ion cyclotron minority heating dynamics in tokamak plasmas,” *Physics of Fluids B: Plasma Physics*, vol. 3, no. 1, pp. 137–150, 01 1991. [Online]. Available: https://doi.org/10.1063/1.859951

[66] L.-G. Eriksson, M. J. Mantsinen, T. Hellsten, and J. Carlsson, “On the orbit-averaged monte carlo operator describing ion cyclotron resonance frequency wave–particle interaction in a tokamak,” *Physics of Plasmas*, vol. 6, no. 2, pp. 513–518, 02 1999. [Online]. Available: https://doi.org/10.1063/1.873195

[67] V. Kiptily, F. Cecil, O. Jarvis, M. Mantsinen, S. Sharapov, L. Bertalot, S. Conroy, L. Ingesson, T. Johnson, K. Lawson, S. Popovichev, and contributors to the EFDA-JET Workprogramme, “Gamma-ray diagnostics of energetic ions in JET,” *Nuclear Fusion*, vol. 42, no. 8, p. 999, aug 2002. [Online]. Available: https://doi.org/10.1088/0029-5515/42/8/308

[68] J. Mailloux, N. Abid, K. Abraham, P. Abreu, O. Adabonyan, P. Adrich, V. Afanasev, M. Afzal, T. Ahlgren, L. Aho-Mantila *et al.*, “Overview of JET results for optimising ITER operation,” *Nuclear Fusion*, vol. 62, no. 4, p. 042026, 2022.

[69] K. K. Kirov, Y. Baranov, J. Mailloux, M.-L. Mayoral, M. Nave, J. Ongena, and J. Contributors, “LH power deposition and CD efficiency studies by application of modulated power at JET,” *Nuclear Fusion*, vol. 50, no. 7, p. 075003, 2010.

[70] J. Noterdaeme, L. Eriksson, M. Mantsinen, M. Mayoral, D. V. Eester, J. Mailloux, C. Gormezano, and T. T. C. Jones, “Chapter 9: Physics studies with the additional heating systems in JET,” *Fusion Science and Technology*, vol. 53, no. 4, pp. 1103–1151, 2008. [Online]. Available: https://doi.org/10.13182/FST08-A1749

[71] I. Monakhov, P. Jacquet, P. Dumortier, F. Durodié, E. Lerche, R. Lobel, M.-L. Mayoral, C. Noble, J. Roberts, and H. Sheikh, “Assessment of the JET ICRH system performance since 2000,” *Plasma Physics and Controlled Fusion*, vol. 67, no. 1, p. 015023, dec 2024. [Online]. Available: https://doi.org/10.1088/1361-6587/ad9e73

[72] F. Durodié, P. Chappuis, J. Fanthome, R. Goulding, J. Hosea, P. Lamalle, A. Lorenz, M. Nightingale, L. Semeraro, and F. Wesner, “Main design features and challenges of the ITER-like ICRF antenna for JET,” *Fusion Engineering and Design*, vol. 74, no. 1, pp. 223–228, 2005, proceedings of the 23rd Symposium of Fusion Technology. [Online]. Available: https://www.sciencedirect.com/science/article/pii/S0920379605004011

[73] F. Durodié, M. Nightingale, A. Argouarch, G. Berger-By, T. Blackman, J. Caughman, V. Cocilovo, P. Dumortier, P. Edwards, J. Fanthome, D. Frigione, R. Goulding, M. Graham, J. Hobrik, S. Huygen, S. Jachmich, P. Jacquet, A. Kaye, P. Lamalle, E. Lerche, T. Loarer, M.-L. Mayoral, A. Messiaen, I. Monakhov, M. Nave, K. Nicholls, J. Ongena, F. Rimini, D. Van Eester, M. Vervier, M. Vrancken, C. Sozzi, D. Stork, M. Tsalas, A. Walden, A. Whitehurst, and K.-D. Zastrow, “Commissioning of the ITER-like ICRF antenna for JET,” *Fusion Engineering and Design*, vol. 84, no. 2, pp. 279–283, 2009, proceeding of the 25th Symposium on Fusion Technology. [Online]. Available: https://www.sciencedirect.com/science/article/pii/S0920379609001057

[74] W. Helou *et al.*, “The ITER ICRF system: latest technological developments, coupling studies and compatibility with high-Z wall,” in *29th IAEA Fusion Energy Conference(FEC 2023), Oct*, 2023, pp. 16–21.

[75] F. Crisanti, G. Giruzzi, and P. Martin, *Divertor Tokamak Test facility Research Plan Version 1.0.* Frascati, ITALY: ENEA, 2024.

[76] EUROfusion and K. H. Nordlund, *European Research Roadmap to the Realisation of Fusion Energy.* Germany: EUROfusion, 2018.

[77] P. Barabaschi, A. Fossen, A. Loarte, A. Becoulet, and L. Coblentz, "ITER progresses into new baseline," *Fusion Engineering and Design*, vol. 215, p. 114990, 2025. [Online]. Available: https://www.sciencedirect.com/science/article/pii/S0920379625001905

[78] P. Agostinetti, E. Benedetti, R. Bonifetto, M. Bonesso, M. Cavenago, S. Dal Bello, M. Dalla Palma, D. D'Ambrosio, R. Dima, G. Favero *et al.*, "Improved conceptual design of the beamline for the DTT neutral beam injector," *IEEE Transactions on Plasma Science*, vol. 50, no. 11, pp. 4027–4032, 2022.

[79] C. De Piccoli, P. Vincenzi, F. Veronese, P. Agostinetti, I. Casiraghi, A. Castaldo, P. Mantica, A. Murari, and T. Bolzonella, "Divertor tokamak test: Impact of NBI shine-through and beam-plasma interaction on divertor tokamak test facility," *Frontiers in Physics*, vol. Volume 12 - 2024, 2024. [Online]. Available: https://www.frontiersin.org/journals/physics/articles/10.3389/fphy.2024.1492095

[80] S. W. Yoon, S. Deshpande, A. Loarte, R. Pitts, I. Nunes, P. De Vries, M. Schneider, S. Kim, T. Waunters, J. Artola, S. Jachmich, Y. Kamada, A. Becoulet, , and T. I. R. P. D. GROUP, "The 2024 new baseline ITER research plan," *Proceedings of the 69th IAEA Conference*, 2025, proceedings of the 69th IAEA Conference.

[81] R. S. Hemsworth, D. Boilson, P. Blatchford, M. D. Palma, G. Chitarin, H. P. L. de Esch, F. Geli, M. Dremel, J. Graceffa, D. Marcuzzi, G. Serianni, D. Shah, M. Singh, M. Urbani, and P. Zaccaria, "Overview of the design of the ITER heating neutral beam injectors," *New Journal of Physics*, vol. 19, no. 2, p. 025005, feb 2017. [Online]. Available: https://doi.org/10.1088/1367-2630/19/2/025005

[82] A. Chakraborty, C. Rotti, M. Bandyopadhyay, M. J. Singh, R. Gangadharan Nair, S. Shah, U. K. Baruah, R. S. Hemsworth, and B. Schunke, "Diagnostic neutral beam for ITER—concept to engineering," *IEEE Transactions on Plasma Science*, vol. 38, no. 3, pp. 248–253, 2010.

[83] M. J. Singh, D. Boilson, A. R. Polevoi, T. Oikawa, and R. Mitteau, "Heating neutral beams for ITER: negative ion sources to tune fusion plasmas," *New Journal of Physics*, vol. 19, no. 5, p. 055004, may 2017. [Online]. Available: https://doi.org/10.1088/1367-2630/aa639d

[84] V. Bobkov, R. Bilato, F. Calarco, L. Colas, R. Dux, G. Grenfell, W. Helou, D. Milanesio, R. Ochoukov, F. Paulus, T. Pütterich, G. Urbanczyk, and M. Usoltseva, "ICRF-specific W sources: Advances in minimization in ASDEX Upgrade and near-field based extrapolations to ITER with W-wall," *Nuclear Materials and Energy*, vol. 41, p. 101742, 2024. [Online]. Available: https://www.sciencedirect.com/science/article/pii/S2352179124001650

[85] A. Messiaen, R. Koch, R. Weynants, P. Dumortier, F. Louche, R. Maggiora, and D. Milanesio, "Performance of the ITER ICRH system as expected from topica and antITER ii modelling," *Nuclear Fusion*, vol. 50, no. 2, p. 025026, jan 2010. [Online]. Available: https://doi.org/10.1088/0029-5515/50/2/025026

[86] V. Bobkov, R. Bilato, F. Calarco, H. Faugel, O. Girka, W. Helou, P. Lamalle, V. Maquet, D. Milanesio, R. Ochoukov, V. Polli, W. Tierens, M. Usoltseva, and W. Zhang, "Multi-strap in-port icrf antenna modeling and development in support of ITER and eu-demo," *AIP Conference Proceedings*, vol. 2984, no. 1, p. 060010, 08 2023. [Online]. Available: https://doi.org/10.1063/5.0163035

[87] O. Asunta, J. Govenius, R. Budny, M. Gorelenkova, G. Tardini, T. Kurki-Suonio, A. Salmi, and S. Sipilä, “Modelling neutral beams in fusion devices: Beamlet-based model for fast particle simulations,” *Computer Physics Communications*, vol. 188, pp. 33–46, 2015. [Online]. Available: https://www.sciencedirect.com/science/article/pii/S0010465514003701

[88] S. Suzuki, T. Shirai, M. Nemoto, K. Tobita, H. Kubo, T. Sugie, A. Sakasai, and Y. Kusama, “Attenuation of high-energy neutral hydrogen beams in high-density plasmas,” *Plasma Physics and Controlled Fusion*, vol. 40, no. 12, p. 2097, dec 1998. [Online]. Available: https://dx.doi.org/10.1088/0741-3335/40/12/009

[89] M. Schneider, E. Lerche, D. Van Eester, O. Hoenen, T. Jonsson, V. Mitterauer, S. Pinches, A. Polevoi, E. Poli, and M. Reich, “Simulation of heating and current drive sources for scenarios of the ITER research plan,” *Nuclear Fusion*, vol. 61, no. 12, p. 126058, nov 2021. [Online]. Available: https://doi.org/10.1088/1741-4326/ac34d8

[90] M. Schneider, O. Asunta, T. Johnson, D. Kalupin, and R. Coelho, “Benchmarking neutral beam injection codes within the european integrated modelling framework,” in *European Physical Society Conference on Plasma Physics.* European Physical Society (EPS), 2015.

[91] D. V. Eester, “Modelling particle heating and current drive in fusion machines: brief overview of adopted techniques,” *Carolus Magnus School proceedings*, vol. 298, pp. 366–373, 2015. [Online]. Available: www.fz-juelich.de/zb/openaccess

[92] P. Lamalle, “Nonlocal theoretical generalization and tridimensional numerical study of the coupling of an ICRH antenna to a tokamak plasma,” Ph.D. dissertation, LPP-ERM/KMS Report 101 Universite de Mons, 1994.

[93] M. Mantsinen, P. Jacquet, E. Lerche, D. Gallart, K. Kirov, P. Mantica, D. Taylor, D. Van Eester, M. Baruzzo, I. Carvalho, C. Challis, A. Dal Molin, E. Delabie, E. De La Luna, R. Dumont, P. Dumortier, J. Eriksson, D. Frigione, J. Garcia, L. Garzotti, C. Giroud, R. Henriques, J. Hobirk, A. Kappatou, Y. Kazakov, D. Keeling, D. King, V. Kiptily, M. Lennholm, P. Lomas, C. Lowry, C. Maggi, J. Mailloux, M. Maslov, S. Menmuir, I. Monakhov, R. Morales, C. Noble, M. Nocente, A. Patel, G. Pucella, C. Reux, D. Rigamonti, F. Rimini, A. Sheikh, S. Silburn, P. Siren, E. Solano, Z. Stancar, M. Tardocchi, and J. Contributors, “Experiments in high-performance JET plasmas in preparation of second harmonic ICRF heating of tritium in ITER,” *Nuclear Fusion*, vol. 63, no. 11, p. 112015, oct 2023. [Online]. Available: https://doi.org/10.1088/1741-4326/aceb08

[94] J. Garcia, F. Casson, L. Frassinetti, D. Gallart, L. Garzotti, H.-T. Kim, M. Nocente, S. Saarelma, F. Auriemma, J. Ferreira, S. Gabriellini, A. Ho, P. Huynh, K. Kirov, E. Lerche, M. Mantsinen, V. Zotta, Z. Stancar, D. Taylor, D. Van Eester, C. Challis, and J. Contributors, “Modelling performed for predictions of fusion power in JET DTE2: overview and lessons learnt,” *Nuclear Fusion*, vol. 63, no. 11, p. 112003, oct 2023. [Online]. Available: https://doi.org/10.1088/1741-4326/acedc0

[95] P. Huynh, E. Lerche, D. van Eester, J. Garcia, G. Frazzoli, P. Maget, J. F. Artaud, J. Ferreira, T. Johnson, D. Yadykin, and P. Strand, “ICRF heating and turbulent transport modelling of the WEST L-mode plasma using ETS: interpretative and predictive code validation,” in *48th EPS conference on plasma physics*, Maastricht (Virtual event), Netherlands, Jun. 2022. [Online]. Available: https://cea.hal.science/cea-03740616

[96] L.-G. Eriksson and M. Schneider, “Monte carlo operators for ions interacting with radio frequency waves,” *Physics of Plasmas*, vol. 12, no. 7, p. 072524, 07 2005. [Online]. Available: https://doi.org/10.1063/1.1951347

[97] D. Van Eester, E. Lerche, P. Huynh, and T. Johnson, "A fast tool for ICRH + NBI modelling within the eu-im framework," *Journal of Plasma Physics*, vol. 87, no. 2, p. 855870202, 2021.

[98] M. Romanelli, G. Corrigan, V. Parail, S. Wiesen, R. Ambrosino, P. Belo, L. Garzotti, D. Harting, F. Köchl, T. Koskela *et al.*, "JINTRAC: a system of codes for integrated simulation of tokamak scenarios," *Plasma and Fusion research*, vol. 9, pp. 3 403 023–3 403 023, 2014.

[99] P. Sirén, J. Varje, S. Äkäslompolo, O. Asunta, C. Giroud, T. Kurki-Suonio, H. Weisen, and T. J. Contributors, "Versatile fusion source integrator AFSI for fast ion and neutron studies in fusion devices," *Nuclear Fusion*, vol. 58, no. 1, p. 016023, nov 2017. [Online]. Available: https://doi.org/10.1088/1741-4326/aa92e9

[100] S. Sipilä, J. Varje, T. Johnson, R. Bilato, J. Galdón-Quiroga, A. Snicker, T. Kurki-Suonio, L. Sanchís, D. Silvagni, J. González-Martín, t. A. Upgrade Team, and t. E. MST1 Team, "ASCOT orbit-following simulations of ion cyclotron heating with synthetic fast ion loss diagnostic: a first application to ASDEX Upgrade," *Nuclear Fusion*, vol. 61, no. 8, p. 086026, jul 2021. [Online]. Available: https://doi.org/10.1088/1741-4326/ac0e71

[101] M. Schneider, L.-G. Eriksson, V. Basiuk, and F. Imbeaux, "On alpha particle effects in tokamaks with a current hole," *Plasma Physics and Controlled Fusion*, vol. 47, no. 12, p. 2087, oct 2005. [Online]. Available: https://dx.doi.org/10.1088/0741-3335/47/12/002

[102] V.-A. Popa, P. Lauber, T. Hayward-Schneider, M. Schneider, O. Hoenen, and S. Pinches, "An IMAS-integrated workflow for energetic particle stability," *Nuclear Fusion*, vol. 63, no. 12, p. 126008, sep 2023. [Online]. Available: https://doi.org/10.1088/1741-4326/acf056

[103] "Imas data dictionary documentation," https://imas-data-dictionary.readthedocs.io/en/latest/, ITER Organization, 2025, version 4.1.0-2-g49455d4, accessed 25 November 2025.

[104] I. Casiraghi, P. Mantica, R. Ambrosino, L. Aucone, B. Baiocchi, L. Balbinot, T. Barberis, A. Castaldo, M. Cavedon, L. Frassinetti, P. Innocente, F. Koechl, S. Nowak, P. Agostinetti, S. Ceccuzzi, L. Figini, G. Granucci, and P. Vincenzi, "Core integrated simulations for the divertor tokamak test facility scenarios towards consistent core-pedestal-sol modelling," *Plasma Physics and Controlled Fusion*, vol. 65, no. 3, p. 035017, feb 2023. [Online]. Available: https://doi.org/10.1088/1361-6587/acb6b1

[105] G. V. Pereverzev and P. Yushmanov, "ASTRA. Automated System for TRansport Analysis in a tokamak," 2002.

[106] I. Casiraghi, P. Mantica, F. Koechl, R. Ambrosino, B. Baiocchi, A. Castaldo, J. Citrin, M. Dicorato, L. Frassinetti, A. Mariani, P. Vincenzi, P. Agostinetti, L. Aucone, L. Balbinot, S. Ceccuzzi, L. Figini, G. Granucci, P. Innocente, T. Johnson, H. Nyström, and M. Valisa, "First principle-based multi-channel integrated modelling in support of the design of the divertor tokamak test facility," *Nuclear Fusion*, vol. 61, no. 11, p. 116068, oct 2021. [Online]. Available: https://dx.doi.org/10.1088/1741-4326/ac21b9

[107] F. Crisanti, R. Ambrosino, M. Falessi, L. Gabellieri, G. Giruzzi, G. Granucci, P. Innocente, P. Mantica, G. Ramogida, G. Vlad *et al.*, "Physics basis for the divertor tokamak test facility," *Nuclear Fusion*, vol. 64, no. 10, p. 106040, 2024.

[108] R. Albanese, R. Ambrosino, and M. Mattei, "CREATE-NL+: A robust control-oriented free boundary dynamic plasma equilibrium solver," *Fusion Engineering and Design*, vol. 96-97, pp. 664–667, 2015, proceedings of the 28th Symposium On Fusion Technology (SOFT-28). [Online]. Available: https://www.sciencedirect.com/science/article/pii/S0920379615302167

[109] G. Spizzo, M. Gobbin, P. Agostinetti, R. Albanese, R. Ambrosino, I. Casiraghi, M. Cecconello, M. V. Falessi, G. Granucci, P. Mantica *et al.*, "Collisionless losses of fast ions in the divertor tokamak test due to toroidal field ripple," *Nuclear Fusion*, vol. 61, no. 11, p. 116016, 2021.

[110] M. Gobbin and G. Spizzo, "Orbit simulations of fast ion power loads on the wall of the divertor tokamak test," *Plasma Physics and Controlled Fusion*, vol. 65, no. 7, p. 075013, 2023.

[111] P. Vincenzi, P. Agostinetti, R. Ambrosino, T. Bolzonella, I. Casiraghi, A. Castaldo, C. De Piccoli, G. Granucci, P. Mantica, L. Pigatto *et al.*, "Interaction of high-energy neutral beams with Divertor Tokamak Test plasma," *Fusion Engineering and Design*, vol. 189, p. 113436, 2023.

[112] P. Vincenzi, M. Schneider, and A. Snicker, "Modelling of NBI shine-through in ITER non-nuclear phase to limit heat fluxes on first wall," *Fusion Engineering and Design*, vol. 200, p. 114178, 2024. [Online]. Available: https://www.sciencedirect.com/science/article/pii/S0920379624000322

[113] P. Vincenzi, P. Agostinetti, J. F. Artaud, T. Bolzonella, T. Kurki-Suonio, M. Mattei, M. Vallar, and J. Varje, "Optimization-oriented modelling of neutral beam injection for EU pulsed DEMO," *Plasma Physics and Controlled Fusion*, vol. 63, no. 6, p. 065014, may 2021. [Online]. Available: https://dx.doi.org/10.1088/1361-6587/abf402

[114] F. Veronese, P. Agostinetti, G. Calabrò, F. Crisanti, P. Fanelli, R. Lombroni, and A. Murari, "Comparison among possible design solutions for the stray field shielding system of the dtt neutral beam injector," *Journal of Instrumentation*, vol. 18, no. 06, p. C06018, 2023.

[115] J. Artaud, F. Imbeaux, J. Garcia, G. Giruzzi, T. Aniel, V. Basiuk, A. Bécoulet, C. Bourdelle, Y. Buravand, J. Decker, R. Dumont, L. Eriksson, X. Garbet, R. Guirlet, G. Hoang, P. Huynh, E. Joffrin, X. Litaudon, P. Maget, D. Moreau, R. Nouailletas, B. Pégourié, Y. Peysson, M. Schneider, and J. Urban, "METIS: a fast integrated tokamak modelling tool for scenario design," *Nuclear Fusion*, vol. 58, no. 10, p. 105001, aug 2018. [Online]. Available: https://dx.doi.org/10.1088/1741-4326/aad5b1

[116] D. Van Eester, E. Lerche, E. Pawelec, and E. Solano, "Transient versus steady-state solutions: a qualitative study," *Journal of Plasma Physics*, vol. 90, no. 2, p. 995900201, 2024.

[117] M. Schneider, T. Johnson, R. Dumont, J. Eriksson, L.-G. Eriksson, L. Giacomelli, J.-B. Girardo, T. Hellsten, E. Khilkevitch, V. Kiptily, T. Koskela, M. Mantsinen, M. Nocente, M. Salewski, S. Sharapov, A. Shevelev, and J. Contributors, "Modelling third harmonic ion cyclotron acceleration of deuterium beams for JET fusion product studies experiments," *Nuclear Fusion*, vol. 56, no. 11, p. 112022, aug 2016. [Online]. Available: https://doi.org/10.1088/0029-5515/56/11/112022

[118] C. De Piccoli. (2025) THED-G git repository. [Online]. Available: https://gitlab.com/chiaradepiccoli97/thed-g.git

[119] R. Hawryluk, "An empirical approach to tokamak transport," in *Physics of plasmas close to thermonuclear conditions*. Elsevier, 1981, pp. 19–46.

[120] D. R. Hammett, "Fast ion studies of ion cyclotron range of frequencies heating in the tokamak fusion test reactor," Ph.D. dissertation, Princeton University, Princeton, New Jersey, 1986, princeton Plasma Physics Laboratory Report No. PPPL-2422.

[121] R. W. Harvey, Y. Petrov, E. F. Jaeger, and R. Group, "Validation studies of quasilinear theory of resonant diffusion in the ion cyclotron range of frequencies by comparison with exact integration results," *AIP Conference Proceedings*, vol. 1406, no. 1, pp. 369–372, 12 2011. [Online]. Available: https://doi.org/10.1063/1.3664995

[122] M. Brambilla, “Numerical simulation of ion cyclotron waves in tokamak plasmas,” *Plasma Physics and Controlled Fusion*, vol. 41, no. 1, p. 1, jan 1999. [Online]. Available: https://doi.org/10.1088/0741-3335/41/1/002

[123] C. Angioni, M. Sertoli, R. Bilato, V. Bobkov, A. Loarte, R. Ochoukov, T. Odstrcil, T. Pütterich, J. Stober, and T. A. U. Team, “A comparison of the impact of central ECRH and central ICRH on the tungsten behaviour in ASDEX Upgrade H-mode plasmas,” *Nuclear Fusion*, vol. 57, no. 5, p. 056015, mar 2017. [Online]. Available: https://doi.org/10.1088/1741-4326/aa6453

[124] R. Bilato, A. Polevoi, M. Schneider, M. Brambilla, E. Fable, M. Weiland, Y. O. Kazakov, E. Lerche, A. Loarte, J. Ongena *et al.*, “Synergies between H-NBI fast-ions and ICRF heating in the non-activated operational phase of ITER,” in *45th EPS Conference on Plasma Physics*. European Physical Society, 2018.

[125] J. Joly, J. Garcia, F. Imbeaux, R. Dumont, M. Schneider, T. Johnson, and J. F. Artaud, “Self-consistent modelling of heating synergy between NBI and ICRH in JET deuterium plasmas,” *Plasma Physics and Controlled Fusion*, vol. 61, no. 7, p. 075017, jun 2019. [Online]. Available: https://doi.org/10.1088/1361-6587/ab1f54

[126] G. Cenacchi and A. Taroni, “JETTO: A Free-Boundary Plasma Transport Code,” ENEA, Italy, ENEA Technical Report ENEA-RT-TIB-88-5, 1988.

[127] J. E. Kinsey, G. M. Staebler, and R. E. Waltz, “The first transport code simulations using the trapped gyro-landau-fluid model,” *Physics of Plasmas*, vol. 15, no. 5, p. 055908, 03 2008. [Online]. Available: https://doi.org/10.1063/1.2889008

[128] D. Fajardo, C. Angioni, S. H. Kim, F. Koechl, E. Fable, A. Loarte, A. Polevoi, G. Tardini, and the ASDEX Upgrade Team, “Theory-based integrated modelling of tungsten transport in ITER plasmas,” *Plasma Physics and Controlled Fusion*, vol. 67, no. 1, p. 015020, dec 2024. [Online]. Available: https://doi.org/10.1088/1361-6587/ad9aca

[129] C. Bourdelle, “Integrated modelling of tokamak plasmas: progress and challenges towards ITER operation and reactor design,” *Plasma Physics and Controlled Fusion*, vol. 67, no. 4, p. 043001, 2025.

[130] J. Lombardo, F. Auriemma, A. Castaldo, T. Luda, P. Mantica, G. Rubino, B. Baiocchi, L. Figini, and R. Lorenzini, “DTT hybrid scenario development with ASTRA-TGLF predictive modelling,” in *51st EPS Conference on Plasma Physics*. European Physical Society, 2025.

[131] S. D. Pinches, H. L. Berk, D. N. Borba, B. N. Breizman, S. Briguglio, A. Fasoli, G. Fogaccia, M. P. Gryaznevich, V. Kiptily, M. J. Mantsinen, S. E. Sharapov, D. Testa, R. G. L. Vann, G. Vlad, F. Zonca, and J.-E. Contributors, “The role of energetic particles in fusion plasmas,” *Plasma Physics and Controlled Fusion*, vol. 46, no. 12B, p. B187, nov 2004. [Online]. Available: https://doi.org/10.1088/0741-3335/46/12B/017

[132] M. Rud, L. Eriksson, J. Eriksson, P. Hansen, O. Hyvärinen, H. Järleblad, Y. Kazakov, S. Korsholm, M. Nocente, J. Rasmussen, B. Reman, A. Snicker, A. Valentini, Y. Dong, D. Moseev, and M. Salewski, “Fast-ion phase-space tomography with wave–particle interactions in the ion cyclotron frequency range as prior,” *Nuclear Fusion*, vol. 65, no. 5, p. 056008, apr 2025. [Online]. Available: https://doi.org/10.1088/1741-4326/adc400

[133] M. Brambilla and R. Bilato, “The present status of the TORIC-SSFPQL codes,” *EPJ Web Conf.*, vol. 346, p. 01030, 2026. [Online]. Available: https://doi.org/10.1051/epjconf/202634601030

[134] C. De Piccoli, T. Bolzonella, P. Vincenzi, M. Cecconello, and M. Vallar, “Evaluation of DTT NBI energetic particle confinement and prompt-losses through the constant of motion phase space,” in *49th EPS Conference on Plasma Physics*, Bordeaux, France, 2023, poster.

[135] C. De Piccoli, P. Vincenzi, and T. Bolzonella, “NBI energetic particle confinement and orbit characterization for Divertor Tokamak Test plasma scenarios,” in *20th European Fusion Theory Conference*, Padova, Italy, 2023, poster.

[136] C. De Piccoli, E. Lerche, M. Schneider, S. Sipilä, D. Van Eester, P. Vincenzi, L.-G. Eriksson, and T. Bolzonella, “ASCOT-RFOF modelling of JET and ITER distribution functions of energetic particles accelerated by ion cyclotron heating within the IMAS framework,” in *51st EPS Conference on Plasma Physics*, Vilnius, Lithuania, 2025, poster.

[137] C. De Piccoli, G. Brochard, E. Lerche, M. Schneider, S. Sipilä, D. Van Eester, P. Vincenzi, and T. Bolzonella, “Modelling NBI and ICRH synergy in ITER plasmas,” in *21st European Fusion Theory Conference*, Aix-en-Provence, France, 2025, poster.